



City Research Online

City, University of London Institutional Repository

Citation: Roldán Restrepo, M. (2022). Non-invasive Multimodal Monitoring in Traumatic Brain Injury. (Unpublished Doctoral thesis, City, University of London)

This is the accepted version of the paper.

This version of the publication may differ from the final published version.

Permanent repository link: <https://openaccess.city.ac.uk/id/eprint/31762/>

Link to published version:

Copyright: City Research Online aims to make research outputs of City, University of London available to a wider audience. Copyright and Moral Rights remain with the author(s) and/or copyright holders. URLs from City Research Online may be freely distributed and linked to.

Reuse: Copies of full items can be used for personal research or study, educational, or not-for-profit purposes without prior permission or charge. Provided that the authors, title and full bibliographic details are credited, a hyperlink and/or URL is given for the original metadata page and the content is not changed in any way.

Non-invasive Multimodal Monitoring in Traumatic Brain Injury

María Roldán Restrepo

A thesis submitted to the graduate faculty
in partial fulfilment of the requirements
for the degree of
Doctor of Philosophy
in
Biomedical Engineering



School of Science and Technology
Research Centre for Biomedical Engineering
City, University of London

2022

CONTENTS

Contents.....	ii
Table of Figures.....	vii
Table of Tables.....	xiii
Acknowledgements.....	xiv
Declaration.....	xv
Abstract.....	xvi
Glossary of Common Abbreviations	xvii
Publications resulting from this work	xviii
Journals	xviii
Conference Proceedings	xviii
Award.....	xviii
1 Introduction	1
1.1 Motivation.....	1
1.2 Aims and objectives.	1
1.3 Report Outline.....	3
2 Pathophysiology of the brain in TBI.....	6
2.1 Nervous tissue.....	6
2.1.1 Electrical Signalling by Neurons	8
2.1.2 Synaptic Transmission Between Neurons.....	9
2.1.3 Wallerian degeneration	10
2.2 Principal parts of the skull, brain, and cranial nerves.....	12
2.2.1 Cranial bones.....	12
2.2.2 Meninges.....	13
2.2.3 Cerebellum	15
2.2.4 Brainstem and cranial nerves.....	16
2.2.5 Diencephalon	19
2.2.6 Cerebrum and limbic system	21
2.4 Summary	25
3 Cerebral haemodynamics	26
3.1 Blood flow in the brain.....	26
3.1.1 Blood structure and functions	26
3.1.2 The heart and cardiac cycle	27
3.1.3 Blood Supply of the Brain	28

3.1.4	Blood pH.....	31
3.1.5	Blood pressure	33
3.1.6	Cerebral Blood Flow.....	34
3.2	Critical concepts in cerebral physiology.....	35
3.2.1	Intracranial pressure (ICP).....	35
3.2.2	Cerebral Perfusion Pressure (CPP).....	35
3.2.3	Compliance.....	36
3.2.4	Partial arterial pressure of carbon dioxide	38
3.2.5	Brain tissue oxygenation.....	38
3.2.6	Jugular venous oxygen saturation	40
3.3	Cerebrospinal fluid (CSF).....	41
3.3.1	Functions of CSF	41
3.3.2	Production and composition of CSF.....	41
3.3.3	CSF's circulatory system.....	42
3.3.4	CSF haemodynamics	44
3.4	Autoregulation	46
3.5	Summary	48
4	Traumatic brain injury (TBI)	50
4.1	Definitions and types	50
4.1.1	Acquired brain injury.....	50
4.1.2	Mild TBI	50
4.1.3	Moderate and severe TBI.....	52
4.2	Epidemiology.....	53
4.2.1	Incidence	53
4.2.2	Mortality	54
4.2.3	Mechanism of injury	56
4.2.4	Risk factors.....	56
4.2.5	Special populations	57
4.3	Demographics and societal cost in TBI	58
4.4	Post-TBI effects	59
4.5	Clinical practice guidelines in TBI.....	61
4.5.1	Recommended clinical evaluation	61
4.5.2	Recommended monitoring techniques	62
4.5.3	Multimodal monitoring.....	68
4.6	Summary	69
5	Non-Invasive monitoring techniques in TBI.....	71

5.1	Introduction	71
5.2	Methodology.....	71
5.3	Results.....	73
5.4	Summary	83
6	NIRS in oxygenation and autoregulation assessment for TBI.....	84
6.1	Introduction	84
6.2	Methodology.....	84
6.3	Results.....	86
6.3.1	Search Results	86
6.3.2	Physical and Technological Description of NIRS	88
6.3.3	NIRS Measurement Techniques.....	91
6.3.4	Subgroups	92
6.3.5	Overall.....	105
6.4	Summary	110
7	Healthy multilayer head simulation with Monte Carlo analysis.....	111
7.1	Introduction	111
7.2	Methodology.....	111
7.2.1	Opto-anatomical parameters.....	112
7.2.2	Monte Carlo simulation strategy	113
7.3	Results and discussion	113
7.4	Summary	116
8	Phantom design and manufacture	118
8.1	The current state of the art in head phantoms	118
8.2	Methodology.....	126
8.2.1	Materials	126
8.2.2	Design and manufacture.....	129
8.3	Results and discussion	155
8.3.1	Materials	155
8.3.2	Design and manufacture.....	160
8.4	Summary	172
9	Design and development of a multimodal sensor for Traumatic Brain Injury monitoring: Analog system coupled to an acquisition LabVIEW interface.....	173
9.1	Introduction	173
9.2	Methodology.....	173
9.2.1	Probe	173
9.2.2	Instrumentation and acquisition system	180

9.2.3	LabView interface	188
9.2.4	Technical evaluation	190
9.3	Results and discussion	191
9.3.1	Probe	191
9.3.2	Instrumentation and acquisition system	192
9.3.3	LabView interface	194
9.3.4	Technical evaluation	195
9.4	Summary	202
10	In-vitro assessment of a non-invasive ICP sensor in a head phantom	203
10.1	Introduction	203
10.2	Methodology.....	203
10.2.1	Phantom set up.....	203
10.2.2	Acquisition system	204
10.2.3	Experiment Protocol	204
10.2.4	Analysis Protocol.....	205
10.3	Results and discussion	209
10.3.1	Resultant model of the first partition approach, Pareto 20/80:.....	216
10.3.2	Resultant model of the second partition approach, k-folds by replicate:	219
10.4	Summary	223
11	In-vitro assessment of a non-invasive Oxygenation sensor in a phantom	224
11.1	Introduction	224
11.2	Methodology.....	224
11.2.1	Phantom set up.....	224
11.2.2	Acquisition system	224
11.2.3	Experimental protocol	225
11.2.4	Analysis Protocol.....	225
11.3	Results.....	226
11.3.1	Liquid phantom setup	226
11.3.2	Head phantom using the liquid phantom fluid as blood	230
11.4	Summary	232
12	Discussion.....	233
12.1	Summary of the current non-invasive multimodal monitoring techniques to assess ICP and cerebral oxygenation in TBI patients	233
12.2	Summary of thesis and findings	234
12.3	Comparisons with other related works	236
12.3.1	Head phantom	236

12.3.2	Probe and instrumentation design	239
12.3.3	Cerebral NIRS systems in multimodal monitoring	241
12.4	Strengths and limitations of this study	245
12.4.1	Strengths	245
12.4.2	Limitations.....	246
13	Conclusion and future work.....	248
14	References	252

TABLE OF FIGURES

Figure 1: Schematic view of the principal components of a typical neuron.....	7
Figure 2: Generation of action potential in a neuron axon to convey information over long distances.[4].....	8
Figure 3: Propagation of action potentials along myelinated axons.[4].....	9
Figure 4: Basic events in typical synaptic transmission. [6].....	10
Figure 5: Evolving pathophysiology of diffuse axonal injury post-trauma, leading to Wallerian degeneration. [7, p. 44]	11
Figure 6: Cranial bones	12
Figure 7: Coronal section through the superior sagittal sinus.	14
Figure 8: Anatomical and functional parts of the cerebellum as seen from the posteroinferior view. [12, p. 682], [13].....	15
Figure 9: Cranial nerve nuclei	16
Figure 10: Sagittal view of the diencephalon parts, showing the projection of the hypothalamus to the pituitary gland.....	20
Figure 11: Lateral view of the cerebrum's primary anatomical and functional areas division, with a translucent view of the limbic system.....	22
Figure 12: components of blood, showing the haemoglobin's iron-oxygen reaction	26
Figure 13: The circulatory system shows the main morphophysiological components involved in tissues' oxygenation and perfusion [23]	28
Figure 14: Arteries on the inferior surface of the brain [24]	29
Figure 15: Series of anteroposterior views after injection of contrast material through the right internal carotid artery [24].	30
Figure 16: Flux of blood substances through the blood-brain barrier to an astrocyte that transports nutrients from the vessel to the neuron [27]	31
Figure 17: Compliance definition based on intracranial volume-pressure behaviour.	37
Figure 18: Intracranial pressure-volume behaviour according to intracranial compliance [52].	37
Figure 19: Patterns of CSF recirculation and flow (modified from [66]).....	44
Figure 20: CSF pressure waveform morphologies (modified from [63], [67]).....	45
Figure 21: Cerebral autoregulation.....	47
Figure 22: Vicious circle of impaired cerebral blood regulation after TBI [42], [74]	48
Figure 23: Worldwide incidence of traumatic brain injury [90].....	53
Figure 24: Cause of injury in England and Wales [93].	54

Figure 25: Cause composition of age-standardised incidence of traumatic brain injury by Global Burden of Disease region for both sexes [99].....	56
Figure 26: Classification of clinical severity of TBI with the Glasgow Coma Scale [90]	61
Figure 27: ICP waveform components [110]	63
Figure 28: Studies selection flow diagram describing the identification, screening, eligibility, and inclusion of the systematic review.....	73
Figure 29: Quality assessment results.	74
Figure 30: Forest plot (a) and funnel plot (b) for the correlation coefficients between non-invasive and invasive ICP monitoring in Huang et al., Gura et al. and Budohoski et al. studies.	80
Figure 31: Flowchart of the methodology used to include 72 out of 207 studies published until July 2020.	85
Figure 32: Global distribution of scientific articles	87
Figure 33: Number of publications per year associating TBI with the various types of NIRS applications.....	88
Figure 34: Percentage of diagnosis papers per subgroup according to the outcome measured: oxygenation, autoregulation, hematomas, and neurorehabilitation monitoring.	88
Figure 35: Light tissue interaction.....	89
Figure 36: Schematic diagram of NIRS detection modes.....	91
Figure 37: Demographics of the evidence on NIRS-derived oxygenation in TBI.	97
Figure 38: Distribution of NIRS techniques used for oxygenation monitoring in TBI patients.....	98
Figure 39: Comparisons found in the evidence on NIRS-derived oxygenation in TBI.	99
Figure 40: Demographics of the evidence on NIRS-derived autoregulation in TBI.	102
Figure 41: Distribution of NIRS techniques used for autoregulation monitoring in TBI patients.....	103
Figure 42: Comparisons found in the evidence on NIRS-derived autoregulation in TBI.	104
Figure 43: Main conclusions of NIRS-derived monitoring in TBI.	105
Figure 44: Stratification of brain tissue layers: real (a) and simulated (b).....	112
Figure 45: Monte Carlo simulated photon path through normal brain tissue at different source-detector separations: 10, 20, 30, 40 and 50mm as shown in (a), (b), (c), (d), and (e), respectively. .	114
Figure 46: Relative absorbance at different head tissue layers at the source-detector separations d= 1, 2, 3, 4 & 5cm.	115
Figure 47: Kurth et al brain phantom for NIRS measurements. Figure from [226].	118
Figure 48: MRI sequence of Chen et al. brain (a) and a pig brain (b) during the 2-hours infusion. Figure from [227].	119

Figure 49: Pfaffenberger et al. skull model for the assessment of ultrasound in the diagnosis of blood clots through the temporal bone.....	120
Figure 50: Iida et al. head phantom to evaluate PET/SPECT image quality [229].	120
Figure 51: Bottan's head phantom for cerebral haemodynamics simulation [230].....	121
Figure 52: Mohammed et al. head phantom for microwave-based imaging [258].....	122
Figure 53: Menikou et al. head phantom compatible with MRI [259].	122
Figure 54: Dempsey et al skull phantom compatible with diffuse optical imaging [260].	123
Figure 55: Afshari et al. head phantom for standardized testing of clinical NIRS oximeters [234]. ...	124
Figure 56: Benninghaus et al. phantom of the CSF system [240].	124
Figure 57: Nagassa et al. head phantom for cerebral aneurysm intervention training [237].	125
Figure 58: Brain and skull samples of the phantom materials and animal models.	128
Figure 59: Both parts of the skull CAD, the calvaria and the maxilla.....	130
Figure 60: Formlabs port-curing process applied to the calvaria	130
Figure 61: Phantom base and clamps design.....	131
Figure 62: Plastic commercial ports.....	132
Figure 63: Calvaria with Luer ports to allow the connection of multiple objects.....	133
Figure 64: Scaled skull hermeticity test using translucent sealant/ glue	133
Figure 65: Gasket alternative for the skull seal	134
Figure 66: Calvaria with brim and seal using screws	135
Figure 67: Final seal, compression system.....	136
Figure 68: 3B Scientific human brain model with arteries, enclosed into the phantom skull.....	137
Figure 69: Brain mould manufacture	138
Figure 70: Brain mould with the middle cerebral artery, ready to receive the brain silicone mix.	139
Figure 71: Brain silicone mixture manufacture process	139
Figure 72: Brain cured in the oven.....	140
Figure 73: Vascular territories of the cerebral arteries included in the phantom.....	142
Figure 74: Brain arteries connectors.....	142
Figure 75: Phantom cardiovascular circulation design	143
Figure 76: Artificial blood mixtures.....	145
Figure 77: Spectra of the dye mixtures	146
Figure 78: Ratio of ratios and Oxygen saturation at different mixtures concentrations.....	147
Figure 79: Blood saturation measurement from one extreme concentration (50%) to the other (95%) using artificial blood.....	148
Figure 80: DC changes on artificial blood mixtures, measured by NIRS	149

Figure 81: Animal blood oxygenation system.....	150
Figure 82: FOSFOR-R response	151
Figure 83: Liquid phantom solutes to mimic changes in blood oxygenation	152
Figure 84: Phantom cerebrospinal fluid circulation design	153
Figure 85: Valves control system	154
Figure 86: LabVIEW summarized Block Diagram for the phantom	155
Figure 87: Spectra from the phantom materials and animal samples	156
Figure 88: Comparison of the brain's optical properties	158
Figure 89: Comparison of the skull's optical properties	159
Figure 90: Maxilla's post-printing process	160
Figure 91: Phantom base and clamps design.....	161
Figure 92: Calvaria with Luer ports allows the connection of multiple objects	162
Figure 93: Final seal with compression structure	163
Figure 94: Seal test by increasing the ICP from 0 to 30 mmHg.....	164
Figure 95: Resultant brain.....	164
Figure 96: Middle cerebral artery and anterior cerebral arteries of the phantom	165
Figure 97: Phantom cardiovascular circulation	166
Figure 98: Phantom blood arterial pressure.....	166
Figure 99: Artificial blood spectra comparisons	167
Figure 100: Blood oxygenation system.....	168
Figure 101: Oxygenation test using the fluid of the liquid phantom in the circulatory system of the head phantom.....	169
Figure 102: Blood samples quality, before and after experiments	169
Figure 103: Phantom CSF circulatory system	170
Figure 104: Intracranial ICP oscillation measure in the phantom over several cardiac cycles.....	171
Figure 105: LabVIEW phantom interface.....	172
Figure 106: Probe configuration of the optical components.....	175
Figure 107: Reflectance probe PCB footprint (a) and PCB's 3D model (b).	178
Figure 108: Sensor case 3D model (a) and diagram of the connectors to the processing system (b).....	179
Figure 109: Detailed block diagram showing the architecture of ZenTBI.....	181
Figure 110: Bus connector 3D model.....	182
Figure 111: Power supply schematic design.....	182
Figure 112: Controls to set the emitters' currents	183
Figure 113: Multiplexing circuit	184

Figure 114: Current source schematic design.....	185
Figure 115: Differential transimpedance amplifier schematic design	186
Figure 116: Core module back end schematic design	187
Figure 117: Black Aluminium Enclosure.....	188
Figure 118: LabVIEW summarized Block Diagram for the TBI sensor.....	189
Figure 119: Multimodal probe for TBI monitoring of ICP and oxygenation	192
Figure 120: ZenTBI instrumentation system.....	193
Figure 121: LabVIEW sensor interface	194
Figure 122: Oscilloscope debug sequence.....	196
Figure 123: TBI system ready for use.....	197
Figure 124: Raw PPG signals	198
Figure 125: Filtered signals from all wavelengths at different source-detector distances	199
Figure 126: Median value of the quality indexes at each S-D distance for all the wavelength.....	200
Figure 127: Experimental protocol where ICP changes were induced on the phantom.....	205
Figure 128: Features extracted from the optical signals	206
Figure 129: Normalized PPG signals from both proximal and distal detectors, full record of one replicate	209
Figure 130: Zoom in view on a 10 second window of the normalized PPG signals from both proximal and distal detectors of one replicate.....	211
Figure 131: Zoom-in views of a 60 second window of the normalised PPG signals at the extreme values (5 mmHg and 30 mmHg) from both proximal and distal detectors of one replicate, including the difference between the detector's signals.....	212
Figure 132: Factorial analysis of the ICP levels and wavelengths effect in the features of the PPG signals, including factors interaction	215
Figure 133: Model performance graphs from Pareto partition.....	218
Figure 134: Online estimation of ICP from 5 seconds windows	219
Figure 135: Online estimation of ICP from 5 seconds windows using the selected k-fold models....	220
Figure 136: Model performance graphs from 15-fold partition.....	222
Figure 138: Phantom set up for non-invasive oxygenation measurements.....	225
Figure 139: Sensor response to the presence of blood	227
Figure 140: Normalized optical signals at 770 nm and 880 nm in comparison with the FOSFOR-R probe measurement	228
Figure 141: Haemoglobin absorption spectra	228

Figure 142: Calculated Tissue oxygenation index (TOI) in comparison with the FOSFOR-R probe measurement.....	229
Figure 143: Normalized optical signals at 770 nm and 880 nm in comparison with the FOSFOR-R probe measurement, acquired from the head phantom using the liquid phantom fluid as blood ...	231
Figure 144: Pulsatile signals acquired from the head phantom using the liquid phantom fluid as blood	232
Figure 145: Experimental setup from Ruesch studies [305]–[308]	242
Figure 146: Histogram of ICP distribution for both train and test sets following a Pareto approach in Ruesch et al study [307].	244

TABLE OF TABLES

Major divisions of the brain [1].....	6
Summary of the cranial nerves' functions and possible consequences after trauma. (summarized from [2]).....	17
Major pituitary hormones and their effects (Modified from: [19, p. 628]).....	20
Summary of the cerebrum functional areas and possible consequences after trauma. (information summarized from [2], [20]).....	22
Average concentrations of lumbar CSF solutes of normal human subjects [63, p. 12].....	42
Potential short and long-term neurologic damage after mTBI.....	51
Criteria used to classify TBI severity.	52
Post-TBI outcomes summary	60
Autoregulation indexes [72]	64
Description of the 12 included studies comparing non-invasive and invasive techniques for ICP or brain oxygenation monitoring in traumatic brain injury. The studies in bold text have been included in the metaanalysis.	76
Summary of the evidence on NIRS-derived oxygenation in TBI.	93
Summary of the evidence on NIRS-derived autoregulation in TBI	100
Strengths and limitations of NIRS-derived oxygenation in TBI.....	109
Optical coefficients of head tissues.	112
Simulated fractional optical path at different tissue layers at S-D separations $d=1-5\text{cm}$	116
Relative plethysmography signals' amplitudes and arterial oxygen saturation (SaO_2) values assuming the transmission intensities are equal. R = red; IR = infrared (Copied from [291])......	148
Mahalanobis, Euclidian and Manhattan distances between the phantom materials spectra and animal samples' spectra.....	156
Optical and electrical characteristics of the LEDs and photodiodes.....	176
Quality evaluation set-up parameters	191
Phantom circulatory parameters.....	204
Description of photoplethysmogram (PPG) features extracted and their clinical relationship	207
Models accuracy comparison	216
Accuracy of the best model for each fold	219
Comparison of the models selected from both partitioning methods.....	223
Comparison of commercial NIRS probes with the ZenTBI probe	239

ACKNOWLEDGEMENTS

First and foremost, I am deeply grateful to my supervisor, Professor Panicos A. Kyriacou, who sincerely cares for his students' wellness. This man of science has guided me and supported me with invaluable words of wisdom and motivation, leaving always his door open to listen. I have found in him a source of inspiration, a trustworthy person, and a remarkable example of a hard worker. Thanks for believing in me and pushing me to do more at the best that I could.

My heartfelt thanks go to Professor Robinson Alberto Torres for providing me with the skills needed to pursue this PhD. I am also thankful for his encouragement and friendship since my early academic career years.

I would also like to thank Dr Tomas Ysehak, for all his guidance in the first years of my PhD. Some ideas in this thesis originated from our conversations, either in front of a lab bench or an espresso bar. I followed your “why” method at each step of my research.

I am indebted to the support staff and technicians who have provided me with technical assistance, laboratory resources, and administrative support. In particular Keith and Kugan, their dedication and professionalism have been crucial in facilitating the smooth progress of my research.

Thanks to my friends and companion of PhD adventures Mahsa Sheikh, Michelle Nomoni and Elisa Mejia, for supporting me daily. The many meals, coffees, and lovely shared moments helped me lose back when I needed it most. In particular, thanks to Elisa for all the hours she spent with me in the lab, her technical suggestions, and the laughs and tears we shared during the last couple of years.

I want to offer my special thanks to the academics and all my colleagues at the Research Centre for Biomedical Engineering for their technical support, friendship, and for sharing this valuable experience. Likewise, I am grateful to City University of London for the studentship that allowed me to conduct my doctoral studies.

Without my friends and family, I could not imagine what it would have been these last challenging years. Overcoming the enormous sacrifices of living so far from my country to pursue this dream, has only been possible thanks to all of you. I am deeply grateful for your love, for always making time for me and being my moral support. I will always be thankful to my parents for providing me with solid values and beliefs to step on my own feet. Likewise, no words can ever be strong enough to express my gratitude to Andres for being my rock and staunch believer on every step of the way.

DECLARATION

I, María Roldán Restrepo, declare that the work presented in this thesis is my work. In the text, any idea, result, or illustration originating from the work of other subjects has been acknowledged. I confirm that the work was carried out entirely as part of my Doctor of Philosophy in Biomedical Engineering candidature at City University of London. I further ensure that this thesis has never been published or submitted elsewhere for obtaining an academic degree or professional qualification.

María Roldán Restrepo

“People think I’m disciplined. It is not discipline. It is devotion. There is a great difference.”

— Luciano Pavarotti

ABSTRACT

Traumatic brain injury (TBI) is a leading cause of death and disability, often resulting in increased intracranial pressure (ICP) and cerebral ischemia. Current ICP measurement methods involve invasive, non-therapeutic procedures. This research aims to develop a non-invasive, continuous optical system for monitoring ICP and cerebral oxygenation. Using backscattered brain optical signals, it leverages cerebral pulsatile photoplethysmograms (PPGs) and non-pulsatile near-infrared spectroscopy (NIRS) signals to assess ICP and oxygenation. The innovation lies in using cerebral NIRS-PPGs to measure ICP, based on the hypothesis that changes in ICP affect cerebral PPG signal morphology. These changes in morphological features, with the support of advanced algorithms including Machine Learning (ML) models, could be utilised in translating the changes in the pulsatile signals in absolute measurements of ICP. The research firstly implemented Monte Carlo simulations to fully understand the effect of multi-source detector separations on brain light tissue interaction. Secondly, a novel reflectance, custom-made TBI multiwavelength and multisource-detector optical sensor and instrumentation, including advanced signal processing algorithms, was designed to acquire, pre-process, and analyse raw PPG signals (AC + DC) from the brain. Thirdly, a novel head phantom and an in vitro brain haemodynamic system were developed for evaluating the sensor. The phantom was the ideal tool for simulating different clinical scenarios that cannot be implemented in real in vivo studies. Fourthly, this research carried out three in vitro studies to investigate the sensor's capability to non-invasively monitor intracranial pressure and oxygenation. The first study evaluated the quality of the optical signals acquired from the developed probe at different source-detector (S-D) separations and multiple wavelengths. It was concluded that the optimal S-D separation to reach the cerebral tissue, and acquire good quality PPG signals, was within 3 cm and 4 cm. The second study assessed the central hypothesis of this research by recording PPG signals from the phantom's brain at different intracranial pressure levels and implementing ML models utilising pertinent features from the PPG. Results from the second study showed a correlation coefficient of 0.86, mean absolute error of 3.7 mmHg, and limits of agreement of ± 4 mmHg, which suggest that NIRS-PPG signals could estimate ICP non-invasively. Finally, a third study demonstrated the sensor's response to in vitro changes in blood oxygenation levels, with less than 33.8% error in half the measurements compared to the reference. This final implementation of spatially resolved spectroscopy algorithms actualize the proposed non-invasive multimodal monitoring sensor for traumatic brain injury. The novel technological developments and the new knowledge acquired from this research paves the way for the development of a transformative non-invasive optical sensor technology for the continuous monitoring of ICP and cerebral oxygenation in TBI patients and beyond.

GLOSSARY OF COMMON ABBREVIATIONS

ABP: Arterial Blood Pressure

AVDO₂: Arteriovenous Difference of Oxygen Content

CSF: Cerebrospinal Fluid

CPP: Cerebral Perfusion Pressure

CPP_{opt}: Optimal Cerebral Perfusion Pressure

CMD: Cerebral Micro-dialysis

CT: Computerised Tomography

GCS: Glasgow Coma Scale

ICP: Intracranial Pressure

LOC: Loss of Consciousness

MAP: Mean Arterial Pressure

MCA: Middle Cerebral Artery

MMM: Multimodality Monitoring

NIRS: Near-Infrared Spectroscopy

O₂: Oxygen

PbtO₂: Brain Tissue Oxygenation

PPG: Photoplethysmography

SAH: Subarachnoid Haemorrhage

SjVO₂: Jugular Venous Oxygen Monitoring

SRS: Spatially Resolved Spectroscopy

TBI: Traumatic Brain Injury

TCD: Transcranial Doppler Ultrasound

THI: Total Haemoglobin Index

TOI: Tissue Oxygenation Index

PUBLICATIONS RESULTING FROM THIS WORK

JOURNALS

M. Roldan and P. A. Kyriacou, "A non-Invasive Optical Multimodal Photoplethysmography-Near Infrared Spectroscopy Sensor for Measuring Intracranial Pressure and Cerebral Oxygenation in Traumatic Brain Injury," *Appl. Sci.*, vol. 13, no. 8, 2023, doi: 10.3390/app13085211.

M. Roldan and P. A. Kyriacou, "Head Phantom for the Acquisition of Pulsatile Optical Signals for Traumatic Brain Injury Monitoring," *Photonics*, vol. 10, no. 5, 2023, doi: 10.3390/photonics10050504.

M. Roldan, T. Y. Abay, and P. A. Kyriacou, "Non-invasive techniques for multimodal monitoring in Traumatic Brain Injury (TBI): systematic review and meta-analysis," *J. Neurotrauma*, p. neu.2020.7266, Aug. 2020, doi: 10.1089/neu.2020.7266.

M. Roldan and P. A. Kyriacou, "Near-Infrared Spectroscopy (NIRS) in Traumatic Brain Injury (TBI)," *Sensors*, vol. 21, no. 1586, p. 30, 2021, doi: 10.3390/s21051586.

CONFERENCE PROCEEDINGS

M. Roldan and P. A. Kyriacou, "Optical sensor for non-invasive intracranial pressure monitoring in traumatic brain injury," in SPIE conference, SPIE, Ed., San Francisco: SPIE West Photonics, 2023. doi: <https://doi.org/10.1117/12.2649746>.

M. Roldan and P. A. Kyriacou, "Head Phantom Optical Properties Validation for Near-Infrared Measurements: A Comparison with Animal Tissue," 2022 44th Annu. Int. Conf. IEEE Eng. Med. Biol. Soc., pp. 641–644, Jul. 2022, doi: 10.1109/EMBC48229.2022.9871103.

Roldan M., Chatterjee S., and Kyriacou P.A., "Light-Tissue Interaction Modelling of Human Brain towards the Optical Sensing of Traumatic Brain Injury," in 43rd Annual International Conference of the IEEE Engineering in Medicine & Biology Society (EMBC), 2021, pp. 1–4. Accessed: Jan. 25, 2022. [Online]. Available: <https://openaccess.city.ac.uk/id/eprint/27326/1/>

AWARD

T. W. C. of Engineers, "Maria Roldan wins the Mercia Award 2022," *Engineers' Company*, London, United Kingdom, 19-Aug-2022.

1 INTRODUCTION

1.1 MOTIVATION

Traumatic brain injury (TBI) is caused by an external force that disturbs the brain's function. Every year 50 to 60 million new cases are reported worldwide, including mild, moderate, and severe cases. The latter associates with mortality rates as high as 40%. However, survivors present disabling outcomes, and their life expectancy is reduced by six years. After a traumatic brain injury, cerebral haemodynamic is disrupted, having intracranial pressure (ICP) and oxygenation as two of the most relevant impaired parameters. Alterations in these variables occur in the first hours after injury and lead to secondary injuries such as ischemia or hyperaemia.

After an injury, patients are clinically assessed by the Glasgow coma scale, which evaluates verbal, eye and motor responses. When the patient is admitted to the hospital, anatomical evaluation involves CT scans or MRI images, which are essential to start treatment. Regrettably, within this critical time window called 'golden period', of approximately two hours, medical professionals possess limited knowledge concerning to the intracranial events occurring. Moreover, these intermittent techniques are unsuitable for continuous evaluation of patient progress. So, guidelines recommend continuous and invasive monitoring of physiological variables, especially for severe cases. Intracranial monitoring methods are invasive, require specialized medical staff to place a pressure sensor, also called bolt, inside the skull and are placed 3 to 4 hours after injury. Consequently, these methods are used only in severe cases, are associated with infection risks, and do not give information during the first hours after injury.

Evidence has shown that access to early monitoring and treatment decreases the risk of secondary injury in TBI patients, resulting in better outcomes and reduced mortality. Similarly, the integration of multimodal monitoring in a patient's management decision has shown better results than treatment guided by just one parameter, such as ICP. Consequently, this research is motivated by the worldwide interest in developing better technologies for this detrimental health problem, considering its impact on patient's lives and their families and the cost it represents to society and the healthcare system.

1.2 AIMS AND OBJECTIVES.

This research aims to develop a non-invasive multimodal monitoring sensor to assess ICP and cerebral oxygenation in TBI patients. This technology would allow a preliminary assessment of TBI-related haemodynamics during an early stage of the injury. This non-invasive and portable technology is aimed to be used by paramedics and physicians in and outside the hospital. As a low-risk technology,

it would allow the assessment of every severity type of head injury, and it will improve the treatment of patients with mild or moderate TBI.

Up-to-date, the evidence has not reported any other multimodal technology that uses optical principles to assess ICP and cerebral oxygenation in TBI patients. NIRS has been broadly interrogated to evaluate cerebral oxygenation, giving the theoretical basis to build a sensor that uses non-pulsatile infrared light reflected from the cerebral tissue. However, in NIRS measurements of the brain, in particular, heartbeat oscillations are very likely to be present due to the dense cerebral arterial network. With every heartbeat, a pressure gradient propagates through the arterial network, causing local changes in blood volume that alter the intensity of light detected. Therefore, the amplitude of the pulse waveform indicates the local blood volume based on the optical pulsation. Considering that increments in the intracranial pressure lead to the deformation of superficial cerebral arteries and hence to changes in the optical pulse waveform, this research will also use the pulsatile components of the reflected NIR light to interrogate intracranial pressure.

Nonetheless, to go forward with the design and development of this sensor, it is critically substantial to develop a phantom of the head where the sensor's efficacy and accuracy can be tested frequently. This testing tool should allow the simulation of head injury by controlled changes in haemodynamic parameters such as intracranial pressure and blood oxygenation. Additionally, it would allow the simulation of different clinical scenarios that cannot be induced in healthy volunteers. The phantom would then be a source of information during the sensor's design, development and testing phases.

In order to achieve this research aim, the fulfilment of the following objectives is required.

- Elaborate on a comprehensive theoretical framework of the brain, cerebral haemodynamics and traumatic brain injury (TBI).
- Collect the evidence published in the last decade on non-invasive techniques for monitoring intracranial pressure and brain oxygenation in TBI patients.
- Investigate the utilisation of NIRS in TBI and provide a synthesis of the available evidence of the association between continuous NIRS-based measurements and commonly monitored neurophysiological parameters, such as oxygenation and cerebral autoregulation.
- Using Monte Carlo simulation, explore the optical interactions of near-infrared wavelengths in a developed multi-layered head model.
- Design, build and assess a model that follows actual anatomical specifications, mimics optical tissue properties and allows changes in intracranial volume, pressure, and blood oxygenation.
- Design, develop and manufacture an optical non-invasive sensor for monitoring TBI parameters like intracranial pressure and oxygenation changes.

- Couple the sensor with a research processing system capable of controlling a four-wavelengths probe and acquiring three reflected optical signals (AC+DC).
- Perform in vitro studies on the phantom in which changes in intracranial pressure and oxygenation levels are induced and acquire a dataset of optical signals.
- Use signal processing techniques and machine learning algorithms to build an estimation model of ICP based on the acquired dataset.
- Apply appropriate statistical methods to evaluate the diagnostic capacity of the sensor for ICP monitoring.
- Test the sensor's capacity to measure changes in blood oxygenation levels using an in-vitro set-up.

1.3 REPORT OUTLINE

After introducing the motivation and aims of this research, this section presents the outline and contents of the chapters in the thesis.

Chapter 2 introduces the brain's most relevant anatomical parts and physiological functions. It discusses the principal cellular elements of the nervous system in order to understand the communication process between the control centre and the rest of the body and how this activity might be interrupted by traumatic injuries in the brain. Likewise, the chapter covers the anatomy and functional roles of the brain areas most relevant to understanding traumatic brain injury.

Chapter 3 describes in detail some physiological concepts. First, the composition and functions of blood are described, with a particular emphasis on haemoglobin and its roles in oxygen transport. The gas exchange at the pulmonary level, between the lungs and blood is explained, as well as the exchange of oxygen and carbon dioxide at the tissue levels. The cardiovascular system is briefly described, as well as the main concepts in cerebral blood supply. Next, some key concepts in cerebral physiology are explained aiding in the better understanding of haemodynamic changes that occur after traumatic brain injury. This key-concepts section includes blood properties, blood flow, intracranial pressure, perfusion pressure, compliance, and oxygenation measurements. Similarly, the second part of the chapter explains the cerebrospinal fluid function, production, and composition, as well as its circulatory system and haemodynamics. Finally, the description of cerebral autoregulation and its importance after TBI is included.

Chapter 4 shows the justification of this research by explaining traumatic brain injury, not just as a clinical definition but also by indicating the number of new cases per year, the percentage of deaths, the most common mechanisms of injury and the risk factors that lead to TBI. This chapter presents

the disabling outputs that survivors are exposed to and the recommended clinical management; both involve social and economic costs to the patients, their families, society, and the healthcare system. Finally, the chapter introduces the clinical practice guidelines for patients' evaluation and monitoring, including their limitations and the motivation for multimodal monitoring.

Chapter 5 presents a systematic review and meta-analysis of non-invasive techniques that monitor ICP and oxygenation in TBI patients. The chapter describes the systematic search strategy and selection criteria used to find recent evidence on the topic and the quality assessment of the included papers. The latter presents a qualitative and quantitative synthesis of the evidence, highlighting the use of Doppler Ultrasound and Near-Infrared Spectroscopy for non-invasive monitoring in TBI patients.

Chapter 6 is a narrative review of the applications of Near Infrared Spectroscopy in Traumatic Brain Injury. The chapter begins by generally describing the demographics of the publications included in the study. Then the physical principles used in NIRS are explained. In particular, the modified Beer-Lambert law is presented as being used in NIRS to infer haemoglobin concentration changes in tissue. Next, different typologies of NIRS instruments, such as Continuous Wave NIRS and Spatially Resolved Spectroscopy, are briefly described. A review of the main clinical applications of NIRS is then presented, especially for cerebral oxygenation and autoregulation monitoring. Finally, some limitations are discussed at the end of the chapter.

Chapter 7 proposes a Monte Carlo Simulation in a healthy multi-layer head model, where the light tissue interaction of NIR light at different source-detector distances was interrogated. The development of the model according to anatomical layers disposition and thickness is described in the methods section, as well as the optical properties used to simulate light absorption and scattering in the tissues. Finally, the relative absorbance and the fractional optical path length are presented for each layer, giving valuable information to define the best source-detector distance for the proposed TBI sensor.

Chapter 8 describes the development of a head in vitro model. First, it describes the design, materials, and manufacture of the skull and the brain. Next, it explains the spectroscopic measurements used to compare the optical properties between the materials proposed to build the skull, and the brain of the phantom, against the respective animal tissues and values reported in the literature. Then, the manufacturing process is described, considering both circulatory systems. The first one involves the brain and cardiovascular arteries. The second one entails artificial cerebrospinal fluid that flows in a closed and regulated circuit to allow changes in intracranial volume and pressure. A liquid phantom has been proposed in this chapter to simulate changes in blood oxygenation levels.

Chapter 9 comprises the multimodal monitoring system's designing, developing and testing phases. The device involves an optical probe, bio-instrumentation hardware, and user interface software. This chapter reviews the functionalities of such PPG system, including light multiplexing (switching), current-to-voltage conversion, and time demultiplexing. The main components of the system are described, along with their evaluation. The latter includes a detailed hardware debug using the oscilloscope, a power consumption calculation and a statistical analysis of the pulsatile signals' quality at different source-detector distances and multiple wavelengths.

Chapter 10 presents the in vitro studies conducted to investigate the feasibility of using features extracted from cerebral PPG signals to estimate intracranial pressure absolute values within normal and pathological ranges. The simulation of both normal and pathological levels of ICP using the head phantom allowed the acquisition of a significant pool of data needed for the quantitative analysis of the features and the development of multiple models for estimating absolute values of intracranial pressure. This chapter displays the accuracy of the non-invasive ICP measurements in real-time in comparison to the invasive ICP reference.

Chapter 11 covers the second in vitro study, where the changes in blood oxygenation levels were simulated from ischaemic to normal values to test the sensor's capability for measuring changes in oxygen concentration based on spatially resolved spectroscopy algorithms. The results from Chapter 10 and Chapter 11 demonstrated the sensor's capability to do multimodal monitoring of intracranial pressure and oxygenation non-invasively. Both parameters were evaluated using the in vitro phantom.

Finally, Chapter 12 and Chapter 13 will conclude the thesis by discussing the main findings from the in vitro studies, the limitations, and suggestions for future work.

2 PATHOPHYSIOLOGY OF THE BRAIN IN TBI

This chapter describes the most relevant anatomical parts and physiological functions of the brain as the central organ of the current research. This chapter includes two sections. The first one discusses the principal cellular elements of the nervous system in order to understand the communication process between the control centre and the rest of the body; It also describes how this activity might be interrupted by traumatic injuries in the brain. The second section covers the anatomy and functional roles of the brain areas most relevant to understanding traumatic brain injury. The end of each chapter presents a summary, along with the current document.

2.1 NERVOUS TISSUE

The nervous system comprises the peripheral nervous system (PNS), which collects sensing information and delivers messages to the body or the central nervous system (CNS). The CNS is composed of the brain and the spinal cord. The cerebrum, cerebellum, and brainstem form the brain; the former splits into the cerebral hemispheres and the diencephalon [1]. Table 1 shows the principal functions and subdivisions of the major divisions of the brain.

Table 1: Major divisions of the brain [1]

Major Division	Subdivision	Principal Function
Cerebral hemisphere	Cerebral cortex	Cognition, Memory, Voluntary movements
	Lenticular nucleus	Part of the basal ganglia: movement control
	Caudate nucleus	Part of the basal ganglia: movement control
	Amygdala	Part of the limbic system: drives and emotions
Diencephalon	Thalamus	Relays information to the cerebral cortex
	Hypothalamus	Controls the autonomic nervous system
Brainstem	Medulla	Cranial nerve nuclei
	Pons	Cranial nerve nuclei
	Midbrain	Cranial nerve nuclei
Cerebellum		Coordination of movement

Two types of cells make up the whole nervous system: neurons and glial cells. The neurons are composed of three structures: the body, the dendrites, and the axon. The body is the synthetic centre of the unit. It has multiple dendrites that receive chemical inputs from other neurons. The axon

delivers the information to the next nervous cell through electrical impulses. Figure 1 (modified from www.biodigital.com) represents the principal components of a typical neuron [1].

The set of cell bodies and dendrites is known as grey matter, and the collection of axons that are part of the CNS is known as white matter. The CNS is well known so by the division into grey and white matter [1]. Clusters of grey matter located deep within the cerebral hemisphere and brainstem are called nuclei and control vital body functions, as will be explained further in this section [2].

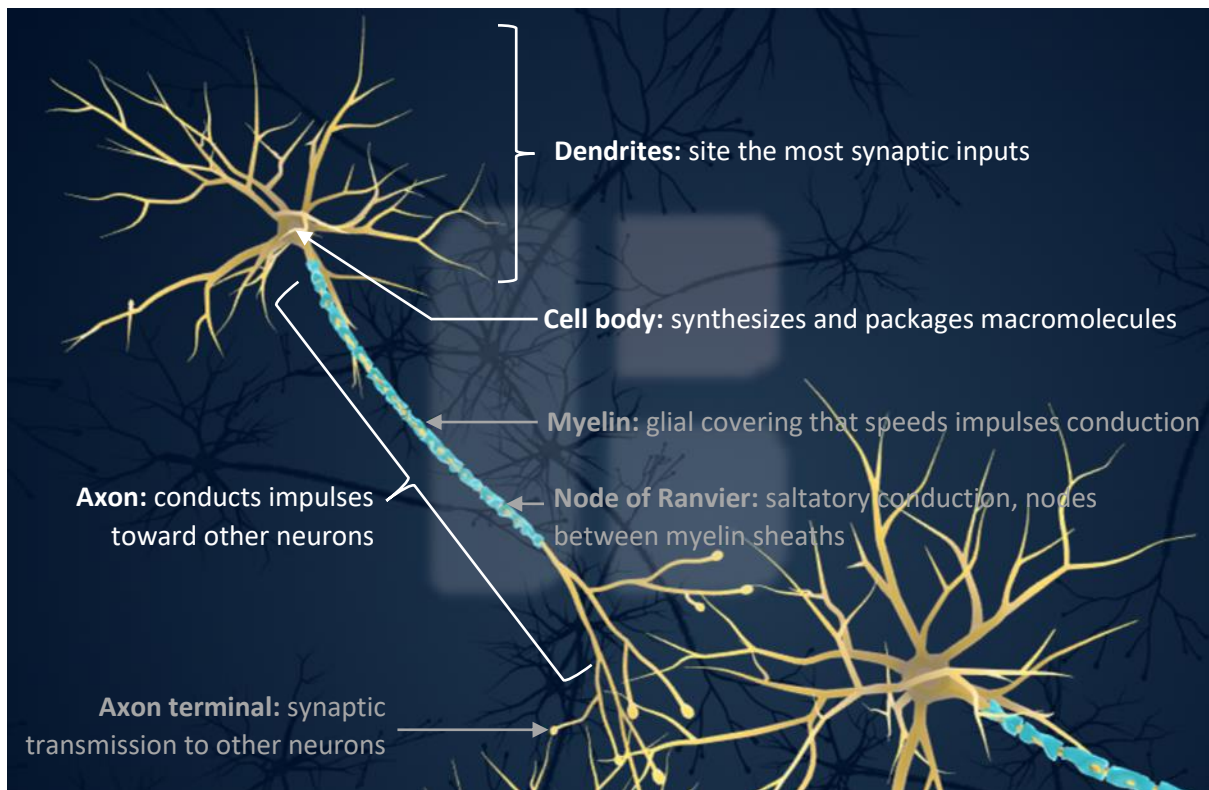


Figure 1: Schematic view of the principal components of a typical neuron

2.1.1 Electrical Signalling by Neurons

Neurons use the movement of ions in their axon's membrane to deliver information from the cell body to the axonal terminals. When the neuron receives a stimulus, the cascade of action potentials leads the unidirectionally conveyed messages over long distances. An action potential is composed of a strong impulse that opens the axon's membrane sodium channels to increase sodium levels at the interior, driving its polarity from -70mV to a positive threshold (depolarization) [3]. Due to the positive intracellular polarity, the sodium channels are inactivated, and the potassium channels are opened to take out potassium ions and repolarize the membrane. During the later process, the cell cannot produce action potentials even if another stimulus is received; this brief refractory period prevents the electrical signal from propagating back toward the cell body [3]. In addition, potassium channels are slower than sodium ones, producing a potential undershoot behind the initial potential (-70mV), at which the channels are closed to return to rest (Figure 2). The sodium-potassium pump aim is to restore the initial state of the ion's gradients, exchanging three sodium ions from the intracellular space for two potassium ions from the extracellular space [3]. Figure 3 illustrates how multiple action potentials conduct the electrical signal jumping from one node of Ranvier to the next in myelinated axons. Myelin acts as an insulator that prevents current from leaving the axon; this increases the speed of action potential conduction [3].

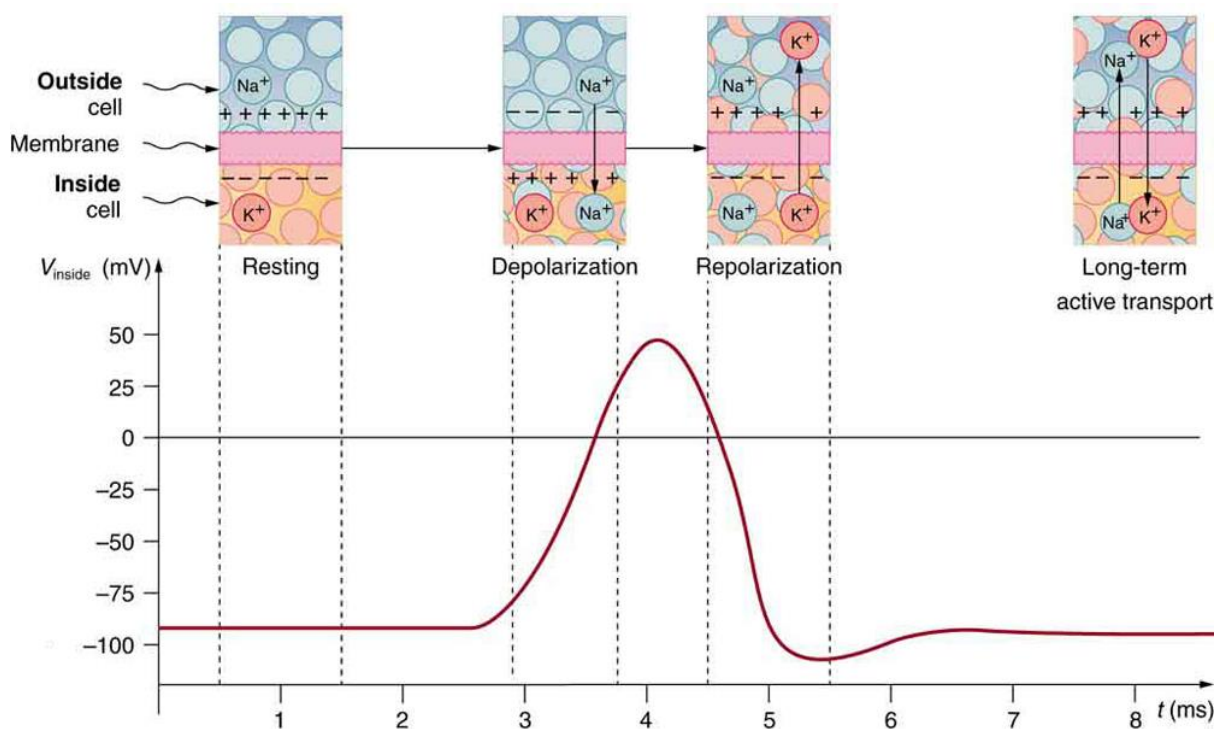


Figure 2: Generation of action potential in a neuron axon to convey information over long distances. [4]

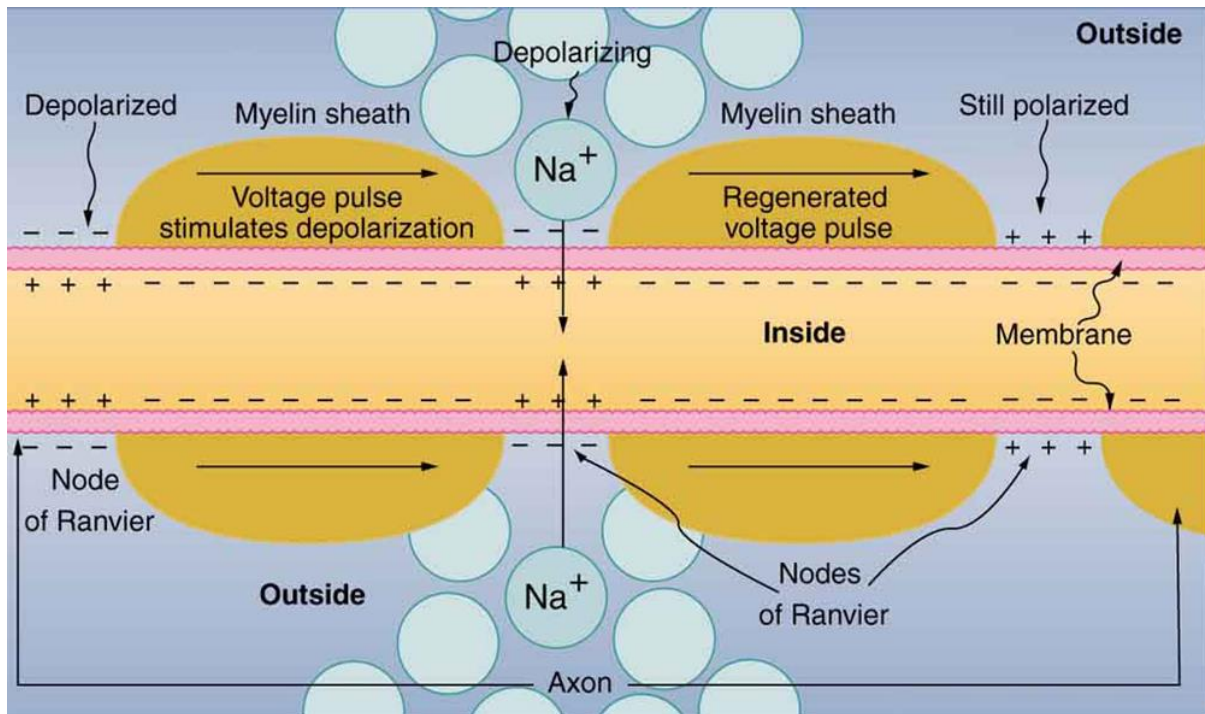


Figure 3: Propagation of action potentials along myelinated axons.[4]

2.1.2 Synaptic Transmission Between Neurons

Information travels inside the neuron as an electrical signal. In contrast, the information is transmitted between neurons through the release of neurotransmitters during synapses. The membrane of the pre-synaptic end bulb contains voltage-gated calcium (Ca^{2+}) channels that open when an action potential reaches the axon terminal. Calcium entry stimulates the release of neurotransmitters to the synaptic cleft [5]. Rapid synaptic transmission happens by binding neurotransmitters to a ligand-gated channel in the postsynaptic neuron. This receptor will allow the entrance of Na^+ and K^+ , causing an excitatory postsynaptic potential, or will become permeable to K^+ and Cl^- , leading to an inhibitory postsynaptic potential [5]. On the other hand, slow synaptic transmission involves receptors linked to G-proteins, which mediates postsynaptic effects, such as ion channels opening, activation of enzymes or even alteration in gene expression. The synaptic effect depends on the number of action potentials, the molecule type (i.e. amine, amino acid, or neuropeptide) and the postsynaptic receptor [5].

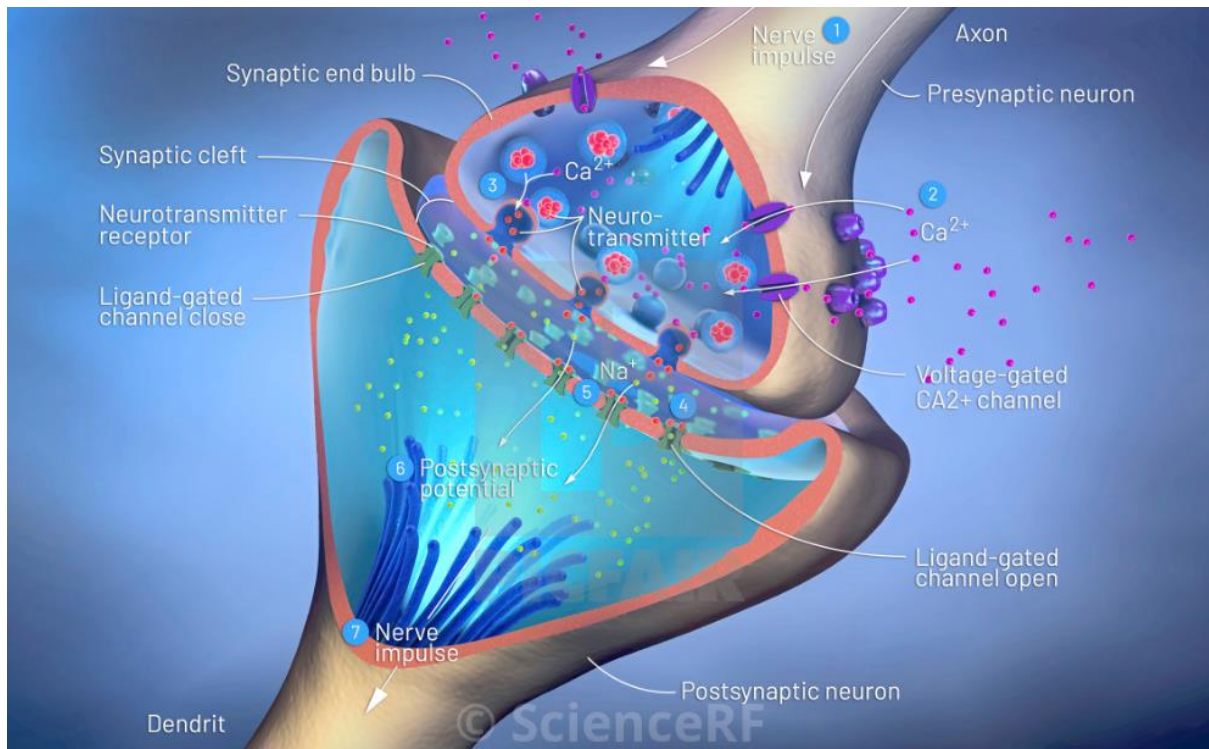


Figure 4: Basic events in typical synaptic transmission. [6]

2.1.3 Wallerian degeneration

From the above section, it is essential to appreciate that the axonal connections give rise to synaptic integrity and the neural network, which are responsible for crucial functions like behaviour and cognition [7]. Unfortunately, during primary injury, diffuse axonal injury occurs in patients who suffered a traumatic brain injury. Rotational forces, implied in TBI, cause grey and white matter to slide over each other [7]. This shear stretches neuron axons, initiating the Wallerian degeneration process in which an influx of calcium into the injured axon leads to the disruption in neural transmission. The latest is followed by the collapse of the myelinated axon membrane, resulting in lobulated and disconnected axonal segments. Wallerian degeneration might take 15 minutes to 2 hours to fully detach. Additionally, the proximal segment swells while downstream fibre disintegrates [7].

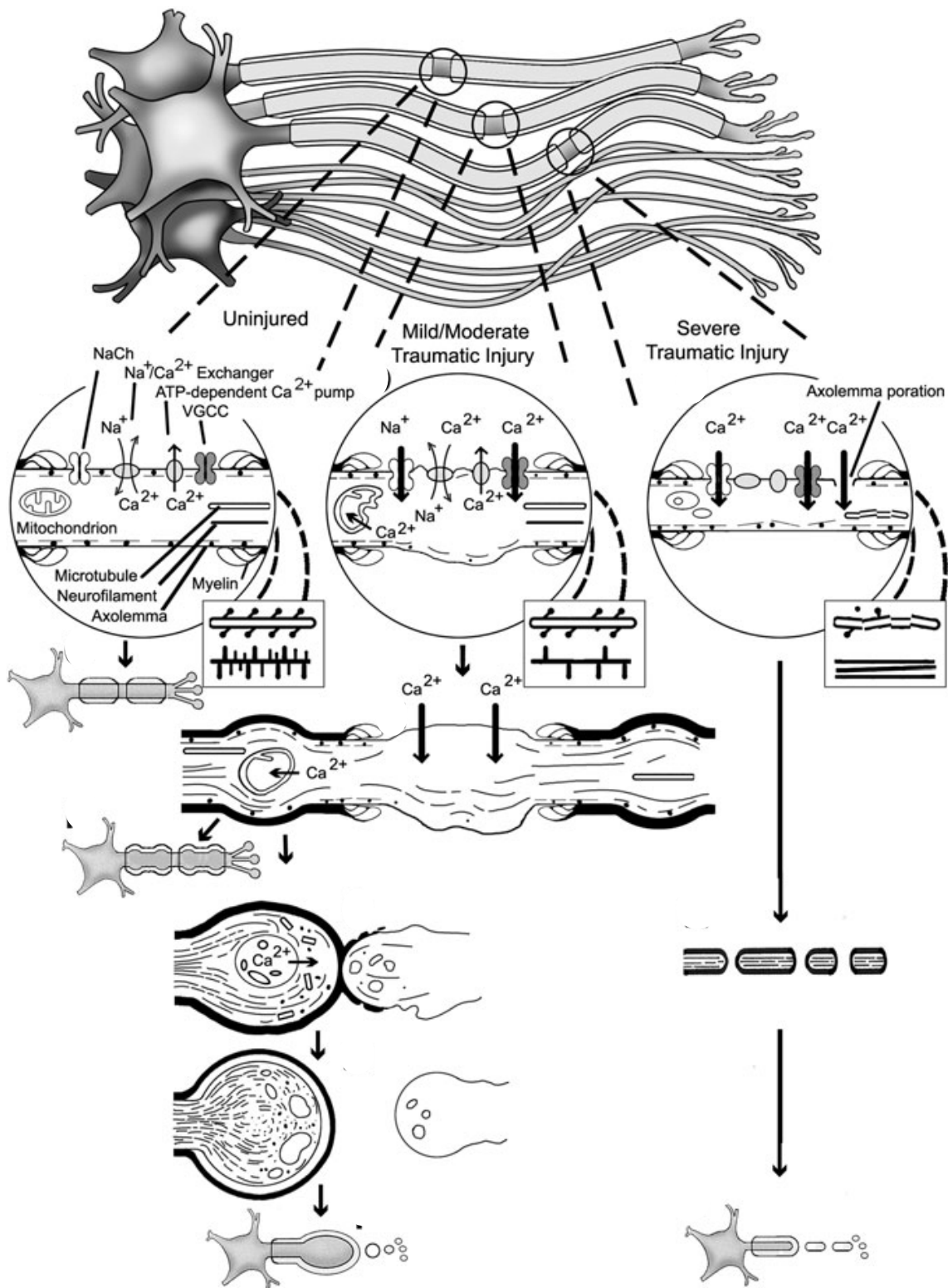


Figure 5: Evolving pathophysiology of diffuse axonal injury post-trauma, leading to Wallerian degeneration. [7, p. 44]

Secondary effects of neuroinflammation, such as parenchyma compression and blood flow restrictions, might lead to secondary ischaemia. Likewise, the pathophysiology of diffuse axonal injury induces enzymatic changes, like the increase in calpains (calcium-mediated proteases) and structural perturbations, which impair neuronal function and neural transmission, even in survived cells [7].

2.2 PRINCIPAL PARTS OF THE SKULL, BRAIN, AND CRANIAL NERVES

To better understand the macro-injuries generated by TBI and their latter implications on the cerebral haemodynamic (3), it is essential to explore the main parts of the central nervous system. Therefore, this section describes the principal functions of each anatomical structure, providing insights of the possible disturbances that could lead to disability after trauma (4).

2.2.1 Cranial bones

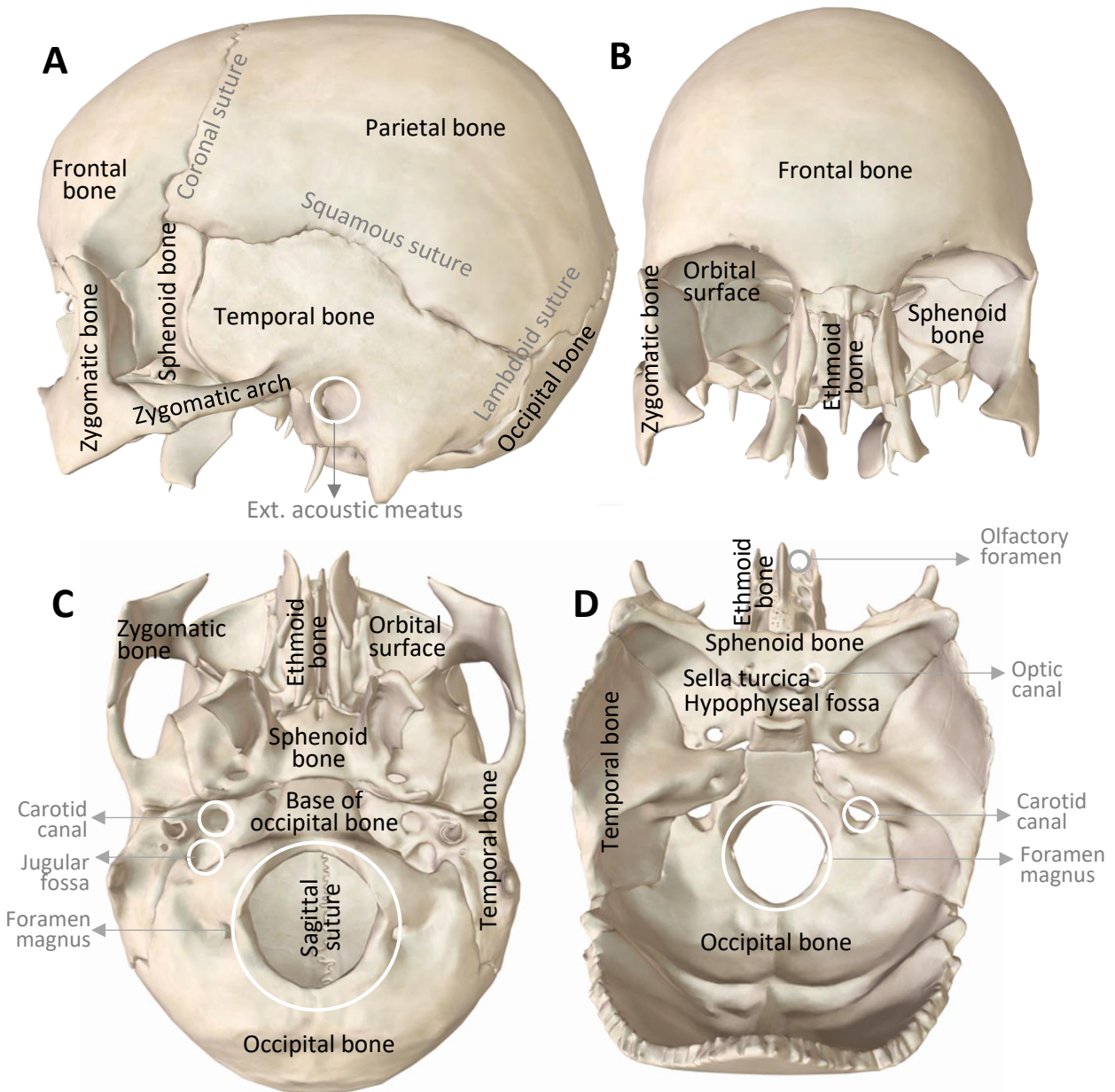


Figure 6: Cranial bones

A. lateral view of the cranial bones and sutures in the skull; B. anterior view of the cranial bones; C. Inferior view of the cranial base bones, canals and foramina; D. Superior view of the cranial base with calvaria removed shows main bones, canals and foramina (models modified from www.biodigital.com and labels referred from [8])

The skull is composed of two categories of bones: the bony framework of the head: Cranial bones, and facial bones. Cranial bones are the most relevant for the current study because they form the cranial cavity, which encloses and protects the brain [9]. The following paragraph describes the main parts and functions of the cranial bones.

The frontal bone forms the forehead and the orbital surface, part of the cranial cavity floor. The two parietal bones incorporate the more significant portion of the cranial cavity's sides and roof, which contain many protrusions and depressions that accommodate the blood vessels supplying and protective tissues covering the brain [9]. The paired temporal bones form the inferior lateral part of the cranium. Its thinnest portion is the pterion, located above the zygomatic arch (Figure 6) [9]. The occipital bone integrates the posterior part and most of the base of the cranium, where the foramen magnum allows the connection between the inferior part of the brain and the spinal cord) [9]. Likewise, the sphenoid bone lies at the middle part of the base of the skull, and it articulates with all the other cranial bones, holding them together. This “keystone” has a critical saddle-shaped structure called Sella turcica, in which the hypophyseal fossa contains the pituitary (master gland for hormonal control) [9]. The sphenoid bone also holds the optic foramen, through which the optic nerve and ophthalmic artery pass into the orbit, as well as the foramen ovale, which transmits nerves through the skull [9]. Finally, the ethmoid bone is in the anterior part of the cranial floor. The ethmoid bone is a primary superior supporting structure of the nasal cavity and contains the olfactory foramina through which the olfactory nerves pass [9].

2.2.2 Meninges

The brain is protected from outside forces by the skull; nonetheless, an additional covering of three meninges stabilizes the shape and position of the brain during head movement. The brain is mechanically suspended in the meninges, which are attached to the skull. Therefore, the brain cannot move independently of the head movements. [10]. Additionally, the brain is partially floating into a layer of circulating cerebrospinal fluid (CSF) within the meninges, creating a buoyant effect that decreases the tendency of forces [10]. Unfortunately, depending on the severity of brain trauma, these protective functions of the meninges can be disrupted, leading to severe consequences in the cerebral haemodynamic (3) and patients' outcomes (4). Because of the above, it is crucial to understand the anatomy and physiology of the dura mater, the arachnoid mater, and the pia mater described below.

The dura mater is a thick collagen layer that connects the skull with the delicate arachnoid. The subdural space between these two meninges might get filled with fluid after trauma, for example, because of a hematoma [10]. Dural reflections split up different components of the brain; for instance,

the falx cerebri separates both hemispheres. After trauma, patients might present herniations as the result of swelling or bleeding [10]. Brains tissue shifting between compartments might compress arteries, vessels, nerves, and other structures, leading to life-threatening events [11]. As well as the dural reflections, there are venous sinuses like the superior sagittal sinus shown in Figure 7 (Modified from www.kenhub.com and McGraw Hill Companies). The function of such structures is to drain brain fluids from small sinuses to the internal jugular vein [10].

The dura mater bundles to the thin arachnoid meninge, which is covered by trabeculae that extend to the pia mater, with which they merge [10]. The space between these two meninges is the subarachnoid space, which is filled with CSF. Certain regions of the subarachnoid space have considerably more volume of CSF than others; they are called cisterns and are essential for CSF circulation (Chapter 3) [10]. Other critical structures related to CSF circulation are the arachnoid villi, which consist of small evaginations of the arachnoid. They are important sites for the reabsorption of CSF to the venous system. These structures allow continuous one-way direction flow of CSF from the subarachnoid space to the venous sinuses. Typically, CSF pressure is higher than venous pressure, but even if the pressure gradient reverses, the flow does not [10]. However, the arachnoid villi's flow can be disrupted or wholly obstructed (causing hydrocephalus) due to haemodynamic changes or cerebral haemorrhages led by traumatic injuries.

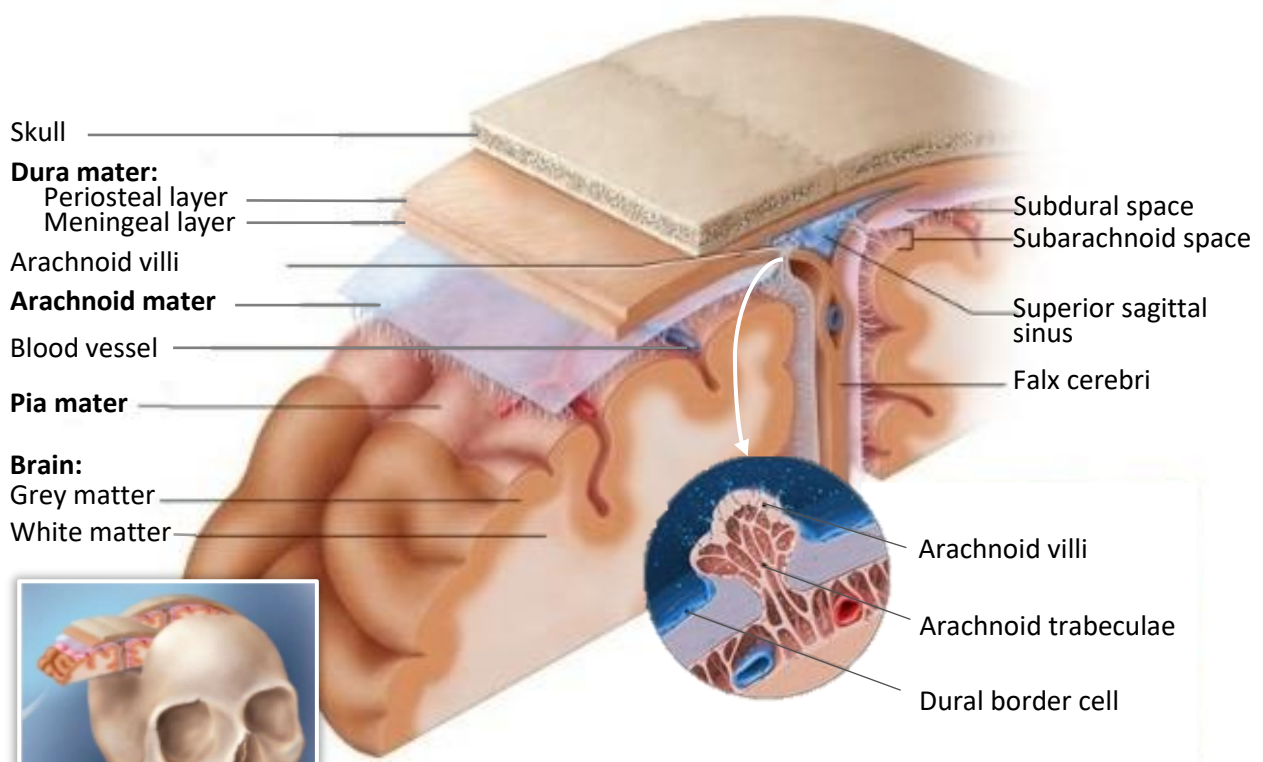


Figure 7: Coronal section through the superior sagittal sinus.

Finally, the pia mater invests all the contours of the CNS, and it carries a perivascular layer where the arteries and vessels become capillaries [10].

2.2.3 Cerebellum

The cerebellum is about a tenth of the brain mass; however, it contains almost half the neurons in the brain. These numerous axons pass through the cerebellar peduncles, which attach the cerebellum to the brain stem and connect it to the midbrain, thalamus, pons, medulla oblongata and spinal cord [2]. Figure 8 shows the anatomical division of the cerebellum into the anterior, posterior and flocculonodular lobes. From a functional perspective, each hemisphere separated by the vermis comprises an intermediate and a lateral zone. For example, the spine cerebellum consists of the vermis and the intermediate zones, which coordinate voluntary muscle movements of the limb and the trunk [12]. Likewise, the cerebral cerebellum involves the lateral zones implicated in planning timing movements, cognition activities and language processing. Finally, the vestibulocerebellum consists mainly of the flocculonodular lobe and provides the circuits to control posture, equilibrium, and eye movements [12].

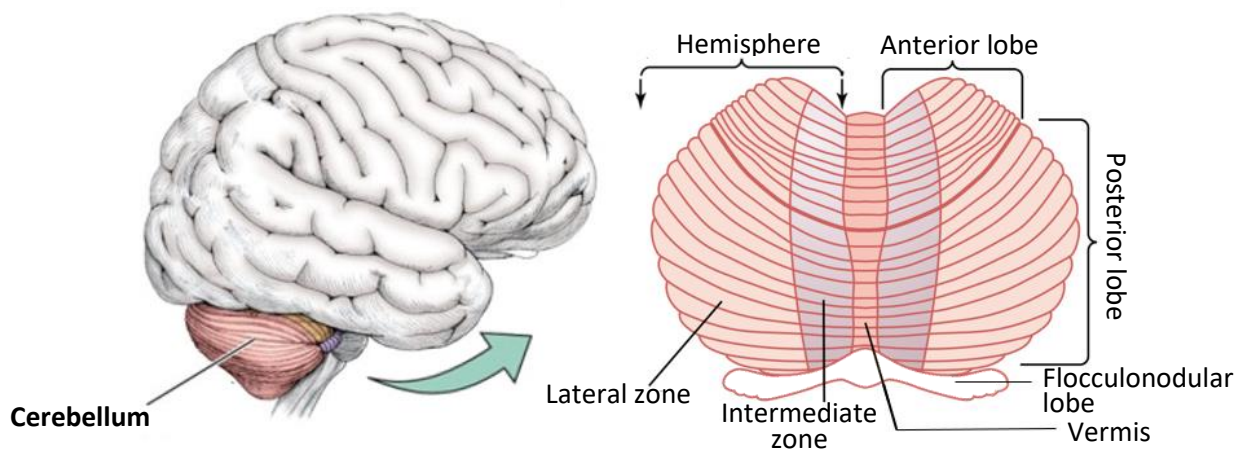


Figure 8: Anatomical and functional parts of the cerebellum as seen from the posteroinferior view. [12, p. 682], [13]

In some cases, brain trauma causes degeneration of cerebellar nuclei. For example, damage on the spine cerebellum or the cerebral cerebellum can result in uncoordinated movements, loss of musculature tone, jerky and oscillatory movements of the limbs, and movements beyond the intended mark manifestations of ataxia and dysmetria [2], [12]. Also, the loss of perception during rapid motor movements, such as talking, leads to a change in the speech pattern, which is often described as dysarthria. Likewise, damages on the Vestibulocerebellum nuclei are associated with an unsteady walk and tremulous movements of the eyes, known as nystagmus [2], [12].

2.2.4 Brainstem and cranial nerves

Cranial Nerves

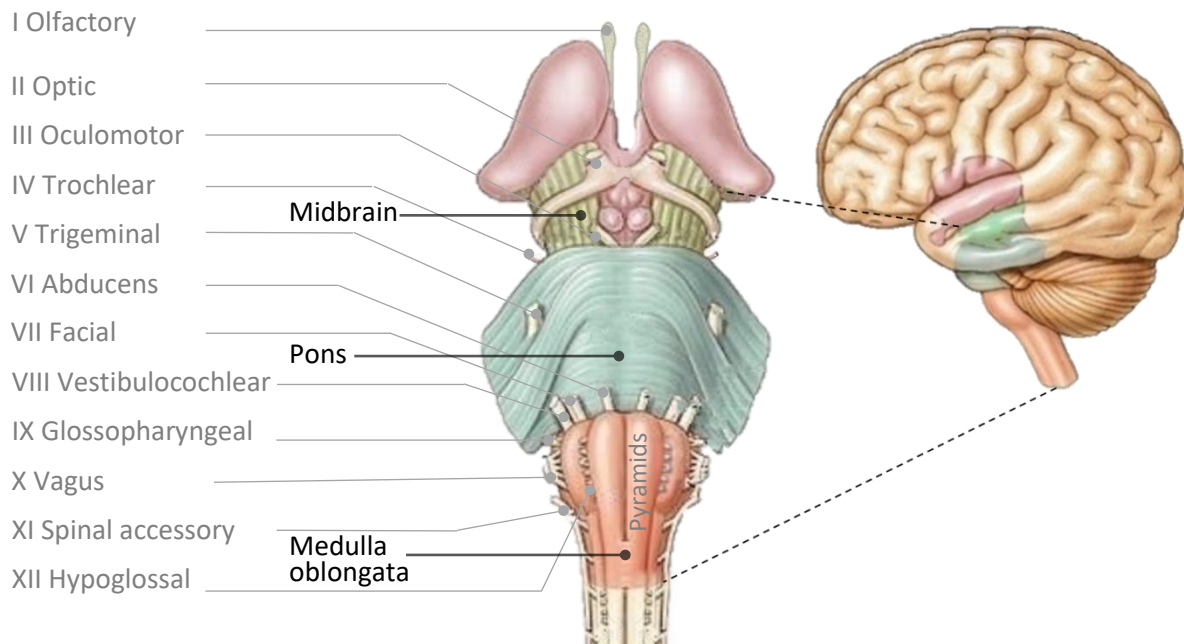


Figure 9: Cranial nerve nuclei

The cranial nerve nuclei are located in an anterior view of the brainstem, composed of the medulla oblongata, pons and midbrain or mesencephalon. (modified from www.austincc.edu)

The brainstem is the part of the brain between the spinal cord and the thalamus; the latest is the pink structure depicted in Figure 9. The stem consists of the midbrain or mesencephalon, pons, and medulla oblongata, in a proximal to distal order. All three parts contain sensory (ascending) and motor (descending) tracts and nuclei. Some of these nuclei control vital body functions, and others are the cranial nerves nucleus [2]. As ten of twelve cranial nerves have their nuclei located in the brainstem, this section includes Table 2 to explain the primary role of each of them, to have a complete understanding of the brainstem functions. The above presents the possible outcomes in a patient after brainstem injury.

The midbrain coordinates head, eyes, and trunk movements in response to visual and auditory stimuli. It contains the cerebral peduncles mentioned in the Cerebellum section, which, collectively with the pons, relay nerve impulses from motor areas of the cortex to the cerebellum, contributing to movement control. The pons and the medulla oblongata are part of the equilibrium pathway of the brain and are responsible for breathing control [2]. The latter also contains all sensory and motor tracts that extend between the spinal cord and the brain, passing through the foramen magnum. On the medullary pyramids, 90% of the right hemisphere axons cross to the left side of the spinal cord and those from the left cross to the right side, explaining why each side of the brain controls voluntary movements on the opposite side of the body [2]. The medulla is responsible for the cardiovascular

centre in charge of heartbeat regulation, vasoconstriction, and vasodilatation. The medulla is the source of many sensory pathways to the brain that allow the coordination of involuntary actions like vomiting, swallowing, sneezing, coughing, and hiccupping, among others. Finally, behind the main three-part of the brainstem is the reticular formation. It involves essential functions like consciousness, awaking and attention maintenance [2].

Injury to the brainstem can be fatal, especially when oedema depresses or even inactivates the respiratory centre. Also, swelling brain tissue leads to the compression of cerebral arteries, which might block the cerebral blood supply generating ischaemia [14]. Brain swelling can also collapse the medulla against the bone, resulting in upper limb paralysis. Likewise, nonfatal injury to the medulla may include cranial nerve malfunctions, as presented in Table 2 [2].

Table 2: Summary of the cranial nerves' functions and possible consequences after trauma. (summarized from [2])

Cranial Nerve	Nuclei	Principal functions	Possible outcomes after TBI
Olfactory (I)	Olfactory peduncle	Olfaction.	Sense of smell loss due to ethmoid bone fracture or any lesion along the olfactory pathway.
Optic (II)	Thalamus	Vision.	Visual field defects, visual acuity loss or blindness due to lesions or compression along the visual pathway.
Oculomotor (III)	Midbrain	<p>Eyeball movements control.</p> <p>Pupil contraction.</p> <p>Lens changes regulation.</p>	<p>Strabismus (both eyes do not fix on the same object).</p> <p>Diplopia (loss of adjustment for near vision).</p>
Trochlear (IV)	Midbrain	Eyeball movements control.	<p>Strabismus.</p> <p>Diplopia.</p>
Trigeminal (V)	Pons	<p>Oversees touch, pain, and thermal sensations from the scalp, face, and oral cavity.</p> <p>Controls the motor components of chewing and middle ear muscle movement.</p>	<p>Neuralgia is a sharp-cutting pain caused by inflammation or a lesion in the nerve. Injuries in the mandibular branch of the nerve may cause paralysis of the chewing muscles and loss of sensation in the lower part of the face.</p>

Cranial Nerve	Nuclei	Principal functions	Possible outcomes after TBI
Abducens (VI)	Pons	Eyeball movements control.	Strabismus. Diplopia.
Facial (VII)	Pons	Taste and sensations in the external ear canal. Controls facial expressions and secretion of tears and saliva.	Trauma might produce paralysis of the facial muscles, loss of taste, decreased salivation, and loss of ability to close the eyes, even during sleep.
Vestibulocochlear (VIII)	Pons and medulla oblongata	Hearing. Equilibrium.	Injury to the VIII nerve branch may cause vertigo (feeling of a rotating environment), ataxia (muscular incoordination), nystagmus, tinnitus (ringing in the ears) or deafness.
Glossopharyngeal (IX)	Medulla oblongata	Taste. Swallowing proprioception. Blood pressure monitoring. O ₂ and CO ₂ levels in blood monitoring. Sensations in the external ear canal and pharynx. Saliva secretion.	Injury in this nerve causes dysphagia (difficulty swallowing), aptyalia (low saliva secretion) and ageusia (loss of taste).
Vagus (X)	Medulla oblongata	Taste. Throat and voice box muscles proprioception. Blood pressure monitoring. O ₂ and CO ₂ levels in blood monitoring. Sensations in the external ear canal, thoracic and abdominal organs. Swallowing, vocalization, and coughing.	The primary outcomes are interruptions of sensation to the organs related to the nerve, leading to dysphagia or increased heart rate (tachycardia).

Cranial Nerve	Nuclei	Principal functions	Possible outcomes after TBI
		Gastrointestinal organs motility and secretion control. Respiratory tract constriction. Decreases heart rate.	
Accessory (XI)	Medulla oblongata	Movement of the head and the bones that connects the upper limb to the axial skeleton.	Nerve damage leads to difficulty in neck and shoulder movements.
Hypoglossal (XII)	Medulla oblongata	Speech. Manipulation of food. Swallowing.	Trauma might cause dysphagia and difficulty in chewing or in speaking.

2.2.5 Diencephalon

The diencephalon is surrounded by the cerebral hemispheres and is organised by masses of grey matter (nuclei) that are spread by tracts of white matter. This structure comprises the thalamus, the hypothalamus and the epithalamus (Figure 10, modified from www.istockphoto.com) [2]. The thalamus's primary function is transmitting sensory information from the spinal cord or brainstem to the sensory parts of the cerebral cortex and motor impulses from the cerebellum and the basal nuclei to the motor areas of the cortex. The thalamus involves seven prominent nuclei that are active in every human action [15]. These nuclei generally function in emotions, learning, memory, cognition, awaking, vigilance, consciousness, and integrating sensory information [2].

After trauma, thalamic damage is attributed to diffuse axonal injury or ischaemia, even months after injury. Severe trauma in the thalamus can lead the patient to a vegetative state due to this structure oversees consciousness. When the lesion does not involve consciousness alterations, it might affect the sleep-wake cycle, resulting in insomnia [16]. Likewise, it has been found that thalamic infarction also contributes to amnesia and is associated with deficits in sustained attention, associative learning, and reaction time. Behavioural changes like apathy can also appear depending on the lesion's location in the thalamus. As the thalamus's principal function is the transmission of motor and sensory impulses to and from the cortex, movement disturbances and loss of senses might be expected after trauma [16].

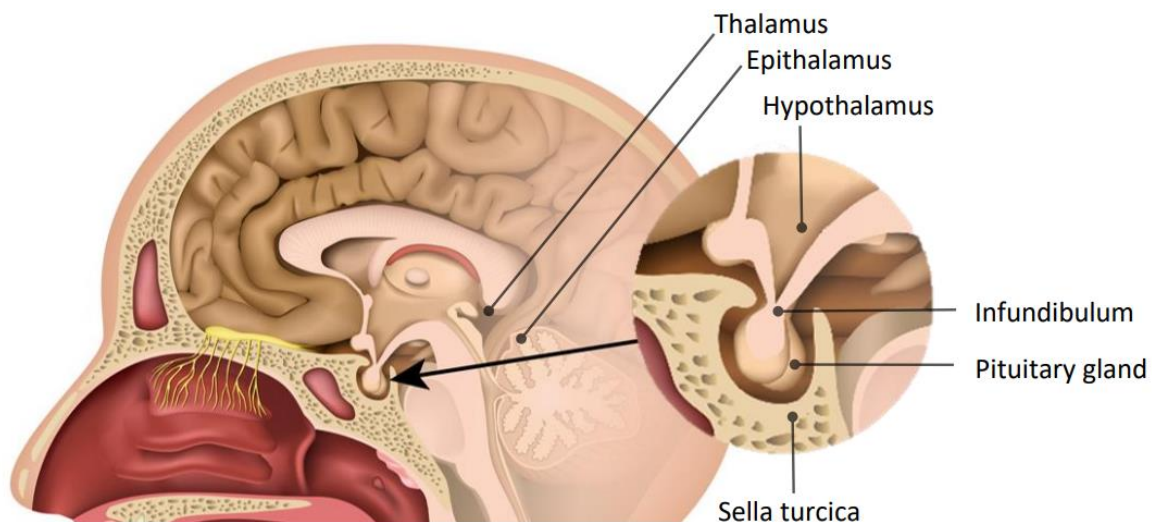


Figure 10: Sagittal view of the diencephalon parts, showing the projection of the hypothalamus to the pituitary gland

The hypothalamus is one of the primary regulators of homeostasis (stability). It oversees autonomic functions and coordinates drive-related behaviour. When it receives inputs from visceral nuclei in the brainstem and spinal cord, it updates information about the body's internal condition, such as the osmotic pressure, blood glucose level, specific hormone concentrations, and the temperature of blood [2], [17]. According to these inputs, the hypothalamus generates impulses that cause the sensation of thirst, fullness, hungry, and promote heat loss or production, among others. Additionally, the hypothalamus regulates visceral activities through the autonomic nervous system, including heart rate, gastrointestinal movements, and bladder contraction [2], [17]. Likewise, when the hypothalamus receives stimuli from the limbic system (described shortly), in conjunction regulates emotional and behavioural patterns like rage, aggression, pain, pleasure, and sexual arousal. Finally, the hypothalamus controls the pituitary gland, where several hormones are released into the circulation [2], [17].

Any damage to the hypothalamus from a traumatic brain injury can disrupt the homeostatic mechanisms described above and the patient's behaviour [17]. Some studies reported that behavioural changes due to TBI increases the risk of violent offending. For instance, a publication in *The Lancet Psychiatry* in 2018 found that up to 60 per cent of people in custody have suffered some head injury in the past, ranging from mild to severe [18]. Moreover, when the brain is in movement during a traumatic episode, the pituitary cannot move from the Sella turcica nest, resulting in partial or total disconnection at the infundibulum (Figure 10) [7]. Significant endocrine consequences are related to inhibiting the hormones presented in Table 3, reducing or avoiding their effects [19].

Table 3: Major pituitary hormones and their effects (Modified from: [19, p. 628])

Hormone	Effects
Antidiuretic hormone (ADH)	Body water balance
Oxytocin (OT)	Prompts uterine contractions during childbirth
Luteinizing hormone (LH)	Production of sex hormones
Follicle-stimulating hormone (FSH)	Production of sperm and eggs
Thyroid-stimulating hormone (TSH)	Releases thyroid hormone, which regulates metabolism
Prolactin (PRL)	Promotes milk production during lactation
Growth hormone (GH)	Insulin production and stimulates body growth
Adrenocorticotrophic hormone (ACTH)	Induces glucocorticoid production and stress response

Finally, the epithalamus consists of the pineal gland and the habenular nuclei. The first one secretes the hormone melatonin, which promotes sleepiness. The second one is involved in creating emotional responses to odours. Therefore, when this part of the diencephalon is injured, the body's internal biological clock, which establishes the circadian (daily) rhythm, might be affected [2].

2.2.6 Cerebrum and limbic system

The cerebrum consists of an external grey matter cortex and an internal white matter region within some nuclei [20]. Anatomically, it is divided into two hemispheres interconnected by the corpus callosum. Each hemisphere is subdivided into lobes, which are named according to the bones covering them. Figure 11 shows the anatomical division of the cerebrum [2], [20] (modified from www.quora.com and [2], p. 497). Likewise, the cerebrum has been mapped by its functional organization in primary, association and limbic areas. Primary areas are closely identified according to sensory and motor functions [2], [20]. The number of connections in the cortical area depends on the sensibility or complexity of the movement of each body part rather than on the size of this part. For instance, the cortical regions devoted to finger sensations or movements are more extensive than those devoted to the thorax because fingers have much more sensory receptors and delicate movements than the thorax [2]. Furthermore, the association areas have more complex response properties, as they respond to multiple types of stimuli and may only respond under a particular behaviour condition. Finally, limbic areas create new memories and emotional responses by interconnecting the hypothalamus with the cortex [2], [20]. Table 4 provides an overview of the primary functional regions within the cerebrum and their potential clinical consequences following trauma. The numbers in Table 4 are aligned with their respective positions in Figure 11.

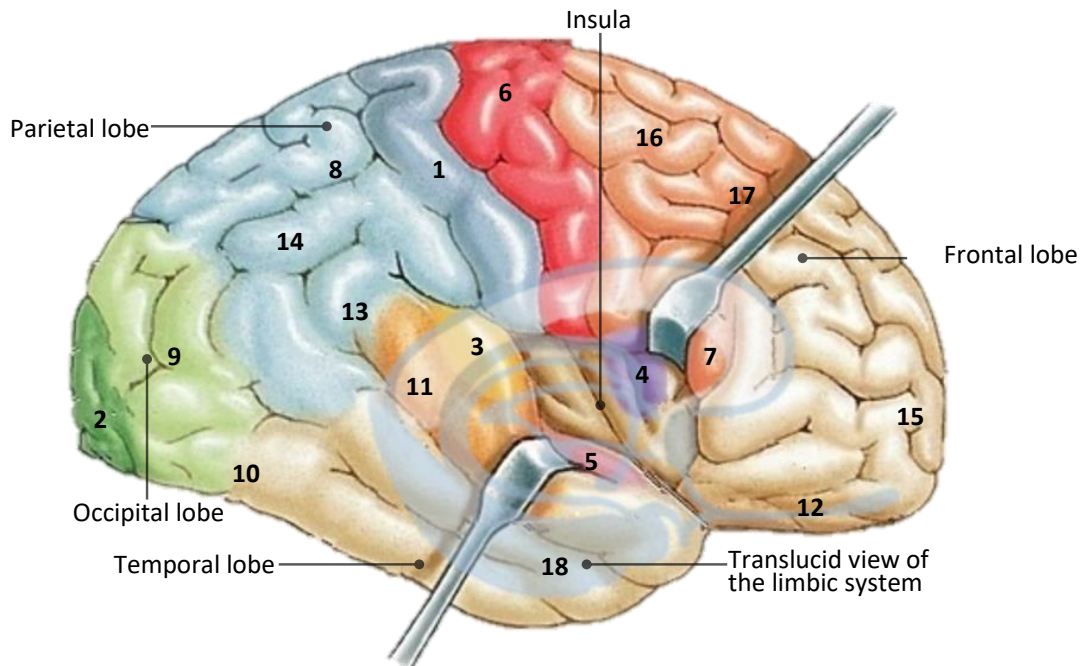


Figure 11: Lateral view of the cerebrum's primary anatomical and functional areas division, with a translucent view of the limbic system.

Table 4: Summary of the cerebrum functional areas and possible consequences after trauma. (information summarized from [2], [20])

Figure 11 #	Functional division	Area	Function	Outcome after trauma
1	Primary	Somatosensory	Perception of somatic sensations and their origin.	Weakness or diminished sensations.
2	Primary	Visual	Visual information perception.	Weakness or diminished ability to see.
3	Primary	Auditory	Sound perception.	Weakness or diminished ability to hear.
4	Primary	Gustatory	Taste perception and discrimination.	Weakness or diminished ability to taste.
5	Primary	Olfactory	Smell perception.	Weakness or diminished ability to smell.
6	Primary	Motor	Voluntary muscular movement control.	Weakness or diminished ability to

Figure 11 #	Functional division	Area	Function	Outcome after trauma
				perform voluntary movements.
7	Primary	Broca's speech	Written and spoken language production. Recognition of rhythm and music.	Nonfluent aphasia, in which comprehension is intact but language is produced with difficulty.
8	Association	Somatosensory	Recognition of the shape, texture, and position of an object. Creation of memories for future recognition.	Inability to categorize objects.
9	Association	Visual	Recognition and evaluation of what is seen.	Colour and movement agnosia. Difficulty with locating objects and production of hallucinations.
10	Association	Facial recognition	Faces information storage for future recognition.	Prosopagnosia, which is the difficulty in recognizing faces.
11	Association	Auditory	Recognition of a particular sound.	Weakness or diminished ability to recognize sounds.
12	Association	Orbitofrontal	Odour identification and discrimination.	Weakness or diminished ability to identify odours.
13	Association	Wernicke's	Written and spoken language comprehension. Recognition of rhythm and music.	Fluent aphasia, in which language can be produced but comprehension is impaired.

Figure 11 #	Functional division	Area	Function	Outcome after trauma
14	Association	Common integrative	Thoughts formation based on integrated sensory interpretations.	Apraxia is the lack of awareness of particular body parts and/or surrounding space.
15	Association	Prefrontal cortex	Concerned with the personality, intellect, complex learning abilities, recall of information, initiative, judgment, foresight, reasoning, conscience, intuition, mood, planning, and development of abstract ideas.	Behaviour and cognition impairments. Attending difficulties. Mood changes. Persistence of a single thought and loss of spontaneity.
16	Association	Premotor	Larynx, pharynx, and mouth muscles control while speaking. Involved are motor activities' learning and storage.	Loss of the ability to coordinate fine movements, walk, grab objects and make rapid movements.
17	Association	Frontal eye field	Control of voluntary scanning movements of the eyes.	Problems with reading (Alexia).
18	Limbic	Limbic	Short-term memory storage and long-term memory consolidation. Formation and expression of associations between objects or events and the emotional reactions they provoke.	Loss of short-term memory items. Impairment to create new long-term memories. Changes in sexual behaviour.

2.4 SUMMARY

This chapter described the most important structures of the brain that are exposed to injury after TBI and their clinical consequences in the patients. From diffuse axonal injury in the neuron until damage in more complex brain structures is expected after TBI, for instance, motor, sensory, cognitive, hormonal or behavioural impairments. Many of these outcomes are associated with secondary injuries that occur some hours after injury, like brain swelling, bleeding and ischaemia. However, those structural variations are highly correlated to cerebral haemodynamic changes, which are vital in TBI monitoring, as explained in the next chapter.

3 CEREBRAL HAEMODYNAMICS

3.1 BLOOD FLOW IN THE BRAIN

3.1.1 Blood structure and functions

Blood is a connective tissue in charge of oxygen (O_2), nutrients and hormones transportation to the tissues and the removal of waste products (e.g. carbon dioxide, CO_2) from them [21], [22]. Circulating blood regulates pH levels, temperature, and osmotic pressure in the body, playing an essential role in protecting against disease. Blood is composed of plasma (55%), white blood cells and platelets (1%), and red blood cells (RBCs) or erythrocytes (44%) [21], [22], as shown in Figure 12 (modified from www.nursekey.com and www.medicinenet.com). The latter has a crucial function for the current research. RBCs are responsible for the transportation of oxygen, waste products and nutrients, such as glucose; all essential in brain metabolism [21], [22]. RBCs are highly specialized in oxygen transportation. Because of the absence of a nucleus, RBCs have low metabolic activity. Also, their biconcave shape increases the surface available for carrying O_2 molecules to the tissues or CO_2 when returning to the lungs. Moreover, these flexible cells can easily pass through tiny capillaries, providing oxygen to every tissue cell in the body. RBCs contain a protein with a high gas-binding capacity called haemoglobin, which allows oxygen transport [21], [22].

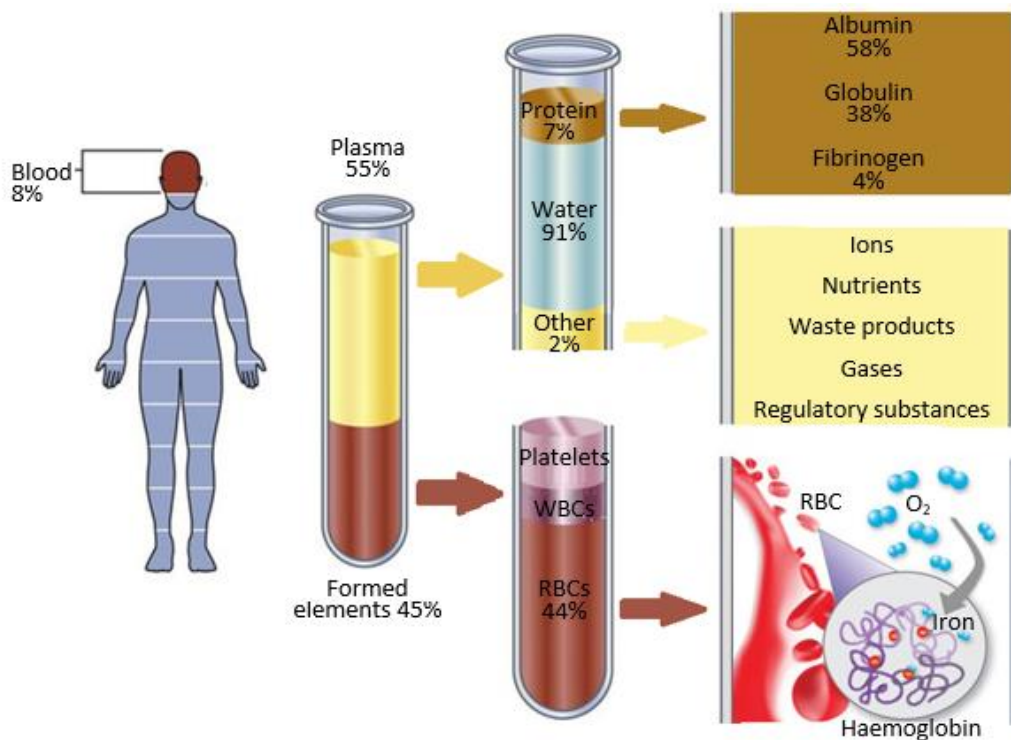


Figure 12: components of blood, showing the haemoglobin's iron-oxygen reaction

Haemoglobin consists of globin protein, which comprises four polypeptide chains. Each chain is bonded to an haeme pigment with an iron ion at the centre. When gas exchange occurs in the lungs, the four iron ions in each haemoglobin molecule bind four oxygen molecules through an iron-oxygen reaction [21], [22]. Then, RBCs carry the oxyhaemoglobin through the arteries to the tissues, where the iron-oxygen reaction reverses as the blood cells flow through the capillaries, this delivery is known as oxygen perfusion. Once haemoglobin is free of oxygen (deoxyhaemoglobin), it can collect part of the CO₂ discharged by the tissues. However, most of the CO₂ is transported in the venous blood plasma and is released into the lungs, where it can finally be expelled by exhalation [21], [22]. As a result, arterial blood, rich in O₂, is bright red, while venous blood's colour is dark red due to its poor O₂ content.

In addition to transportation, haemoglobin has another crucial function related to the current research: regulating blood flow and blood pressure [22]. When tissue requires more oxygen than that available in the blood flow, nitric oxide (NO) is released by the vessel's endothelium, producing vasodilatation of the capillaries. In addition, an increased blood vessel diameter improves flow and oxygen delivery to the tissue cells and decreases blood pressure [22]. The above physiological response is mainly vital in the haemodynamic of the brain after trauma, as will be explained in section 3.4. Autoregulation.

3.1.2 The heart and cardiac cycle

Once the blood structure and its functions have been explained, it is necessary to recognize the morpho-physiology involved in blood circulation, perfusion, and oxygenation of the tissues.

The heart consists of the atria, two superior receiving chambers, and the ventricle, two inferior pumping chambers. With each beat, the heart pumps blood into systemic and pulmonary circulation. The output of one circuit is the input of the other, with the hearth in between. The left atrium receives oxygenated blood from the lungs, which is ejected by the left ventricle to the systemic circulation through the aorta artery [23]. The ascending aorta is divided into the internal carotid and the descending aorta; both arteries give rise to smaller-diameter arterioles, which finally lead to extensive beds of systemic capillaries. Nutrient and gas exchange occur on the capillary's walls, where oxygenated blood delivers O₂ to the tissue. Then, venules pick up disposed CO₂ and carry deoxygenated blood to more prominent systemic veins, returning the blood to the right atrium [23]. Next, the dark-red deoxygenated blood is ejected from the right atrium to the right ventricle into the lungs, where gas exchange occurs. In pulmonary capillaries, blood unloads CO₂, which is exhaled and picks up O₂ from inhaled air. Newly oxygenated blood flows back to the left atrium, and the cardiac cycle starts again [23].

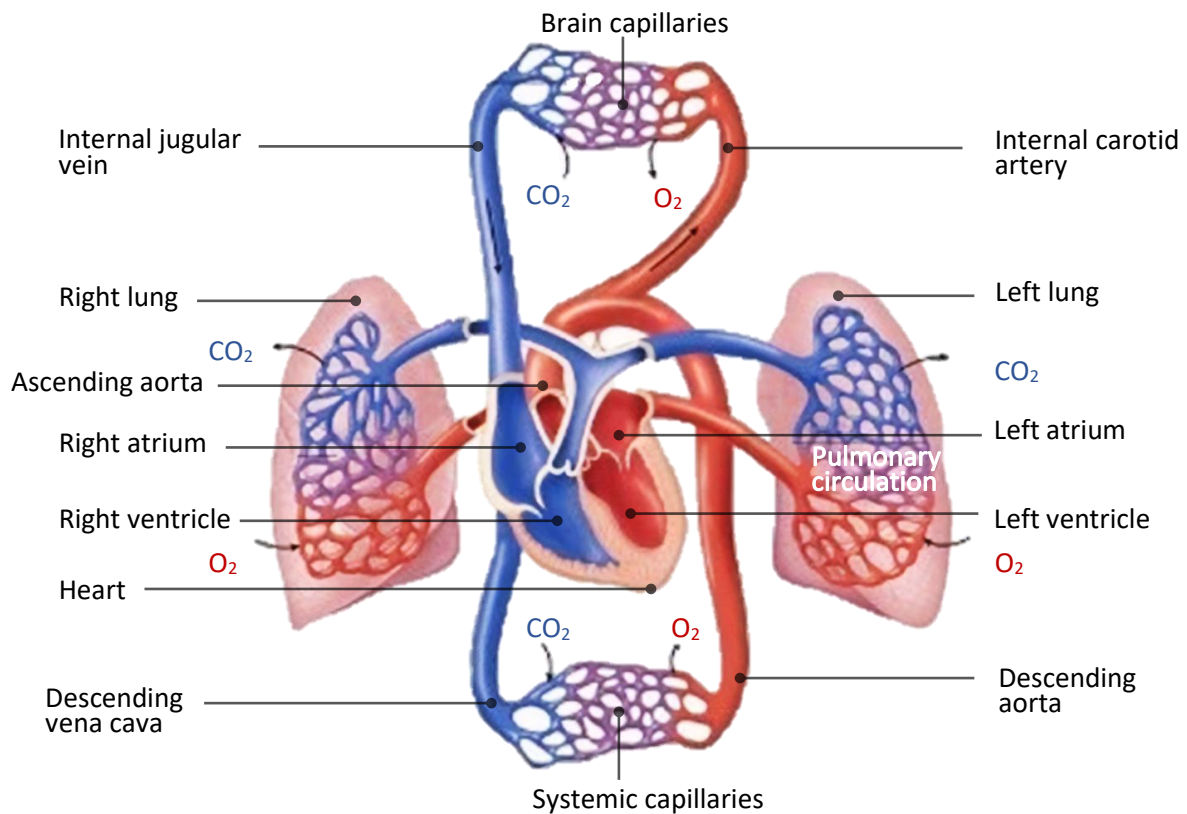


Figure 13: The circulatory system shows the main morphophysiological components involved in tissues' oxygenation and perfusion [23]

Without going into detail, the cardiac cycle consists of diastolic and systolic phases. Diastole is the relaxation period when the atria receive blood and eject it into the ventricles. At the end of this period, the arterial pressure decreases in a healthy adult to 70 mmHg. On the other hand, systole comprises the contraction of the ventricles that forces blood into systemic and pulmonary circulation. The fast ejection of fluid from the heart produces an arterial pressure peak of 110 mmHg in a healthy adult at rest [23].

3.1.3 Blood Supply of the Brain

The brain is dependent on a continuous oxygenated blood supply. Ten seconds of ischaemia leads to unconsciousness, 20 seconds ceases neuronal activity, and after a few minutes, irreversible damage starts [24]. Two pairs of vessels are the leading blood suppliers of the brain (Figure 14). The internal carotid system provides 80% of cerebral blood. Each internal carotid supplies an ipsilateral cerebral hemisphere, except for some parts of the occipital and temporal lobes. The vertebral-basilar system supplies those parts of the cerebrum, as well as the brainstem and the cerebellum, which corresponds to the remaining 20%. Both pairs of vessels supply the diencephalon [24].

Each internal carotid artery has two branches, the anterior and middle cerebral arteries. Both give rise to penetrating arteries that supply most of the cerebrum and hypothalamus. Likewise, vertebral arteries give rise to the posterior inferior cerebellar arteries just before they fuse to form the basilar

artery, which supplies numerous branches such as the anterior inferior cerebellar arteries, pontine arteries and superior cerebellar arteries. The basilar artery proceeds rostrally and bifurcates at the midbrain level into the two posterior cerebral arteries. Penetrating arteries of the vertebral-basilar system supply part of the cerebrum and most of the brainstem, cerebellum and thalamus [24].

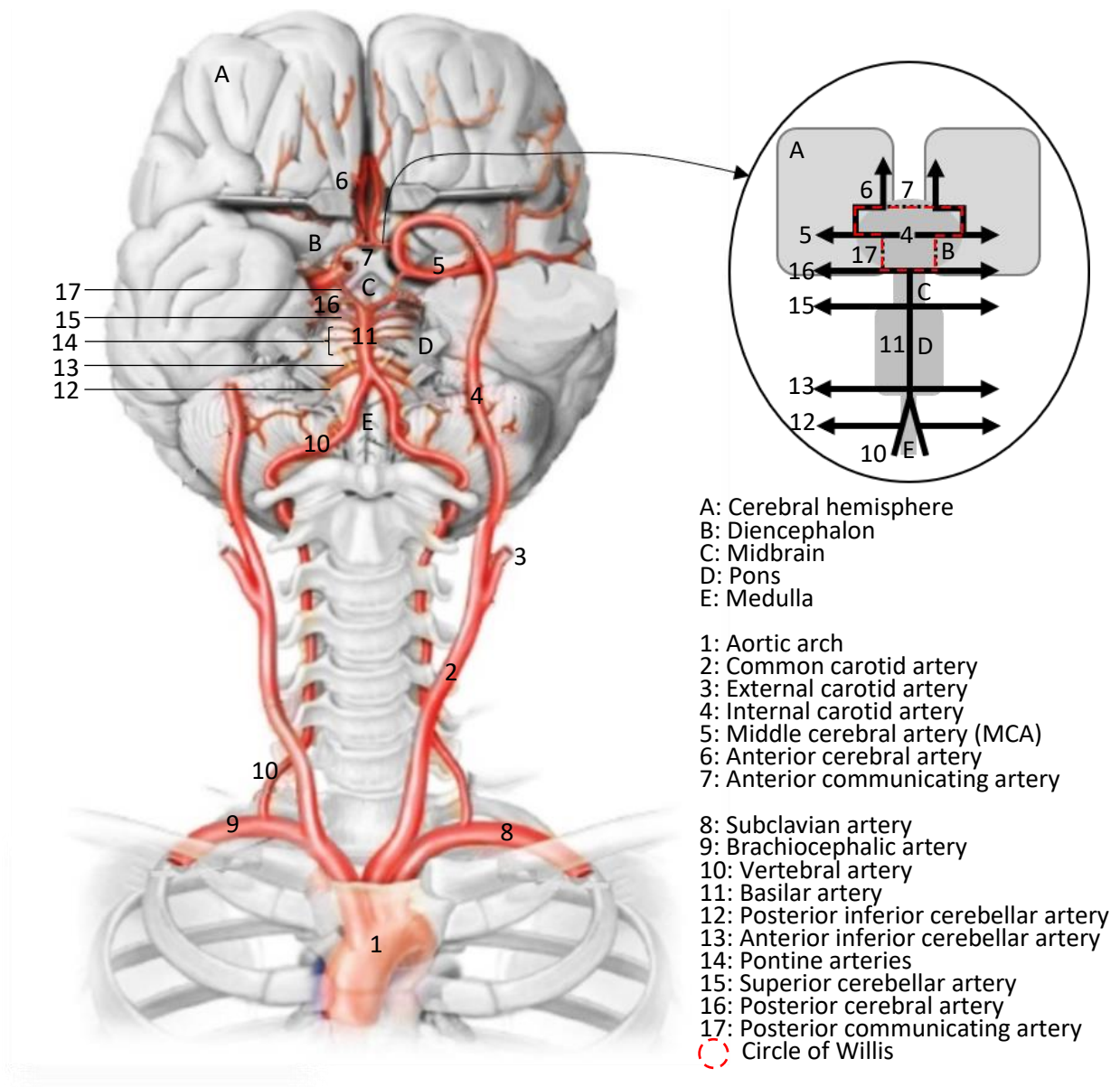


Figure 14: Arteries on the inferior surface of the brain [24]

The anterior communicating artery interconnects both hemispheres. These communicating arteries complete the circle of Willis, which in the case of a vessel's occlusion proximal to the cerebral arterial circle, provides an alternative pathway for blood flow [24].

Once blood reaches the capillary bed, oxygen and nutrient delivery are exchanged for disposable substances such as CO₂. Two sets of veins drain the deoxygenated blood, the superficial and deep veins. As their name implies, superficial veins drain blood from the top of each brain hemisphere into the superior sagittal sinus. In contrast, deep veins converge on the internal cerebral veins, joining the straight sinus. Both sinuses meet at the confluence sinuses, then after blood circulation through the transverse and sigmoid sinuses, deoxygenated blood reaches the internal jugular vein, which returns blood to the right atrium (Figure 13) [23], [24].

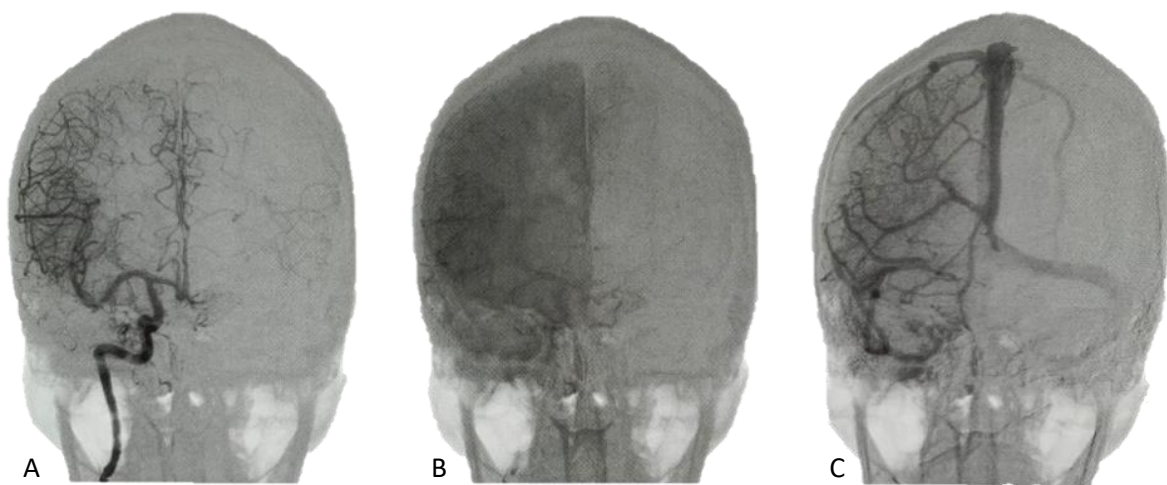


Figure 15: Series of anteroposterior views after injection of contrast material through the right internal carotid artery [24].

Figure 15 shows the whole circulatory process in the brain's right hemisphere. Just 2 seconds after the injection of contrast material through the right internal carotid artery, brain arteries are filled with blood (A). After 3 seconds, blood has moved to the capillary bed, so the image is diffuse (B). Finally, 2 seconds after gases and nutrients exchange, blood flows through the deep and external veins (C) into the sinuses, in its path to return to the heart [24].

The blood-brain barrier (BBB) partially separates the nervous system from the body, which highly restricts the entry of blood molecules and circulating immune cells into the brain. The BBB is formed by endothelial cells connected by tight junctions, as shown in Figure 16. Astrocytes are the most abundant glial cells in the brain; they are associated with synapsis modulation, neurons support and transport of nutrients from the blood to neuron [25], [26].

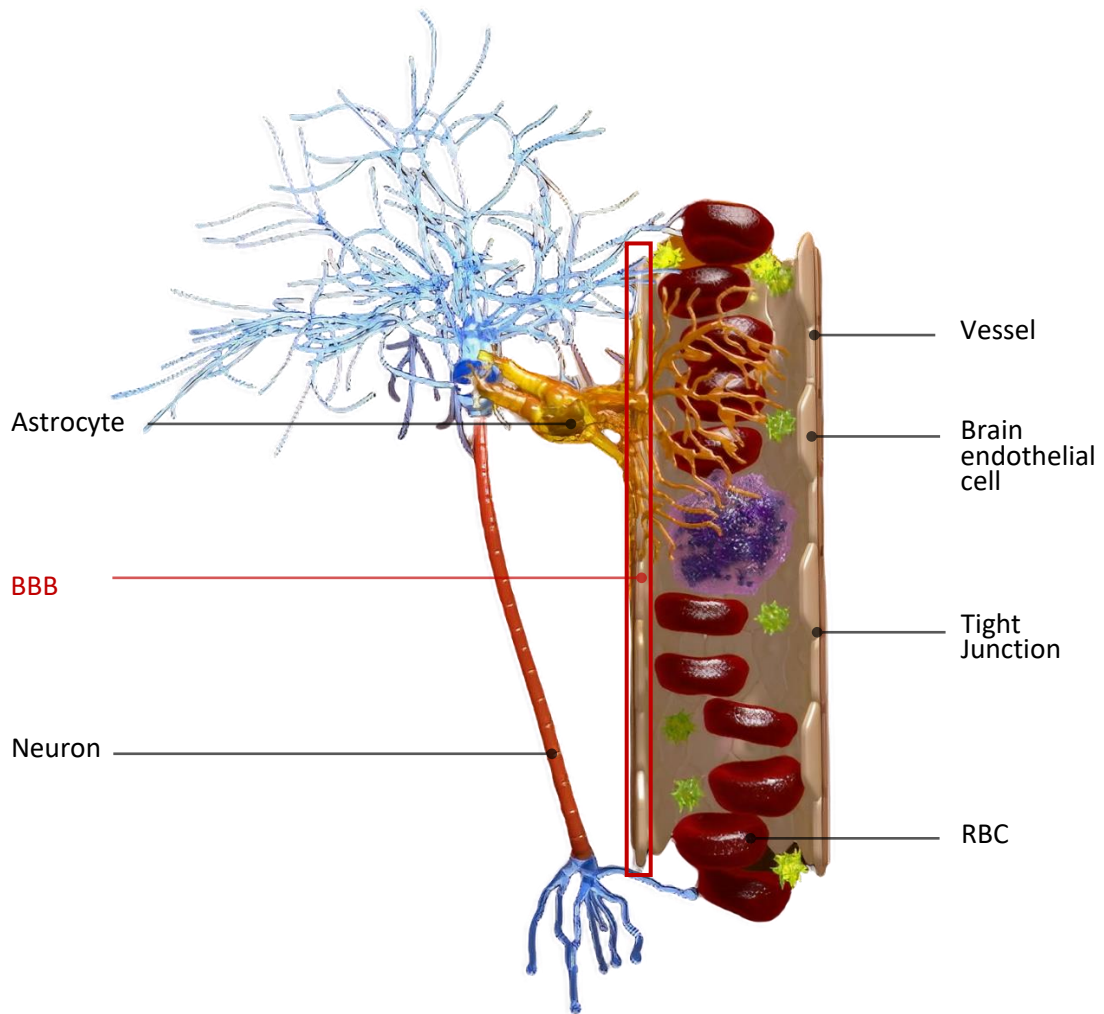


Figure 16: Flux of blood substances through the blood-brain barrier to an astrocyte that transports nutrients from the vessel to the neuron [27]

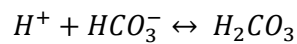
A traumatic brain injury could lead to mechanical disruption of vascular integrity and/or increased permeability of the BBB. For example, microvessel wall rupture rapidly activates intravascular coagulation, lowering cerebral blood flow and increasing the risk of ischaemia. Likewise, the disruption of tight junctions might be an attempt to restore brain metabolism when decreased brain perfusion fails to deliver the metabolites necessary for normal brain function. Consequently, the barrier increases its permeability to solve the crisis, which allows the non-selective entrance of blood-borne factors into the brain. Also, the increased production of proinflammatory mediator after trauma promote the influx of inflammatory cells through the BBB. In conclusion, the pathological increase in BBB's permeability leads to an interstitial accumulation of substances that exacerbates vasogenic oedema [25], [26].

3.1.4 Blood pH

Homeostasis requires balanced levels of acids and bases in the body. Acid solutions have more hydrogen ions (H^+), while basic or alkaline solutions are rich in hydroxide ions (OH^-). A solution's

acidity or alkalinity is expressed on the pH scale, which extends from 0 to 14. The midpoint 7 represents equal concentrations of H⁺ and OH⁻; thus, levels below this point are acids and alkaline above it. Blood is slightly alkaline; its pH range is between 7.35 and 7.45 for a healthy person. Three effective mechanisms exist to maintain blood pH range: buffers, breathing rate and kidney excretion [22], [28], [29].

Buffers are chemical compounds that remove or add H⁺ to compensate for either an excess or lack of H⁺ through temporary molecular binds. Bicarbonate ion and carbonic acid are two essential buffers in blood pH regulation. Equation 1 shows how the excess of H⁺ can be transformed into carbonic acid (H₂CO₃), changing the pH from acid to balanced. Likewise, this reaction can be reversed when there are low levels of H⁺, moving the pH from alkaloid to balanced [28], [29].



Equation 1: buffers used in maintaining acid-base balance [28], [29].

As mentioned, about 70% of CO₂ is transported in blood plasma from tissue cells to the lungs. As Equation 2 explains, when CO₂ diffuses into red blood cells, it reacts with water to form carbonic acid (H₂CO₃), dissociating into H⁺ and bicarbonate ion (HCO₃⁻). Then, CO₂ travels in the form of HCO₃⁻ from the tissues to the lungs, but the H⁺ released decreases blood's pH, making it more acid. Once the bicarbonate reaches the lungs and the central chemoreceptors in the medulla oblongata identify high levels of H⁺, the reaction reverses, and breathing becomes forceful and frequent, leading to CO₂ exhalation. Conversely, when CO₂ levels decrease, H⁺ concentration falls, and blood pH returns to normal [29], [30].



Equation 2: Reversible reaction involved in carbon dioxide exhalation [29], [30].

The last mechanism is kidney excretion. Kidneys maintain the body fluids' pH in two ways: excreting excess H⁺ when blood is acidic and excreting excess HCO₃⁻ when blood is alkaline. Even if this is the slowest mechanism, urine can eliminate other acids in addition to carbonic acid [29].

TBI is responsible for a complex brain energy metabolism dysfunction, leading to brain tissue acidosis. Due to ischaemia, hypoxia or mitochondrial impairments after trauma, neurons must rely upon the anaerobic metabolism of glucose for energy. Hydrogen ions, pyruvate and abundant lactate molecules are derived from this process. Hydrogen ions accumulate in the blood and eventually overwhelm the bicarbonate and other buffering systems that maintain blood pH within normal limits. The combination of hyperlactatemia and acidosis is called lactic acidosis, the most common cause of metabolic acidosis. Cerebral lactic acidosis is usually followed by cell death at a pH of 5.3 and is

associated with mortality and poor outcomes in TBI patients. Consequently, extracellular reflections of brain trauma are reduced glucose and pyruvate and increased lactate and lactate/pyruvate ratio (LPR). The latter is assessed through micro dialysis and is the most sensitive biomarker of brain tissue ischaemia. [31]–[33]

3.1.5 Blood pressure

Blood pressure is defined as the pressure exerted by blood on the walls of a blood vessel. Blood pressure progressively falls from systemic arteries into capillaries, where the pressure fluctuations disappear [34].

Blood pressure variations have multiple causes. However, the current research is highly interested in changes related to oxygen and perfusion requirements after trauma. As explained further, vasoconstriction happens when intracranial pressure (ICP) increases due to cerebral haematoma or oedema. Narrow vessels increase the pressure required to pump blood through them, leading to a general rising in the mean arterial pressure (MAP) [34].

MAP is the average pressure all over the cardiac cycle. According to the diastole's and systole's duration, a time-wave average calculation is determined by Equation 3 [35].

$$MAP = \frac{\text{systolic pressure} + (2 * \text{diastolic pressure})}{3}$$

Equation 3: Mean arterial pressure (MAP) traditional formula [35].

Many other models have been proposed for MAP calculation, as it is an essential factor in calculating haemodynamic variables [35]. However, the current research will not focus on monitoring mean arterial pressure but recognizes its relevance in cerebral autoregulation and as a relevant variable in TBI multimodal monitoring.

MAP also depends on the cardiac output, known as the blood volume ejected to the systemic circulation (stroke volume) multiplied by the heart rate and the vascular resistance. Equation 4 describes the relation between MAP, cardiac output and vascular resistance. The latter is the opposition to blood flow due to friction between vessel walls. Vasoconstriction increases vascular resistance due to the inverse relationship between resistance and the vessel's diameter ($R \propto \frac{1}{r^4}$) [34].

$$MAP = (\text{stroke volume} * \text{heart rate}) * \text{vascular resistance}$$

Equation 4: Mean arterial pressure is a function of cardiac output and vascular resistance [23].

Blood pressure also depends on the volume of blood in the cardiovascular system. After TBI, substantial blood loss might occur due to haemorrhage, decreasing cardiac output. In this case, homeostatic mechanisms try to maintain blood pressure through vasoconstriction, increasing vascular

resistance. Nevertheless, blood pressure drops when the loss is higher than 10% of the total volume. Consequently, a decrease in cerebral perfusion and oxygenation exacerbates secondary brain injury and subsequently increases mortality [34], [36], [37].

Even if the haemorrhage is the leading cause of hypotension after TBI, other mechanisms of brain injury might induce hypotension [38]. For example, mass hematomas or oedema can herniate the brainstem through the foramen magnum, disrupting central autonomic nuclei of the cardiovascular and motor responses that control blood pressure [38]. Also, chemicals released by the sympathetic nervous system after injury, such as catecholamines, epinephrine and norepinephrine, are directly related to myocardial injury and decreased cardiac output [38].

3.1.6 Cerebral Blood Flow

Blood flow varies significantly among tissues and does not match the organ weights. In the case of the brain, it receives 14% of the cardiac output despite its weight being just 2% of the total body mass [39]. According to the aim of the current research and because the brain has its particular circulation, this section describes only cerebral blood flow (CBF).

CBF is the volume of blood passing through a brain tissue portion per unit of time [40]. The flow must ensure adequate and continuous delivery of oxygen and nutrients to the brain; otherwise, it can suffer dramatic effects, as reported in TBI patients, due to hypoperfusion [39]. The standard unit of measurement for CBF is millilitres of blood per 100 grams of brain tissue per minute. In a healthy adult, CBF can be approximately 60 mL/100 gr/min. Therefore, under normal conditions, every second, approximately 1% of the brain's total tissue volume is supplied with newly delivered blood [41].

Flow is a crucial concept in cerebral haemodynamic and autoregulation. As explained below, the autoregulation mechanism might fail mostly in severe TBI patients. When this failure occurs, CBF becomes linear dependent on MAP, leading to brain ischaemia if blood pressure decreases or to hyperaemia if there is a slight increase in MAP. Changes in arterial pressure and many other factors can initiate vasodilation and vasoconstriction cascades [42].

The association between decreased CBF and poor outcomes following head trauma suggests that TBI and ischaemic stroke share a common mechanism of pathologic progression. In addition, it has been established that the degree of hypoperfusion needed to develop irreversible tissue damage following stroke is approximately 5–8.5 mL/100 g/min; however, after TBI, that critical threshold is around 15–20 mL/100 g/min [41].

3.2 CRITICAL CONCEPTS IN CEREBRAL PHYSIOLOGY

3.2.1 Intracranial pressure (ICP)

Intracranial pressure is the pressure within the cranial cavity. It is influenced by brain tissue (80%), the circulatory system (10%), cerebrospinal fluid dynamics (10%), and skull rigidity [43]. Due to the fixed nature of the cranium and the incompressible property of the components inside, any increase in the volume of one component produces a reciprocal decrease in the volume of another. This compensatory mechanism is well known as the Monro-Kellie Doctrine, which maintains the intracranial volume and preserves normal intracranial pressure [39], [44].

After brain trauma, pathological conditions might exhaust this compensatory mechanism. In consequence, ICP rises due to increased intracranial volumes. Defining intracranial hypertension cause is not always possible, primarily if it is caused by contusion, oedema or vasodilatation [45]. Increased ICP from oedema may exacerbate the immune reaction and restrict delivery of nutrients and oxygen-rich blood to the brain, further exacerbating the neuroinflammatory reaction [7]. Although, it is relatively easy to identify pathological masses such as hematomas, haemorrhages or herniations [45]. Also, all the mentioned causes might lead to the obstruction of cerebrospinal fluid paths, which promotes hydrocephaly or other CSF pathologies related to intracranial hypertension [45].

In some cases, brain trauma involves axonal injuries, traumatic subarachnoid haemorrhage or minor bleeding from broken capillary vessels. Those disruptions do not necessarily increase ICP, meaning only ICP does not give enough information to diagnose or discard TBI [37]. However, it is a good indicator of an underlying pathophysiological process [32]. Moreover, normal physiologic ICP ranges between 5 and 15 mmHg, and an ICP above 20-22 mmHg reflects a predisposition to cerebral injury, herniation and significantly higher lactate pyruvate ratio values. The latter is the most sensitive biomarker of brain tissue ischaemia [32], [37]. Considering the aforementioned, ICP has become the most common monitoring tool globally for TBI care, which highly correlates with patient functional outcomes [32], [46].

3.2.2 Cerebral Perfusion Pressure (CPP)

Cerebral perfusion pressure (CPP) allows blood to perfuse the brain, thereby allowing for the delivery of oxygen and vital metabolites [41]. It is defined as the difference between mean arterial pressure (MAP) at the entrance of the brain and the exit pressure in the cerebral veins just before they enter the sinuses (CVP) [37]. However, the haemodynamic of veins is a much more complicated subject than the arteries [47]. Because of this, previous studies have demonstrated that a progressive increase in ICP will raise a similar increase in CVP [48]. In consequence, intracranial pressure accurately

represents the CVP, and it is valid to define cerebral perfusion pressure as the difference between mean arterial pressure and intracranial pressure (Equation 5) [47], [48].

$$CPP = MAP - ICP$$

Equation 5: Cerebral perfusion pressure as a function of the difference between mean arterial pressure and intracranial pressure [47], [48].

As mentioned, MAP usually decreases and ICP increases after TBI because of injury responses such as oedema, haemorrhage, herniation, hematoma, and chemical disruption. Either a reduction in MAP or an elevation in ICP deleteriously decreases the effective CPP [37]. When the CPP decreases below 50 mmHg, the risk of brain ischaemia increases, affecting the electrical activity of neuron cells [44]. According to The Brain Trauma Foundation recommendations, the CPP threshold should be between 50–70 mmHg for traumatic brain injury [44]. While The Guidelines for the Management of Severe Traumatic Brain Injury, Fourth Edition, recommends values for survival and favourable outcomes between 60 and 70 mmHg [49].

ICP and CPP monitoring is the gold standard for assessing brain injury and the patient's response to treatment [32]. However, monitoring only ICP and/or CPP limits the ability to assess the most critical parameter, which is the adequacy of the supply of energy substrates concerning the metabolic demand of the injured brain [32].

3.2.3 Compliance

By definition, intracranial compliance (C) is the change in intracranial volume per unit change in intracranial pressure (dV/dP), which can be obtained by measuring the slope of a volume- pressure curve inside the skull [50]. According to this definition, the intracranial volume changes lightly when pressure changes by an amount equal to ΔICP happens at a low compliance value. In contrast, when pressure changes the same amount (ΔICP), but in this case, compliance is high, the intracranial volume changes significantly [50].

Due to the pressure-volume behaviour inside the skull, ICP is higher in normal conditions at lower compliance values, as is shown in Figure 17. The autoregulatory response to cerebral perfusion pressure variation influences cerebral blood volume, which is an essential determinant of compliance [51]. Thus, there is a positive association between CPP and compliance when ICP is low, suggesting preserved autoregulation. Figure 18 shows on colour blue the baseline intracranial volume with an excellent compensatory reserve and high compliance under normal levels of ICP. Then, it shows on colour yellow the gradual reduction of the compensatory reserve as intracranial volume increases, leading to a higher change in ICP [51][52].

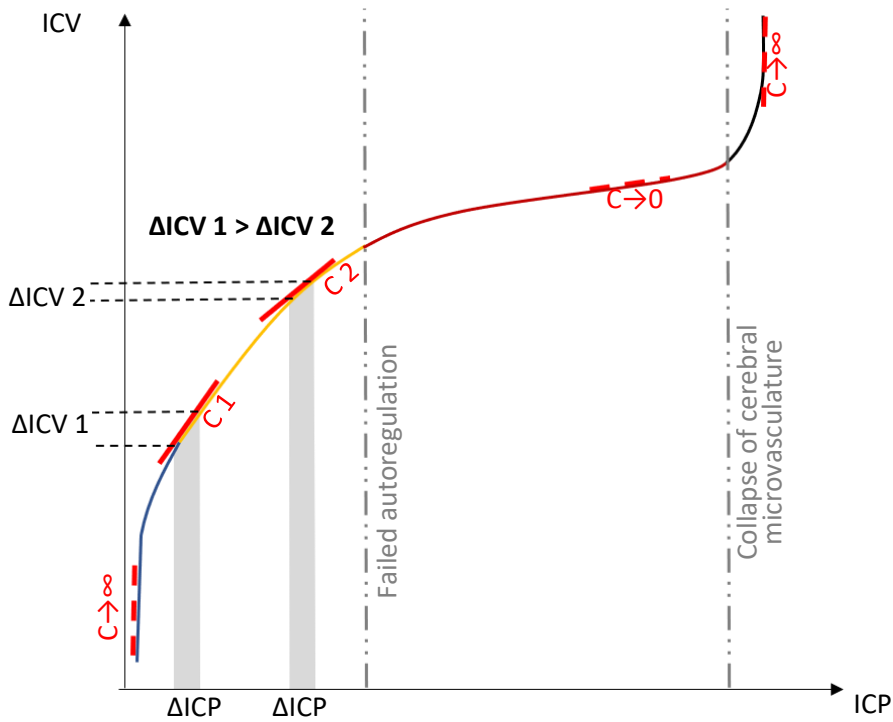


Figure 17: Compliance definition based on intracranial volume-pressure behaviour.

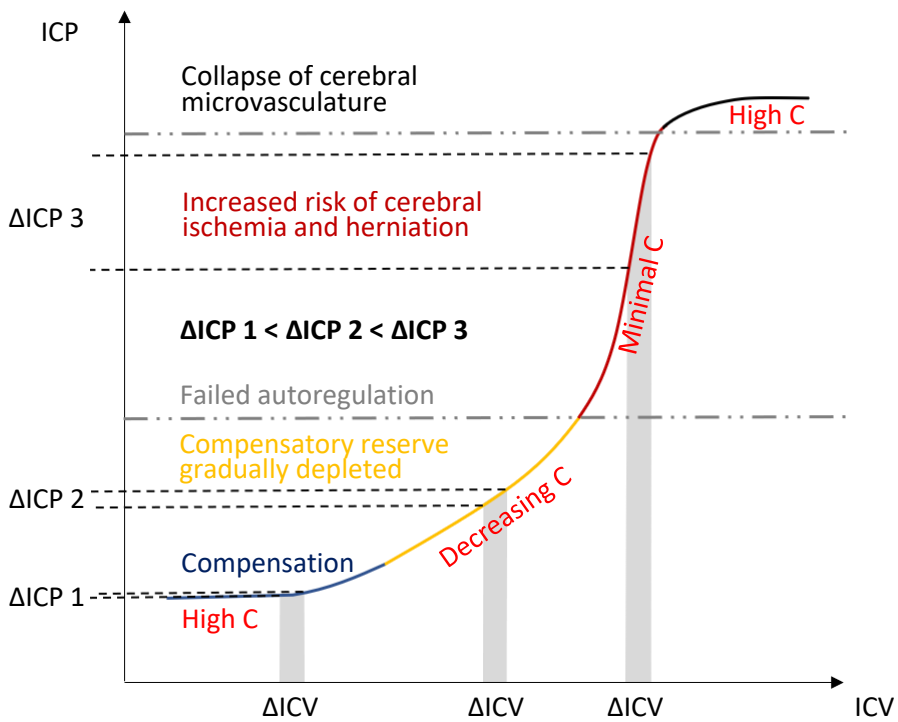


Figure 18: Intracranial pressure-volume behaviour according to intracranial compliance [52].

However, when ICP is higher than 20 to 22 mmHg, compliance shows a tendency to decrease even if CPP is too low (<50 mmHg) or too high (>150 mmHg), where autoregulation fails. Such an impaired autoregulatory status would lead to dramatic increments in ICP, even when intracranial volume slightly changes. Figure 18 shows this poor compensatory reserve in red, which increases the risk of

cerebral ischaemia and herniation. Finally, critically high ICP collapses cerebral microvasculature and disturbs cerebrovascular reactivity, which might lead to vasogenic oedema (colour grey) [51][52].

Nowadays, physiological values of normal cerebral compliance are still to be carried out [51].

3.2.4 Partial arterial pressure of carbon dioxide

The partial arterial pressure of carbon dioxide (PaCO_2) measures carbon dioxide within arterial blood. Therefore, it is a biomarker of enough alveolar ventilation within the lungs. Normal physiologic conditions range between 35 to 45 mmHg or 4.7 to 6.0 kPa [53]. As explained in the section “Blood pH”, as PaCO_2 increases, the bicarbonate buffer system attempts compensation by generating bicarbonate and hydrogen ions. The latter decreases systemic pH creating acidaemia, which increases the minute exhalation of CO_2 and decreases H^+ concentration to normal levels [53].

Blood-brain barrier damage and cell metabolic impairment after TBI increase CO_2 levels in the cerebral circulation (hypercapnia) [54]. A sudden change in PaCO_2 causes vessel dilatation due to cerebrovascular CO_2 reactivity, leading to proportional increments in CBF. On average, in the middle of the physiological range, each unit (kPa) change in PaCO_2 produces a change of about 15 ml/100 g/min in CBF. Brain blood vessel dilatation might also increase ICP and contribute to brain volume. The above is associated with intracranial hypertension, oedema and poor outcomes in patients with severe TBI [42].

In contrast, hypocapnia induces vasoconstriction, which decreases cerebral blood volume and ICP. This reduction in cerebral blood volume and, consequently, in ICP forms the rationale for using hyperventilation in the treatment of raised ICP. However, the risk of this approach is induction or exacerbation of ischaemia caused by reduced CBF. Because of the above, hyperventilation in severe head injury is currently controversial [55].

3.2.5 Brain tissue oxygenation

As suggested in the sections above, one of the fundamental pathophysiological consequences after TBI is an imbalance of oxygen delivery to neural tissue. Accordingly, understanding the physiology of brain tissue oxygenation (PbtO_2) is significantly important in this research. However, there are several misunderstandings about PbtO_2 . Firstly, brain tissue oxygenation has multiple names in the literature: cerebral oxygenation, cerebral tissue oxygen, cerebral partial pressure of oxygen, brain tissue oxygen tension, BtO_2 , PtO_2 , PbrO_2 , BTpO_2 or PbtO_2 [56]. Secondly, PbtO_2 reflects the dissolved oxygen within the plasma that diffuses across the blood-brain barrier rather than the entire oxygen content or cerebral metabolism [57]. The latter is because PbtO_2 is significantly related to the product of CBF and arterio-venous oxygen tension difference (Equation 9), which is influenced by the oxygen diffusion gradient [57], [58],[59]. Finally, PbtO_2 is not simply an ischaemia biomarker since several variables

might modify oxygen diffusion or metabolism, even under normal CBF conditions [59]. However, PbtO₂ low values can provide information about low PaO₂, local O₂ extraction impairment (i.e. oedema) or decreased cerebral blood flow [57], [59].

According to the Fick principle, the total amount of oxygen that crosses the BBB into the cerebral tissue per unit of time is defined as [58]:

$$O_{2\text{BBB}} = \text{CBF} * (\text{CaO}_2 - \text{CjO}_2)$$

*AVDO₂: arteriovenous oxygen
content difference*

Equation 6: Fick principle applied to the total amount of oxygen that crosses the BBB

Where arterial oxygen concentration (CaO₂) and jugular oxygen concentration (CjO) are given by [58]:

$$\text{CaO}_2 = \text{SaO}_2 * 1.34[\text{Hb}] + 0.0031 * \text{PaO}_2$$

$$\text{CjO}_2 = \text{SjO}_2 * 1.34[\text{Hb}] + 0.0031 * \text{PjO}_2$$

Equation 7: Oxygen content equations

Consequently, the sum of the oxygen that diffuses across the BBB is thus equal to the total oxygen that is off-loaded from the haemoglobin plus the dissolved plasma oxygen that diffuses from the plasma into the brain [58].

$$O_{2\text{BBB}} = \text{CBF} * (\text{SaO}_2 * 1.34[\text{Hb}] - \text{SjO}_2 * 1.34[\text{Hb}]) + \text{CBF} * (0.0031 * \text{PaO}_2 - 0.0031 * \text{PjO}_2)$$

Equation 8: Total oxygen that diffuses across the BBB

Then, the last term on the equation indicates the amount of dissolved plasma oxygen diffusing across the BBB in millilitres of oxygen per 100 g of brain per minute. A conversion factor of 1mmHg = 0.0031 mL/100gr helps to compare brain tissue oxygen concentration to standard oxygen tension measurements (PbtO₂). Equation 9 presents the association between PbtO₂, oxygen diffusion and cerebral blood flow in mmHg [58].

$$\text{PbtO}_2 \approx \text{CBF} * (\text{PaO}_2 - \text{PjO}_2)$$

*AVT_{O2}: arteriovenous oxygen
tension difference*

Equation 9: Fick principle applied to brain tissue oxygenation [57]

PbtO₂ values of around 23-35 mmHg are typical in health. Values below 20 mmHg are considered abnormal and are associated with evidence of cerebral ischaemia and energy dysfunction. Some authors describe treatment when PbtO₂ is below 15 mmHg [59]. Thresholds for ischaemia are not yet clearly defined, but a PbtO₂ below 8-10 mmHg indicates a high risk of ischaemia in patients with subarachnoid haemorrhage. Low sustained values of PbtO₂ are associated with poor outcomes after

traumatic brain injury, and there is some evidence that brain tissue oxygen-directed therapy may improve outcomes in such patients [60].

Even if ICP and/or CPP have become the most common monitoring tools for severe TBI care [32], [46], those parameters cannot assess the adequacy of the supply of energy substrates concerning the metabolic demand of the injured brain [32]. Nevertheless, because of the above, TBI management based on PbtO₂ and ICP/ CPP monitoring decrease hypoxia risk, mortality and poor outcomes compared with ICP/ CPP-only treatment [32],[61].

3.2.6 Jugular venous oxygen saturation

SjO₂ or SjvO₂ are abbreviations for jugular venous oxygen saturation. As explained in the section “Blood Supply of the Brain”, deoxygenated blood and remaining oxygen molecules flow through the internal jugular veins to return to the heart. Therefore, the measurement of SjO₂ helps to establish the balance between CBF and the metabolic requirement (CMRO₂), giving an idea of the use of oxygen by the brain [62]. Accordingly, when oxygen demand increases, the brain extracts a more significant amount of oxygen, resulting in decreased jugular venous oxygen saturation. Conversely, venous oxygen saturation is higher when CBF exceeds the metabolic requirement [62]. The following equations explain the physiology behind SjO₂ and its dependency on CBF and CMRO₂.

The total amount of oxygen that crosses the BBB must also be equal to the total amount of oxygen consumed by the tissue (CMRO₂) plus the amount of oxygen that is accumulated in brain tissue per unit of time (C_iO₂) [58]. Accordingly, Equation 8 and Equation 9 are rearranged as follows:

$$CBF * (SaO_2 * 1.34[Hb] - SjO_2 * 1.34[Hb]) + PbtO_2 = CMRO_2 + C_iO_2$$

Equation 10: The total oxygen that diffuses across the BBB is a function of the cerebral metabolic rate for oxygen and the amount accumulated in the tissue.

In order to calculate the cerebral metabolic rate for oxygen (CMRO₂), Kety and Schmidt assumed that C_iO₂ is so tiny compared to the CMRO₂ that it is negligible. As PbtO₂ is the end concentration of oxygen in brain tissue, it must also be smaller than the standard measures of total oxygen delivery and metabolism, so it can safely neglected [58], [60]. Therefore, CMRO₂ is simplified as follows:

$$CMRO_2 \approx CBF * (SaO_2 * 1.34[Hb] - SjO_2 * 1.34[Hb])$$

Equation 11: Kety and Schmidt's calculation of the cerebral metabolic rate for oxygen.

Solving SjO₂ from Equation 11 and assuming constant arterial oxygenation, SjO₂ represents the balance between oxygen supply and demand, as is shown by Equation 12 [60].

$$SjO_2 = SaO_2 - \text{constant} * (CMRO_2/CBF)$$

Equation 12: Venous oxygen saturation.

The coupling between $CMRO_2$ and CBF is lost after TBI. As explained, intracranial hypertension leads to brain hypoperfusion, which is not accompanied by a proportional reduction in $CMRO_2$. Consequently, SjO_2 falls from a normal range between 60-75% to values below 55%, which is associated with poor outcomes. SjO_2 might decrease below 50% when at least 13% of the brain has become ischaemic due to the oxygen supply may be critically low for the metabolic demand [37], [62]. Likewise, when cerebral autoregulation fails because of trauma, the vasodilatory response increases CBF leading to cerebral hyperaemia with a decreased oxygen extraction. Therefore, SjO_2 values rise by over 75%, representing unbalance between CBF and $CMRO_2$ [62].

3.3 CEREBROSPINAL FLUID (CSF)

Cerebral haemodynamics are highly related to changes in blood characteristics, especially after TBI, yet another fluid within the skull has a massive impact on the development of secondary injuries. This section describes the morpho-physiology of cerebrospinal fluid (CSF), with the aim of highlighting the importance of this fluid and its relationship with TBI.

3.3.1 Functions of CSF

Cerebrospinal fluid within and around the brain and the spine has several benefits for humans. The first advantage is closely related to this research, as CSF provides a cushion against external trauma. As mentioned in the section "Meninges", the brain and spine are floating in CSF which prevents the delicate nervous tissue from being damaged by surrounding bones [63]. Another protective function of CSF occurs when ICP increases. According to the Monroe-Kelli doctrine, CSF is drained to the spine through the foramen magnum to decrease ICV, followed by a reduction in ICP [63].

The second function of CSF is the removal of neuronal metabolic waste. As mentioned, veins and BBB collect a substantial number of products from the brain; even so, the arachnoid membrane also reabsorbs molecules present in CSF and drains them to the venous sinuses [63]. Finally, CSF can distribute biological substances through the brain, leading to neuronal responses based on the concentration of such substances [63].

3.3.2 Production and composition of CSF

The choroid plexuses do not produce CSF; instead, it is a filtrate of the blood with the active filtration performed by the highly specialized cells of the choroid plexus. The functional units of the plexus are known as villi, which consist of loops of tiny capillaries separated from the ventricle by a layer of a single ependymal cell thick [63]. This characteristic allows the transport of ions and molecules to and

from the capillaries. Likewise, these specialized cells can generate a polarized electrical charge across their membranes, moving sodium, chloride and bicarbonate into the ventricle [63]. This ionic flow creates an osmotic gradient that draws water molecules via aquaporin channels from the basolateral membrane in the capillaries into the apical membrane in the ventricle. So, most of the composition of CSF is water and the ions mentioned above, as well as some amino acids, proteins, glucose and monocytes (Table 5) [63].

Table 5: Average concentrations of lumbar CSF solutes of normal human subjects [63, p. 12].

Solute	The average concentration in CSF (mEq/Kg)
Sodium	147.00
Potassium	2.86
Magnesium	2.23
Calcium	2.28
Chloride	113.00
Bicarbonate	23.30
Amino acids	0.72
Total protein (mg/dL)	39.20
Glucose (mg/dL)	59.70

The pH of CSF is slightly alkaline (7.3), reflecting its higher PCO₂ content (50.5 mmHg) and lessened buffering capacity compared to plasma (41.1 mmHg). Moreover, CSF volume ranges from 140 to 270 ml in a healthy adult, and it is completely replaced about four times per day. CSF production rate is around 0.4 ml/min, and the choroid plexus produce it at a rate of 0.21 ml/min/choroid plexus gram [63].

3.3.3 CSF's circulatory system

The cerebral ventricles are four CSF-filled cavities within the brain. There are two lateral ventricles at each cerebrum hemisphere, which are separated by the septum pellucidum. Both C-shape structures comprise choroid plexuses. The CSF secreted in the lateral ventricles flows through the Foramen of Monro into the third ventricle [2], [63], [64]. The latter is a midline slit in the diencephalon, with walls formed by the thalamus and hypothalamus [65]. The choroid plexus adds additional CSF in the roof of the third ventricle. Lateral and third ventricles are supplied by a group of choroidal arteries that are irrigated by the middle and posterior cerebral arteries [2], [63], [64]. The fluid within the third ventricle flows downward along the Aqueduct of Silvius into the fourth and last ventricle. Here, another amount of fluid is added before it is delivered into the central canal of the spinal cord and the subarachnoid space via the foramina of Luschka and Magendie. The choroidal plexus of the fourth ventricle are

supplied by cerebellar arteries as it is located behind the brain stem and in front of the cerebellum [65].

Although most CSF is produced within the ventricles, most fluid is located in the subarachnoid space [65]. This cavity between the pia mater and the arachnoid membrane contains the arachnoid granulations and villi, which act like one-way valves for the flow of CSF into the venous blood, and hydrostatic pressure is the primary stimulus that causes these valves to open ($ICP - P_{\text{venous sinuses}} > 1.5 \text{ mmHg}$). CSF is mainly reabsorbed in the sagittal sinus, but there is also a flow of CSF into venous blood throughout the cranial and spinal compartments [63].

Traumatic skull base fracture in some patients with TBI allows CSF to flow from the subarachnoid space out of the nose or ear. Leakage of CSF is highly related to subsequent meningitis and intracranial hypotension. However, a head injury in the acute setting does not usually alter CSF dynamics. The development of intracranial volume pathologies, such as haemorrhage or oedema, are often associated with increased intracranial pressure, which activates CSF compensatory mechanisms. Likewise, blood accumulating in the ventricular system may prevent CSF reabsorption, and herniation may cause a cisternal block; all are possible causes of obstructive hydrocephalus [63].

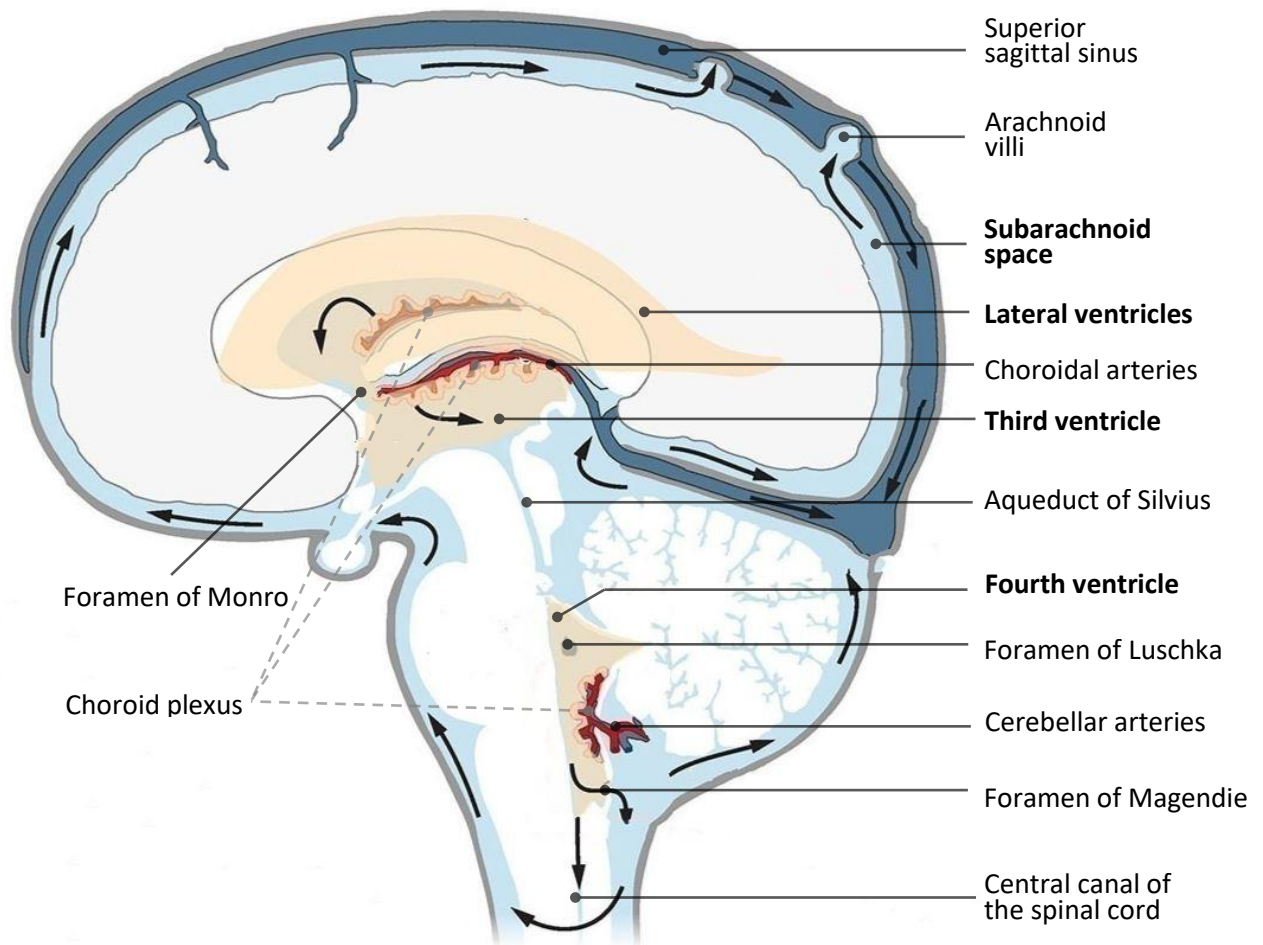


Figure 19: Patterns of CSF recirculation and flow (modified from [66]).

3.3.4 CSF haemodynamics

The dynamics of CSF flow are poorly understood; even so, magnetic resonance imaging has demonstrated that CSF flow is pulsatile rather than laminar, primarily through anatomical narrowing areas such as the Foramen Monro, Sylvius' aqueduct or cervical cord [65]. Small pulsations of the CSF column are related to respiration and the cardiac cycle. During normal breathing, CSF pressure drops during inspiration and rises during expiration by 2–5 mm in the CSF column. The latter is due to the negative intrathoracic pressure and improved venous return during the inspiratory phase [63]. Likewise, pulsations of the basal arteries comprising the circle of Willis contribute to the CSF waveform, and the arterial pulse is transferred to the CSF through the choroid plexus [63].

The ventricular CSF pressure waveform has three distinct components, as shown in Figure 20. The first peak (P1) is known as the “percussive wave”, resulting from arterial pressure transmission from the choroid plexus to the CSF. The second peak (P2), or “tidal wave,” reflects intracranial compliance as its amplitude is inversely related to this variable. Finally, the “dicrotic wave” (P3) marks the closing of the aortic valve [63]. Moreover, Lundberg described three distinct types of ICP waveforms. Plateau

waves (Figure 20 A) are characterized by sudden rapid elevations from normal to 50–100 mmHg values. The plateau lasts for 5–20 min and terminates rapidly, suggesting low compliance, intracranial hypertension and a high risk of herniation. B waves are characterized by intracranial pressure elevations of 5–10 mmHg above baseline, occurring every 0.5–2 min, which also suggests low compliance and is associated with an abnormal breathing pattern (Figure 20 B). Finally, C waves' amplitude rarely exceeds 20 mmHg and occur every 4 and 8 minutes (Figure 20 C), representing non-pathological waves of the transmission of arterial blood pressure to the ICP [63], [67], [68].

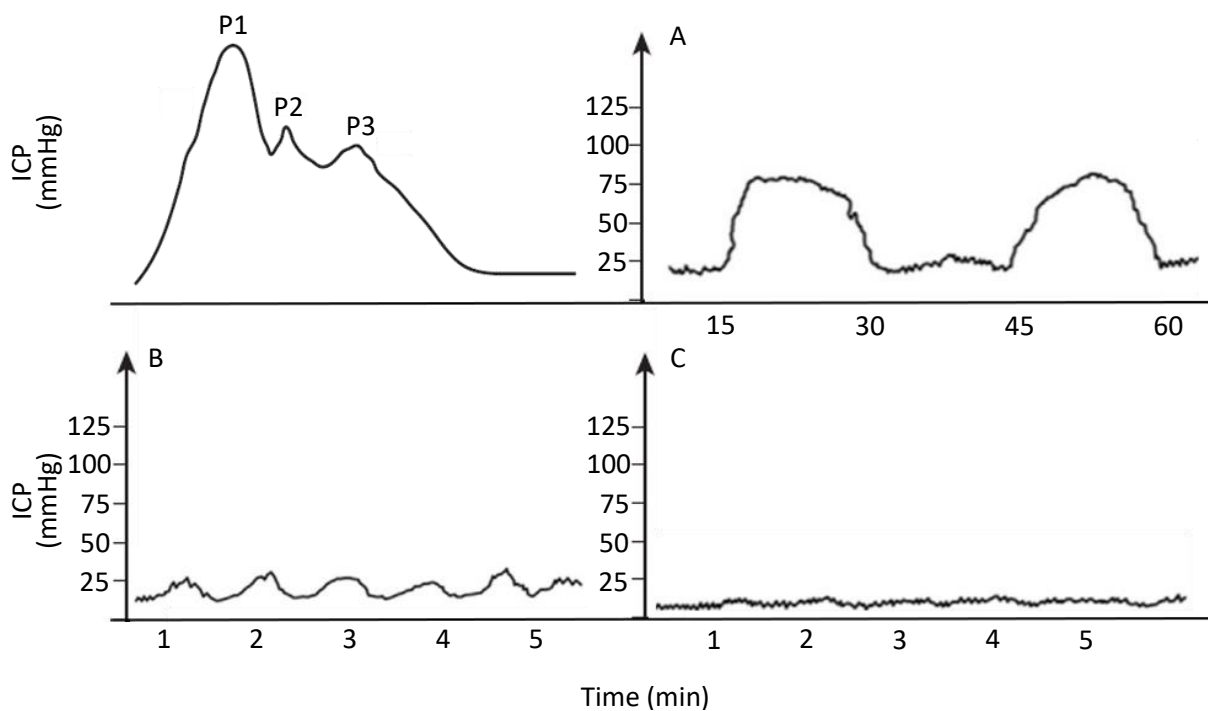


Figure 20: CSF pressure waveform morphologies (modified from [63], [67]).

Outcomes in TBI patients with plateau waves (Figure 20 A) are better compared to patients without plateau waves, which might be explained because Lundberg's A waves occur in the presence of intact cerebral autoregulation and low compliance. Nonetheless, plateau waves that exist for more than 30-40 minutes do have a negative effect on outcomes, as prolonged periods of intracranial hypertension and low CPP can lead to cerebral ischaemia [69], [70]. The ICP peak is induced by the cerebral vasodilatory cascade initiated by a disruption in oxygen delivery. An abrupt increase in CBV leads to an elevation in ICP, a decrease in CPP, further vasodilation, and a further rise of ICP until the maximum vasodilation is reached. Due to cerebral autoregulation mechanisms, a vasoconstrictive stimulus stops the cycle and restores a normal ICP [69], [70].

As plateau waves, B waves also occur in the presence of intact cerebral autoregulation and low compliance [71]. The difference in B waves amplitude and frequency is influenced by the transmission of rhythmic changes in cerebral blood volume to ICP, such as brain-stem rhythm, rhythmic changes of

arterial CO₂ partial pressure, the time constant of autoregulation, the speed of ABP reduction, and the value of CPP [71]. Accordingly, Plateau waves have much more clinical application than B waves for intracranial hypertension monitoring in TBI patients [71].

In addition to the morphological changes in the ICP waves, secondary pathologies might be developed when the pressure increases in the CSF system. One common condition caused by CSF hypertension is papilledema. When the pressure rises in the cerebrospinal fluid system, it also rises inside the optic nerve sheath, which is bathed within CSF. Because of the above, the nerve diameter size strongly correlates with increases in ICP [64]. Another frequent condition caused by CSF disruption is hydrocephalus. Two types of hydrocephalus are described in TBI patients. Non-communicant hydrocephalus occurs when aqueducts get obstructed because of the brain's oedema, leading to ventricular distension and ICP elevation. The second type is communicant hydrocephalus, which occurs in patients with haemorrhages where red blood cells cause severe blockages in the subarachnoid spaces and arachnoid villi. Partial or total blockages prevent normal CSF absorption into the venous sinuses, followed by CSF accumulation and raised ICP [64].

3.4 AUTOREGULATION

Autoregulation is the capacity of the cerebral circulation to maintain a continuous and independent CBF and adequate oxygen supply, despite changes in blood pressure, cerebral perfusion pressure, and partial pressures of arterial oxygen and carbon dioxide [42], [72]. Multiple physiological processes are engaged in cerebral autoregulation. For instance, the myogenic mechanism relies on the cerebrovascular reactivity (CVR) that provokes dilation to decrease MAP/ CPP and constriction to increase MAP/ CPP [54]. However, CVR is not exclusively associated with variations in pressure. Changes in other physiological processes, such as CO₂ or O₂ reactivity, mediated by activation of nitric oxide, H⁺ ions and other metabolites in the arterial endothelium, can also lead to a rapidly cerebral vasomotor response that regulates CBF [54], [73]. The latter is known as the metabolic mechanism and is initiated by hypoxia, dehydration, or hypercapnia [42]. Finally, the neurogenic mechanism focuses on neurotransmitter-mediated vascular tone changes initiated by fluctuations in the sympathetic and parasympathetic systems [72].

When autoregulation is intact, a suitable coupling has been observed between a slight rise in CBF and metabolism [42]. In most cases, autoregulation pressure lies in the 50 to 150 mmHg range [44]. In chronic arterial hypertension, autoregulation limits are displaced to higher levels, shifting the curve to the right as high as 40mmHg [44]. Another characteristic of this protector mechanism is its temporal response, which occurs within two to ten seconds after a sudden change in MAP/ CPP [73]. Figure 21 represents the behaviour of relevant haemodynamic variables as a function of CBF; it depicts that out

of the autoregulatory plateau, CBF becomes pressure-dependent, resulting in too much or too little blood perfusion to the brain [41], [42].

As mentioned, cerebral haemodynamic variables change after brain trauma as a response to secondary injuries like haemorrhages, oedema or BBB disruption. In accordance, blood pressure drops when there is a considerable loss of blood, the central autonomic nuclei are disrupted by increased ICP, or PaCO₂ levels decrease under 2.7 kPa. Then, hypotension leads to vessels' passive collapse, reducing CBF and increasing ICP. The latter diminishes CPP and increases oxygen extraction from haemoglobin, but for CBF below 20mL/100g/min brain becomes ischaemic.

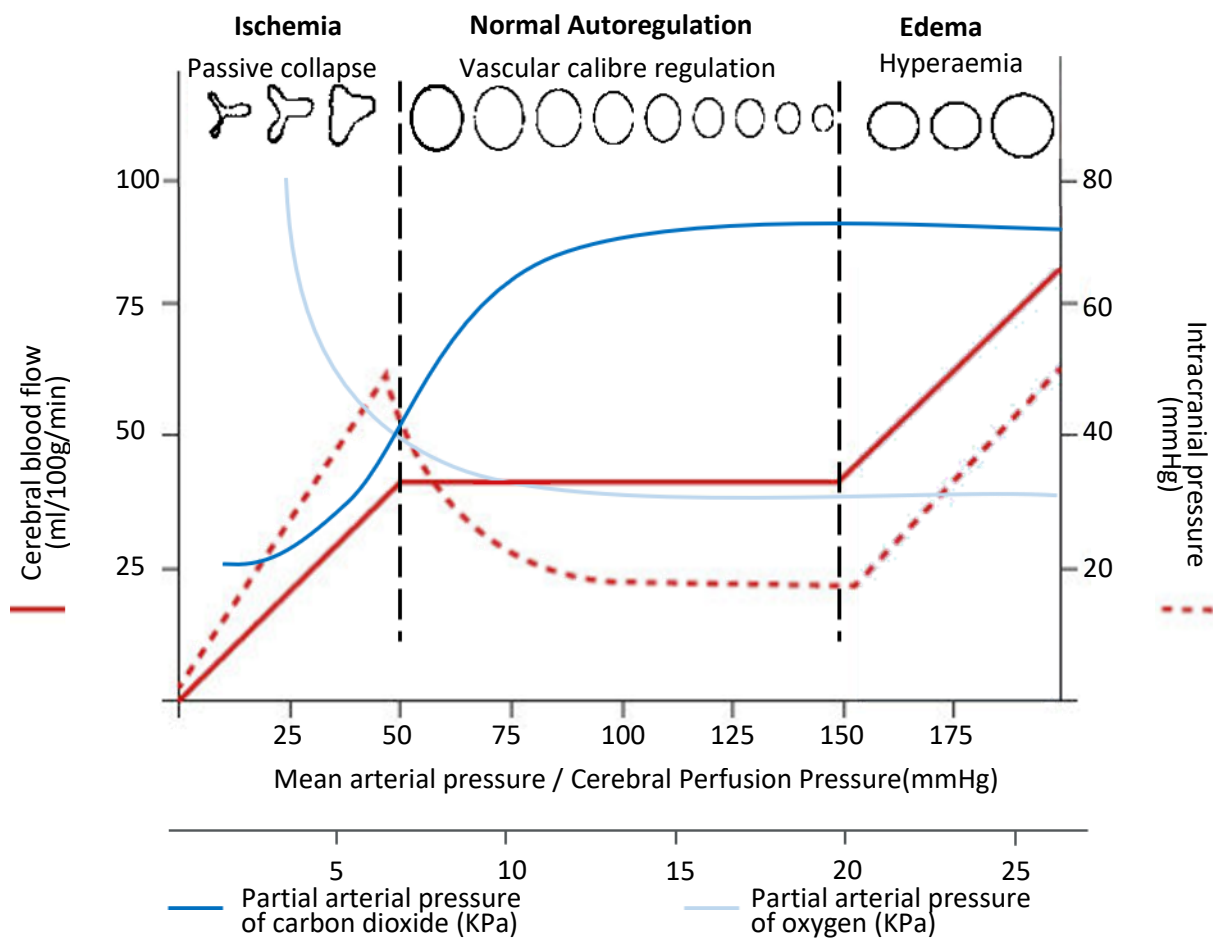


Figure 21: Cerebral autoregulation

Cerebral blood flow is maintained constant over a range of MAP/ CPP in the face of varying levels of PaCO₂ and PaO₂. Out of the autoregulatory plateau, CBF becomes pressure-dependent and intracranial pressure dangerous rises (modified from [44], [73]).

Likewise, during acute hypertension at pressures above the autoregulatory limit, the myogenic constriction of vascular smooth muscle is overcome by the excessive intravascular pressure, and forces dilatation of cerebral vessels occurs. The loss of myogenic tone during forced dilatation decreases cerebrovascular resistance, producing a significant increase in cerebral blood flow (300–

400%), which aggravates vascular engorgement and brain oedema, followed by the development of irreversible intracranial hypertension [64].

3.5 SUMMARY

In conclusion, TBI secondary injuries can lead to increased intracranial pressure and reduced cerebral blood flow, followed by a reduction in CPP. This response causes a “vicious circle” as reduced cerebral blood flow decreases oxygen delivery which might provoke ischaemia and initiate a vasodilation cascade. In addition, widening blood vessels under impaired autoregulation increase blood flow and ICV, which turns into aggravated brain oedema with intracranial hypertension [74]. Figure 22 summarizes the main factors explained in this chapter and their effect on the “vicious circle” [42], [74].

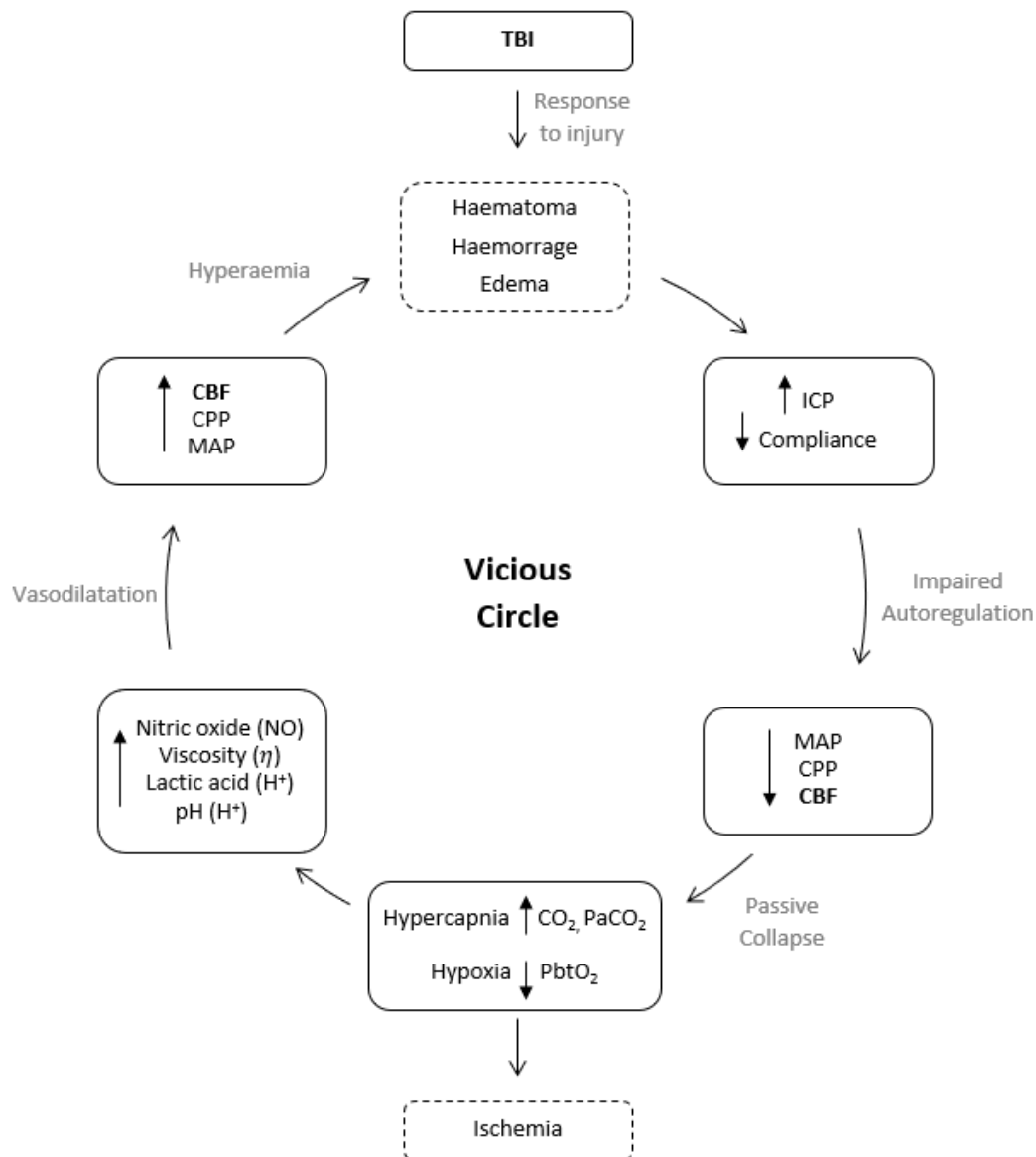


Figure 22: Vicious circle of impaired cerebral blood regulation after TBI [42], [74]

The current review of the anatomy, physiology and dynamics of TBI allows the future understanding of the clinical classification of trauma, its impact on society and the current guidelines for diagnosing, monitoring and treating TBI patients. Likewise, the ongoing description is the theoretical foundation of TBI's neurological, structural and physiological effects that are used as biomarkers in TBI assessment.

4 TRAUMATIC BRAIN INJURY (TBI)

4.1 DEFINITIONS AND TYPES

4.1.1 Acquired brain injury

Acquired brain injuries (ABI) include a wide range of situations in which the brain has been damaged since birth. The latter excludes hereditary, congenital, degenerative, or induced-by-birth trauma injuries [75], [76]. An ABI can be traumatic or not; for instance, tumours, strokes, aneurysms, encephalitis, meningitis, and hydrocephalus, among others, are non-traumatic acquired brain injuries [75], [76]. On the other hand, traumatic brain injury (TBI) is, as its name indicates, a traumatic acquired brain injury that is caused by an external force that disturbs the brain's function [75], [76]. TBI is among the most severe types of injury in terms of fatality and lifelong disability for survivors [77], [78].

External forces are distinct by mechanism as close/blunt force, blast injury or penetrating injury. Direct forces are the first mechanism of injury to the head, such as acceleration-deceleration or rotational forces. Likewise, blast injuries are caused by overpressure waves generated by explosives, which transfer a lot of thermal, mechanical and electromagnetic energy through the skull or indirectly by blood vessels. Finally, penetrating injuries, as its name implies, are induced by penetrating objects into the cranial vault [79].

Different scales have been developed to assess a traumatised patient's clinical severity and probable survival. Scales evaluate psychological and anatomical features as the Glasgow Coma Scale (GCS) [80], the Paediatric Trauma Scale (PTS) [81], the Revised Trauma Score (RTS) [82], the Injury Severity Score (ISS) [83] among others. However, the GCS has been the most valuable and used scale for assessing head trauma severity [84]; therefore, it will be explained in detail in section 4.5, "Clinical practice guidelines in TBI."

TBI classification of injury severity has focused on three parameters: duration and depth of loss of consciousness (LOC), duration of memory disturbance such as amnesia and Glasgow Coma Score [85].

4.1.2 Mild TBI

Among people surviving TBI, around 90% experienced a Mild injury or concussion [86]. The definition of concussion is subjective, but it generally refers to an altered mental state after trauma that reflects functional disturbance rather than structural injury [79], [86]. This silent injury is often invisible for the victim, who presents a GCS of 15 and no LOC [84]. Thus, recurrent concussions might be turned into mild TBI (mTBI) with potential short and long-term neurologic damage (Table 6) [85], [86].

Table 6: Potential short and long-term neurologic damage after mTBI

*** Short-term sequelae (3 months after injury):**

- Cognitive: decreased memory, attention, and concentration.
- Somatic: headache, fatigue, insomnia, dizziness, tinnitus, and sensitivity to noise or light.
- Affective: depression, irritability and anxiety.

*** Long-term sequelae: (5-6 months after injury):**

- Cognitive: decreased memory and learning problems.
- Somatic: headaches, dizziness, vision difficulties, and alcohol intolerance.

The American Congress of Rehabilitation Medicine and the World Health Organization agreed that mTBI could be diagnosed either 1) in the absence of LOC but in the presence of altered or disturbed consciousness (GCS of 13-15); or 2) with an upper limit of the duration of loss of consciousness or amnesia of 30 min [84], [85]. Some indicators of mTBI with their prevalence are mentioned above: Disorientation or confusion (18% -44.7% immediately), Impaired balance (23.8% - 36.5% one day after), Slower reaction time (41.7% - 71.4% two days after), Impaired verbal learning and memory (0% to 41.7% one day after), LOC (1%-14.3%), Post-traumatic amnesia (2%-29.7%) or Retrograde amnesia (7.4% -53.5%) [87].

The early detection and diagnosis of mild TBI and early treatment results in the best outcomes and will help prevent a second concussion before recovery from the first [86]. However, obtaining reliable measures of LOC, amnesia and GCS on time can be very difficult as these parameters may be unwitnessed, and consciousness may not be impaired during medical assistance [85]. The latter reduces the odds of timely and appropriate treatment, increasing the risk of neurologic damage and subsequent injuries [86].

Moreover, the symptoms of increased ICP include but are not limited to headache, behavioural problems, nausea, and vision problems, which overlap with the symptoms of mTBI and concussion. Invasive ICP monitoring have high risk of complications, and is not justified for mTBI, thus ICP has not been studied in much detail in mTBI. Nonetheless, literature suggests an elevation in ICP (± 5 mmHg) for days which returns to baseline as the patient is recovered [88].

Concussions and mTBI primarily affect military and contact sports athletes. According to US data, 82.4% of all military TBI cases are mild [86]. Likewise, evidence reports between 1.6 million and 3.8

million new cases of sport-related concussion per year in the USA. Sadly, athletes may underreport post-injury symptoms in hopes of being cleared to return to play [89].

4.1.3 Moderate and severe TBI

Moderate to severely traumatized patients are at high risk of clinical deterioration, so they must be carefully monitored [79]. According to the three parameters explained before to assess trauma's severity, moderate trauma patients present a GCS between 9 and 12; their consciousness level is lost for more than 30 minutes, but they are not comatose. Instead, they are drowsy or obtunded; and could present amnesia due to brief LOC after trauma [79]. Likewise, severe trauma patients are scored within 3 to 8 on the GCS and present a poorly LOC, often comatose. In addition, these patients may exhibit decerebrate posturing and are at high risk of secondary injury [79]. Finally, moderate and severe TBIs can significantly impact ICP levels, where normal ICP values (8-14 mmHg) can be raised up to 40 mmHg. Guidelines have defined values above 20-22 mmHg as the gold standard for intracranial hypertension [49]. Table 7 summarizes the criteria used to classify TBI severity [90].

Table 7: Criteria used to classify TBI severity.

Criteria	Mild	Moderate	Severe
Structural imaging	Normal	Normal or abnormal	Normal or abnormal
Loss of consciousness 24 hours	<30 minutes	30 minutes to 24 hours	24 hours
Post traumatic amnesia	0–1 day	>1 and <7 days	>7 days
Glasgow Coma Scale score (best available score in 24 hours)	13–15	9–12	3–8

4.2 EPIDEMIOLOGY

4.2.1 Incidence

4.2.1.1 Worldwide

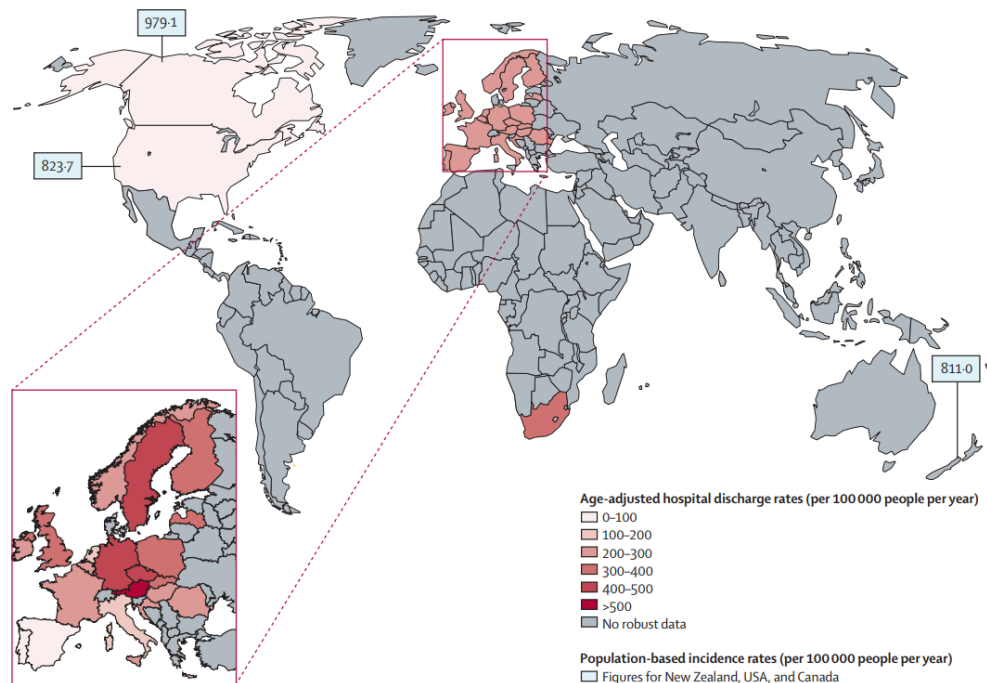


Figure 23: Worldwide incidence of traumatic brain injury [91]

Reported TBI incidence and mortality rates across the world vary considerably, with substantial gaps in robust data from different countries and populations (Figure 23) [77] [91]. Predominantly low-middle-income countries have insufficient data, but TBI rates are likely higher than in high-income countries [77] [91]. In 2017 The Lancet Neurology Commission of TBI reported 50 to 60 million new cases per year worldwide, of which over 80% occurred in low-middle-income countries [92]. Additionally, the Commission concluded that about half the world's population have had a TBI, of which around 90% experienced a mild injury or concussion [86] [92].

4.2.1.2 European Union

The European Union (EU) is an international organization comprising 28 member states, which reports at least 2.5 million new cases of TBI each year [92]. Crude incidence rates in country-level studies of this community range from 47.3 per 100,000 to 694 per 100,000 population per year [77]. In accordance, 1.5 million hospital admissions for TBI occur annually in the EU [92]. Unfortunately, the risk of presenting a recurrent trauma (rTBI) within the first year since injury varied from 0.43% to 41.92%, from which at least 5.5% require medical attention [93]. rTBI intensifies the potential short and long-term neurologic damage in the individual and amplifies the overall TBI burden in the general population [85], [86], [93].

4.2.1.3 United Kingdom

Approximately 1.4 million TBI patients attend hospital annually in the UK, of which 20% require hospitalization [94],[95]. Figure 24: Cause of injury in England and Wales shows the incidence of TBI by age and the most relevant mechanism of injury in England and Wales [94].



Figure 24: Cause of injury in England and Wales [94].

4.2.1.4 United States of America

Similarly, in the USA, the number of new cases of TBI approaches 3.5 million per year, with a growing tendency [92]. For instance, the number of TBI-related visits to the emergency department increased by more than 50% between 2007 and 2013 [96]. Moreover, this problem affects people several times during their life. For example, survey research in Colorado reported that 42% of respondents had suffered at least one TBI in their lifetime [92].

4.2.2 Mortality

4.2.2.1 Worldwide

The literature has not reported a worldwide TBI mortality rate that includes all types of severities. Most studies have focused on severe TBI, which has mortality rates as high as 30-40%, but little is known about the contribution of non-severe TBIs to mortality [92]. However, physical, psychiatric, emotional and cognitive disabilities are not restricted to severe cases [92]. In addition to the disabling outcomes, TBI has been shown to shorten life expectancy by six years [92].

4.2.2.2 European Union

A total of 57,000 TBI-related deaths occurred in 2012 in the 28 Member States of the EU [92]. From country-level studies, the crude mortality rates vary from 9 to 28.10 per 100,000 population per year

[77]. Each death means many years of life lost per patient but also substantially impacts society. For instance, an average of 24.3 (22–26.6) is the years a person would have lived if he or she had not died prematurely from a TBI [92]. Moreover, nearly 74% of all years of life are lost in age groups with the potential to work (15–64 years) [92]. The previous figures do not include the productive years lost due to TBI-related disability [92].

4.2.2.3 United Kingdom

In 2012 the age-adjusted mortality rate was 5.6 per 100.000 people in the UK [97]. In England and Wales, mortality is over 12% in TBI patients, with an in-hospital probability of death of 17% [98]. As mentioned before, most of the evidence focuses on severe TBI, which has a mortality rate of 23% in England and Wales [98]. Also, TBI is responsible for 50% of trauma losses, with around 5.400 deaths annually in England and Wales [99]. Finally, head injury has an enormous impact on the number of years lost by UK society, where TBI is the most common cause of death in the population under 25 years old [94], [95].

4.2.2.4 United States of America

Each year, over 56,000 Americans die due to TBI, contributing to about 2.2% of all deaths [92],[96]. In 2010 the Centre for Disease Control and Prevention established a mortality rate in the USA of 17.1 per 100.000 people [92]. Additionally, survivors are 2.23 times more likely to die than the comparable no-TBI population, and their life expectancy is reduced by nine years after the trauma [96]. Actually, 20% of TBI patients die within the next five years after trauma, mainly due to the permanent sequelae of the injury. It has been estimated that 3.17 million people live in the United States with TBI-related disabling conditions, corresponding to 0.7 - 2% of the US population [92], [96].

4.2.3 Mechanism of injury

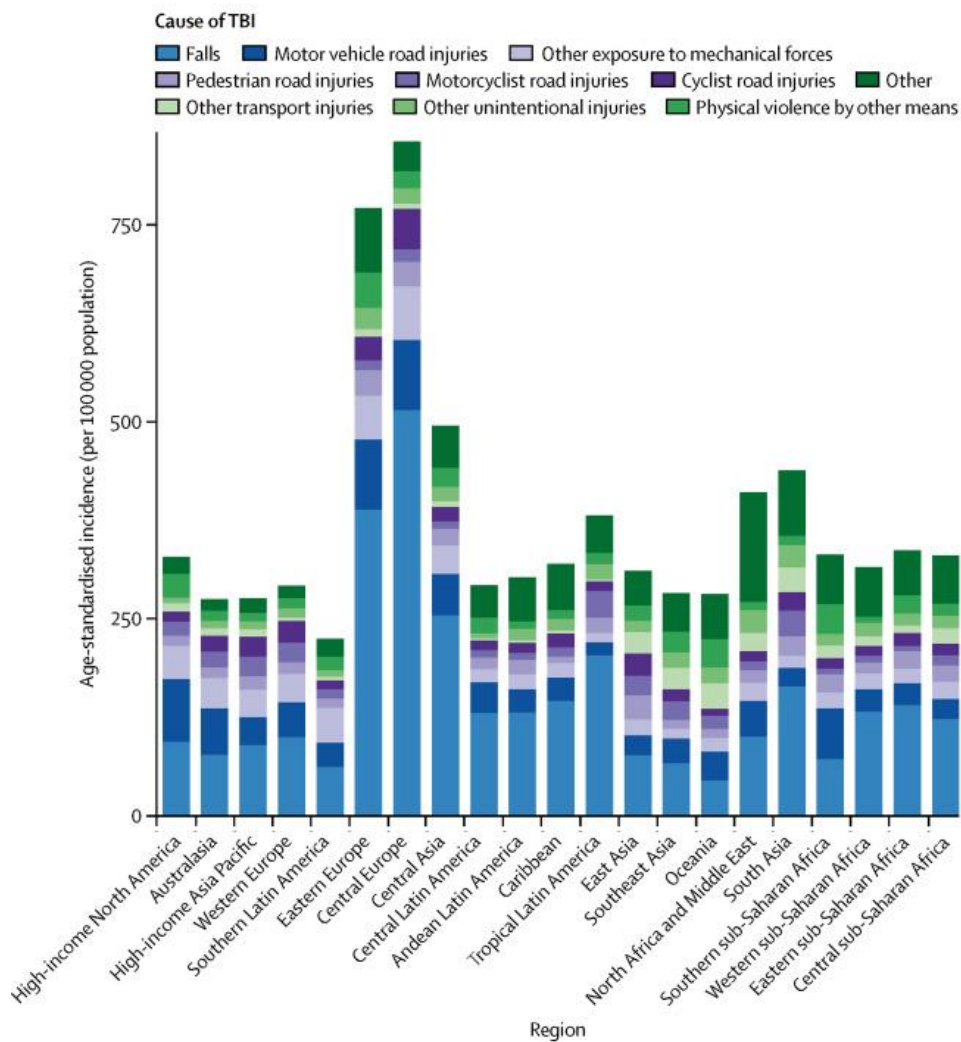


Figure 25: Cause composition of age-standardised incidence of traumatic brain injury by Global Burden of Disease region for both sexes [100]

Worldwide, the most common causes of head injury are road traffic incidents, falls and violence, followed by other mechanisms of injury like sports, accidents in the home or at work as machinery incidents, and suicide attempts (Figure 25) [77],[92],[101]. Nowadays, TBI incidence may still be increasing due to the broader use of motor vehicles in low-middle-income countries and an increase in falls among older people in high-income countries [77].

4.2.4 Risk factors

Most studies reporting sex ratios show more male patients than female patients are diagnosed with TBI [77]. Men generally have more than double the risk of women suffering head injury [92]. Also, the male sex is significantly associated with a higher risk of recurrent TBI [93]. Likewise, TBI presents a bimodal distribution where younger children and older adults are at higher risk [93]. For instance, the highest rate of emergency department visits because of TBI are in children under four years old and

increasing [92]. Also, patients over 50 years old with severe TBI have increased by a factor of three since the '80s [92]. Finally, lower socioeconomic status and alcohol/substance intoxication are also significantly associated with a higher risk of TBI and recurrent injury [93]. Regarding the latter, previous evidence demonstrates that shorter intervals between the first injury and rTBI are associated with greater disability since the injured brain is still recovering from the initial injury [93].

4.2.5 Special populations

4.2.5.1 *Military*

Between 2000 and 2019, more than 310.000 US army members suffered at least one head injury [86]. After deployment, the risk of being diagnosed with TBI is 8.4 times the risk before deployment. Mild TBI or concussion occur in 82.4% of all military TBI cases [86]. However, combat-related TBI is a substantial cause of morbidity and mortality, often including blast-related TBI and extracranial polytrauma [86]. Furthermore, a decline in outcomes from 1 year to 5 years after the injury has been reported in 72% of US military service members [92].

4.2.5.2 *Children and adolescents*

In the US, children below four years old have the second-highest incidence of TBI after adults over 75 years of age [92]. TBI is the predominant cause of death in this group in high-income countries [92]. Falls and abusive trauma are the most common causes of severe TBI in children under two years of age [92]. In the UK, more than 220 infants have been killed or injured due to being shaken in the past decade [102].

4.2.5.3 *Elderly*

The ageing population has raised TBI incidence in people over 65, who represent 10% of TBI cases but account for 50% of TBI-related mortality [92]. The in-hospital fatality rate is between 43% to 71% in adults over 60 years, and it increases to 75% after six months after injury [92]. These alarming figures have been associated with therapeutic nihilism and less aggressive treatment for older patients with TBI [92]. Falls are the leading cause of TBI in the “silver tsunami group”. However, loneliness and depression might also lead to alcohol abuse, which increases the risk of falls [92],[96].

4.2.5.4 *Sports-related*

Sports-related concussion is a frequent cause of TBI [92]. However, the actual incidence rate remains unclear, as most of these injuries are not reported deliberately or because of a lack of awareness [92]. Still, some studies have shown that 70% of sports and recreation-related mTBI occurred among individuals ages 0-19 years [96].

4.2.5.5 *Offenders*

Over half of all assault admissions to accident and emergency departments are diagnosed with a head injury [103]. For instance, in the USA, 3,227 abusive head trauma happened in children under five between 2001 and 2006, of which 2/3 resulted in hospital admission [96]. Similarly, in a sample of women who suffered domestic violence, 81% of the sample reported having been hit in the head or being made to have their head hit another object at least once, with close to 50% reporting “too many times to remember” [104]. Actually, assaults or violent acts, including self-inflicted injuries, are a significant cause of death among women, with a fatality rate of 40% among women who suffer a TBI [101].

Of all types of violent penetrating injuries, gunshot wounds to the head are the most fatal ones (75%–80%) [105]. On the other hand, TBI shares risk factors with criminal behaviour, such as socioeconomic adversity, risk-taking behaviour, and conditions such as attention deficit hyperactivity disorder (ADHD), mental health disorders, and alcohol or drug misuse [91]. Accordingly, it is unsurprising that the prevalence of TBI in imprisoned populations is over 60.3% [90].

4.3 DEMOGRAPHICS AND SOCIETAL COST IN TBI

TBI has an estimated global annual burden of US\$ 400 billion, where in-hospital costs represent a substantial part of it, especially in patients with severe TBI who have the highest individual costs [106]. Severe TBI patients have the highest number of surgical and medical interventions; they usually go under intracranial pressure monitoring and/or mannitol medication. Such interventions are related to more extended hospital or intensive care unit length of stay (LOS), ranging from 10 to 36.8 days and 7.9 to 25.8 days, respectively [106]. Worldwide, the median in-hospital cost per patient is US\$55,267, varying from US\$2,130 to US\$401,808 [106]. However, just 46% to 67% of total hospitalization costs are related to acute care; the remaining costs are associated with rehabilitation in patients with unfavourable outcomes [106]. For instance, the costs of rehabilitation of TBI patients in Europe were about 10% higher than medical care prices in 2010 [107]. Still, there are relevant unaccounted costs on a long-term or lifetime horizon as those related to disability or quality-adjusted life-year [106]. An example of these costs takes place during the first three months of post-rehabilitation discharges, when at least 80% of patients visit a doctor, of which 42% reported four or more visits, over 50% attended day rehabilitation programs, 42% had physical therapy, 36% occupational therapy, 33% speech pathology, and 11% had psychological counselling [107]. All the above, in addition to the unaccounted costs for lost productive years due to TBI-related disability [92].

4.4 POST-TBI EFFECTS

The most common effects of brain injury are grouped into physical, cognitive, behavioural, and emotional effects. Table 4 from Chapter 2 summarizes some possible outcomes after a specific area of the cerebrum, or limbic system has been damaged. However, this section expands on the information previously summarized.

Physical conditions affect mobility, also described as how the body moves. Thus, after TBI, some patients would need a wheelchair or other assistive technologies because of their poor balance and coordination. Also, they might present spasticity, which limits limbs' strength and range of movement and can cause pain or discomfort. In some cases, weakness or paralysis of one side of the body occur depending on the side of the brain that got injured; these are known as hemiparesis and hemiplegia, respectively [108]. Moreover, TBI patients may develop ataxia, referring to irregular, uncontrolled movements that affect coordination. In addition to the muscular outcomes mentioned, there might also be sensory impairments such as reduced, lost or exaggerated touch sense. Likewise, proprioception, eyesight, taste or sense of smell may be impaired or lost in the short or long term. Fatigue or excessive tiredness is also common in all TBI-severity patients, even during the execution of simple tasks such as getting dressed [108]. The group of physical effects also include epileptic seizures or fits as the result of sudden onsets of random and erratic electrical activity in the injured brain. Also, some patients may suffer pituitary gland or hypothalamus damage, leading to hormonal imbalances. Symptoms can include depression, impotence, mood swings, fatigue, muscle weakness, reduced body hair, fluctuating body weight, sensitivity to cold, increased thirst, excessive production of dilute urine, and many others [108].

On the other hand, cognitive impairments mainly affect concentration, memory and general speed of thought. However, a broad spectrum of cognitive skills, like perception, language and the awareness of self and others, can also be disturbed. Executive function alterations are particularly debilitating as the patient may lose the capacity for planning, organisation, multi-tasking and flexible thinking. Diving deeper into each of these cognitive effects, it has been seen that patients with damage to the amygdala after a head injury have problems creating short-term new memories, including remembering faces, names, and things that had been read or said. In contrast, they have intact memories of previously learned skills [108]. Reduced concentration is also affected by impaired memory, leading to difficulties in starting and completing a task.

Similarly, these patients may find it challenging to organise facts in their minds, which causes anger and frustration. Furthermore, patients who suffered a disruption in Wernicke's area may have difficulty making sense of what they say or read, while patients who have damaged Broca's speech

area may understand what they want to say but cannot find the right words to say or write. Both of these language losses are called aphasia. Likewise, they may repeat the same topic repeatedly in a conversation [108]. Moreover, the patient might have difficulty recognising ordinary objects or human faces when the visual sense is intact from a physical perspective. Also, they can present visual neglect, which causes people to only attend to one-half of the objects, for example, eating just food on one side of the plate. Finally, this group of cognitive effects post-TBI involves impaired reasoning, where the patient may not think logically, understand rules or follow the discussion. Also, impaired insights cause difficulties in perceiving and interpreting others' behaviours and feeling, leading to a lack of empathy [108].

In some cases, family relatives describe emotional and behavioural effects as the worst consequences of brain injury due to the feeling that the loved person slipped away. The patient might present personality changes and mood swings, with a tendency to suddenly move from one emotional state to another [108]. Depression, a sense of loss and anxiety are common and might be related to damage to the brain's emotional control areas or grief feelings. The latter causes the loss of skills, independence, lifestyle, career, and companionship, among others. As is expected in any human being, this set of resignations leads to frustration and anger. Furthermore, behavioural changes after TBI might include disinhibition in how patients behave with others, such as in an over-familiar or sexual manner. Likewise, they can be impulsive, speak or act without thinking first; and develop obsessive behaviours [108].

Table 8: Post-TBI outcomes summary

Emotional effects	Fatigue	Hormone imbalances	Physical effects	Post-traumatic amnesia	Sexual dysfunction
Controlling emotions Mood swings Depression Anxiety Frustration and anger Stress disorder	Sleep difficulties Eyes and limbs feeling heavy Muscle weakness Headaches Vision disturbance	Reduced fertility Weight gain Increased sensitivity to cold Dry skin Low blood pressure Diabetes insipidus	Slow and balance disruption (can't walk) Spasticity Paralysis Ataxia Epilepsy	Confusion Agitation Distress Anxiety Uncharacteristic behaviours	Problems to have: Sexual arousal Intercourse Orgasm Sexual satisfaction

Behavioural effects	Cognitive effects	Reduce awareness	Communication problems	Executive dysfunction
Disinhibition Impulsiveness Obsessive behaviour Irritability and aggression Apathy and loss of initiative Egocentricity	Memory Impairments in visual-perceptual skills Reduced concentration Reduced information processing Impaired reasoning	Coma Vegetative state Minimally conscious state Locked-in syndrome	Aphasia (language impairment) Dysarthria (control of muscles used for speech) Dyspraxia (difficulty saying what you are consciously thinking) Repetition	Planning and organisation problems Multi-tasking Making decisions

4.5 CLINICAL PRACTICE GUIDELINES IN TBI

Clinical practice guidelines (CPGs) are a set of recommendations systematically developed to assist health professionals in making decisions for addressing a specific clinical condition [109]. Systematic reviews have evaluated the quality of all currently available international CPGs on treating TBI [109], [110], as the lack of systematic and rigorous assessment of the best available evidence could lead to unreliable or even harmful patient recommendations. The quality assessment done by these reviews used the tool AGREE II, which involves the following six domains: scope and purpose, stakeholder involvement, rigour of development, clarity of presentation, application, and editorial independence [121]. Each review assessed 12 CPGs and recommended for use those that had scored above 50 in at least four domains of AGREE II [109], [110]. Based on the results of these reviews, the current research picked the latest published recommended guideline titled: “Guidelines for the Management of Severe Traumatic Brain Injury, Fourth Edition” [49].

4.5.1 Recommended clinical evaluation

As it was explained in the definition and types of TBI section, a head injury can be classified by mechanism of injury (open or close), by morphology (fractures, focal or diffuse injuries), or by severity (mild, moderate, severe). Scores have been developed to triage patients immediately after trauma and assess their injury severity [84]. The Glasgow Coma Scale (GCS) is the most valuable and frequently used score in head trauma, and it is divided into three domains: eye, motor and verbal response, adding to a total score of 3-15 points [84]. GCS individual components should be recorded rather than just the total sum, as patients with the same total score may have different outcomes due to differences in the individual components. As tracheal intubation precludes a verbal response and, in some cases, eye response is compromised by facial injuries, the motor component is valued as the most robust and relevant part of GCS evaluation, which also is regarded as the most accurate estimator of outcome [37], [111]. Figure 26 shows TBI classification according to GCS total score.

Eye opening			
Eyes open spontaneously	4		
Eyes opening to verbal stimuli	3		
Eyes opening to painful stimuli	2		
No eye opening	1		
Verbal response			
Orientated	5		
Confused	4		
Inappropriate words	3		
Incomprehensible sounds	2		
No verbal response	1		
Motor response			
Obeys commands	6		
Localising pain	5		
Normal flexion to pain	4		
Abnormal flexion to pain	3		
Extension to pain	2		
No motor response	1		
		Add scores	
		GCS 13-15	Mild TBI
		GCS 9-12	Moderate TBI
		GCS 3-8	Severe TBI

Figure 26: Classification of clinical severity of TBI with the Glasgow Coma Scale [91]

Morphology is also assessed immediately after a patient with a GCS<13 arrives at the hospital and within the first 24 hours in comatose patients (GCS<8). Computerised tomography (CT) remains the most widely recommended imaging study for the evaluation of severe TBI, which provides clinical information quickly and relatively economically, especially in cases of bone damage, blood presence and significant alterations in tissue structure [112]. However, CT depends on radiation, has low spatial and tissue density resolution, and is susceptible to movement artefacts. The standard scoring system has been widely used for TBI prognostication, such as Marshall CT classification and the Rotterdam CT score. There are also more recent scoring systems as the Stockholm CT score and Helsinki CT score [112]. Another option to assess morphology after a head injury is Magnetic resonance imaging (MRI), which is generally used to identify more subtle pathology, including contusion and microhaemorrhages. MRI does not have the risk of radiation and has the potential to inform long-term prognosis, yet it requires significant postprocessing and its scales are not as standardized as those that existed for CT scans [112].

Morphology assessment studies the presence of a concussion, swelling, herniation, compressed basal cisterns, cortical thickness, midline displacement, the width of a hematoma and its apex, microhaemorrhages, diffuse axonal injury, among other imaging indexes as EVANS index [112]. MRI and especially CT scans are essential in the diagnosis of TBI lesions. Unfortunately, it can take at least two hours from the moment of injury to get the images and decide on therapeutic interventions such as surgery [94]. Hence during this “golden period”, paramedics and doctors know almost nothing about what is going on in the skull, increasing the risk of poor outcomes [91]. Also, these intermittent techniques are unsuitable for evaluating patients' progress, so the guidelines recommend continuous and invasive monitoring of physiological variables, especially for severe cases [49].

4.5.2 Recommended monitoring techniques

The primary role of the use of neuromonitoring is the potential to provide a very early warning of secondary cerebral deterioration. As was explained in chapter 3, crucial secondary insults after a head injury, like cerebral ischemia or hyperaemia, increase the risk of mortality and worse neurological outcomes in survivors [32]. In consequence, bedside monitoring is focused on systemic indicators and the following cerebral haemodynamic parameters: intracranial pressure, cerebral perfusion pressure, mean arterial pressure, cerebral blood flow, metabolism, oxygenation, or electrophysiological changes that can occur after an acute injury [37].

4.5.2.1 Intracranial pressure

As explained in chapter 3, intracranial pressure (ICP) is the primary focus of monitoring head injury. There are several methods of measuring ICP, yet the intraventricular catheter remains the gold

standard [32], [113]. This catheter has therapeutic advantages as it can drain excess CSF in hypotensive cases. However, technological advances in piezoresistive strain-gauge and fibre-optic microsensors have allowed the appearance of parenchymal micro-transducers that are easy to place anywhere within the cranial cavity and have less risk of infection than intraventricular sensors [111]. The most widely accepted ICP threshold for therapy is 20 mmHg, although the latest guidelines suggest 22 mmHg [91]. Guidelines recommend ICP monitoring in all severe TBI patients with an abnormal CT scan. Severe patients with a normal CT scan should also be monitored if they are above 40 years old and have signs of motor posturing or if they present a systolic blood pressure over 90 mmHg at the hospital arriving time [49].

ICP waveform components are examined with mathematical analysis in the time or frequency domain, leading to the extraction of features that correlate with physiological changes such as arterial pulse, respiratory cycle or reduced cerebral compliance. For instance, Figure 27 shows the ICP pulse waves from the same patient at two periods. The panel on the top shows normal ICP pulses, while the bottom panel displays pulses at hypertensive levels, demonstrating three distinctive peaks: P1 (percussion wave), P2 (tidal wave) and P3 (dicrotic wave). Note that the peak-to-peak amplitude metric at normal ICP reflects P1 and at hypertensive levels P2.

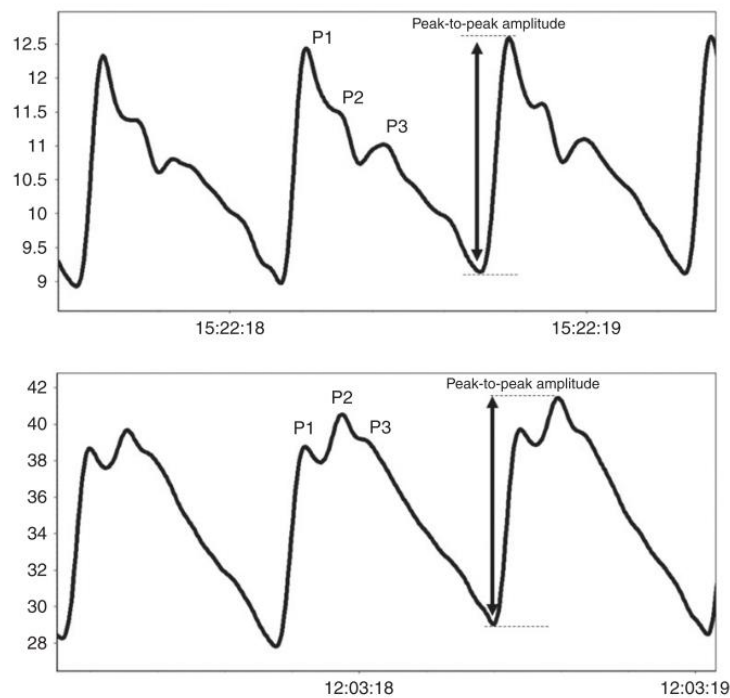


Figure 27: ICP waveform components [111]

ICP monitoring alone does not track the underlying pathophysiological processes that govern the degree of injury and potential for recovery after brain injury [57]. Therefore, to complement ICP monitoring, several technologies have been developed to measure cerebral physiologic and metabolic

parameters related to autoregulation, oxygen delivery, CBF, and metabolism, to improve the detection and management of secondary brain injury [32], [113].

4.5.2.2 Autoregulation

Advances in real-time data processing and computerized bedside monitoring have opened the possibility of analysing autoregulation indexes, such as the ones reported in Table 9. Most of them are calculated as Pearson correlation coefficients between 10 seconds averaged signals over a 5-minute window and are typically updated every minute [72]. The method for monitoring the pressure reactivity index (PRx) is widely accepted in clinical practice even though a gold standard for cerebral autoregulation monitoring does not exist [114]. When cerebral autoregulation is impaired, cerebral vessels do not regulate CBF; thus, intracranial volume (ICV) and ICP increase and decrease passively with MAP. As PRx is the moving correlation between ICP and MAP, a positive PRx value indicates impaired autoregulation with a critical threshold of +1, reflecting complete impairment of cerebral autoregulation [114]. Accordingly, negative values of PRx are the result of opposite changes in ICP and ABP when normal autoregulatory reactions maintain CBF stable [114].

Table 9: Autoregulation indexes [72]

Invasive ICP monitoring	PRx – correlation between ICP and MAP PAx – correlation between AMP and MAP
TCD flow velocity derived from MCA (typically)	Mx – correlation between FVm and mean CPP Sx – correlation between FVs and mean CPP Dx – correlation between FVd and mean CPP Note: Mx/Sx/Dx can be derived non-invasively from MAP, instead of CPP.
NIRS derived bifrontal signal acquisition	TOx – correlation between TOI and CPP THx – correlation between THI and CPP Note: TOx/THx can be derived non-invasively from MAP, instead of CPP.
Brain tissue oxygen (PbtO2)	ORx – correlation between PbtO2 signal and CPP

AMP: fundamental amplitude of ICP; Dx: Diastolic Flow Index; CPP: cerebral perfusion pressure; FVm: mean flow velocity; FVd: diastolic flow velocity; FVs: systolic flow velocity; ICP: intracranial pressure; MAP: mean arterial pressure; MCA: middle cerebral artery; NIRS: near-infrared spectroscopy; ORx: Oxygen Reactivity Index; PbtO2: brain tissue oxygenation; PRx: Pressure Reactivity Index; Sx: Systolic Flow Index; TCD: Transcranial Doppler; THI: Total Haemoglobin Index; TOI : Tissue oxygenation index.

It is essential to remember that cerebral oxygenation depends on oxygen delivery and consumption (CMRO₂). Thus, CPP, as the difference between MAP and ICP, represents the driving pressure for CBF and, thus, oxygen and metabolite delivery. Therefore, target CPP treatment is considered more critical than traditional targeted ICP care [37]. According to TBI guidelines, CPP should rest between 60-70mmHg; below this threshold, there is a high risk of ischaemia, while over the threshold, brain hyperperfusion might lead to oedema, BBB leakages and hyperaemia [72]. However, new clinical studies have suggested favourable outcomes in patients treated using optimal autoregulation targets [32], [113]. PRx can help to find an optimal cerebral perfusion (CPP_{OPT}) value to maintain the patient's cerebral oxygen delivery. CPP_{OPT} is determined from the lowest PRx value plotted against all of the CPP values within a recorded period of usually 4 hours. Nonetheless, a recent systematic review on this topic concluded that there is not enough high-quality evidence to make recommendations for implementing CPP_{OPT} over the usual CPP thresholds for TBI treatment [115].

4.5.2.3 *Microdialysis*

Cerebral microdialysis consists of a thin probe with a semipermeable dialysis membrane in the tip that is inserted into the parenchyma to measure biochemical samples of the brain interstitial fluid that reflect its metabolisms, such as glucose, lactate, pyruvate, and glutamate. First, the probe is perfused with a sterile fluid using a microdialysis precision pump. Then, the highest concentration molecules in the extracerebral fluid are equilibrated across the membrane, allowing the collection and following analysis of the concentration.

As mentioned in Chapter 3, TBI is responsible for a complex brain energy metabolism dysfunction, leading to brain tissue acidosis. Furthermore, due to ischaemia, hypoxia or mitochondrial impairments after trauma, neurons must rely upon the anaerobic metabolism of glucose for energy [32], [113]. Consequently, extracellular reflections of brain trauma are reduced glucose and pyruvate and increased lactate and lactate/pyruvate ratio (LPR). The latter is the most sensitive biomarker of brain tissue ischaemia, as lactate concentration may increase due to hyperglycolysis. Similarly, LPR is increased even though lactate concentration may be normal during periods of herniation [32], [113]. Moreover, glutamate is responsible for excitotoxicity after Wallerian degradation (chapter 2), where a massive calcium influx into the brain cell disposes a large amount of glutamate into the cerebral interstitial fluid. Currently, the following thresholds indicate that the area of the brain being monitored is 'at risk', based on observational studies: glucose <0.2 and glucose <0.8 mmol/L, and LPR>25 and LPR>40 [32], [113]. However, there is not enough high-quality evidence on cerebral microdialysis yet. Therefore, it has not been included in the latest guidelines and recommendations as a sufficient monitoring technique on its own [49]. Nonetheless, there has been increasing interest in sampling the

brain's chemistry in neurocritical ill patients; therefore, cerebral microdialysis is a relevant research tool with growing clinical implications [32], [113].

4.5.2.4 Cerebral oxygenation

The assessment of brain oxygenation is an essential part of the management of the neurocritical ill patient, providing information about oxygen supply and utilization after acute brain injury [32], [113]. Advanced monitoring techniques for cerebral oxygenation include the differences between arterial and arterio-jugular venous oxygen content ($SjvO_2$), also known as $AVDO_2$, and measurements of the local partial pressure of oxygen ($PbtO_2$) in the extracellular fluid of the brain [49], [116].

Continuous monitoring of $SjvO_2$, which estimates the balance of global oxygen delivery and consumption [32], is performed through a fibre optics catheter placed in the internal jugular vein. Lights from red and near-infrared wavelengths are transmitted down the fibres and absorbed proportionally to the percentage of oxygenated haemoglobin; hence the total haemoglobin is reflected and measured by the fibre photodetector [62], [117]. Arterio-jugular $AjVDO_2$ is an overall measure of cerebral oxygen extraction. However, this value can potentially differ between hemispheres in TBI patients [49].

For invasive $PbtO_2$ monitoring, a fluorescence-quenching sensor is placed on the cerebral cortex and directly measures the dissolved oxygen in the surrounding/measurement area [49], [118]. The device comprises excitation light sources, a substrate film attached to fluorescence-sensitive substances and an optoelectronic detection element. The fluorescence quenching reaction occurs at the interface of the sensitive film when the fluorescence sensor is in contact with the tissue and stimulated by the light source [118], [119]. After the fluorescent substance absorbs light (photons) at a specific wavelength, its electrons gain energy and become excited to a higher state. If additional energy is not provided, the electron undergoes a natural decay in energy returning to the ground state and the simultaneous release of a photon (fluorescence). Since the oxygen molecules interfere with the excitation process of fluorescent substances, the concentration of oxygen can be determined according to the fluorescence intensity [118], [119]. This technique is used by commercial devices such as Neurotrend (Diametrics Medical, Minneapolis, USA) and Neurovent-PTO (Raumedic, Germany and Mills River, USA) [57].

Another invasive $PbtO_2$ monitoring system is based on Clark electrodes, which work by opposing two metallic surfaces in an aqueous electrolyte potassium-chloride solution and allowing oxygen to diffuse into the solution [57]. The oxygen conducts an electrochemical reaction and creates an electric potential between the gold cathode and the silver anode, which is directly proportional to the oxygen content in the solution. The oxygenation or oxygen concentration is then measured by recording the

current flowing between the electrodes and relating this to the oxygen content [57]. This technique is commonly used in commercial devices such as Licox (Integra NeuroSciences, England) [57].

In clinical practice, brain oxygenation is a source of information for management decisions, which in addition to ICP and CPP monitoring, leads to lower mortality rates and better outcomes at 3- and 6-months post-injury [32], [37], [113]. Nevertheless, near-infrared spectroscopy is a non-invasive technique that has been developed and tested during the last decades, which investigates the oxygenation status of blood chromophores to provide a continuous real-time measurement of cerebral regional tissue oxygenation [120]. Its application will be the topic of discussion in chapter 5: “Non-Invasive monitoring techniques in TBI”.

4.5.2.5 Cerebral blood flow

Cerebral blood flow (CBF) is a fundamental parameter for life, which depends on the proper delivery of oxygen and metabolites to the brain tissue. Low CBF is associated with higher mortality and poorer outcomes in TBI patients [41]. Nowadays, measurement of blood cerebral blood flow is performed using Xenon CT scans, which allow the quantitative and regional evaluation of intracranial blood flow. Also, non-invasive and continuous techniques have been developed to assess this critical variable, such as laser Doppler and transcranial Doppler (TCD) ultrasonography [32], [113].

In TCD, the ultrasound probe uses an array of piezoelectric crystals, which vibrate when an electric signal is applied and produce a high-frequency acoustic wave (>20KHz). Moreover, this kind of crystal can also work in reverse, producing electrical signals when it detects ultrasound pressure waves (echoes) [121], [122].

The raw signals for most ultrasound techniques are obtained by detecting the ‘echoes’ generated by the reflections and scattering during the propagation of the ultrasound wave through different structures within the body. The process of sending echoes back to the transducer is often called ‘backscatter’. Returning echoes are then converted into electrical signals, which are transformed into brightness points corresponding to the anatomic position and tissue density [121], [122].

The Doppler effect (or Doppler shift) is the change in the observed frequency of a wave due to the motion of the source concerning the observer, with the resulting shift in frequency being directly related to the velocity of the movement. When a source moves toward a static observer, the wavelength is compressed, increasing the frequency, while if the motion of the source is moving away from the observer, the wavelength stretches and decreases frequency [121]. If the Doppler shift and the beam angle are known, the velocity can be calculated according to Equation 13.

$$v = \frac{f_d * c}{2 * f_t * \cos \theta}$$

Equation 13: Flow velocity in Doppler effect

where v is the velocity, f_d is the doppler shift, f_t is the transmitted frequency, θ is the transducer's angle, and c is the speed of ultrasound in vacuum (typically, 154.000 cm/s) [121]. If the angle is zero, or the emitted wave is parallel to the direction of flow, the cosine of zero is 1, which is the most accurate measure of flow velocity [123].

Transcranial Doppler is used to measure relative changes in flow velocity in the basal arteries of the brain. Spectral analysis can then be used to obtain the following parameters: peak systolic velocity (Vs), end-diastolic velocity (Vd), systolic upstroke or acceleration time, pulsatility index (PI), and time-averaged mean maximum velocity (Vmean) [123]. The main applications of TCD in TBI are related to developed methods to assess ICP and cerebral autoregulation based on TCD-derived parameters [124]. These applications will be further discussed in chapter 5: "Non-Invasive monitoring techniques in TBI".

On the other hand, laser Doppler flowmeter consists of a fibre-optic probe that uses monochromatic light in the range of 670 to 810 nm. The movement of red blood cells induces a Doppler shift in the light that is proportional to the velocity and number of red blood cells [111]. However, LDF cannot be calibrated in absolute units, and the outputs may not be linear, which means that LDF can determine a change in CBF but does not give an absolute value of flow or its direction [125].

4.5.2.6 Electrophysiologic monitoring

Electroencephalography (EEG) assesses electrical brain activity even in patients with depressed brain function, like those in a comatose state. EEG is based on the principle of differential amplification, where voltage differences between a pair of electrodes are recorded and compared with a distant reference electrode. Thus, the electrodes detect the summation of the electrical synaptic potentials generated by cortical pyramidal neurons in the cerebral cortex [126]. EEG does continue monitoring and is recommended in all TBI patients with unexplained and persistent altered consciousness because it can detect subclinical seizures and non-convulsive status epilepticus [32], [113]. Likewise, evoked potentials (EP) are used in patients in whom sedation, sepsis, or metabolic derangement confounds the neurologic evaluation [32], [113].

4.5.3 Multimodal monitoring

Multimodal monitoring (MMM) is defined as the simultaneous measure and analysis of multiple relevant vital parameters. Evidence in the literature has highlighted that the use of multimodal neuromonitoring is likely to improve outcomes, provide an early warning of secondary cerebral

deterioration and can help understand the patterns of perfusion, oxygenation and autoregulation [127] [32]. However, even if ICP evaluation is the most used tool for assessing TBI, the evidence surrounding the intensive management of patients, based directly on the absolute values of this parameter, is equivocal [128]. Instead, multimodal monitoring (MMM) management of TBI is targeted to the patient's specific pathophysiology, bearing in mind that TBI involves heterogenic pathophysiological processes [32]. Then the integration of a variety of neuromonitoring technologies can differ between pathophysiological mechanisms, thus individualising treatment targets and thresholds [37], [91], [113].

MMM gathers a variety of information, including ICP, autoregulation, real-time brain metabolism, cerebral oxygenation, cerebral blood flow, and the electrical status of the brain, all of which allow for a better understanding of any physiological changes in the brain [32], [91], [113]. Recent clinical trials showed that such improved understanding, and appropriate targeting of treatment, improved treatment results [91]. For instance, management of TBI through brain oxygenation and ICP monitoring reduces the risks of brain hypoxia and lowers mortality and improves favourable outcomes [128]. Therefore, these two variables are highlighted as the main biomarkers to monitor changes in patient severity; thus, they are critical parameters to consider during the patient's treatment selection. Also, the assessment of both measurements at the same time through MMM has shown better outcomes in mortality and disability than the assessment of just one variable at the time [37].

However, as most of the current technologies are invasive, this multimodal approach has the inherent disadvantage of requiring multiple intracranial sensors, each with its own operative risk [91]. Although these risks can be partly mitigated by using a single access device, a better solution would be the development of multiparametric sensors, which incorporate all the monitoring modalities into a single device [91]. Nowadays, multimodal monitoring is emerging as a clinical tool, but more research is still needed to improve the precision of diagnosis, classification, and characterisation of TBI using multidomain approaches [91].

Finally, an alternative approach to removing invasive devices' risks is developing and validating non-invasive multimodal monitors. Unfortunately, current non-invasive neuromonitoring cannot yet wholly replace invasive methods but has great potential if it is used as a MMM tool. Still, such advances require substantial input from industry, academia, and funding bodies [91], [129].

4.6 SUMMARY

In summary, Traumatic brain injury (TBI) is an alteration in brain function pathology caused by an external force. [77] TBI can be categorised into mild, moderate or severe, and it is often caused by:

road accidents, falls, or violent acts [77], [87], [96]. It is estimated that there are 50 million new cases of TBI yearly, with one person dying every ten minutes, and TBI is the most dominant cause for neurological disabilities [91]. The economic burden for the treatment and rehabilitation of TBI patients is significant. Costs are often related to direct hospital treatment, without considering productivity loss, disability and reduced quality of life for patients and their careers [107].

Traumatic brain injuries can alter cerebral autoregulation as well as increase intracranial pressure and reduce cerebral oxygenation, thus potentially leading to secondary injury if not promptly treated [37], [130], [131]. Continuous and simultaneous monitoring of multiple physiological parameters could significantly contribute towards a more optimised monitoring and treatment of TBI, which can result in lower mortality and disability outcomes [37]. In current clinical practice, ICP, CPP, CBF, cerebral oxygenation and metabolism are mainly measured by invasive methods, thus introducing additional risks for the patient and relying on neurosurgical expertise, which could potentially delay treatment [132] [61]. An alternative approach to removing invasive devices' risks is the development and validation of non-invasive multimodal monitors. The first step to achieving this goal is to investigate the current state of the art of non-invasive technologies used in TBI monitoring.

5 NON-INVASIVE MONITORING TECHNIQUES IN TBI

5.1 INTRODUCTION

Management of TBI patients aims to lower mortality and improve neurological outcomes by decreasing ICP (i.e. increase in CPP) and increasing brain oxygenation [128]. Hence, these two variables (ICP and brain oxygenation) are considered the main biomarkers for guiding TBI patients' treatment and monitoring their severity.

Therefore, monitoring brain oxygenation and ICP non-invasively and continuously could provide significant benefits by providing safe and easily obtainable clinical information within the first hours after trauma [113]. Although not yet adopted in standard clinical practice, several techniques have been investigated in the last decade in order to respond to the current demand for non-invasive monitoring of brain oxygenation and ICP. Previous reviews summarised these efforts, but the results on the efficacy of these techniques are scattered and different from each other [32], [133]–[135].

The following chapter is a systematic review and meta-analysis published in *The Journal of Neurotrauma* (DOI: 10.1089/neu.2020.7266) [124], which aimed to collect the evidence published in the last decade on non-invasive techniques for monitoring ICP and brain oxygenation in TBI patients. Allowing them to identify the most promising, optimal and impactful non-invasive technique(s) for monitoring and assessing TBI, which are state of the art for the future development of a multimodal non-invasive sensor for ICP and cerebral oxygenation monitoring in TBI patients.

5.2 METHODOLOGY

This review was performed in accordance with the PRISMA guidelines [136]. There was no funding source for this study nor any competing interests. The protocol was designed following the Cochrane Handbook for Systematic Reviews of Interventions [137], and it was registered at the International prospective register of systematic reviews in PROSPERO before the data extraction started (ID: CRD42020164739).

The authors performed a systematic search of PubMed, Embase, Scopus, Cochrane Library and Web of Science between January 15, 2010, and January 22, 2020, for studies that reported ICP and/or brain oxygenation monitoring in TBI patients. In consultation with the Institutional librarian with experience in conducting systematic review searches, the search strategy was designed, and it was focused on the intersection of keywords “traumatic brain injury”, “intracranial pressure”, “brain tissue oxygen”,

“non-invasive”, “monitoring”, “correlation” and “accuracy” with all kind of variations and MeSH/EMTREE indexing terms to include all potentially eligible studies.

After the removal of duplicates, the two independent authors reviewed the titles and abstracts of potentially eligible papers. Studies that satisfied the inclusion criteria were retrieved for full-text assessment. The inclusion criteria were as follows: 1) studies on patients diagnosed with TBI; 2) comparison of non-invasive ICP and/or brain oxygenation monitoring with invasive ICP and/or brain oxygenation monitoring, respectively; 3) studies reporting correlation and/or accuracy; 4) papers with accessible full text; and 5) cohort studies. The exclusion criteria were as follows: 1) reviews, conference proceedings, case reports, letters, editorials, animal and *in vitro* studies, case-control studies, summaries, expert opinions and comments; 2) studies in patients with open fontanelle; 3) medical imaging studies; 4) insufficient data; 5) duplicate publications of the same data set or non-independent data; 5) studies misreporting data and 6) articles published in a language other than English.

Any disagreement between the two authors during the full-text review was resolved by an independent arbitrator. The main authors independently completed data extraction and quality assessment using a data extraction MS Excel® sheet and quality assessment form. The following variables were extracted: bibliometric characteristics, variable monitored, non-invasive and invasive monitoring tool, number of patients, inclusion and exclusion criteria, mean age, sex proportion, cause of TBI, TBI severity according to the Glasgow Coma Scale (GCS), monitoring time, correlation and/or accuracy between non-invasive and invasive techniques, thresholds relating with the biomarker used.

Quality assessment was completed using the *Newcastle-Ottawa Scale*, which evaluates the quality of cohort studies [138]. With this quality assessment tool, three domains were assessed: selection, comparability, and outcome. Each domain was scored with one to two stars, which classifies studies' quality as good, fair, or poor, following the *Agency for Healthcare Research and Quality standards* [138].

Statistical aspects of the exploratory meta-analyses were performed using MedCalc software. The correlations between non-invasive and invasive techniques for each variable were measured by r values after converting the Fisher's z values back into correlation coefficients [139], [140]. The pooled correlation for both ICP monitoring was estimated using a random-effects model. In terms of statistical heterogeneity, a quantitative analysis was performed using the I-square test [137]; with an $I^2 > 40\%$ indicating heterogeneity. A funnel plot was analysed to detect systematic heterogeneity.

5.3 RESULTS

The flow diagram in Figure 28 illustrates the process of identification, screening, eligibility, and inclusion of publications in this systematic review. The search identified 228 potentially relevant citations and 20 publications, which seemed to meet the selection criteria by titles and abstracts assessment; those were selected for full-text review. Upon reviewing the full text of the 20 selected studies, only 12 fulfilled the inclusion criteria in assessing the correlation or accuracy between non-invasive and invasive methods for ICP or brain oxygenation monitoring in TBI patients. None of the selected papers reported a multimodal non-invasive monitoring technique in order to evaluate both variables simultaneously.

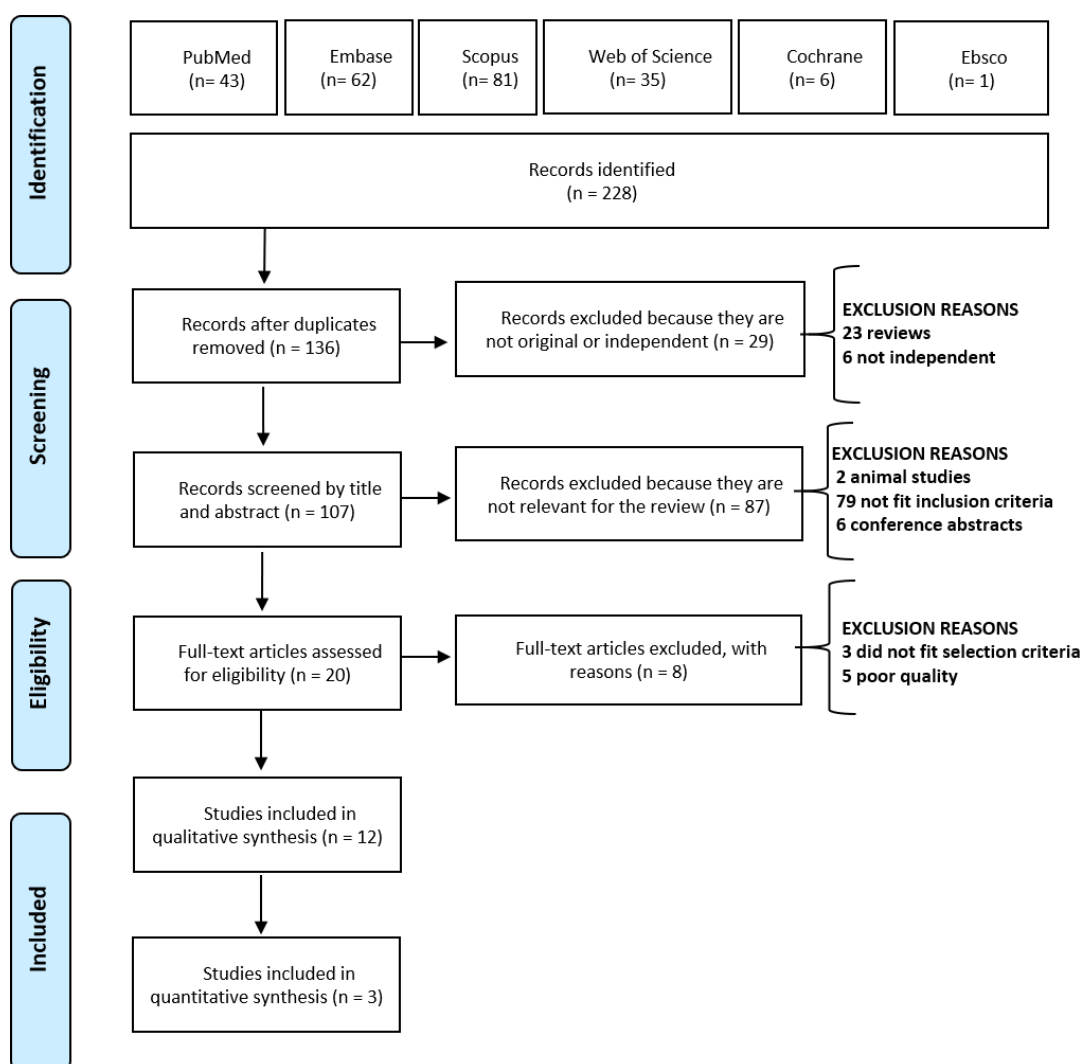


Figure 28: Studies selection flow diagram describing the identification, screening, eligibility, and inclusion of the systematic review.

From the 20 studies selected after the title and abstract screening [46], [61], [127], [128], [131], [132], [141]–[154], three were excluded after full-text reading as they did not fit the selection criteria [131], [141], [151]. Both reviewers (MR, TYA) agreed to the quality assessment results presented in Figure

29. Twelve papers were classified as ‘good quality’ and five as ‘poor quality’. The main reasons for poor quality were: 1) user-dependent data in Transcranial Doppler measurements affecting the ascertainment of exposure; 2) the design or analysis of the study did not control the confounders; 3) the monitoring window expected by the reviewers (MR, TYA) was below 48 hours, or it was not reported.

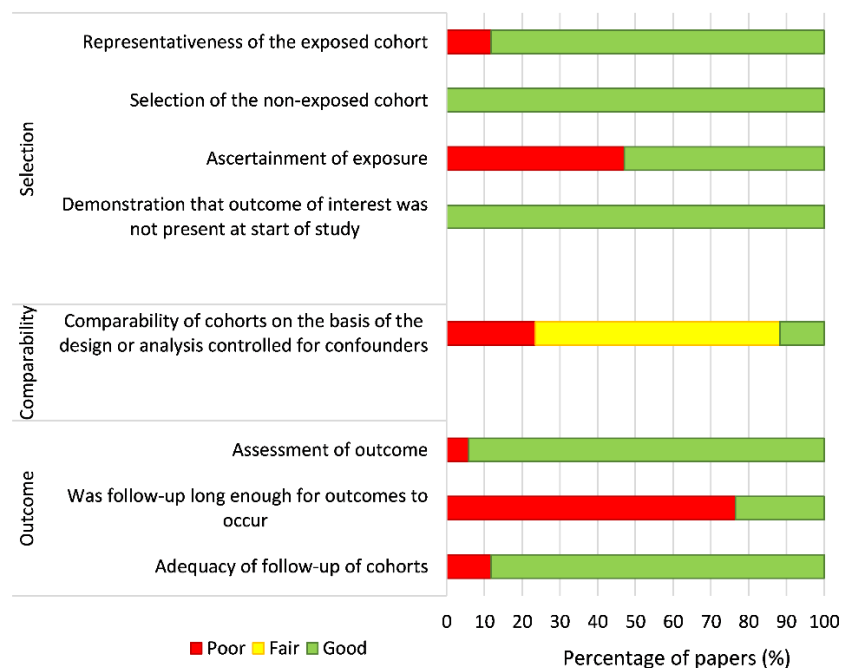


Figure 29: Quality assessment results.

A total of 78 TBI patients, with a weighted average age of 33.2 years, received non-invasive and invasive brain oxygenation monitoring [61], [128], [143], [144]. Most of these patients had moderate to severe TBI. In the group of ICP monitoring, a total of 701 patients with severe TBI with a weighted average age of 31 years received non-invasive and invasive ICP monitoring [127], [132], [145]–[150]. Table 10 depicts the bibliometric, demographic and technological characteristics of each study, while the synthesis presented below describes mainly the outcomes founded on the assessment of non-invasive techniques.

Four of the publications included were studies related to brain oxygen monitoring [61], [128], [143], [144]. Leal-Noval S *et al.* 2010, used the NIRS monitor INVOS 5100 (Medtronic, Minneapolis, USA) for non-invasive ipsilateral oxygen measurements and compared the measures with the Licox (Integra NeuroSciences, England) PbtO₂ catheter in 27 patients with TBI. The INVOS 5100 NIRS uses light at two different wavelengths (730 and 810 nm) to maximize the absorption contribution of oxygenated and deoxygenated haemoglobin while minimizing the absorption contribution of other compounds [155].

The continuous wave of near-Infrared light can penetrate several millimetres into cerebral tissue, travelling from the sensor's light-emitting diode to either a proximal or distal photodetector. The light detected by the distal photodetector travels deeper into the tissue, while the light collected by the proximal photodetector detects signals that only pass through the scalp. The signals from the distal and proximal photodetectors are then analysed in order to estimate the brain tissue oxygenation index (rSO₂) [144], [156].

Normal PbtO₂ is in the range of 35–50 mmHg, whereas ischaemic thresholds have been suggested between 5 and 20 mmHg, with values below 20 mmHg being associated with worse outcomes after TBI [37]. The implementation of NIRS had no significant results with a PbtO₂ ≤ 15 mmHg threshold based on the study by Leal-Noval S *et al.* But the rSO₂ accuracy improved when the PbtO₂ threshold was reduced to 12 mmHg, resulting in an area under the curve (AUC) of 0.82 with a sensitivity and specificity of 73% and 86%, respectively [144]. These results suggest that rSO₂ cannot estimate the early stages of hypoxia.

Likewise, Davies DJ *et al.* 2019, compared the OxiplexTS (ISS, Illinois, USA) with the Neurovent-PTO (Raumedic, Germany and Mills River, USA) in 16 patients diagnosed with TBI. The OxiplexTS is a non-invasive diagnostic tool using frequency-domain Near-Infrared Spectroscopy (FD-NIRS) [128]. Continuous-wave NIRS devices emit light into the target tissue at a constant intensity, whereas FD-NIRS continuously modulates this intensity [128]. Oxygenated and deoxygenated haemoglobin concentrations are determined from the measured intensity and phase shift, allowing the calculation of StO₂ or rSO₂ [155]. The results by Davies DJ *et al.* 2019 indicate that FD-NIRS does not provide enough reproducibility in its ability to estimate changes in PbtO₂ in order to replace the current invasive gold standard (fluorescence-quenching sensor or Clark electrodes placed in the cerebral cortex). Also, the OxiplexTS has almost the same estimative power seen in similar investigations utilising continuous-wave NIRS instruments [128].

Table 10: Description of the 12 included studies comparing non-invasive and invasive techniques for ICP or brain oxygenation monitoring in traumatic brain injury. The studies in bold text have been included in the metanalysis.

Author	Year	Country	Variable	N	Non-invasive commercial device	Non-invasive technique	Invasive technique	Mean age	Sex M/F	GCS	Follow time	Losses	Outcome	Value
Leal-Noval S <i>et al.</i> [144]	2010	Spain	Brain O ₂	27	INVOS 5100	NIRS	PbtO ₂ (Brain)	33.0	NR	6.0	16 h	5	AUC SE-SP (%)	0.82 73-86
Davies DJ <i>et al.</i> [128]	2019	UK	Brain O ₂	16	Oxiplex TS	FD-NIRS	PbtO ₂ (Brain)	50.5	NR	8.0	<30.5 h	4	AUC	Per patient
Rosenthal G <i>et al.</i> [143]	2014	Israel	Brain O ₂	18	CerOx 3110	UT-NIRS	SjvO ₂ (Jugular)	45.3	2.6	5.0	2 h/d	0	Correlation	0.6
Sokoloff C <i>et al.</i> [61]	2019	Canada	Brain O ₂	17	NR	MCA TCD	PbtO ₂ (Brain)	44.0	4.7	NR	5 d	0	Correlation SE-SP (%)	0.41 38-58
Soliman I <i>et al.</i> [145]	2018	Saudi Arabia	ICP	40	HD11XE	ONSD	Intraparenchymal catheter	37.0	2.6	4.5	48 h	0	Correlation	0.74
Martin M <i>et al.</i> [132]	2019	France	ICP	58	Vivid I	ONSD MCA TCD	Intraparenchymal catheter	36.5	5.8	6.0	24 h	4	AUC AUC	0.73 0.67
Rasulo F <i>et al.</i> [150]	2017	Italy	ICP	38	DWL	MCA TCD	Intraparenchymal or ventricular catheter	57.8	NR	NR	3h	0	AUC	0.96

Huang GD <i>et al.</i> [146]	2012	China	ICP	52	DWL	MCA TCD	Intraparenchymal catheter	37.0	4.8	7.0	5-7 d	0	Correlation	0.881
Gura M <i>et al.</i> [127]	2011	Turkey	ICP	52	DWL	MCA TCD	Intraparenchymal catheter	33.5	4.2	7.3	5 d	0	Correlation	0.779
Budohoski K <i>et al.</i> [147]	2012	UK	ICP	292	DWL	MCA TCD	Intraparenchymal catheter	33.0	NR	6.0	74.8 m	0	Correlation	0.510
Brandi G <i>et al.</i> [149]	2010	Switzerlan d	ICP	45	Sonoline G40	MCA TCD	ICP probe	37.0	4.6	NR	14 d	8	$\Delta \bar{x} \pm SD$	3.2 \pm 12.6
Melo J <i>et al.</i> [148]	2011	France	ICP	124	Waki 1-TC	MCA TCD	Intraparenchymal catheter	07.6	2.4	6.0	20 m	7	SE-SP (%)	94-41

The correlation values were not adjusted by confounders, because each study adjusted the coefficient by different variables. **Abbreviations:** Oxygenation (O₂), Intracranial Pressure (ICP), Frequency Domain Near-Infrared Spectroscopy (FD-NIRS), Frequency Domain Near-Infrared Spectroscopy (FD-NIRS), Near-Infrared Spectroscopy (NIRS), Arterio-jugular venous Oxygen (SjvO₂), Partial Pressure of Cerebral Oxygen (PbtO₂), Middle Cerebral Artery (MCA), Transcranial Doppler (TCD), Area Under the Curve (AUC), Sensibility and specificity (SE-SP), Mean difference($\Delta\bar{x}$), Standard deviation (SD), No reported (NR)

Meanwhile, Rosenthal G *et al.* 2014 compared the CerOx 3110 (Ornim Medical Ltd, Dedham, USA) with the Licox in 18 patients [143]. The CerOx 3110 uses Ultrasound Targeted NIRS principles (UT-NIRS), in which near-infrared light illuminates the tissue while brief pulses of ultrasound waves induce a local and artificial modulation in the detected light intensity. By adopting this method, the device can localise and select the signal originating from a specific volume of brain tissue [143]. The researchers found a significant and strong correlation between the UT-NIRS and the ipsilateral SjVO₂, even when the former was adjusted by multiple measurements, but PbtO₂ measurements were not significantly related [143].

The last paper included in the current review assessing brain oxygenation is from Sokoloff C *et al.* 2019, who also used the Licox, but in this case, the comparison was made with the mean ipsilateral flow velocity (V_{mean}) of the Middle Cerebral Arteries (MCA) assessed with a 2D Color-Coded Transcranial Doppler (TCD) in 17 patients [61]. The authors found a limit of 40 cm/s to correlate low CBF flow velocity in the MCA with brain hypoxia (PbtO₂ < 20 mmHg), which could be estimated during the first 7 hours of TBI. TCD's sensitivity and specificity diminish as the time after the trauma increases. Despite a statistically significant correlation between PbtO₂ and V_{mean}, this association does not seem to be clinically relevant, according to Sokoloff C *et al.* 2019 [61].

Eight of the twelve papers compared invasive and non-invasive techniques for ICP monitoring in TBI patients. The intraparenchymal catheter and ultrasound were the invasive and non-invasive techniques respectively used to measure the ICP in all the papers selected. Six papers used Transcranial Doppler (TCD), and two papers utilized the optic nerve sheath diameter (ONSD). TCD was used to measure relative changes in flow velocity in the basal arteries of the brain. Spectral analysis was then used to obtain the following parameters: peak systolic velocity (V_s), end-diastolic velocity (V_d), pulsatility index (PI), and time-averaged mean maximum velocity (V_{mean}) [123].

Four of the eight ICP-related papers included in this review utilized a DWL TCD transducer (Compumedics, Australia) for monitoring the blood flow in the MCA [127], [146], [147], [150]. Non-invasive ICP was estimated by Huang GD *et al.* 2012 and Rasulo F *et al.* 2017, based on mean arterial pressure (MAP) and assessing the proportion of the end-diastolic velocity and the mean flow velocity of both MCAs [146], [150]. Both papers concluded that non-invasive monitoring of cerebral hemodynamics might be used as an effective real-time ICP monitoring tool for TBI patients [146], [150]. Budohoski K *et al.* 2012, also used MCA blood flow and mean arterial pressure into a black-box plugin of ICM + software to estimate ICP non-invasively. This mathematical model showed an overall good correlation with the invasive measurements of ICP, with an optimal non-estimation cut-off in 17 mmHg [147]. Likewise, Gura M *et al.* 2011 used their own non-invasive ICP regression model from

the TCD-derived pulsatile index, finding a significant and strong correlation between PI and ICP in the first five days after trauma [127].

Compared to the studies described above, three more studies used different TCD probes. Martin M *et al.* 2019 used a 7.5 MHz Vivid I ultrasound probe (GE Healthcare, Boston, USA), Brandi G *et al.* 2010 utilized the Sonoline G40 (Siemens, San Jose, USA), whereas Melo J *et al.* employed the Waki 1-TC (Atys Medical, France). The authors calculated the pulsatile index multiple times ($PI = sV - dV/mV$) and compared those measurements with intraparenchymal ICP values [132], [148], [149]. Martin M *et al.* 2019 reported a PI that did not correlate with ICP (coefficient not reported) and an AUC of 0.67, defining a threshold for hypertension (>20 mmHg) on $PI > 1.4$ [49], [132]. Brandi G *et al.* 2010, used the Bellner equation [157] to calculate a non-invasive ICP value based on the pulsatile index, establishing a not significant difference of means between invasive and non-invasive measurements [149]. While Melo J *et al.* 2011 also looked for the accuracy of PI to identify ICP levels above 20 mmHg. Melo's paper considered an altered TCD when the end-diastolic velocity was less than 25 cm/s or when the PI was greater than 1.31. The thresholds above had excellent sensitivity but low specificity in identifying intracranial hypertension [148].

Two of the papers included in this review utilized the ONSD as a non-invasive measurement of ICP. As the dura matter contains cerebrospinal fluid and is contiguous to the optic nerve sheath, Soliman *et al.* 2018 used an HD11XE transducer (Philips, Amsterdam) to assess whether the ONSD was correlated with increases in invasive ICP values. Soliman *et al.*, found that ONSD was strongly correlated with invasively ICP monitoring, even when the estimation model was adjusted for sex and weight [145]. Likewise, Soliman's paper defined elevated ICP when the diameter was above 6.4 mm, resulting in good accuracy results for the cut-off value [145]. Similarly, Martin M *et al.* 2019 measured ONSD using a 7.5 MHz Vivid I probe and defined an intracranial hypertension parameter of 5.6 mm. Martin's paper also reports good accuracy results in estimating elevated ICP in the first 48 hours after TBI, with an area under the curve of 0.73 [132].

A meta-analysis for the brain oxygenation monitoring group was not completed due to significant methodologic heterogeneity between the included studies. The four papers of this subgroup used four different non-invasive techniques, which do not allow for a quantitative synthesis and comparison between their results [61], [128], [143], [144]. In contrast, mostly all the ICP papers are methodologically homogenous. However, a quantitative comparison between all of them was not feasible due to the different types of outcomes reported. Melo J *et al.* 2011 is the only evidence found in the current review that assessed paediatric patients (mean age = 7.6 ± 4.4 years) [148]. Only three of the eight papers, which made comparisons between techniques for ICP monitoring, are

methodologically homogenous and have comparable outcomes. The quantitative synthesis below put together this evidence through an exploratory meta-analysis to find a pool correlation coefficient. Huang GD *et al.* 2012, Gura M *et al.* 2011 and Budohoski K *et al.* 2012 reported the correlation between DWL and intraparenchymal probe for ICP monitoring in TBI patients [127], [146], [147].

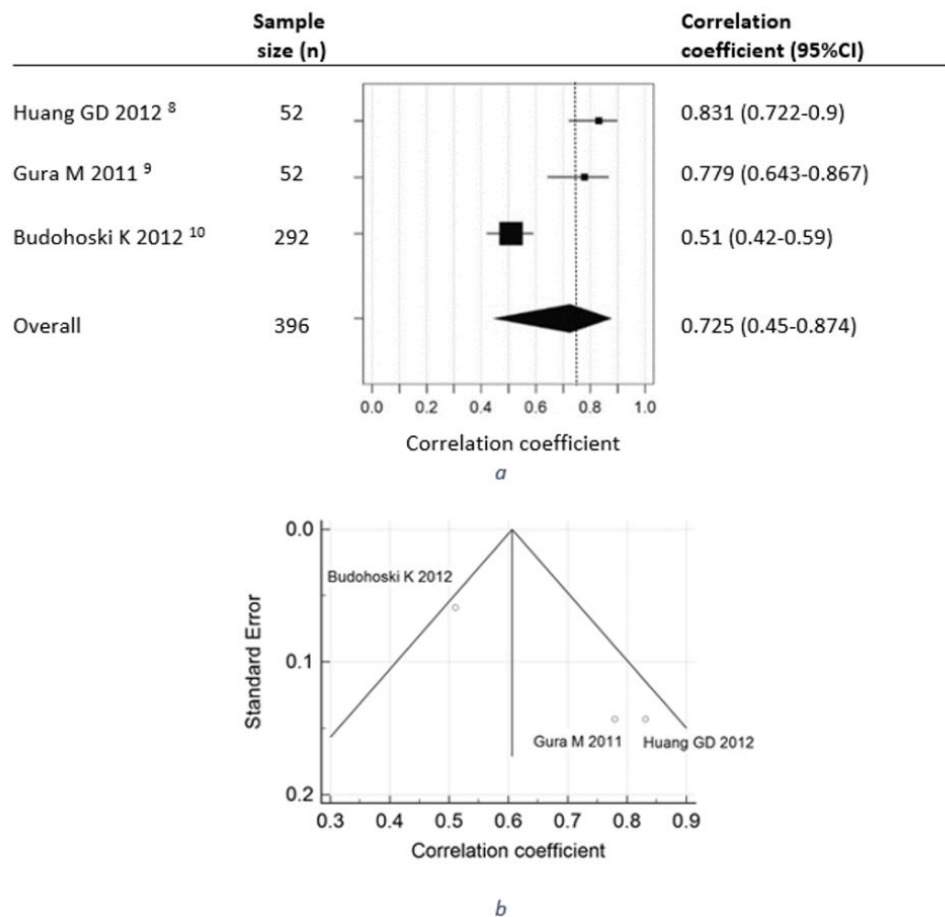


Figure 30: Forest plot (a) and funnel plot (b) for the correlation coefficients between non-invasive and invasive ICP monitoring in Huang *et al.*, Gura *et al.* and Budohoski *et al.* studies.

According to these three authors, blood pressure and flow velocities are the indirect non-invasive measurements required for ICP calculation. A total of 396 severe TBI patients within a mean age range of 33 to 37 years and a mean GCS below 7.3 were followed up for a maximum time period of 7 days. The meta-analyses results presented in Figure 30a show a pooled correlation coefficient of 0.725 (95% CI: 0.450 to 0.874; I^2 91.31%) corresponding to a random-effects analysis. A random-effects analysis was used due to the high statistical heterogeneity between studies (Figure 30a). According to this, a non-invasive ICP value based on blood pressure and MCA's flow velocities measured by transcranial Doppler significantly correlated with invasive ICP measurements ($p < 0.001$). Finally, the asymmetry in the funnel plot in Figure 30b indicates the heterogeneity induced by the study sizes and the outcomes. In Budohoski *et al.* 2012, the sample size was larger than the other two

studies by Huang GD *et al.* 2012, Gura M *et al.* 2011 (n=292 vs. n=52 for both Huang GD *et al.* 2012 and Gura M *et al.* 2011 respectively). In addition, the monitoring lasted for a shorter time, compared with the monitoring time of the other two studies, resulting in a smaller effect estimate and a higher standard error. As all studies fell within the triangular region, no subgroup analysis was required.

This systematic review identified Transcranial Doppler and Near-Infrared Spectroscopy as the main non-invasive techniques used currently to assess changes in intracranial pressure and brain oxygenation in TBI patients. Eight out of the twelve studies included in this review focused on the non-invasive measurement of ICP, indicating that this biomarker has attracted most of the interest in the last decade.

When compared to PbtO₂, Near Infrared spectroscopy showed low correlation and limited accuracy in detecting hypoxic events [128], [143], [144]. As suggested by Davies *et al.*, these results may be due to limitations of the technique in distinguishing the oxygenation of the different layers of tissue that are interrogated when shining near-infrared light transcutaneously [128]. Interestingly, it appears that ipsilateral measurement by ultrasound-targeted NIRS can provide a promising correlation with SjVO₂ [143]. However, there is still a need for more clarity on whether these results are due to the benefits of combining ultrasound and NIRS or on the reference measurements (i.e. SjVO₂ vs PbtO₂).

Transcranial Doppler was the technique mostly used to assess ICP non-invasively, where different algorithms have been developed to estimate ICP from TCD signals. The methods based on MAP changes in the features of the pulse signals seem to be the most robust in estimating ICP [146], [147], [150]. Compared to brain oxygenation, the analysis of the results for non-invasive ICP, either qualitative or quantitative, are simplified by the more standardised use of intraparenchymal ICP sensors as a reference measure. Although TCD has shown promising results, further efforts are needed to reduce the risks of bias, as the technique is heavily operator-dependent and mostly based on intermittent measurements.

The exploratory meta-analyses included with this systematic review allowed the synthesis of correlation results between invasive and non-invasive measurements of ICP. However, only three studies fit the inclusion criteria for a meta-analysis, and it was difficult to infer an exhaustive conclusion from this limited number of studies. All three papers investigated the measurement of ICP through TCD [127], [146], [147], while a meta-analysis on brain oxygenation techniques could not be performed due to methodological heterogeneity. Although the relatively small number of studies included, the results from the meta-analysis are in line with correlation values reported previously in similar reviews [32], [133]–[135]. Despite sharing similarities, these reviews cannot be fully compared with the current systematic review due to methodological differences.

The studies included in this systematic review presented a significant degree of heterogeneity, which decreased the overall comparability between the results. Understandably, this resulted in the inclusion of a very limited number of studies in the meta-analyses and the analysis of only one of the two biomarkers investigated (i.e. intracranial pressure). Therefore, it is vital to homogenize the research methods, with attention to the reported outcomes. Correlation and/or accuracy should be reported methodically, confounders controlled, reference measurements standardised, and length of monitoring defined.

All the studies in this review investigated populations of severe TBI patients only. Considering that brain oxygenation and ICP are often measured in this group of patients, this result is not surprising. However, most traumatic brain injuries are categorised as mild to moderate and future research on non-invasive techniques for brain oxygenation or ICP would greatly benefit these patients who often do not receive brain oxygenation or ICP monitoring [85].

The literature has indicated that there may be additional techniques that may be used to measure ICP non-invasively. Techniques such as tympanic membrane displacement or pulse phase lock loop may be adopted to measure ICP, but there is little or no evidence of their use in TBI patients. Only two studies included in this review used optical nerve sheath diameter measurements to assess ICP, but the results could not be quantitatively compared between them or to any other similar study. Also, imaging techniques were not included in this systematic review due to their intrinsic non-continuous nature.

Although this review was limited up to January 2020, additional papers in the topic have been released after the review was published. It has been of the authors interest the use of Diffuse Correlation Spectroscopy (DCS) to estimate ICP non-invasively. DCS is an optical technique that estimates blood flow in deep tissues, including the brain. It relies on the principles of diffuse optics and correlation spectroscopy. DCS works by analysing the fluctuations in the intensity of laser near-infrared light that has been scattered by moving red blood cells within the tissue. The degree of correlation and the decay rate of intensity fluctuations, determine the velocity of the moving red blood cells, thus it is used to measure the velocity of blood flow. When ICP increases, it can affect the cerebral blood flow, so alterations on the characteristics of these fluctuations can be associated with changes in ICP. The recent publications in the topic are discussed in detail on Chapter 12.

Including only studies published since 2010 has considerably restricted the number of studies analysed in this review. However, this criterion provided the added ability to focus on the results in the literature in line with the recent technological advancements of the last decade. A minimum monitoring window of 48 hours was set as one of the quality assessments in the screening of the

studies. Although the length of monitoring in such studies may be limited due to technological, logistical, clinical, or ethical restrictions, a long monitoring window allows the capture of variations in the parameters measured that would be likely missed by shorter monitoring windows. This will also play an important role in the range of changes measured, if any, and therefore provide a wider representation of correlation or accuracy in the population investigated.

5.4 SUMMARY

Two main technologies, Near-Infrared Spectroscopy (NIRS) and Transcranial Doppler (TCD) have been used in the last ten years in order to assess the accuracy or correlation between non-invasive and invasive techniques for brain oxygenation and intracranial pressure in TBI patients. The considerable variability in the methods and reported outcomes of the cohort studies assessed in this review did not offer robust conclusions on their monitoring capability. Nevertheless, a good correlation was found in the approach of non-invasive ICP monitoring through the assessment of the pulsatile index by Transcranial Doppler. This systematic review confirms that there is noticeable work to be done in the quest for non-invasive, continuous, portable, and multimodal monitoring of brain oxygenation and intracranial pressure in TBI patients.

Additionally, current evidence has shown that NIRS not only allows the assessment of brain tissue oxygenation and cerebral perfusion, but it has also been applied in the evaluation of cerebral autoregulation and intracellular metabolic state during the early post-traumatic period, as well as during neurorehabilitation [158]. This evidence suggests the hypothesis that NIRS might be the most promising non-invasive technology to develop a multimodal sensor for TBI monitoring, as it can investigate multiple parameters of cerebral haemodynamics. So far there has been no published evidence related to its application in ICP monitoring. In consequence, the first step to prove such a hypothesis is to rigorously investigate the utilisation of NIRS in TBI and provide a synthesis of the available evidence of the association between NIRS-based measurements and commonly monitored neurophysiological parameters, such as oxygenation and cerebral autoregulation.

6 NIRS IN OXYGENATION AND AUTOREGULATION ASSESSMENT FOR TBI

6.1 INTRODUCTION

Since 1977, when near-infrared spectroscopy (NIRS) was first described for monitoring cerebral perfusion and brain oxygenation [159], clinical interest in this optical technology has increased. Near-infrared (NIR) represents wavelengths within the range of 700 nm and 1000 nm, where the absorption contribution of chromophores, such as oxygenated and deoxygenated haemoglobin, is maximized, while the absorption contribution of other compounds, such as water molecules, is minimized. NIR light can penetrate bony structures and several millimetres into cerebral tissue, where according to the Beer-Lambert law, light absorption is directly proportional to the concentration of chromophores. The reflected light attenuation represents information regarding regional cerebral oxygen saturation (rSO_2) and the balance between oxygen delivery and oxygen consumption, making NIRS a very sensitive technology to changes in cerebral oxygenation [155]. Based on the aforementioned, NIRS could potentially address ideal neuromonitoring requirements, detect brain tissue at risk of secondary injury, and complement or even replace current invasive practices [158], [160].

This chapter was published on *Sensors* (DOI: 10.3390/s21051586) [120], and aimed to rigorously investigate the utilisation of NIRS in TBI and provide a synthesis of the available evidence of the association between NIRS-based measurements and commonly monitored neurophysiological parameters, such as oxygenation and cerebral autoregulation. So far, no review is known by the authors that synthesized multiple clinical applications of NIRS in TBI nor considered the different types of NIRS technologies in relation to TBI physiology. This synthesis highlights several factors that are important for future research, including literature trends, the comparison between NIRS measurements and validated neuromonitoring parameters and their relationship with brain physiological changes following trauma.

6.2 METHODOLOGY

PubMed, EMBASE, Web of Science, Scopus, and Cochrane library databases were used to search for literature that investigates the use of NIRS in TBI monitoring. As this review aims to describe every technological advancement of NIRS in TBI monitoring, the studies were included without time restriction. The search terms used were a combination of the terms “near-infrared spectroscopy,” “NIRS,” “TBI,” and “traumatic brain injury”, assessed on the title, abstract, and keywords. The database search yielded 139 results, seven of which were review papers. The references from these reviews were examined, resulting in 68 publications of interest for the current research. In total, the search resulted in 207 papers, 90 of which were duplicates and were removed. From the remaining

117 papers, 72 met the inclusion criteria and were included in the analysis. Papers were included in the review if they used NIRS in TBI monitoring and were written in English. Review articles, nonoriginal, nonindependent documents and animal studies were excluded (see Figure 31). It is recognized that a potential limitation of this review is the possibility of search engine bias. Only articles that were tagged with these terms were included, and therefore, qualifying articles may have been missed in the search.



Figure 31: Flowchart of the methodology used to include 72 out of 207 studies published until July 2020.

Demographics, study characteristics, and outcome measures were extracted from the selected articles and compiled in an electronic database. Data fields included bibliographic data, sample size, patients' characteristics, NIRS application, outcome measures, limitations, and conclusions. Papers were classified into five categories according to NIRS applications: diagnosis, prognosis, treatment, correlation, and comparison between NIRS technologies capacities. The diagnosis group was also

subdivided into subgroups relating to the outcome measured: oxygenation, autoregulation, hematomas, and neurorehabilitation. Oxygenation, autoregulation, and hematoma monitoring are relevant during TBI's "golden hour", while neurorehabilitation monitoring usually takes place some months after injury. Moreover, oxygenation and autoregulation monitoring utilize similar NIRS sensors and algorithms, while hematoma monitoring involves multiple NIRS sensors and a specific algorithm for hematoma detection. Thus, this review examined the main applications of NIRS for TBI monitoring, and it presents a thorough revision of those applications on oxygenation and autoregulation for TBI patients' diagnosis.

6.3 RESULTS

6.3.1 Search Results

The literature search returned 72 scientific publications that met the inclusion criteria, all of which were included in the general analysis of NIRS application in TBI monitoring. To gain a better understanding of the trends and geographical distribution of the included papers, the data were analysed by year and country as well as by NIRS applications and outcomes measured. The distribution of the published literature by country indicates that the United States of America (USA) provided the most significant contribution in the field with 28 publications, followed by the United Kingdom (UK) with 14 publications, as shown in Figure 32. With the USA as the front runner in terms of volume of research, it is recommended that other countries continue or increase their investigations in this field, given the substantial impact of TBI on mortality and disability rates [96]. This recommendation is also justified by the fact that 80% of the incident cases per year are from low and middle-income countries [91], while most of the scientific contribution is from high-income countries. As this research intended to describe the characteristics and advantages of NIRS in TBI monitoring for its future use across various populations, ideally, NIRS should be assessed across individuals of various ethnic backgrounds from around the world.

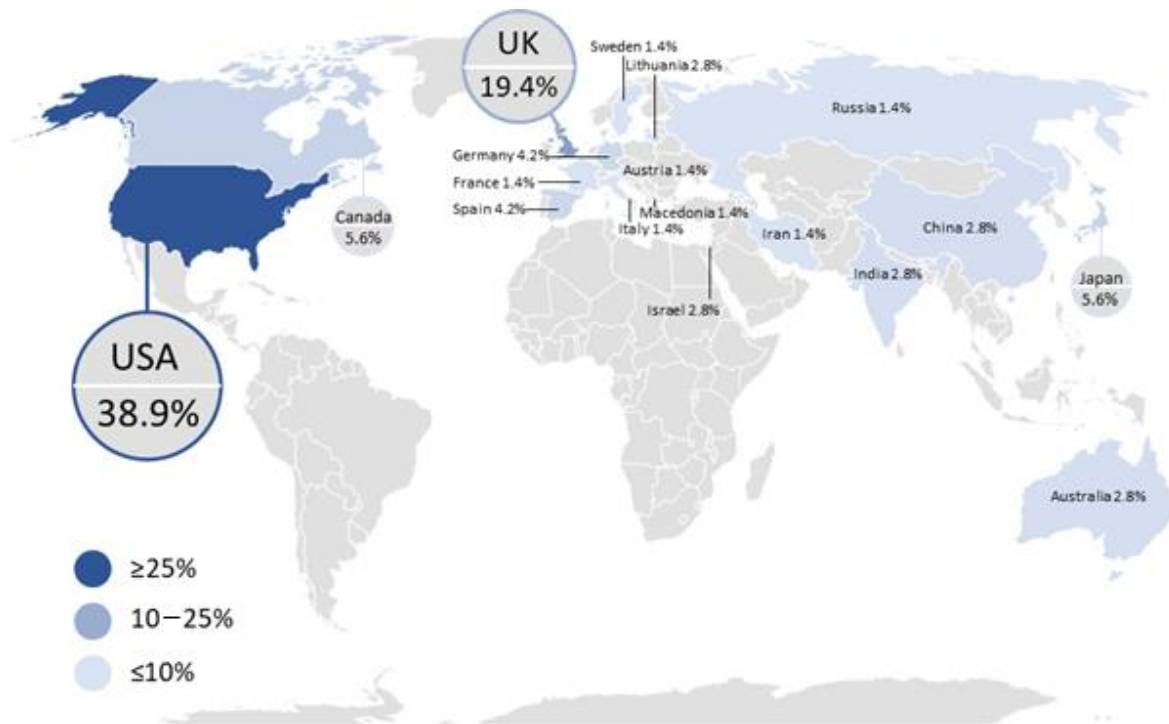


Figure 32: Global distribution of scientific articles

Articles that discussed the use of near-infrared spectroscopy (NIRS) technology in traumatic brain injury (TBI) monitoring until July 2020. The number of publications per country is indicated by the intensity of the colour, with darker colours representing a higher number of articles than lighter colours.

Until July 2020, the number of papers published that have used NIRS in TBI monitoring experienced a downward trend. The largest amount of publications on the topic was in 2014. However, since 2003, other applications in addition to diagnosis have been reported (Figure 3). In total, 46 (64%) publications were found that used NIRS as a diagnostic tool in TBI monitoring. Figure 4 shows the percentage of diagnosis papers per subgroup. The outcome of neurorehabilitation is mainly related to prefrontal cortex features. All the prognosis papers ($n = 18$) assessed patients' neurorehabilitation using NIRS; however, there was just one diagnosis publication where NIRS was used to identify regions within the prefrontal cortex that contributed to distinguishing between TBI and healthy subjects [161]. Likewise, 18 studies were included that explored NIRS accuracy for hematoma detection after trauma. Hematoma detection using NIRS technology is based on differential light absorption of the left versus the right side of the brain [162]–[164]. Brain absorption is symmetrical under normal circumstances, and when extravascular blood is present due to a hematoma, the reflected component of light is significantly lower [162]–[164]. The absorption differential can be detected via NIRS units placed over symmetrical locations on both sites of the head [162]–[164]. Neurorehabilitation and hematomas monitoring are relevant outcomes in TBI monitoring; however, the current research presents a thorough revision of NIRS applications on oxygenation and autoregulation due to the relevance of those outcomes in TBI's "golden hour" and their technological similarities [165], [166].

NIRS APPLICATIONS IN TBI MONITORING

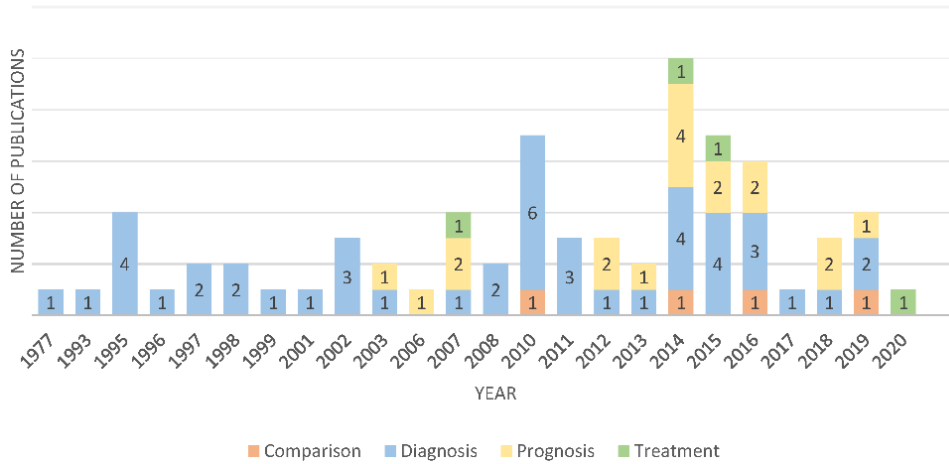


Figure 33: Number of publications per year associating TBI with the various types of NIRS applications.

DIAGNOSIS STUDIES OUTCOMES

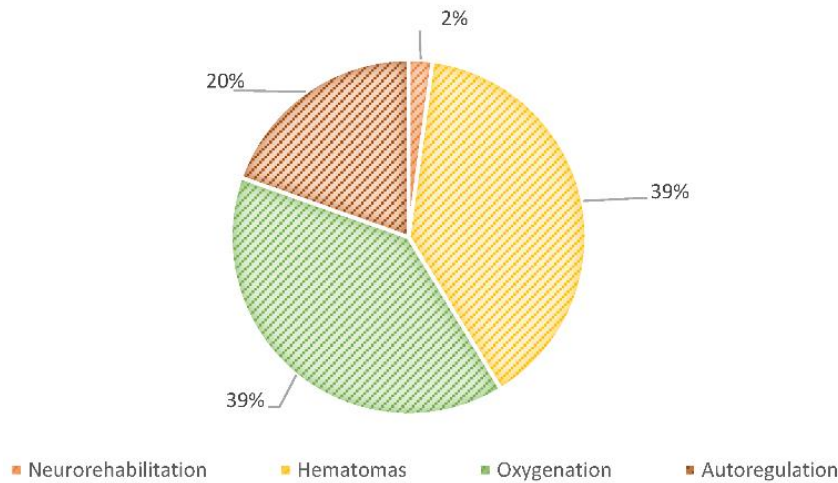


Figure 34: Percentage of diagnosis papers per subgroup according to the outcome measured: oxygenation, autoregulation, hematomas, and neurorehabilitation monitoring.

6.3.2 Physical and Technological Description of NIRS

As mentioned in previous chapters, red blood cells (RBC) contain a protein with a high gas-binding capacity called haemoglobin, which allows oxygen transport [155], [167]. When gas exchange takes place in the lungs, each haemoglobin binds to four oxygen molecules. Then, RBCs carry this oxyhaemoglobin (HbO₂) through the arteries to the tissues, where oxygen is delivered through a process known as oxygen perfusion. Although some oxygen can still be bound to haemoglobin, when it has released most of the oxygen molecules (deoxyhaemoglobin HHb), it can collect part of the CO₂ discharged by the tissues. Finally, CO₂ is transported in venous blood and is released into the lungs, where it is expelled by exhalation [21], [22].

Arterial blood, rich in O₂, has a bright red colour, while venous blood colour is dark red due to its poor O₂ content. This physical property is used by near-infrared spectroscopy (NIRS), as explained below [21]. Near-infrared (NIR) light is absorbed to different degrees by the chromophores, oxyhaemoglobin, deoxyhaemoglobin, and cytochrome-c-oxidase, at wavelengths near 700–1300 nm [168]. Within this range, light has low absorption and high scattering properties, causing the light to go deeper into the tissue, therefore enabling real-time noninvasive monitoring of brain tissue oxygen saturation [21]. NIRS uses the different absorption properties of these chromophores to quantify their concentrations in tissues [169]. NIRS bases its principles on the Beer-Lambert law, which correlates the absorption of light passing through the tissue to the absorption coefficient ($\mu_a = \epsilon \cdot c$) and the pathlength (l) travelled by light (Equation 14) [170].

$$A = \ln \frac{I_0}{I} = \epsilon \times c \times l$$

Equation 14: Beer-Lambert law

where A is light attenuation, also known as optical density, I is transmitted light intensity, I_0 is incidence light intensity, ϵ is the tissue's extinction coefficient (Figure 35a), c is chromophore concentration, and l is the distance travelled by light in the tissue on the assumption that light only undergoes absorption [171].

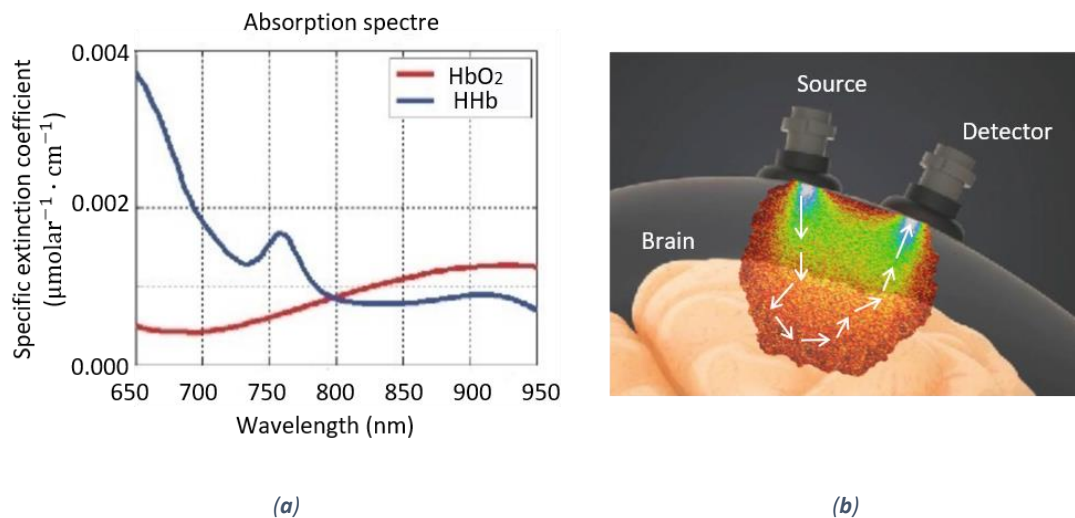


Figure 35: Light tissue interaction

(a) Absorption coefficient spectra of oxyhaemoglobin (HbO₂) and deoxyhaemoglobin (HHb). (b) The probabilistic trajectory of photons from the source to a detector of incident near-infrared light is described as a "banana shape" [172]. Figure modified from [173].

When the tissue contains multiple chromophores, total light attenuation (A) can be defined as the linear sum of the contribution of each chromophore's concentration. Thus, the tissue is illuminated with as many wavelengths as chromophores are being assessed. The result is a system of equations with the specific purpose of calculating the concentrations of HbO₂ and HHb by NIRS [174]:

$$A_{\lambda_1} = \left(\varepsilon_{\text{HbO}_2\lambda_1} \times [\text{HbO}_2] + \varepsilon_{\text{HHb}\lambda_1} \times [\text{HHb}] \right) \times l$$

$$A_{\lambda_2} = \left(\varepsilon_{\text{HbO}_2\lambda_2} \times [\text{HbO}_2] + \varepsilon_{\text{HHb}\lambda_2} \times [\text{HHb}] \right) \times l$$

Equation 15: System of equations with the specific purpose of calculating the concentrations of HbO₂ and HHb by NIRS

In Equation 15, λ_1 and λ_2 are two different wavelengths. However, this assumption is not entirely valid in tissues, where near-infrared light attenuation (A) is highly dominated by scattering (roughly 80% scattering vs 20% absorption) [171]. Scattering in tissue causes an increase in the path length travelled by light, as well as the loss of scattered light because it cannot reach the detector (Figure 35b). The modified Beer-Lambert law considers the effects of scattering in tissues [171]–[175], where the distance travelled by light (l) is replaced by the product of the differential path factor (DPF) and the separation distance (d) between the sensor's emitter and detector [175], as is shown in Equation 16. The DPF is the increase in the light's path length due to scattering, where this coefficient depends on the wavelength, tissue type, and emitter detector distance [172]. Finally, the modified Beer-Lambert law adds the factor G, or scattering coefficient (μ_s), to the equation, which represents both the nature and the geometry of the tissue [175]. Assuming that DPF and d remain constant during the measuring period and d and DPF are known, quantitative data on changes in the concentration of chromophores can be derived.

$$\Delta A_{\lambda} = \left(\varepsilon_{1\lambda} \times \Delta[C_1] + \varepsilon_{2\lambda} \times \Delta[C_2] + \dots \varepsilon_{n\lambda} \times \Delta[C_n] \right) \times d \times \text{DPF} + G$$

Equation 16: modified Beer-Lambert law

Considering this, the changes in concentration of these chromophores can be separately identified (but not quantified) from measurements of ΔA . Nonetheless, later in this thesis, it will be explained how the further combination of several detectors housed in a single probe allowed the calculation of chromophores' relative concentrations, leading to one major parameter of interest in perfusion analysis known as tissue oxygen saturation index (rSO₂) or tissue oxygenation index (TOI). This parameter represents the percentage of oxygenated haemoglobin in the sample volume [176], and it is expressed as the percentage of oxygenated haemoglobin relative to total haemoglobin [177], as is shown in Equation 17.

$$\frac{k[\text{HbO}_2]}{k[\text{HbO}_2] + k[\text{HHb}]} \times 100\%$$

Equation 17: rSO₂ and TOI are expressed as percentages of oxygenated haemoglobin relative to total haemoglobin

Finally, NIRS cannot discriminate between arterial blood, capillaries, and venous blood. Consequently, oxygen saturation measured by NIRS represents a mixed saturation between arterial and venous blood. This measure is predominantly from venous oxygenation, as approximately 75% of cerebral

blood is venous [60]. The above explains why NIRS measurements are always lower than arterial oxygen saturation measured by pulse oximetry (SpO_2), which assesses only arterial blood by utilizing the pulsatile arterial component of the signal [171].

6.3.3 NIRS Measurement Techniques

Four measurement techniques have been developed since NIRS was invented. All of them aim to quantify HbO_2 and HHb concentration by applying different measurement principles [170], as shown in Figure 36.

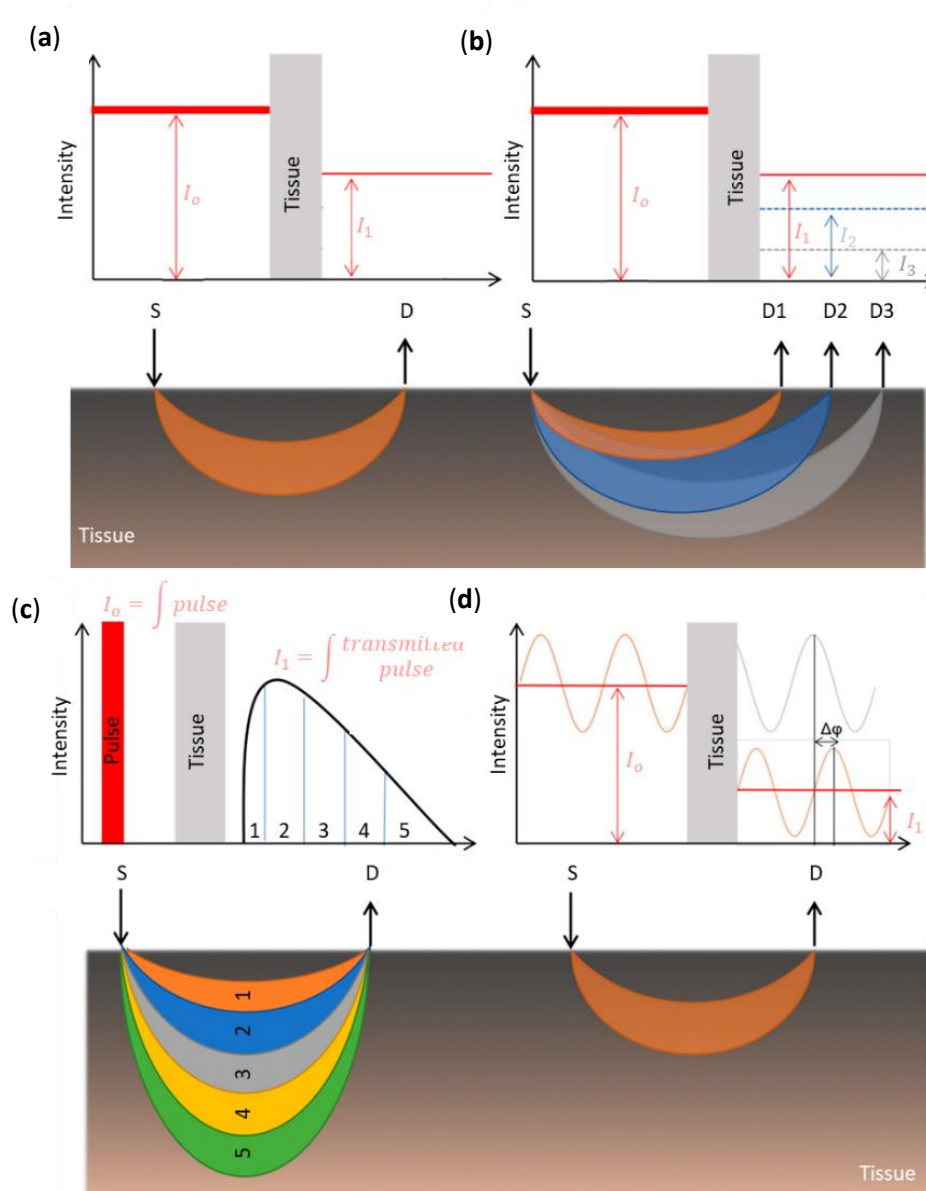


Figure 36: Schematic diagram of NIRS detection modes.

(a) Continuous-wave NIRS (CW-NIRS), (b) spatially resolved spectroscopy (SRS), (c) time-resolved spectroscopy (TD-NIRS), and (d) phase-modulated spectroscopy (PMS). The figure also shows a representation of the photon path in tissues for each technique. S: source, D: detector. (Figure modified from [178]).

In continuous wave NIRS (CW-NIRS), as the name suggests, the light of constant intensity is “injected” into the tissue, and then the attenuated light signal is measured at a distance from the light source (Figure 36a). This technique assumes that HbO₂ and HHb are the only absorbers in tissue. It also assumes that scattering is constant during the entire measurement ($\Delta G = 0$), and DPF is considered to be between one-half and one-third of the actual emitter–detector separation distance. In consequence, the modified Beer-Lambert law (MBL) is used to calculate the change in chromophore concentrations [169], [172], [179], [180]. However, CW-NIRS presents major challenges; for instance, it is only fit to do oxygenation trend monitoring. Also, it does not consider any superficial layer contamination from the brain signal, taking into account that the brain is covered by multiple layers which are perfused by vessels that carry haemoglobin, leading to extracerebral signals that play a contaminating role on CW-NIRS [181].

Spatially resolved spectroscopy (SRS) is based on the measurement of light attenuation at several source-detector separations (Figure 36b), where relative concentrations of HbO₂ and HHb can be calculated by solving the diffusion equation as a function of the photodetectors’ distance [170], [175], [182], [183]. This method enhances the contribution of deeper tissues (S-D2 or S-D3) while reducing the contribution of more superficial tissues (S-D1). These are the most significant advantages of the SRS design over the MBL algorithm when using CW-NIRS. The math behind SRS is explained in a further chapter where the technique was implemented. On the other hand, time-resolved spectroscopy mode (TD-NIRS) uses short light pulses to illuminate the tissue, where the scattered photons take more time to be detected than the unscattered photons (Figure 36c). Average photons’ arrival time allows the calculation of the light path length, therefore enabling the calculation of the chromophores’ absolute concentrations by solving the diffusion equation [170], [175], [179], [180]. In phase-modulated spectroscopy (PMS), the emitted light is modulated in frequency and intensity; thus, measured attenuations and frequency shifts are used to estimate the light path length and the absorption and scattering properties of the tissue (Figure 36d). Once these are derived, at least from two wavelengths, absolute concentrations of HbO₂ and HHb can be calculated from the modified Beer-Lambert law [170], [175], [179], [180].

6.3.4 Subgroups

The previous sections described the principles of NIRS. Many clinical and research applications using NIRS in TBI monitoring have been reported in the last 40 years. This section provides an overview of its application in oxygenation and autoregulation monitoring for TBI diagnosis, considering different types of NIRS technologies and TBI’s physiology.

6.3.4.1 Oxygenation

6.3.4.1.1 Summary of the Evidence on NIRS-Derived Oxygenation in TBI

The literature search returned 18 scientific publications that assessed NIRS-derived oxygenation in TBI patients. Table 11 summarizes the main characteristics of the methodology and results presented in each paper. The documents were sorted chronologically, as shown in the author's column and year of publication. Moreover, sample size (n) is reported with the proportion of males and females (m:f) included in the studies. Table 1 also includes the type of NIRS devices used, the manufacturer, and the main technical specifications. Additionally, all the comparisons between the NIRS output and the control measurements were extracted from the papers. In four cases, the comparison was between the outcome of the basal condition and after an intervention (i.e., hyperventilation, MAP changes). Finally, the main conclusion of each author is shown in the last column of the table.

Table 11: Summary of the evidence on NIRS-derived oxygenation in TBI.

Author, Year	N (m:f)	Device (Type)	Output	Control	Conclusion
(Jöbsis, 1977) [167]	1 (1:0)	Inhouse NIRS, non commercial (CW; S-D 13.3 cm)	Photon count	Paired measure: hyperventilati on	Oxygen sufficiency can be monitored noninvasively.
(Tateishi et al., 1995) [184]	9 (9:0)	NIRO-500, Hamamatsu Photonics, Hamamatsu, Japan. (CW; S-D 4 cm)	HbO ₂	SjvO ₂	Cerebral HbO ₂ magnitude and direction, measured by NIRS, were similar to changes in invasive measurements of SjvO ₂ .
(Kirkpatrick et al., 1995) [185]	14 (12:2)	NIRO 1000, Hamamatsu Photonics U.K. Ltd., Enfield, UK. (CW; S-D 6 cm)	HbO ₂	CPP, ICP and CBF SjvO ₂	A close correlation between NIRS signals and intracranial parameters strengthens the belief that the observed chromophore concentration changes are derived primarily from cerebral tissues.
(Lewis et al., 1996) [186]	10 (6:4)	INVOS 3100, Medtronic, Minneapolis, MN, USA. (SRS; S-D 3&4 cm)	rSO ₂	SjvO ₂	Tissue oxygen saturation determined by near-infrared spectroscopy does not reflect significant changes in cerebral oxygenation detected by the global

					measurement of jugular venous bulb oximetry.
(Kampfl et al., 1997) [187]	8 (5:3)	INVOS 3100A, Medtronic, Minneapolis, MN, USA. (SRS; S-D 3&4 cm)	rSO ₂	ICP	rSO ₂ values in patients with an ICP > 25 mmHg were significantly lower than in patients with an ICP < 25 mmHg after the hyperoxygenation period.
(Kerr et al., 1998) [188]	28 (25:3)	INVOS 3100A, Medtronic, Minneapolis, MN, USA. (SRS; S-D 3&4 cm)	rSO ₂	SaO ₂ , SjvO ₂ , extracranial SO ₂	rSO ₂ index represented a summation of a differential weighting of SaO ₂ (20%), SjvO ₂ (75%), and extracranial O ₂ saturation (5%).
(Ter Minassian et al., 1999) [189]	9 (NR)	INVOS 3100, Medtronic, MN, USA. (SRS; S-D 3&4 cm)	rSO ₂	SjvO ₂	rSO ₂ assessed by NIRS does not adequately reflect changes in SjvO ₂ in patients with severe head injury.
(Cheng et al., 2002) [190]	9 (7:2)	CCD detector system, noncommercial John Wright, UK. (CW; S-D 3.5 cm)	HbO ₂ oscillations	NR	The presence of oscillations at 0.013–0.033, 0.11, and 0.19–0.28 Hz are compatible with B-waves, vasomotion, and respiratory cycles, respectively.
(Brawanski et al., 2002) [191]	12 (11:1)	INVOS 3100, Medtronic, Minneapolis, MN, USA. (SRS; S-D 3&4 cm)	rSO ₂	PbtO ₂	rSO ₂ and PbtO ₂ contain similar information from a mathematical point of view.
(McLeod et al., 2003) [192]	8 (8:0)	NIRO 300, Hamamatsu Photonics, Hamamatsu City, Japan. (SRS; S-D 4 cm)	TOI	SjO ₂ and PbtO ₂	Altering the fraction of inspired oxygen changes significantly with each variable measured of cerebral oxygenation. Each variable represents a different physiologic process.
(Kim et al., 2010) [193]	8 (5:3)	Inhouse, noncommercial (CW; S-D 2.5 cm)	DCS and HbO ₂	XeCT	Significant moderate correlations between DCS measurements of relative CBF and NIRS measurements of delta HbO ₂ were demonstrated.

(Leal-Noval et al., 2010) [144]	22 (NR)	INVOS 5100, Medtronics Inc., MI, USA. (CW; NR)	rSO ₂	PbtO ₂	PbtO ₂ and rSO ₂ were directly and significantly related. However, the diagnostic accuracy of rSO ₂ was limited; therefore, that measurement by NIRS should not be considered to be an acceptable substitute for PbtO ₂ .
(Tachtsidis et al., 2011) [194]	6 (5:1)	Broadband NIRS, noncommercial (CW; S-D 3.5 cm)	oxCCO	Paired measure: hypercapnia	Despite the increase in total HbO ₂ in all patients, only four of the six patients showed an increase in the oxidation states.
(Ghosh et al., 2013) [195]	10 (3:7)	Inhouse, noncommercial (SRS; S-D 3.5 cm)	oxCCO	Paired measure: normobaric hyperoxia	Optical measurement of chromophore concentration in the injured brain is not confounded by changes in optical scattering or path length.
(Rosenthal et al., 2014) [143]	18 (13:5)	CerOx 3110, Ornim Medical Ltd. Dedham, MA, USA. (UT-NIRS; NR)	rSO ₂	SjO ₂ PbtO ₂	The correlation between UT-NIRS measurements and SjvO ₂ indicates that the CerOx may be able to provide a noninvasive estimation of cerebral oxygenation status in brain-injured patients. However, rSO ₂ was not correlated with PbtO ₂ .
(Vilke et al., 2014) [196]	61 (42:19)	INVOS, Medtronics Inc., MI, USA. (SRS; NR)	rSO ₂	Mortality	rSO ₂ values were determined as a strong discriminator and estimator of hospital mortality. When rSO ₂ < 68.0% in the left hemisphere HR = 17.7.
(Durnev et al., 2017) [197]	15 (10:5)	INVOS 5100, Medtronics Inc., MI, USA. (CW; NR)	rSO ₂	Paired measure: changes on MAP	NIRS signals of cerebral hypo-oxygenation reacted first to MAP changes.
(Davies et al., 2019) [128]	16 (9:3)	Oxiplex TS, ISS, IL, USA. (PMS; NR)	rSO ₂	PbtO ₂	A clear estimative relationship between NIRS and invasively

measured PbtO₂ has been established. However, FD enhances NIRS device tested did not demonstrate sufficient reproducibility in its ability to estimate changes in PbtO₂ to replace the current invasive gold standard.

Abbreviations: regional tissue oxygen saturation (rSO₂), haemoglobin concentration (HbO₂), jugular bulb venous saturation (SjO₂), cerebral perfusion pressure (CPP), intracranial pressure (ICP), cerebral blood flow (CBF), arterial oxygenation (SaO₂), brain tissue oxygen tension (PbtO₂), diffuse correlation spectroscopy (DCS), xenon-enhanced computed tomography (XeCT), mean arterial pressure (MAP), hazard ratio (HR), frequency domain (FD), near-infrared spectroscopy (NIRS), cytochrome-c-oxidase concentration (oxCCO), continuous wave modified Beer–Lamber law (CW), spatially resolved spectroscopy (SRS), phase-modulated spectroscopy (PMS), ultrasound-tagged near-infrared spectroscopy (UT-NIRS), source-detector distance (S-D), not reported (NR).

6.3.4.1.2 Sample Size and Patient Demographics

This review identified 17 publications spanning between 1995 and 2019 where NIRS was used for oxygenation monitoring in TBI patients. The only publication that was included in this review without meeting the inclusion criteria was Jöbsis publication. This exception was made due to Jöbsis's pioneering work being the first approach to NIRS application in vivo, which demonstrated that oxygen sufficiency could be monitored noninvasively using NIR light [167]. Moreover, Figure 37 shows that 75% of the studies had a sample size smaller than 15 patients, which is a limitation in the results of almost all these publications. Likewise, it was not surprising that in 15 of the 16 papers that included the sex ratio, the number of men was significantly higher than the number of women. Literature has always reported a proportion of males greater than that of females [97], where men have more than double the risk of TBI than women [91]. Finally, the mean or midrange age (grey line) was stated in 16/18 papers; therefore, a weighted average of 43.4 years was calculated (yellow line). Interestingly, all studies included mostly middle-aged people who are at risk of suffering severe TBI but can also be rapidly stabilized in intensive care.

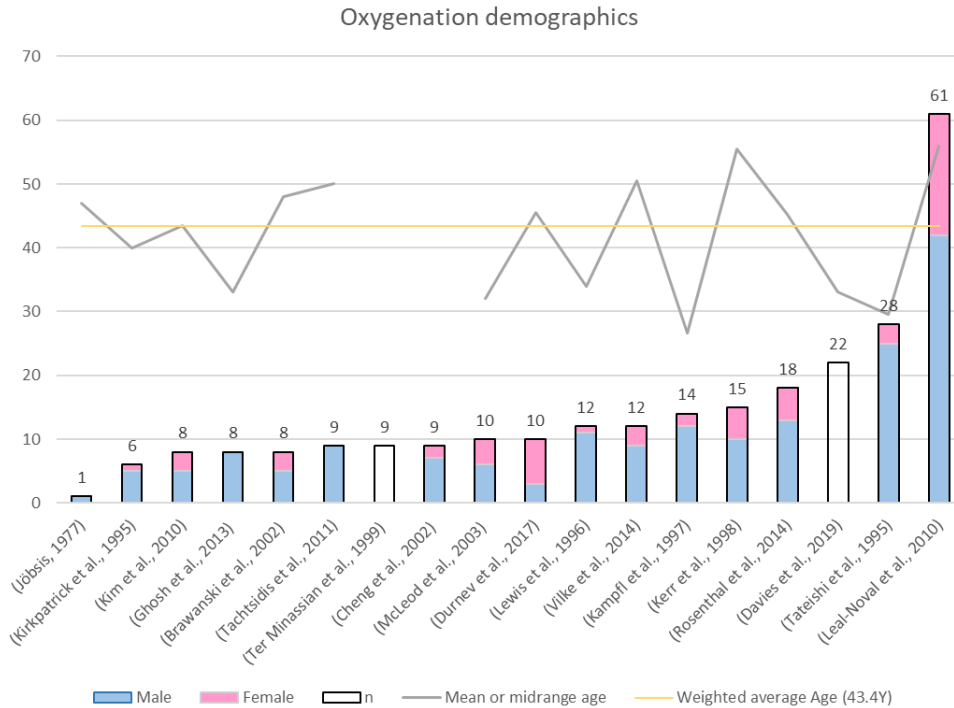


Figure 37: Demographics of the evidence on NIRS-derived oxygenation in TBI.

6.3.4.1.3 Distribution of NIRS Techniques

Figure 38 shows the distribution of NIRS techniques used for oxygenation monitoring in TBI patients. As it was expected, the most-used technique was continuous wave (CW) NIRS, analysed by either the modified Beer-Lambert law or spatially resolved spectroscopy (SRS) algorithms. The latter considered source-detector (S-D) distances between 2.5 and 6 cm in reflectance mode. Jöbbsis is the only author who utilized transmission mode with an S-D distance of 13.3 cm. Time-resolved spectroscopy has not been reported in TBI monitoring yet, as nowadays, this technique is mainly used in research laboratories [173]. Davies et al. reported the only paper included in this review, which compared phase-modulated spectroscopy with the invasive measurement of brain tissue oxygenation tension [128]. Finally, Rosenthal et al. used a novel technique called ultrasound-tagged near-infrared spectroscopy (UT-NIRS), which is a hybrid technology that induces an artificial modulation in the detected light intensity by applying ultrasound waves. In this manner, only light from a specific volume of brain tissue is selected for analysis [143].

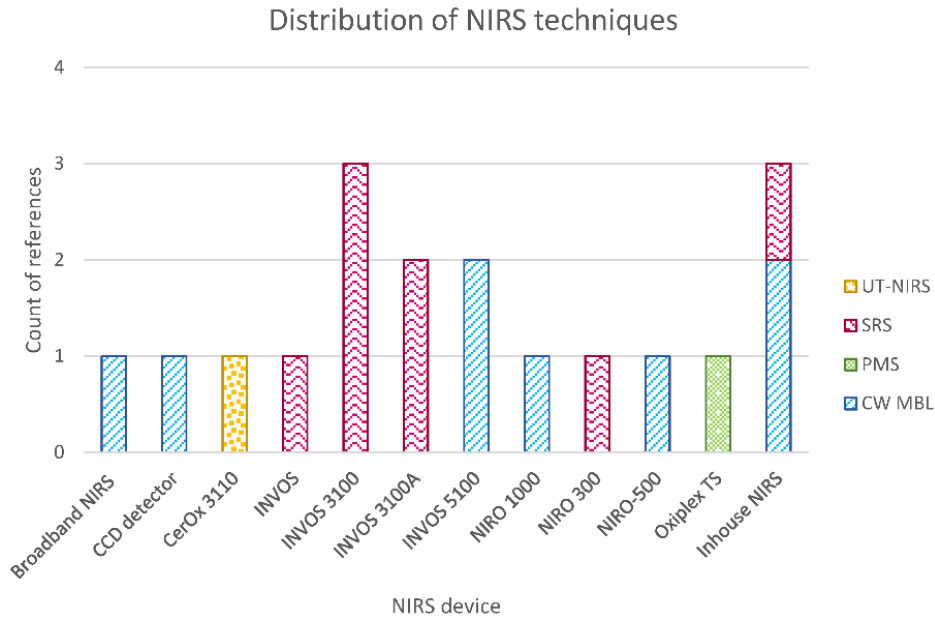


Figure 38: Distribution of NIRS techniques used for oxygenation monitoring in TBI patients. Where continuous-wave modified Beer–Lambert law (CW MBL), spatially resolved spectroscopy (SRS), phase-modulated spectroscopy (PMS), and ultrasound-tagged near-infrared spectroscopy (UT-NIRS).

6.3.4.1.4 Appropriate Clinical Comparable Parameters

Different comparisons have been made in the last few years to assess the capability of NIRS in oxygenation monitoring. Primarily, five papers have compared NIRS-derived measurements before and after an intervention. Jöbsis compared the number of photons detected by the photodetector at different stages of hyperventilation [167], while Tachtsidis et al. and Ghosh et al. assessed the variations in oxidized–reduced cytochrome c oxidase (oxCCO) concentration before and after changing PaCO₂ and FiO₂, respectively [194], [195]. Likewise, Durnev et al. correlated rSO₂ with changes in MAP, while Cheng et al. assessed the signal oscillations present in haemoglobin concentration [190], [197]. The distribution of these paired measurements is shown in light blue in Figure 39.

On the other hand, independent comparisons were found between the NIRS-dependent outcome and a group of physiological variables. In these evaluations, each variable of the control group was not compared with NIRS outcome directly. In Kirkpatrick’s paper, ICP, CPP, and relative CBF changes were not compared individually with haemoglobin concentration, yet it was reported that NIRS only registered obvious changes when the control group varied [185]. Similarly, McLeod et al. did not assess the correlation between TOI and invasive measurements; however, by altering the fraction of inspired oxygen, each cerebral oxygenation variable changed significantly [192]. Furthermore, Kerr et al. used a regression model to define rSO₂ as a function of the control variables SaO₂, S_{jv}O₂, and extracranial SO₂. The coefficients in this model were the weights of each control variable adjusted by all the parameters included in the regression [188].

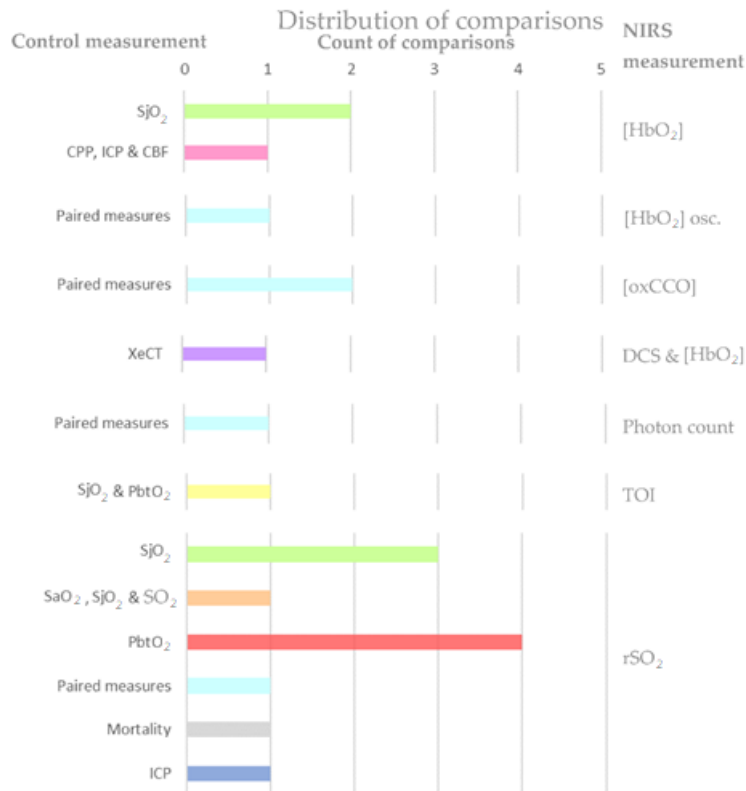


Figure 39: Comparisons found in the evidence on NIRS-derived oxygenation in TBI.

Finally, independent comparisons were reported between NIRS measurements and reference variables such as SjvO₂, PbtO₂, ICP, or XeCT. The latter was only used by Kim et al. to examine the correlations between changes in NIRS parameters and changes in CBF, determined by XeCT [193]. Another specific comparison that was reported only in one paper was made by Kampfl et al., who evaluated rSO₂ values in patients with high and low ICP (threshold = 25 mmHg) after hyperoxygenation [187]. Conversely, invasive oxygenation parameters SjvO₂ and PbtO₂ were widely used as reference variables or gold standard measurements. Both variables' distributions are shown in Figure 39 in green and red, respectively. Jugular venous oxygen saturation monitoring using a fiberoptic catheter is the method that is currently accepted as a technique for continuous measurement of cerebral oxygenation [58], [184]–[186], [189]. However, it entails technical difficulties, including a relatively small amount of time for collecting good quality data and the need for frequent recalibrations [143]. Also, as NIRS measurements represent the average value of arterial, capillary, and venous blood, there can be a difference in the time course of oxy- and deoxyhaemoglobin from that in SjvO₂ [62]. On the other hand, PbtO₂ is not yet an accepted gold standard technique for cerebral monitoring, although some studies used it as such [58], [144], [191], [198]. Simultaneous comparison of PbtO₂ and rSO₂ is problematic, as each monitor utilizes a distinct physical principle and measures a distinct physiological parameter [144].

6.3.4.2 Autoregulation

6.3.4.2.1 Summary of the Evidence on NIRS-derived Autoregulation in TBI

The literature search returned nine scientific publications that assessed NIRS-derived autoregulation in TBI patients. Table 2 summarizes the relevant data extracted from each document. The papers were sorted chronologically by publication year, as presented in the first column of the table, along with the author. Moreover, sample size (n) is reported with the proportion of males and females (m:f) included in the studies. Column three of Table 12 includes the NIRS devices used, the manufacturer, and some technical specifications in brackets. Furthermore, NIRS outputs and control measurements are shown in columns four and five. Only in one case the comparison was between TBI patients and healthy control volunteers. Finally, the main conclusion of each paper is shown in the last column of the table.

Table 12: Summary of the evidence on NIRS-derived autoregulation in TBI

Author, Year	N (m:f)	Device (Type)	Output	Control	Conclusion
(Adelson et al., 1998) [199]	10 (6:4)	INV03100A, Medtronic, MN, USA and NIRO500, Hamamatsu Photonics, Hamamatsu, Japan. (SRS and CW respectively; S-D NR)	THb, HbO ₂ , Hb, and rSO ₂	CPP, MAP, ICP and PaCO ₂	High ICP and decreased CPP correlated with increased THb and HbO ₂ , indicating raised CBV and hyperemia. MAP was not associative. NIRS positively estimated cerebral oxygen desaturations with hyperventilation.
(Dunham et al., 2002) [200]	4 (3:1)	INVOS 4100, Medtronic, MN, USA. (SRS; S-D NR)	rSO ₂	CPP, MAP, ICP	Cerebral oximetry correlated significantly with CPP. As such, it could be an adjunct to CPP management.
(Zweifel et al., 2010) [201]	40 (31:9)	NIRO 200, Hamamatsu Photonics U.K. Ltd., Hertfordshire, UK. (SRS; S-D NR)	THx	PRx	THx showed a significant correlation with the validated volume reactivity index PRx.
(Shafer et al., 2010) [202]	22 (10:12)	INVOS 5100, Medtronic, MN, USA. (CW; S-D NR)	rSO ₂	XeCT	The relationship between either the left or right NIRS values and Xe/CT scan was not significant.
(Diedler et al., 2011) [203]	37 (NR)	NIRO 200, Hamamatsu Photonics U.K. Ltd., Hertfordshire, UK.	THx	PRx	The agreement between PRx and THx is a function of the power of slow oscillations in the input signals.

		(SRS; S-D NR)			
(Taussky et al., 2012) [204]	8 (2:6)	Bifrontal NIRS optodes, Casmed, Branford, CT, USA. (CW; S-D 4.5 cm)	rSO ₂	CBF	CT perfusion CBF has a significant linear correlation with NIRS derived rSO ₂ .
(Kim et al., 2014) [205]	10 (7:3)	Inhouse, DCS and NIRS system, Noncommercial. (SRS; S-D 2.5 cm)	CBF, ΔHbO ₂ , ΔHb and ΔTHb in 10 TBI patients	CBF, ΔHbO ₂ , ΔHb and THb in 10 healthy controls	HbO ₂ , Hb, and THb concentration increased significantly in the brain-injured cohort with head-of-bed lowering. Accordingly, DCS/NIRS hybrid device is well-suited to provide non-invasive, continuous hemodynamic monitoring.
(Highton et al., 2015) [206]	27 (13:14)	NIRO 100, Hamamatsu Photonics U.K. Ltd., Hertfordshire, UK. (SRS; S-D 4 cm)	THx, TOx	PRx, Mx	Significant agreement among PRx and THx, and between Mx and TOx. However, the strength of the interrelationship between ICP or TCD and NIRS signals, THI or rSO ₂ , limits the degree of agreement between these reactivity indices.
(Bindra et al., 2015) [207]	19 (12:7)	ForeSight, Casmed, Connecticut, USA. (CW; S-D NR)	nTOx	iTOx	nTOx from Finometer photoplethysmography and NIRS gives a similar measurement of cerebrovascular autoregulation to iTOx.

Abbreviations: regional tissue oxygen saturation (rSO₂), oxyhaemoglobin concentration (HbO₂), total haemoglobin concentration (THb), deoxyhaemoglobin concentration (Hb), concentration change (Δ), cerebral perfusion pressure (CPP), intracranial pressure (ICP), cerebral blood flow (CBF), partial pressures of arterial carbon dioxide (PaCO₂), xenon-enhanced computed tomography (XeCT), mean arterial pressure (MAP), pressure reactivity index (PRx), total haemoglobin reactivity index (THx), tissue oxygen reactivity index (TOx), mean velocity index (Mx), noninvasive tissue oxygen reactivity index (nTOx), invasive tissue oxygen reactivity index (iTOx), near-infrared spectroscopy (NIRS), continuous wave modified Beer-Lambert law (CW), spatially resolved spectroscopy (SRS), source-detector distance (S-D), not reported (NR).

6.3.4.2.2 Sample Size and Patient Demographics

This review identified nine documents spanning between 1998 and 2015 where NIRS was used for autoregulation monitoring in TBI patients. Figure 40 shows that only 25% of the studies had a sample size larger than 27 patients, which is a limitation in the results of almost all these publications. As aforementioned, men are at more than double the risk of TBI than women [91], which agrees with the weighted average of the sex ratios (m/f = 1.9). Finally, the mean or midrange age is presented in Figure 12 with a grey colour line. One outlier in the age dataset can be noticed in the figure, and this is because this study by Adelson et al. assessed TBI pediatric patients [199]. Therefore, the age median is 46 years, and its interquartile range is between 34 and 56 years. Interestingly, all studies included mostly middle-aged people who are at risk of suffering severe TBI but can also be rapidly stabilized in intensive care.

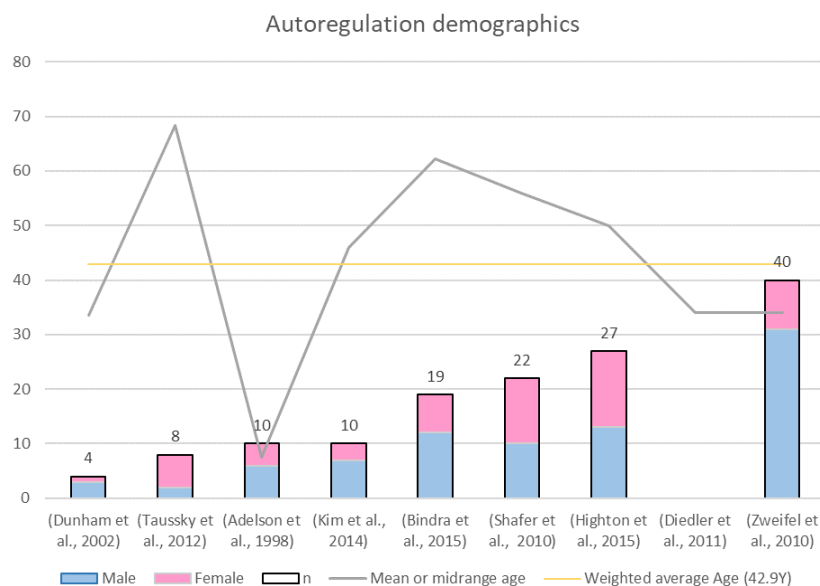


Figure 40: Demographics of the evidence on NIRS-derived autoregulation in TBI.

6.3.4.2.3 Distribution of NIRS Techniques

Figure 41 shows the distribution of NIRS techniques used for autoregulation monitoring in TBI patients. Similarly, with the studies on oxygenation, the two most used techniques for autoregulation assessment were continuous wave (CW) NIRS and spatially resolved spectroscopy (SRS). Only three papers reported the source-detector (S-D) distance, having values between 2.5 and 4.5 cm in reflectance mode [204]–[206]. The following three brands were repetitively used in cerebral autoregulation papers: NIRO monitor from Hamamatsu Photonics, INVOS system from Medtronic, and ForeSight Oximeter from Casmed. However, the device model changed between authors. An in-house hybrid system was used in one of the included publications. Kim et al. presented a custom-built device containing both diffuse correlation spectroscopy (DCS) and NIRS. DCS is a novel optical technique for probing continuous changes in regional microvascular blood flow, while NIRS was used for

oxygenation parameters' changes. Together, both techniques were used to detect differences in cerebral hemodynamic responses of brain-injured patients to posture change [205].

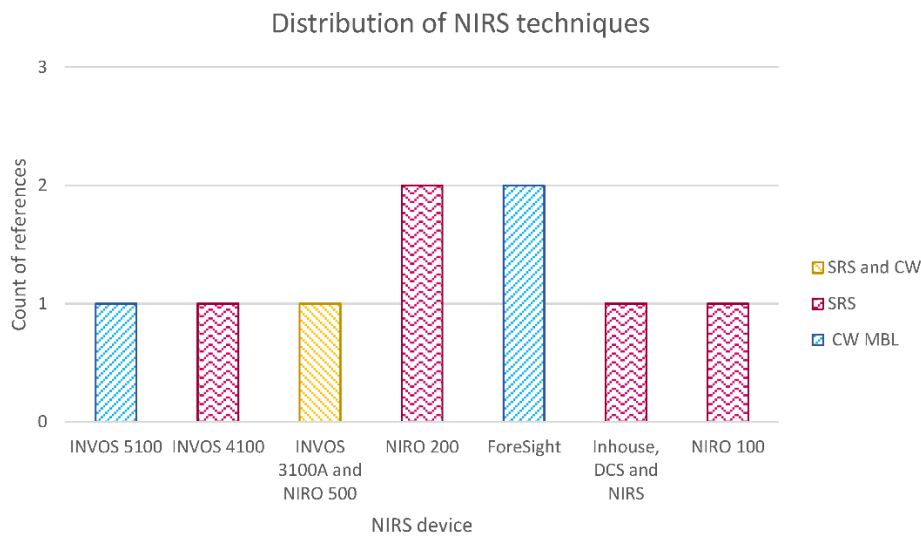


Figure 41: Distribution of NIRS techniques used for autoregulation monitoring in TBI patients.

6.3.4.2.4 Appropriate Clinical Comparable Parameter

This section presents the different comparisons found in the literature to assess the capability of NIRS in cerebral autoregulation monitoring. Comparisons are divided into three types: (1) When NIRS-derived values are associated with physiological measurements, (2) when the comparable clinical parameter is an index, and (3) when TBI patients are compared to healthy controls. The latest relates specifically to Kim's paper, where two cohorts were exposed to postural changes in order to identify whether a noninvasive in-house system is able to detect CBF and haemoglobin changes (orange bar of Figure 42) [205].

In the first type are the comparisons made between NIRS variables, such as rSO_2 or the concentration of different forms of haemoglobin, and physiological parameters that are measured invasively or through tomographic images. As was explained in the section "Physiology of Autoregulation in TBI", the main variables involved in cerebral autoregulation are CBF, CPP, MAP $PaCO_2$, and ICP. In consequence, it is not surprising that some authors aim to associate NIRS outcomes with these comparators [199], [200], [202], [204].

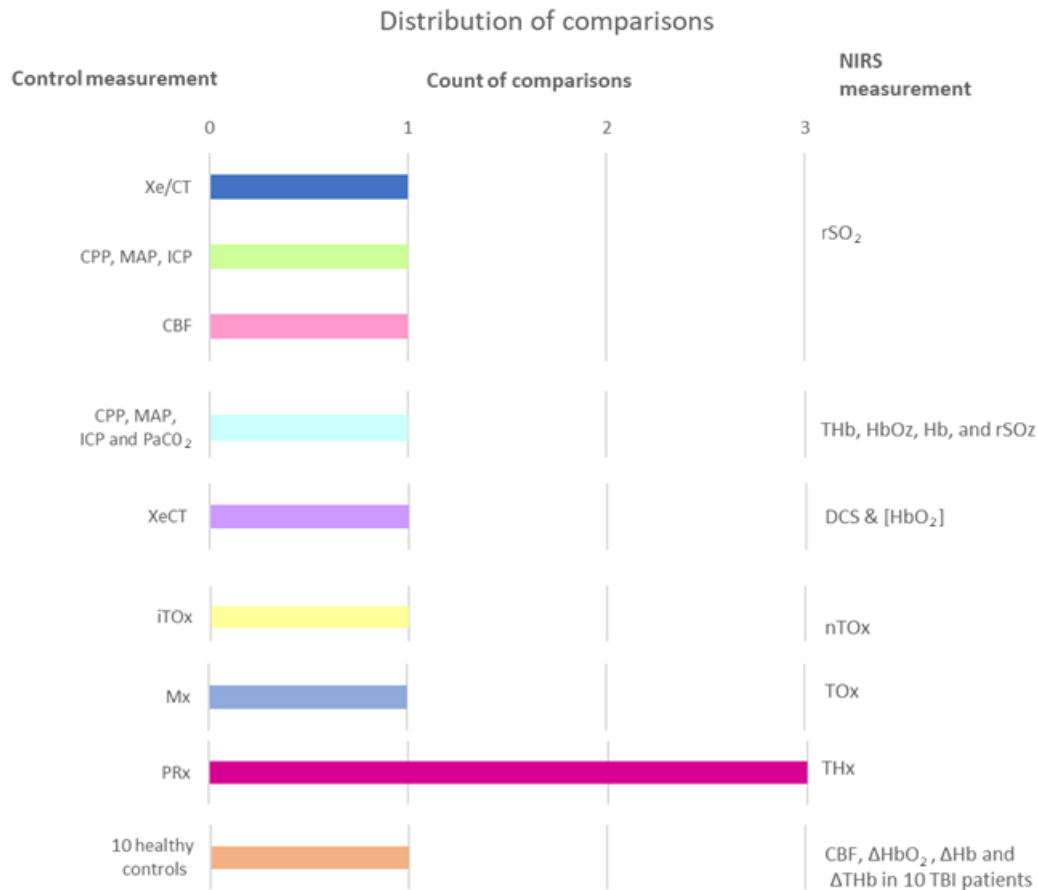


Figure 42: Comparisons found in the evidence on NIRS-derived autoregulation in TBI.

In the second type, the comparisons are made between invasive and noninvasive indexes. The most frequent observation is between pressure reactivity index (PRx) and its noninvasive analogous total haemoglobin reactivity index (THx), as is shown by the fuchsia column in Figure 42 [201], [203], [206]. The pressure reactivity index is defined as the moving correlation between MAP and ICP. When cerebrovascular reactivity is impaired, intracranial volume (ICV) and ICP increase and decrease passively with MAP. Thus, a negative value for PRx, when ICP is inversely correlated with MAP, indicates normal reactivity, and a positive value indicates impaired autoregulation Figure 42 [201], [206]. Likewise, THx is calculated as the moving correlation between the total haemoglobin index ($\text{THI} = [\text{HbO}_2] + [\text{HHb}]$) and arterial blood pressure (ABP) [203].

Other comparisons between indexes were presented by Highton et al., who compared the mean velocity index (Mx) with the tissue oxygen reactivity index (TOx). Interestingly, both indexes are obtained using noninvasive techniques. For instance, Mx is derived from transcranial Doppler-measured flow velocity and ABP, while TOx is the correlation between NIRS-derived rSO₂ and ABP. However, arterial blood pressure was measured invasively using a 20-G radial cannula and a transducer placed at the level of the tragus [206]. Unlike Highton's study, Brinda et al. compared tissue

oxygen reactivity indexes calculated as the moving correlation coefficient between invasive ABP and rSO₂ (iT_{Ox}), and the moving correlation coefficient between noninvasive ABP and rSO₂ (nT_{Ox}). The latter used a Finometer photoplethysmograph (Finometer pro, Finapres Medical Systems, Netherlands) for noninvasive arterial blood pressure monitoring [207].

6.3.5 Overall

The results presented in this review provide readers with a comprehensive summary of the technological advancements in the field of NIRS for TBI monitoring. This analysis not only considered applications for TBI, but also investigated the use of NIRS in different patients' demographics, and described the most-used techniques and testing comparable clinical parameters.

Figure 43 summarizes the final conclusions from all reviewed papers on the suitability of NIRS in monitoring oxygenation or autoregulation in TBI patients. Positive results are defined as results where the comparison between NIRS and gold standard techniques yielded high correlations or agreements, and negative results where such correlations were not high. Figure 15 provides a general representation of the results presented by each author, despite the heterogeneity in their hypothesis, methods, and outcomes. Additionally, the chart depicts the risk of publication bias, where papers with positive results are more likely to be published by indexed journals than those which rejected their hypothesis.

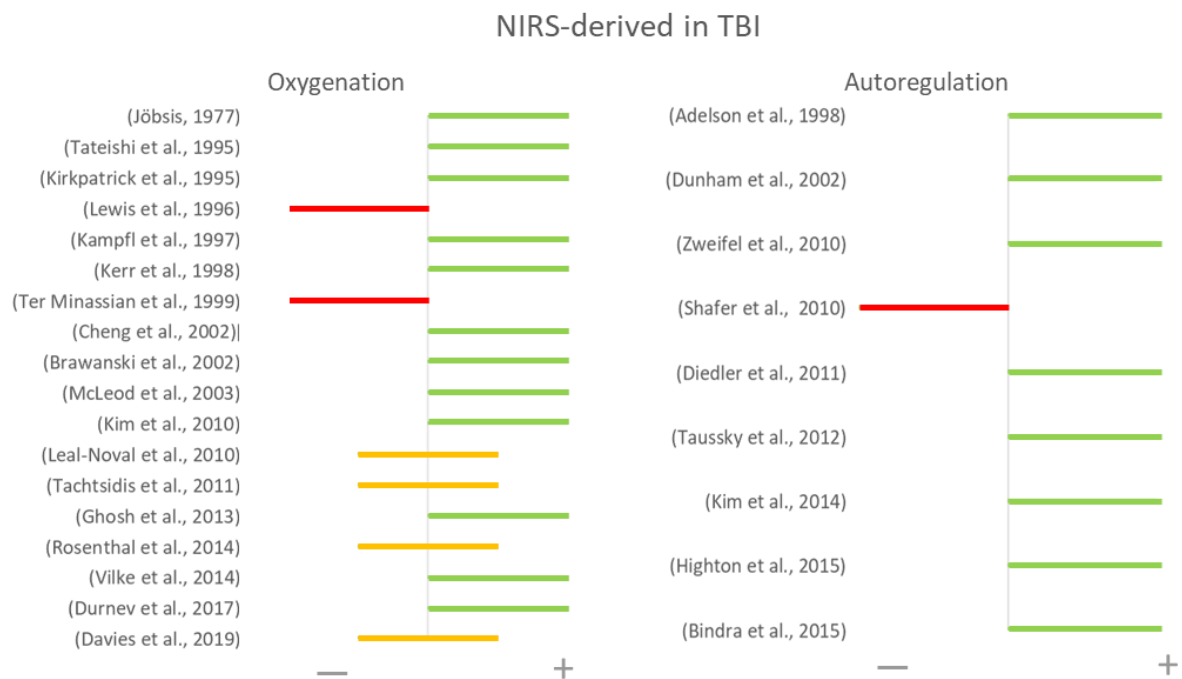


Figure 43: Main conclusions of NIRS-derived monitoring in TBI. Each author concluded with positive (green) or negative (red) statements. In a few cases, the authors reported positive results with some limitations (yellow).

Regarding the application of NIRS in oxygenation monitoring, patients' samples were homogeneous among the evidence. However, there is still a lot of variation in NIRS techniques and the reference measurements, which decreased the overall comparability between the results. Technical parameters such as the algorithm used within NIRS, wavelengths, and source-detector(s) separation differ between the commercially available devices, making it difficult to draw robust comparisons between them. All the papers which assessed paired oxygenation measurements reported positive results, which can be considered as a significant change in NIRS signals before and after an intervention (change on MAP, hyperoxia, hypercapnia, etc.). The interventions aim to disrupt normal cerebral hemodynamics, so significant changes in NIRS outcomes strengthen the belief that these are derived primarily from cerebral tissues and are highly correlated with brain hemodynamic changes [167], [190], [194], [195], [197]. For example, papers related to oxCCO monitoring reported that changes in concentration during normobaric hyperoxia represent an actual increase in mitochondrial aerobic metabolism [194], [195]. On the other hand, in those cases where NIRS-derived oxygenation parameters were compared with variables that are not directly related to oxygenation, such as ICP, CBF or mortality, the authors also reported positive findings [143], [187], [206]. For instance, rSO_2 values in intracranial hypertensive patients were significantly lower than in nonhypertensive patients [187]. Likewise, DCS cerebral blood flow measurements had a moderate correlation with rSO_2 [205]. Finally, rsO_2 was more accurate in discriminating and estimating hospital mortality than the traditional clinical parameters [196].

Conversely, studies that compared NIRS measurements with invasive oxygenation monitoring techniques, such as SjO_2 and $PbtO_2$, had heterogeneous results. Haemoglobin concentration measured by NIRS was correlated with SjO_2 [184], [185]. It was found that NIRS detected visible changes in the chromophores levels when desaturation events occurred, even with twice the sensitivity of $SjvO_2$, which might be explained by the fact that $SjvO_2$ sensitivity is affected by the venous blood that is drained from the sinuses to the jugular veins [185]. Nonetheless, the agreement between regional tissue oxygen saturation and $SjvO_2$ was significant in only a few papers [143], [186], [189], [192]. Similarly, rSO_2 and $PbtO_2$ contain similar information from a mathematical point of view, but NIRS outcomes have not demonstrated enough reproducibility in its ability to estimate changes in $PbtO_2$ in order to replace this invasive measurement [128], [144], [191]. The technological heterogeneity between the papers due to the use of CW-MBL or SRS may explain the contradictory nature of the data.

On the other hand, papers that used NIRS in autoregulation monitoring generally reported positive conclusions despite the various methodological and technological limitations of NIRS. For instance, some papers where NIRS-derived values were compared with physiological measurements found

significant correlations. Dunham et al. reported an association between rSO_2 levels above 75% and $CPP \geq 70$ mmHg, while Taussky et al. found a correlation between pairs of values of rSO_2 and CBF [200], [204]. However, Shafer et al. reported no significant correlation between the above relationship and mentioned that an expansion of the study to a greater number of patients might uncover such a relationship [202]. It is interesting that both authors Taussky et al. ($n = 8$) and Shafer et al. ($n = 22$) compared rSO_2 measurements with CT-derived CBF and had such conflicting results. However, these conflicting results might be due to methodological heterogeneities, including differences in the NIRS devices used [202], [204]. The last type 1 comparison (when NIRS-derived values are associated with physiological measurements) showed that during hyperventilation, ICP, CPP, and $PaCO_2$ correlated with total haemoglobin concentration measured by NIRS. As it is known, during hyperventilation, decreased $PaCO_2$ results in cerebral oxygen desaturation, regardless of ICP levels. Then, NIRS positively estimated cerebral oxygen desaturation and indicated increased total haemoglobin (relative CBV) [199]. These results are encouraging, suggesting that NIRS can be used as a noninvasive monitoring method for the earlier recognition and subsequent treatment of TBI secondary insults.

Likewise, the agreement between indexes was assessed successfully by several authors [201], [203], [206], [207]. Most of these papers used the NIRO systems from Hamamatsu Photonics and reported significant a correlation between THx and PRx [201], [206]. Diedler et al. suggested that this agreement is a function of the power of slow oscillations in the input signals [203]. Moreover, Highton also found significant agreement between the TOx-NIRS index and Mx-TCD index [206]. However, THx and TOx were not completely noninvasive indexes, as they depended on the continuous invasive monitoring of MAP [201], [206]. In order to respond to this limitation, Bindra et al. calculated MAP using a Finometer photoplethysmography system and found similarities between partially invasive TOx and completely noninvasive TOx [207]. Likewise, Kim et al. tested their hybrid DCS/NIRS instrumentation in TBI patients and healthy controls [206]. The aforementioned paper suggested that future studies in cerebral autoregulation should use multimodal monitoring combining NIRS analysis of indexes, such as THx and TOx.

There is still a need for more research in NIRS-derived monitoring in TBI patients. Current results are limited due to the small number of subjects evaluated. Studies with a representative sample size are needed in order to have inferable results in the TBI population. Despite the positive results that NIRS showed in these research studies, there is still more work to be done in comprehensively evaluating NIRS in order to be established as a reliable and routine monitoring technique in TBI. Considering that brain oxygenation and autoregulation are often measured in severe TBI patients, it is not surprising that the studies included in this review investigated populations of severe TBI patients only. However, most traumatic brain injuries are categorized as mild to moderate, and future research on NIRS

application would greatly benefit these patients who often do not receive brain oxygenation or autoregulation monitoring [85].

Moreover, high metrological heterogeneity decreased the possibility of an overall conclusion, even between studies that utilized the same NIRS technique. Also, it is important to define a valid clinical comparable parameter that reflects tissue brain oxygenation and autoregulation, as the current invasive references utilize distinct physical principles and measure distinct physiological parameters. For instance, SjO_2 and $PbtO_2$ techniques provide complementary information reflecting different aspects of the cerebral oxygenation cascade, but do not represent the regional tissue oxygen saturation. Likewise, a standardized clinical comparable parameter for autoregulation monitoring in neuro-critical care centres is still missing, which may be due to the lack of dedicated autoregulation monitors [72].

Additionally, the global outcome measures were not uniform across all studies, therefore, for future purposes of quantitative synthesis of the evidence, it is recommended that the authors report Bland–Altman analysis. It is a simple and accurate way to assess the agreement between two clinical variables and may help clinicians to compare a new measurement method against a standard reference [208]. Table 13 summarizes some strengths and limitations of this technology as reported in the papers included in this review. The limitations presented below are highly related to the lack of standardization of NIRS devices and some to patient-related factors.

The main strength of this review is that it presents a synthesis of NIRS applications specifically for TBI patient monitoring. Additional challenges are related to measuring light tissue interaction changes after TBI, due to alterations in the pathophysiological process and damage in post-traumatic tissue. The latter makes it difficult to extrapolate NIRS results in normal tissue to TBI patients with the possible presence of extracranial blood, subdural air, haemorrhages, cerebral oedema, and some other clinical scenarios. However, TBI as an inclusion criterion restricted the number of studies included in this review. Likewise, no attempts were made to identify or translate non-English language publications, and this may have limited the inclusion of some relevant studies in this review. Also, publication bias may have occurred because only peer-reviewed literature was included, and public health reports on NIRS monitoring in TBI may be available in the grey literature. However, these criteria provided the added ability to focus on the results in the literature in line with NIRS technological advancements in TBI monitoring.

Table 13: Strengths and limitations of NIRS-derived oxygenation in TBI.

STRENGTHS OF NIRS

- Effective transmission of nir light in biological tissue allows non-invasive monitoring of cerebral Hbo₂ and HHb, blood volume, the redox state of cytochrome, and thereby cerebral oxygen sufficiency [167].
- Near-infrared spectroscopy findings demonstrated visible changes in Hbo₂ and HHb levels in approximately twice as many desaturation events as those registered with Sjvo₂ monitoring [185].
- The close correlation between NIRS signals and those derived from known intracranial parameters strengthens the belief that the observed chromophore concentration changes are derived primarily from cerebral tissues [185].
- NIRS may be a valuable tool in the detection of impaired microcirculation and/or local brain tissue oxygenation in patients with increased intracerebral pressure, which may not be detectable employing monitoring of CPP, blood gas analysis, and TCD velocities [187].
- The rStO₂ index provides an easy, noninvasive method to measure decrements in oxygen delivery or utilization of O₂ within the brain [188].
- NIRS provides a clinically accessible, continuous, and noninvasive measurement of cerebral hemodynamics and therefore has considerable potential as a noninvasive monitor of cerebral autoregulation [206].

LIMITATIONS OF NIRS

- Penetration of light is limited to several centimetres in-depth, and the precise sampling volume and site of measurement are not fully clear [184].
 - Haemoglobin in vessels of superficial structures may add extracerebral signals, hence adding interference to CW-NIRS measurements [184].
 - Bulky, sensitive to variations in room temperature, and exquisitely sensitive to outside light [185].
 - The signals also display drift and are sensitive to movement artefacts [185].
 - Alterations in cerebral blood flow and metabolism following severe head injury are heterogeneous, and regional differences measured by NIRS may not be reflected by a global measurement such as jugular venous bulb oximetry [186].
 - The rSO₂ index reflects a regional measure, while the jugular venous gas analysis is global [188].
 - The pathlength factor and the depth concerning head swelling following trauma make the site of measurement and the volume sample ambiguous [188].
 - The cerebral signal could be contaminated by a reflected signal from extracerebral structures (e.g., bone, muscle) with unestimateable partition and O₂ saturation characteristics [189].
 - The clinical use of NIRS remains limited by potential sources of error that include contamination of the signal by the extracerebral circulation (principally the scalp), extraneous light, and the presence of extravascular blood [192].
-

-
- Hematomas may prevent sufficient photon transmission through the cortex due to excessive absorption by the concentrated blood [193].
 - Oedema directly beneath the optical probes may also prevent signal detection when light absorption is high [193].
 - In NIRS studies, many severe TBI patients are excluded from data analysis because of intra- and extracranial problems [144].
 - Other patient-related factors affecting the NIRS-derived values include patient agitation, skin conditions (burn, infection, or scar), brain malformation, polycythemia, and subcutaneous fat [209].
-

6.4 SUMMARY

This review is a synthesis of the characteristics and advantages of NIRS use in TBI and the available evidence of the association between continuous NIRS-based measures and commonly monitored neurophysiological parameters, such as oxygenation and cerebral autoregulation. So far, evidence is primarily focused on monitoring adults with severe TBI, where CW and SRS are the most-used NIRS technologies. However, the methodological approaches between studies remain heterogenous. The above might be due to the lack of “dedicated autoregulation monitors”; likewise, the comparison of oxygenation gold standards with NIRS-derived parameters is problematic, as each monitor utilizes a distinct physical principle and measures a distinct physiological parameter. As oxygenation and autoregulation seem to play a crucial role in patient treatment and outcome, the potential use of NIRS in combination with multimodal monitoring is in the best interest of both TBI patients and clinicians.

Precise modelling of light propagation in the head to deduce the spatial sensitivity profile is crucial to the development and optimization of non-invasive optical technologies that aim to assess cerebral hemodynamic [173],[210]. The latter defines how deep the light travels into the tissue, where a large penetration depth carries more accurate monitoring of the brain [173]. Also, the spatial sensitivity profile, the so-called banana-shaped photon distribution, investigates the absolute absorption and scattering coefficients of the multiple tissue layers of the head, which can be used to quantify chromophores’ concentrations within the tissues [211].

Therefore, several theoretical and experimental studies have been performed to investigate the propagation of light in various head models based on diffusion theory and Monte Carlo (MC) calculations. Thus, having in mind the range of pathophysiological changes related to TBI, the foremost step is to characterize the optical sensor that will be designed and tested in this research on a healthy brain model.

7 HEALTHY MULTILAYER HEAD SIMULATION WITH MONTE CARLO ANALYSIS

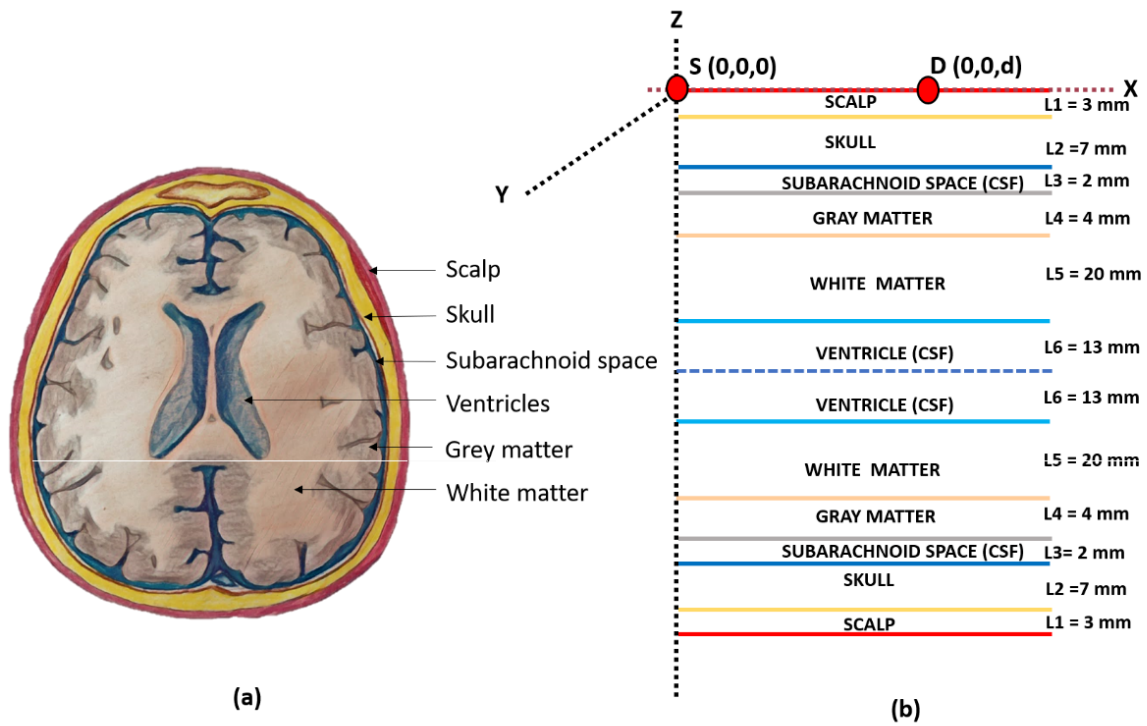
7.1 INTRODUCTION

Except for a few studies that investigated the propagation of light in head models, most approaches rely on homogeneous semi-infinite models of the head because of their simplicity [212]. However, the lack of realism might introduce bias in the measured optical properties [212]. In consequence, novel approaches based on heterogeneous structures have been considered [212]–[218]. These models consist of multiple layers, such as the scalp, the skull, cerebrospinal fluid (CSF) and the brain, which can be divided into grey and white matter. For instance, Okada et al. employed models consisting of three and four layers to analyse photon propagation [219]. Although a few theoretical and experimental investigations on light propagation in the human head have been performed, knowledge of which layers in the brain are sampled by light at different source-detector distances remains incomplete. Such information is of the utmost importance to optimize the design and determine the sensitivity of an optical sensor for interrogating the brain.

In order to investigate the efficacy of an optical sensor to monitor the range of physiological changes related to TBI, the foremost step is to characterize the sensor on a healthy brain model. Therefore, the optical interactions of near-infrared wavelengths were explored in a developed multi-layered tissue model. This work was presented at the EMBC conference 2021 [220].

7.2 METHODOLOGY

The light-tissue interaction model simulated in this work used the Monte Carlo (MC) computational method. MC is a stochastic process to simulate the photon paths through a tissue volume based on the probabilities of scattering and absorption. The MC model has a range of proven advantages over other available modelling methods such as diffusion approximation, random walk theory or finite element method in terms of its straightforward approach, ability to incorporate random anisotropic scattering, inclusiveness of tissue heterogeneity and structural complexity, and flexibility regarding the sensor design and location [221]. Available MC models of brain-optics are either too complex and resource-consuming to replicate or inadequately simplified. In the current work, a simple yet realistic multilayer brain-tissue model was developed and evaluated in a reflectance optical sensing geometry through a range of source-detection separations of 1, 2, 3, 4 and 5 cm.



(a)

(b)

Figure 44: Stratification of brain tissue layers: real (a) and simulated (b).

The simulated tissue volume is presented in a 3D Cartesian coordinate system. A linear slab-geometry was chosen for the simulation due to its simplicity.

7.2.1 Opto-anatomical parameters

The layer stratification of the Monte Carlo tissue model is illustrated in Figure 44. The full anatomical structure presented in Figure 44(a) was represented by a 12-layered semi-infinite slab-tissue model, as shown in Figure 44 (b) [31]. Healthy head layers' thicknesses have been adopted from the literature as presented in Figure 44 [222], [223].

Table 14: Optical coefficients of head tissues.

Layer	$\mu_a(\text{mm}^{-1})$	$\mu_s(\text{mm}^{-1})$	g	n
Scalp	0.016	19	0.9	1.60
Skull	0.018	16	0.9	1.56
Subarachnoid space	0.004	0.3	0.0	1.33
Grey matter	0.090	21.5	0.9	1.40
White matter	0.090	38.4	0.9	1.47
Ventricles	0.004	0.3	0.0	1.33

The tissue layers were characterized by their optical properties, namely, absorption coefficient (μ_a), scattering coefficient (μ_s), anisotropy function (g) and refractive index (n). The ideal wavelength for the sensor is the isosbestic point, i.e., 810nm, since the absorption properties of the oxy- and deoxy-haemoglobin are the same at this wavelength; therefore, an optical signal independent of blood oxygenation can be recorded [169]. However, due to a lack of adequate published information, the tissue-layer optical parameters through a near-infrared optical wavelength window (between 650-800nm) were adapted from the literature and are illustrated in Table 14 [224].

7.2.2 Monte Carlo simulation strategy

The details of the MC simulation steps and algorithm are discussed in previous publications [225], [226]. In the current work, a 10^9 number of photons were simulated through the brain tissue volume at each source-detector separation. Reflection loss at the air-tissue boundary and the interface between two tissue layers were considered in the model. In order to replicate a laser source, a Gaussian beam of a radius of 0.6mm was simulated. Photons were detected through a circular photodetector having an effective area of 5mm^2 .

The two simulated quantities discussed in this research are 1) layer-specific absorbance and 2) fractional optical path length. According to the modified Beer-Lambert law, the absorbance and optical path through the tissue will likely vary with the sensor geometry [32]. Such information is important to optimize the source-detector separation for TBI monitoring. The relative absorbance (presented in a percentage form) was calculated by recording the absorbance of each photon packet in each layer concerning the total absorbance of the photon packet within the entire head. Similarly, the fractional optical path length was calculated as the fraction of the path length of each photon concerning its total path length between the source and the detector. The absorbance and path length are the manifestations of the absorption and scattering properties of the tissue, respectively. Therefore, an analysis of both quantities leads to a comprehensive assessment of the sensor-tissue optical profile towards TBI investigation.

7.3 RESULTS AND DISCUSSION

The Monte Carlo model investigated sensor-tissue optical profiles at the reflectance sensor geometry having source-detector separations 1-5cm at the near-infrared optical window are shown in Figure 45. The sampled thickness and width are presented at the y- and x-axes of the 2D projections of the 3D simulated distributions. The number density of the interaction events between the light and tissue are shown in the colour bar.

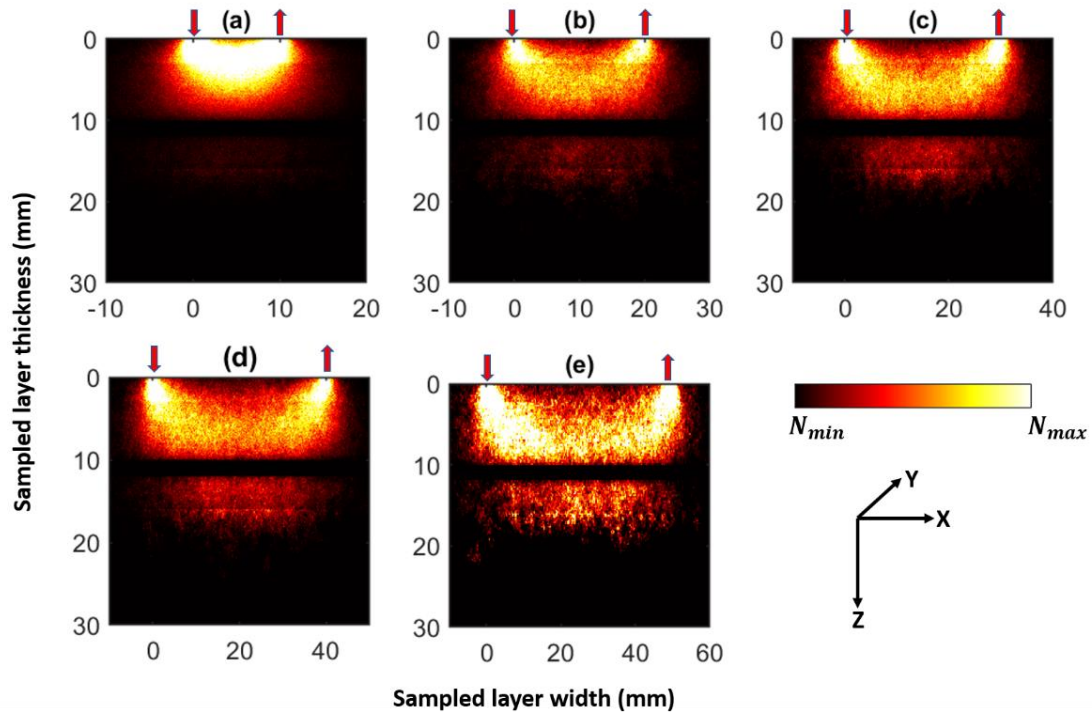


Figure 45: Monte Carlo simulated photon path through normal brain tissue at different source-detector separations: 10, 20, 30, 40 and 50mm as shown in (a), (b), (c), (d), and (e), respectively.

The x- and y-axis represent the sampled width and thickness of the tissue volume. The downward and upward arrows are the locations of the source and the detector, respectively. The y-axes are presented on the same scale. The x-axes scales are different due to the semi-infinite width of the simulated tissue volume. The colour bar represents the distribution of the number of photon-tissue interactions (N) between its minimum and maximum values.

An accumulation of the interaction events is found near the source and the detector, and the number density decreases along with the depth interrogated by the sensor. Through the head tissue layers, the interaction events are the lowest within the subarachnoid space (SAS), which has the lowest scattering coefficient and exhibits isotropic scattering ($g = 0$), as shown in Table 14. The anisotropy function (g) is a parameter that characterizes the angular distribution of scattered photons in a biological medium. When g is close to zero, it suggests a relatively symmetric or isotropic scattering behaviour, which leads to deeper light penetration into the tissue, as it is scattered more in all directions. This can be advantageous in medical applications such as NIRS. If a higher g value is considered for the subarachnoid space, then less photons would reach the subsequent layer (grey matter).

The changes in the x-axes limit show the spatial distribution of light with the increasing source-detector separation; for example, the spatial distribution of light at 1cm and 4cm separations are about 20mm and 45mm, respectively. The mean depth of penetration at $d = 1, 2, 3, 4$ and 5cm separation distances are about 6mm (scalp), 8mm (skull), 11mm (subarachnoid space), 13mm (grey matter) and 15mm (white matter).

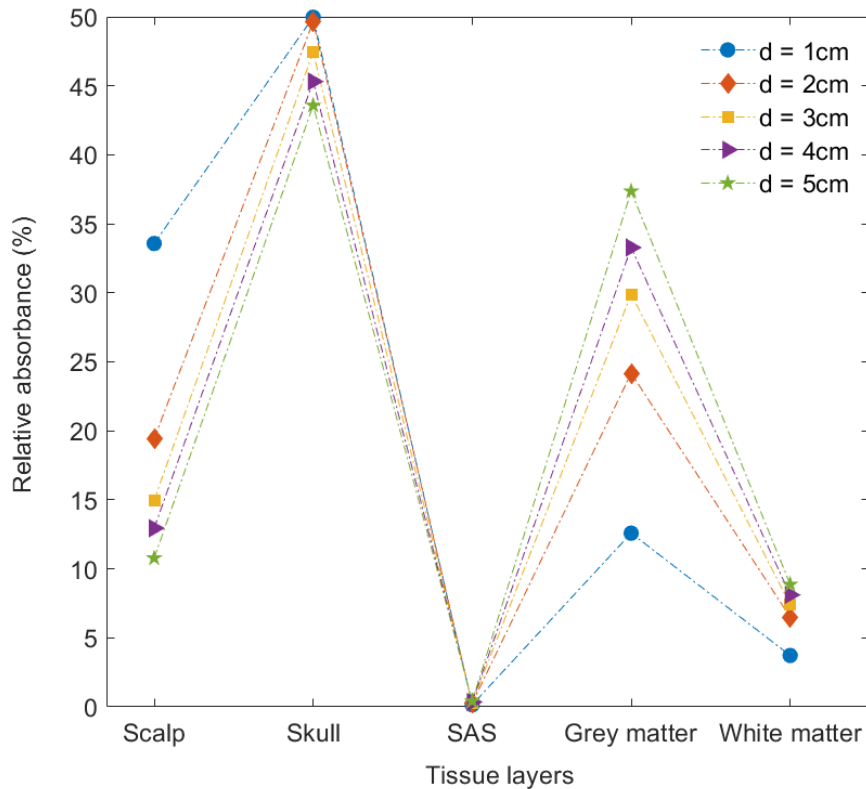


Figure 46: Relative absorbance at different head tissue layers at the source-detector separations $d = 1, 2, 3, 4$ & 5cm . The absorbance of the head tissue layers scalp, skull, subarachnoid space (SAS), grey matter and white matter are presented. No photons could reach beyond the white matter, so the rest of the simulated tissue layers are not shown. The maximum and minimum relative absorbances are shown in the skull and subarachnoid spaces, respectively.

The relative absorbance at each tissue layer is shown in Figure 46. The total relative absorbance amounts to 100% at each S-D separation (1cm, 2cm, 3cm, 4cm and 5 cm). Utilizing the current sensor design, the maximum tissue layer that can be interrogated is grey matter. The maximum and minimum absorbances are found in the skull and the subarachnoid space, respectively, at all source-detector separations. Interestingly, at the superficial tissue layers, such as the scalp and skull, the relative absorbance decreases with the increasing source-detector separations, whereas, at the deeper layers, such as grey and white matter, the reverse incident takes place. This is a combined effect of the sensor geometry and the optical wavelength that will be helpful in assessing brain tissue with less interference of extracerebral tissues, especially at source-detector distances above 3cm.

The Partial Volume Pathlength at different tissue layers is presented in Table 15. Optical path length depends on (a) the scattering coefficient and (b) the number of photons scattered in the tissue layer. The highest fractional optical path length at the skull is the result of the maximum photon scatters density at this layer, as shown in Figure 46. Even though the scattering coefficients of the grey and white matter are relatively high, the numbers of photon scatter at these tissue layers are lesser since fewer photons can penetrate to this depth. The fractional optical pathlength information is invaluable

to calculate the differential pathlength factors of the tissue at the TBI sensor geometry to quantify the tissue perfusion [33].

Table 15: Simulated Partial Volume Pathlength at different tissue layers at S-D separations d=1-5cm.

Partial Volume Pathlength					
d (cm)	Scalp	Skull	Subarachnoid space	Grey matter	White matter
1	0.41	0.54	0.01	0.027	0.008
2	0.28	0.63	0.014	0.061	0.016
3	0.23	0.65	0.017	0.082	0.020
4	0.21	0.64	0.022	0.095	0.023
5	0.18	0.65	0.0278	0.112	0.023

One of the key aspects of carrying out the present Monte Carlo simulation was to determine the source-detector separation for the TBI sensor. From the investigation, it is inferred that with a source-detector separation as high as 5cm, light can interrogate through white matter, and no light reaches the ventricles. Several serious TBI conditions, including haemorrhage (subdural, epidural, subarachnoid and intracerebral) and oedema (vasogenic and cytotoxic), are mostly found within or around the tissue layers, such as the subarachnoid space, grey matter and white matter which can be accessed utilizing one of the simulated sensor geometries.

7.4 SUMMARY

A robust yet simplistic Monte Carlo model of a multi-layered human head has been developed, enabling the comprehensive investigation of light tissue interaction of the adult brain. Investigation reveals that maximum light (40-50%) is absorbed in the skull, and the minimum light is absorbed in the subarachnoid space (0-1%). These results have a similar trend in comparison to other Montecarlo simulations of the human head using NIRS. However, the absolute values for spatial sensitivity can vary depending on specific parameters such as the layers' thicknesses, wavelengths of interest and the tissues optical coefficients.

Light's absorbance decreases with increasing source-detector separation up to 3 cm, where light travels through the subarachnoid space, after which the absorbance increases with the increasing separation. The findings demonstrate the potential of non-invasive optical sensors in TBI. Such sensors could enable the non-invasive monitoring of some of the most prominent TBI biomarkers, such as intracranial pressure and cerebral oxygenation.

In order to go forward with the sensor's design, it is critically substantial to develop first a phantom of the head where the sensor's efficacy and accuracy can be tested frequently. This testing tool should allow the simulation of head injury by controlled changes in haemodynamic parameters such as intracranial pressure and blood oxygenation. Additionally, it would allow the simulation of different clinical scenarios that cannot be induced in healthy volunteers. The phantom would then be a source of information during the sensor's design, development and testing phases that will be created in this research.

Based on the literature evidence presented in the previous chapters, the sensor would apply NIRS principles to monitor ICP and cerebral oxygenation in TBI patients. Accordingly, the phantom should mimic the optical properties of the actual head's animal tissues in order to replicate light-tissue interaction. Therefore, it is found relevant to have a spectroscopic analysis of the phantom's materials and its comparison with animal tissues. Consequently, the next chapter reports the phantom's design and development, including the spectroscopic test on the materials chosen for its construction.

8 PHANTOM DESIGN AND MANUFACTURE

8.1 THE CURRENT STATE OF THE ART IN HEAD PHANTOMS

This section presents a synthesis of the current state of the art in head phantoms. The researcher (MR) performed the search on Google Scholar using the search strategy focused on the intersection of the following keywords; “brain”, “head”, “cerebral”, “In vitro model”, “phantom”, “simulation”, “optic*”; excluding the term “blood-brain barrier”. After the title screening, 11 documents were selected to be included in this short evidence synthesis. The author recognises the limitations of the search and screening process, which may have limited the inclusion of some relevant studies in this short review of the state of the art.

In 1995 Kurth et al. [227] described the design and application of a dynamic neonatal brain phantom that permitted direct testing of NIRS-derived oxy- and deoxyhaemoglobin concentration. The brain phantom was constructed of a clear polyester plastic resin mixed with titanium dioxide in a 1.2% ratio. The cylindrical 567 cm³ solid resin contained an array of 500 channels, each with a radius of 500 μm, which represents the cerebral vascular network. Oxygenated human blood with heparin was pumped through the channels, adjusting the flow of oxygen, nitrogen and carbon dioxide utilizing an oxygenator reservoir, as is shown in Figure 47 [227]. Continuous-wave NIRS and time-resolved NIRS measurements were recorded to find the absorption coefficient, reduce scattering coefficient and optical path length by diffusion theory. These optical properties changed at various levels of the total haemoglobin concentration (THb); for instance, the absorption coefficient at 830 nm varied from 0.060 cm⁻¹ when THb=0 g/dl to 0.158 cm⁻¹ when THb=17 g/dl. Finally, Kurth et al. compared their results with NIRS-derived measurements in neonatal piglet heads in vivo [227].

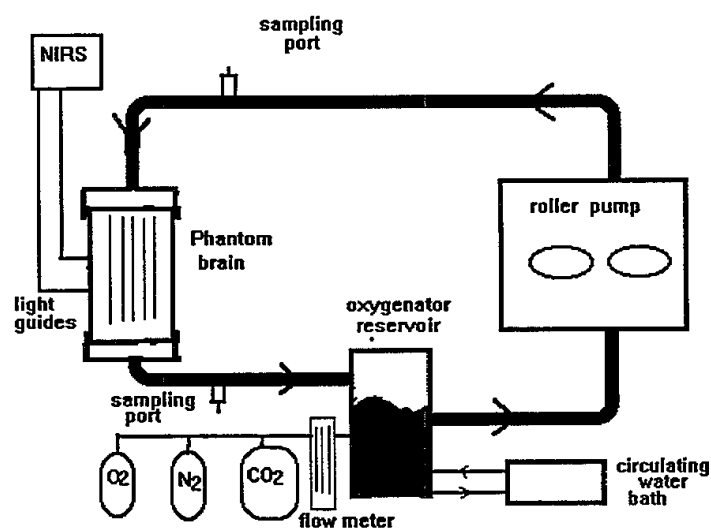


Figure 47: Kurth et al brain phantom for NIRS measurements. Figure from [227].

In 2004 Chen et al. [228] validated a brain phantom material for its use in drug infusion studies. The brain model consisted of a mix of 0.6% agarose powder and TBE (89 mM Tris, 89 mM Boric acid, and 2 mM Ethylenediaminetetraacetic acid; at a pH of 8.4). The 500 ml solution was solidified at room temperature in a transparent Plexiglas container with an imaging-compatible trajectory guide placed in the lid [228]. The phantom was compared against six anaesthetized pigs; in both models, a dilution of Omniscan was delivered at a 0.5ul/min infusion rate during the first hour and a 1ul/min rate for the second hour. The volume of distribution was observed using magnetic resonance imaging for 60 minutes after cessation of the infusion (Figure 48 [228]). The agreement found between the volume of distribution and the volume of infusion ratios for the gel and pigs' brains was adequate to warrant the use of the gel in a variety of infusion testing protocols [228].

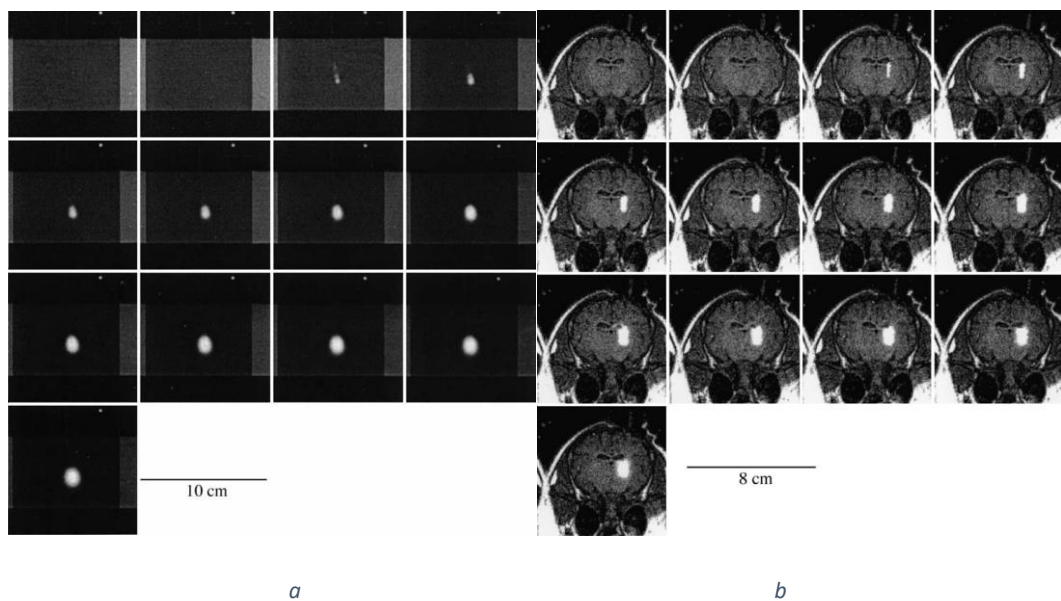


Figure 48: MRI sequence of Chen et al. brain (a) and a pig brain (b) during the 2-hours infusion. Figure from [228].

In 2005 Pfaffenberger et al. [229] investigated the potential of a diagnostic ultrasound device in the detection of blood clots using an in vitro skull model. The phantom consisted of half of a macerated human skull without calvaria, completely immersed into a sonication chamber which was connected to a water bath at 37°. The middle cerebral artery was mimicked by a silicone tube with an inner diameter of 4.8 mm and 0.8 mm wall thickness [229]. Human blood clots were placed inside the tube at a 50 mm distance from the ultrasound transducer, as is shown in Figure 49 [229]. The experiment was done in 5 skulls of different thicknesses and revealed no benefit of ultrasound in clots diagnosis through the temporal bone. The latter was explained as a consequence of the intensity loss (86.8%, 8.8 dB) even on the thinnest bone [229].

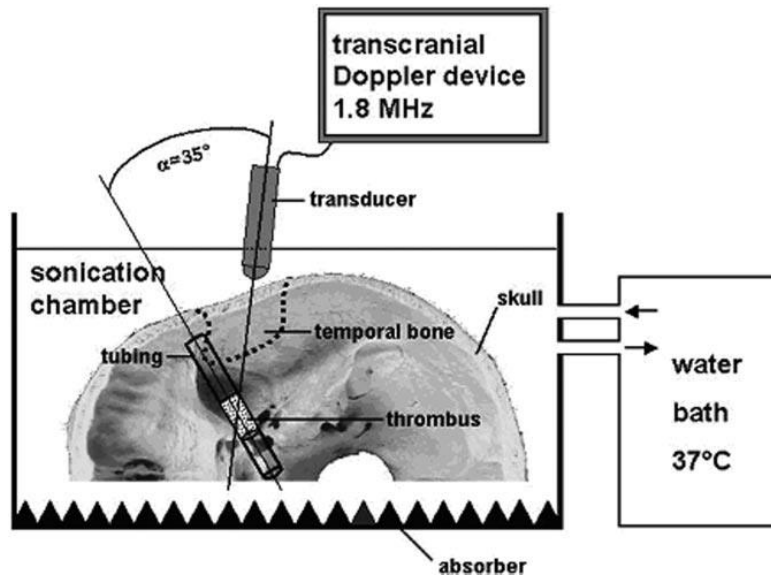


Figure 49: Pfaffenberger et al. skull model for the assessment of ultrasound in the diagnosis of blood clots through the temporal bone.

In 2013 Iida et al. [230] developed a 3-dimensional brain phantom that simulates a static cerebral blood flow distribution in the grey matter with an inclusion of the skull structure and a realistic head contour. A 3-dimensional CAD was created from healthy adult MR images, where the grey matter and skull compartments were designed so that they could be filled with liquid solutions, water and K_2HPO_4 , respectively [230]. The remaining area was filled with a transparent photo-curable polymer resin using a stereo-lithographic machine with the laser-modelling technique. The phantom was tested using CT images (Figure 50 [230]), and the resulting attenuation was compared to real human CT scan data. Iida et al. study suggested that this phantom is an adequate tool to evaluate PET/SPECT image quality [230].

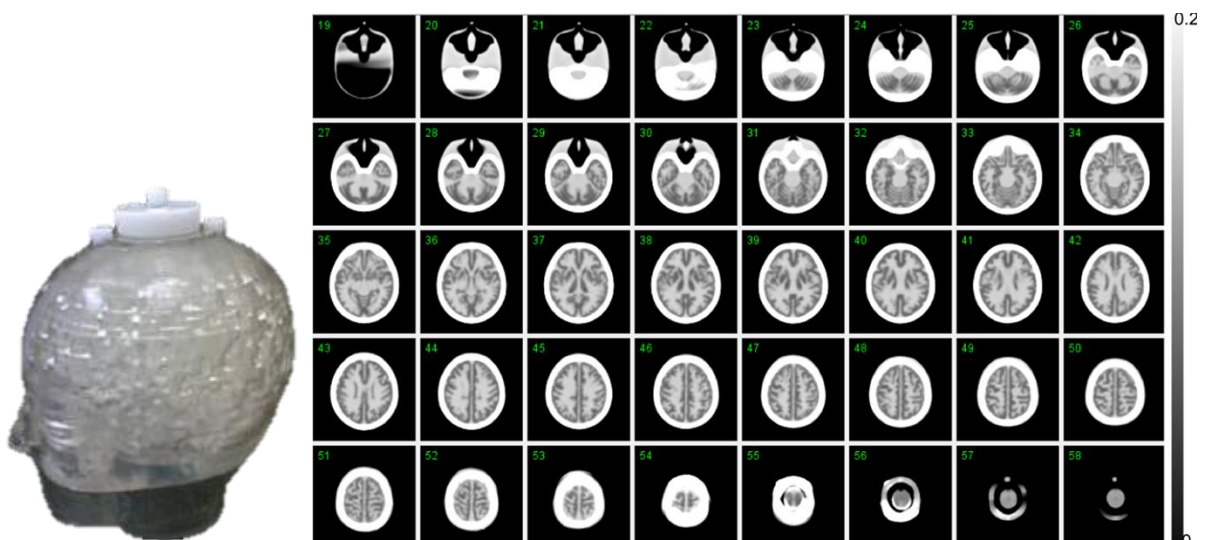


Figure 50: Iida et al. head phantom to evaluate PET/SPECT image quality [230].

In 2013 Simone Bottan published his doctoral thesis titled “In-vitro model of intracranial pressure and cerebrospinal fluid dynamics” [231]. Bonnet created a life-sized silicone brain using Sylgard 527 that included the ventricular system and the circle of Willis. The latter is the main blood cerebral circulatory system; it was created from real MRI images and resulted in a silicone vessel network. Then the brain was placed in a plastic human skull model from 3B Scientific and filled with water, allowing the connection of different inputs to the system [231]. At the base of the skull, the ventricles were connected to a hole called a cistern that evacuates into a PMMA pillar configuration. This structure represents the subarachnoid space and is outside the water box that encloses the head phantom. Finally, Bottan included an active compliance device shown in Figure 51 [231]. The phantom allowed the simulation of cerebral haemodynamics related to changes in ICP, ICV and CBF.

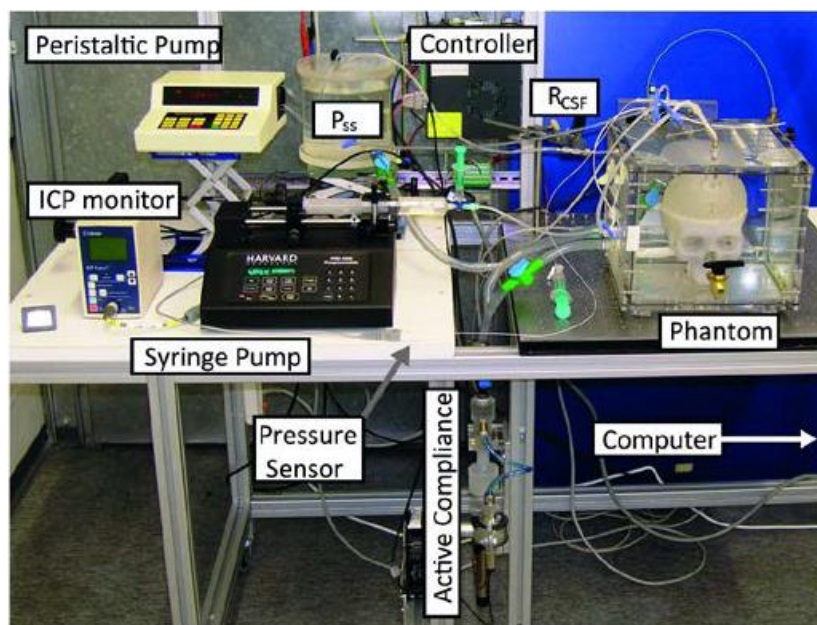


Figure 51: Bottan's head phantom for cerebral haemodynamics simulation [231].

In 2014 Mohammed et al. [232] presented the fabrication of a realistic head phantom to test microwave-based brain imaging. A polyvinyl chloride skull was used as a shell for the phantom. Different concentration solutions of polyvinyl chloride, water, corn flour, gelatin, agar, and sodium azide were used to mimic the cerebral spinal fluid (CSF), grey matter, white matter, and scalp. The cavity inside the skull was covered with a 2mm layer of CSF and was filled with grey matter [232]. After that, a scalpel was used to remove part of the grey matter mixture to make space for the white matter (Figure 52 [232]). Finally, a thin layer of the scalp mix was used to cover the skull, and a wig was included to represent the hair. Mohammed et al. compared the phantom's relative permittivity and conductivity against real human tissues, validating that the head phantom can emulate the electrical properties of the real human brain across the band used for microwave-based imaging (1-4 GHz) [232].

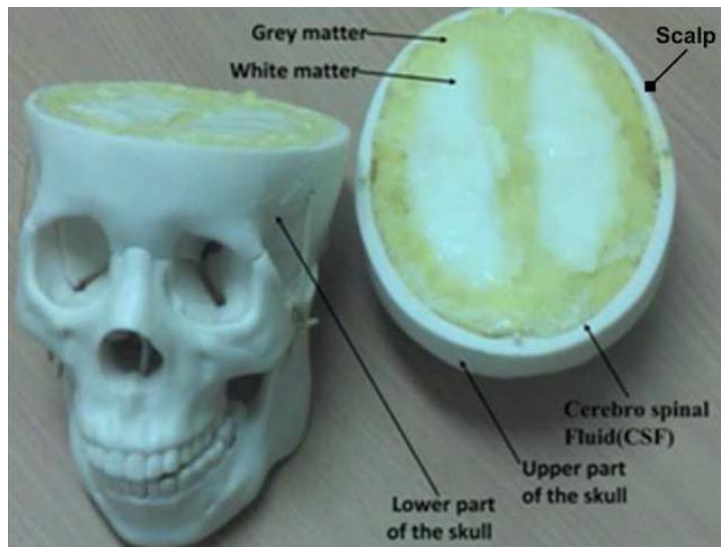


Figure 52: Mohammed et al. head phantom for microwave-based imaging [258].

In 2015 Menikou et al. [233] developed a magnetic resonance imaging compatible head phantom with acoustic attenuation closely matched to human attenuation and suitable for evaluating ultrasonic protocols. In this research the most critical design considerations were the acoustic attenuation coefficients of the materials and the anatomical geometry of the skull. An STL file was created from an adult CT head scan and 3D printed in white and grey ABS [233]. Different concentration mixes of agar gel and silica dioxide were used to create multiple phantoms on the two coloured skulls (Figure 53 [233]). The samples were scanned with a pulse-receiver 3.6 MHz planar transducer and an MRI machine. Finally, the white skull matched closely to the typical human skull's attenuation coefficient and the agarose gel mix by varying the concentration of silica dioxide, allowing the acquisition of MRI images from the in vitro model [233].



Figure 53: Menikou et al. head phantom compatible with MRI [259].

In 2017 Dempsey et al. [234] presented a skull phantom compatible with diffuse optical imaging. A premature neonatal head was selected from an MRI atlas to create an STL file of a skull with a hollow brain space. The model was 3D printed in methacrylate photopolymer resin mixed with titanium dioxide polyester pigment using a stereolithography printer. The concentration of pigment changed linearly with the scattering coefficient; for instance, 9.3×10^{-4} grams of titanium dioxide per gram of resin were required to create a phantom of optical properties: $\mu_s' = 1.0 \text{ mm}^{-1}$ and $\mu_a = 0.04 \text{ mm}^{-1}$ at a wavelength of 800 nm [234]. The skull was 3D printed in four parts and glued using resin; once it was hermetic, a mixture of intralipid and an aqueous solution of NIR dye was injected into the hollow space. Finally, to assess the phantom's feasibility, 32 fibre bundles were attached to the skull holders, and time-resolved data were then recorded before and after an optically black cylindrical target was inserted into the phantom (Figure 54 [234]). The latter proved the phantom skull's capacity to mimic skull optical properties [234].

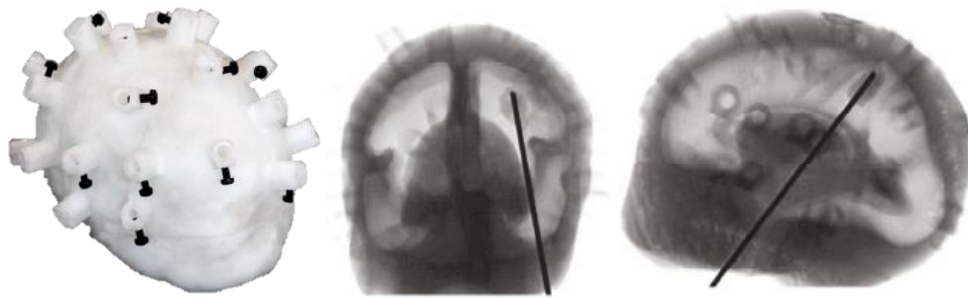


Figure 54: Dempsey et al skull phantom compatible with diffuse optical imaging [260].

In 2019 Afshari et al. [235] 3D-printed a cerebrovascular module (CVM) for standardized testing of clinical NIRS oximeters. The CVM consisted of a box of 130x120x50 mm with 148 channels with diameters of 0.5 and 1.2 mm. The module was 3D printed in a photopolymer resin (VeroWhite) using a stereolithography printer. Likewise, the CSF layer was modelled as a low turbidity medium, while the scalp/skull layer was moulded from 30 grams of polydimethylsiloxane mixed with 0.28 grams of titanium dioxide and 0.01 grams of India ink (Figure 55 [235]). The optical properties of all three layers were characterized using an integrating sphere module of the Lambda 1050 spectrophotometer, and they were in good agreement with the literature. The CVM was filled with whole bovine blood tuned over an oxygen saturation range of 30-90%, which was controlled by the introduction of oxygen and nitrogen gas. Finally, two commercial NIRS oximeters were used to test the phantom performance, finding an excellent agreement between phantom StO_2 measurements collected using NIRS devices and the reference [235].

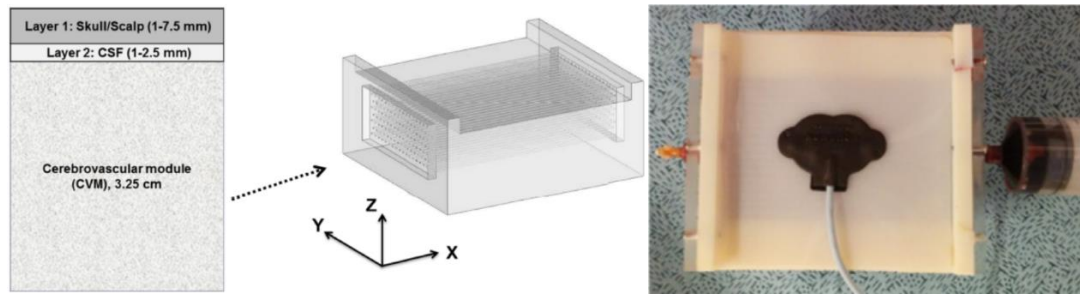


Figure 55: Afshari et al. head phantom for standardized testing of clinical NIRS oximeters [235].

In 2022 Afshari et al. [236] added an epidermis layer to the previous phantom to investigate the effect of skin pigmentation on NIRS measurements.

In 2019 Benninghaus et al. [237] presented an enhanced and validated in vitro model of the CSF system, where blood dynamics and active compliance can be investigated. The head phantom consisted of an anatomically shaped brain with ventricles made of silicone (Sylgard 527). It was glued to the lower part of a plastic skull but was not close on the top. This part of the model was placed in a hermetic PMMA box which was filled with water [237]. The ventricles ended in a compliance chamber located outside the box, which also simulated a simplistic subarachnoid space (SAS). A pulsatile pump was connected to the compliance chamber/SAS, and two valves were placed between this and the model. The first valve adjusted the pulsations from the compliance chamber/SAS to the parenchyma, transmitted by the surrounding water in the box [237]. The second valve connected to the ventricles simulated an adjustable flow resistance within the chamber/SAS. Finally, a second compliance chamber was also plugged into the ventricles to simulate spinal compliance (Figure 56 [237]). Some tests including changes in resistance, compliance and blood dynamics were done in the model and were compared to real human phase-contrast MRI data. The study found good agreement on flow measurements and demonstrated the stability of the model and pressure curves [237].

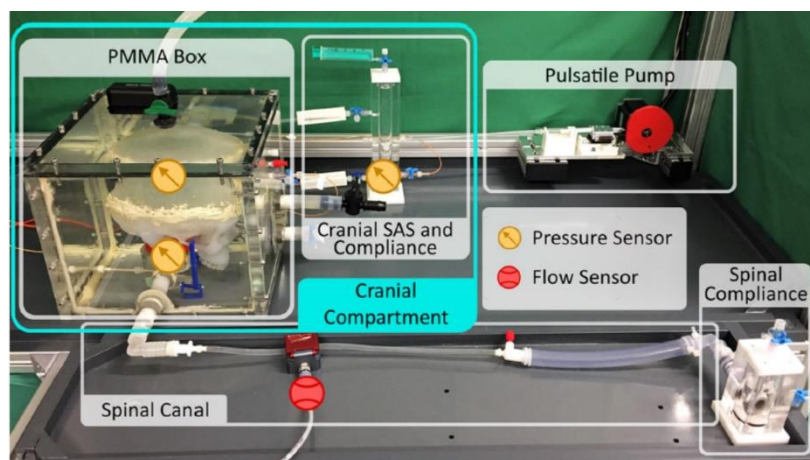


Figure 56: Benninghaus et al. phantom of the CSF system [240].

In 2019 Nagassa et al. [238] designed a human head phantom with a middle cerebral artery aneurysm, which would be helpful for cerebral aneurysm intervention training. These included models of the cerebral vasculature, cranial nerves, brain, meninges, and skull. The CAD of each of these components was developed from various patient medical imaging and pre-existing computational 3D models. Nagassa et al. successfully constructed a multi-component cerebral aneurysm surgery simulator and skin [238]. Half of the Willis circle was 3D printed in photopolymer resin to create a two-part mould of it in silicone rubber (SRT-30). Then a water-soluble circle of Willis was created from the mould, and it was brush-coated with Smooth-On™ Dragon skin 10 to create the final vessels. The part was placed on water to remove the wax and establish a vessel lumen. The aneurysm was built following the same method. The circle of Willis was then connected to the Waterpik® Waterflosser Ultra, which projected fluid in a pulsatile manner into the circulatory system [238].

Moreover, the cranial nerves (optic chiasm, optic nerve and olfactory tract) were included as anatomical landmarks and were 3D printed in thermoplastic elastomer Polymaker Polyflex. Furthermore, another 3D model was printed as a mould for the brain, which was used to cast a replica of each hemisphere in Clear Ballistics medical gel combined with Silc Pig® pigment additives [238]. Additionally, the meninges were included in the model using two successive layers of Smooth-On Dragon Skin 10 combined with Silc Pig® pigment additives; one was created from the surface of the skull and the other one from the surface of the brain. Finally, the skull was 3D printed in 2 parts utilizing a gypsum powder composite material, while a full-size human head skin layer was cast from a 3D printed mould in Smooth-On Eco-flex 10® with Silc Pig® pigment (Figure 57 [238]). Quantitative measures of the insignificant differences between the computational 3D mesh and the physical models confirmed the accuracy of the phantom anatomy compared to the original imaging or computational data [238].

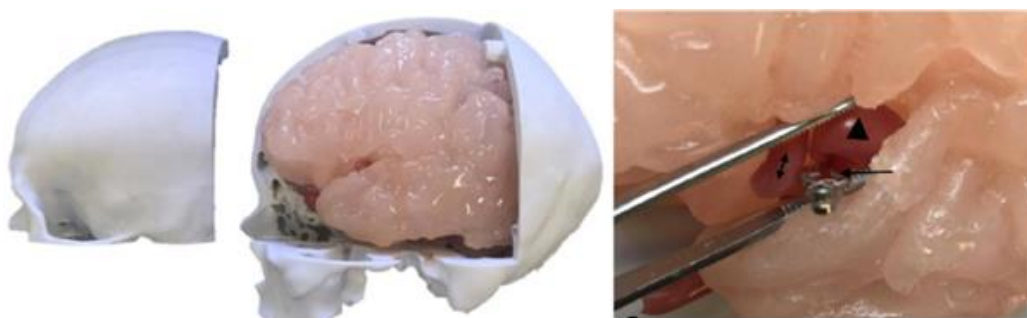


Figure 57: Nagassa et al. head phantom for cerebral aneurysm intervention training [238].

The presented synthesis pooled different designs, materials and manufacturing tools that have been used in a variety of head, brain, or skull phantoms. Three requirements of this group of models are highlighted, including complex anatomical geometry, cerebral haemodynamics and optical properties

of the materials. In order to achieve similar human anatomy, some authors created their phantoms based on human clinical images, commercial anatomical models or pre-existing computational 3D files. Moreover, some of the included papers carefully considered cerebral haemodynamics parameters, where ICP, flow and compliance were successfully replicated. Finally, the materials' optical properties were compared to spectrophotometric analysis of real animal tissues or pre-existing values from the literature. This last requirement was key in studies related to imaging and optical diagnostic tools such as ultrasound or NIRS. Particularly, the papers that used NIRS technologies implemented an interesting method to control changes in blood oxygenation within the phantoms. Aware of the presented compilation, this chapter describes a new head phantom that 1. mimics the human adult anatomical geometry, 2. replicates some optical tissue properties, and 3. allows controlled changes in haemodynamic parameters such as intracranial pressure and blood oxygenation.

8.2 METHODOLOGY

The assembly of a phantom was included as part of the development of a non-invasive multimodal sensor for the early and continuous monitoring of traumatic brain injury. The in vitro model allows for mimicking cerebral pathophysiological conditions that cannot be simulated in vivo. In addition, the production of a device capable of simulating cerebral haemodynamics, anatomical geometry, mechanical properties, and optical characteristics of the tissues would offer an ideal platform for the evaluation in the prototyping phase of the sensor development. The material presented in this were published on *Photonics* (DOI: 10.3390/photonics10050504) [239].

8.2.1 Materials

Spectrophotometry is the gold standard in the assessment of materials' optical properties. It consists of the quantitative measurement of the interaction of ultraviolet, visible, and infrared light with a material. The nature of this interaction depends upon the material's physical properties, and its phenomenological measurements include spectral reflectance, transmittance, absorptance, emittance, scattering, and fluorescence [240].

Based on the advantages of spectrophotometry, this study compared the optical properties of the materials chosen to build a head phantom against the optical properties of real brain and skull tissues extracted from animal models. This work was presented at the EMBC conference in 2022 [241].

8.2.1.1 Samples:

8.2.1.1.1 Phantom materials

As one of the aims was to assess the optical properties of the materials chosen to build the head phantom, these were compared against the optical properties of real brain and skull tissues extracted from animal models.

The phantom brain sample (10 x 10 x 20 mm) was developed in silicone gel (Sylgard 527, DOWSIL – Dow Corning, Michigan, U.S.A) as this material resembles the mechanical properties of the brain under dynamic and static conditions [231], [237]. The casting mixture was prepared by adding the two-part silicone gel in a ratio of 1:1 and, as the silicone gel is transparent with minimal scattering properties, Titanium Dioxide (TiO₂) particles with a primary crystal size of 550 nm (Altiris 550, Venator Corporation, Teesside, UK) were added in the mixture in a ratio of (weight/volume) of 0.1 g/100 mL to simulate near-infrared scattering [242]. The solution of Sylgard 527 and Titanium Dioxide particles was then hand-mixed and sonicated for ten minutes. The mix went into three vacuum chamber cycles before undergoing a degassing cycle of another 10 minutes (i.e., to remove air bubbles which may cause optical heterogeneities within the phantom). After an initial curing cycle in the oven of 4 hours at 125 °C temperature, the silicone phantom was removed from the casting and placed in the oven at 125 °C for one extra hour. Once the sample was at room temperature, it was placed in a UVette® plastic cuvette to protect the sample from damage due to its adhesive texture.

On the other hand, the phantom skull sample (6 x 10 x 20 mm) was 3D printed in the Form 2 printer from Formlabs (Somerville, MA, USA), which uses a laser to cure solid isotropic parts of a liquid photopolymer resin. The sample printed in resin (RS-F2-GPCL-04), enables good visibility of the brain, yet it got a yellowish colour after cure. All standard Formlabs' resins have comparable material properties to the reported from the cranial bone. For instance, evidence reports a tensile strength of the human skull of 67.73Mpa, which is close enough to the tensile strength of the phantom's resin (65Mpa) [243]. Moreover, according to McElehaney the human skull elastic module ranges between 2.41 and 5.58 GPa; in comparison, Formlabs resin has an elastic module of 2.8GPa, which is in the range reported by McElehaney [244]. However, other authors have found a higher value for the skull elastic module (mean: 8.51 GPA). Therefore, the phantom resin would be more compliant than the actual cranial bone [245]. Phantom's resin got its recommended tensile modulus after 15 minutes of post-curing at 60°C in the UV chamber. For consistency between the samples, each was placed in a UVette® plastic cuvette.

8.2.1.1.2 Animal samples

Multiple animal models have been used in traumatic brain injury (TBI) research, yet rodents are the most used due to their accessibility and low cost [246]. The substantial anatomical differences

between rodents and humans have led to a greater interest in the assessment of large animal models, such as cats, dogs, sheep, pigs, and monkeys [246]. Nonetheless, given the availability of mice and pigs' tissues, this study utilized brain and skull samples from both animal models. Five animals of each model were considered as tissue donors for this research, and only one sample of each tissue was extracted per animal. Thus, a total of 20 animal samples were obtained: 5 from mouse skulls, 5 from mouse brains, 5 from pig skulls and 5 from pig brains. Nevertheless, it is noteworthy to mention that pigs' brain samples consist of 40% grey matter and 60% white matter; in contrast, the whole brain of a mouse was contained in a single cuvette. Figure 58 shows the brain and skull samples of the phantom materials and both animal models.

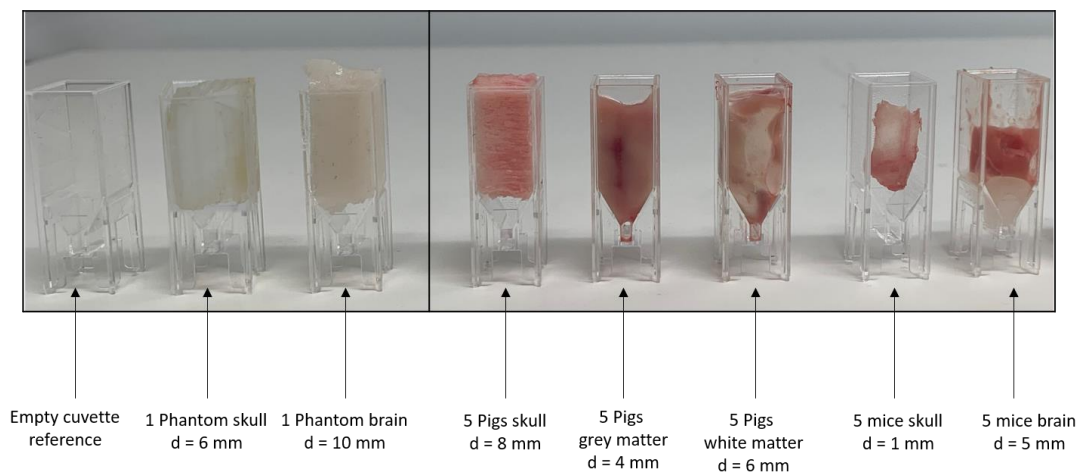


Figure 58: Brain and skull samples of the phantom materials and animal models.

8.2.1.2 NIR Spectroscopy:

The spectra of the prepared samples were collected using a Lambda 1050 dual-beam spectrophotometer from Perkin Elmer Corp. (Waltham, MA, USA). A 100 mm InGaAs integrating sphere detector set at 0 deg was used for the detection of diffuse reflectance and diffuse transmittance measurements. In order to test the selected skull resin colour, a sample of the resin was assessed in the spectrophotometer in reflectance mode within the range of 370–1100 nm at 5 nm intervals. Likewise, for the animal test comparison, the spectra were acquired in the wavelength range and interval as the resin, yet the analysis was focused on the wavelength range 660-900 nm, the same as where pulse oximetry and cerebral NIRS devices work. The absorption contribution of chromophores, such as oxygenated and deoxygenated haemoglobin, is maximized in this spectral range, while the absorption contribution of other compounds, such as water molecules is minimized [155].

Moreover, the Gain and Response Times for the spectrophotometer were maintained at 0 and 0.2 s, while both slit sizes were kept at 2 nm. These settings prevented the detectors from oversaturation.

Reference beam attenuation was set at 100%, and UVette® disposable plastic cuvettes of 10 mm path length from Eppendorf® (Hamburg, Germany) were used. Also, for the acquisition of measurements in reflectance mode, a Spectralon Diffuse Reflectance Standard from Labsphere (North Sutton, NH, USA) was placed at the aperture of the sphere detector for both baseline corrections and sample spectra collections. In this technique, one spectrum was produced per scan and three cycles were collected from each sample, and later were averaged to obtain 23 spectra dataset.

8.2.1.3 Analysis:

Spectra collection and visualisation were performed using the software packages: UVWin Lab for LAMBDA 1050 from Perkin Elmer (Waltham, MA, USA).

Spectra were compared mathematically for their similarity and differences using various numerical techniques. These algorithms compared an unknown spectrum, which in this case were the phantom's brain and skull spectra, against candidates in a known spectra library, as those measured from animal tissue samples. The similarity of the two spectra was decided using many evaluation metrics, which usually should be zero when both spectra are the same; however, the two spectra are never absolutely identical due to instrumental noise [247].

Three distance methods were implemented in the analysis. The Mahalanobis distance represents a highly rapid, robust and statistically sound means of searching large libraries. The Mahalanobis distance is a measure of the distance between a point and a distribution, taking into account the covariance structure of both independent spectra [248], [249]. The lower the distance, the higher the similarities between the samples [247]. Likewise, the Euclidian and Manhattan metrics are full spectral matching algorithms that make a point-by-point comparison employing simple geometry to evaluate the distance between two spectra. The shorter the distance, the better the match between them [247].

Distance methods helped to know if the phantom's spectra matched the animal tissue's spectra for both brain and skull samples. However, as one of the phantom requirements is to match the optical properties of these tissues, thus the optical properties were characterized using the Inverse Adding Doubling (IAD) approach based on diffuse reflectance and total transmittance measurements of samples in an integrating sphere spectrophotometer [250].

8.2.2 Design and manufacture

8.2.2.1 Skull

The skull phantom was produced using a pre-existing computational model consisting of three parts: the calvaria, the maxilla and the mandible. The model was downloaded from the medical library of a free access site (www.grabcad.com). The STL files of the calvaria and the maxilla were scaled down to

correspond with the size of an adult human skull (67.5% of the original model size), as is presented in Figure 59. The maxilla model was edited in SolidWorks 2020 to fill the anatomical foramina and canals.

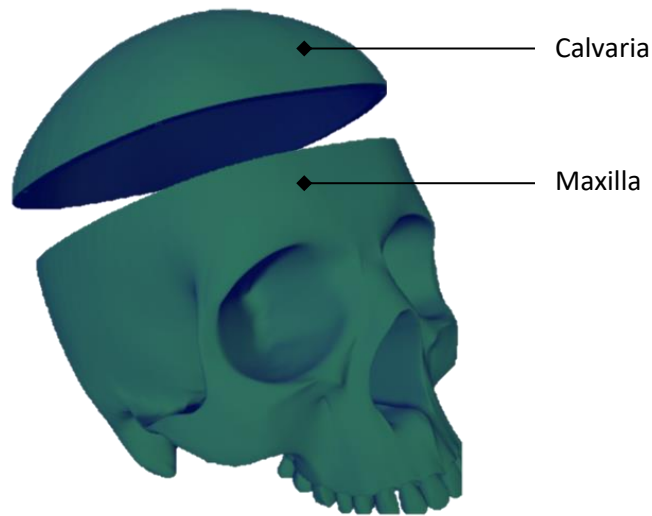


Figure 59: Both parts of the skull CAD, the calvaria and the maxilla

The calvaria is the part of the skull formed by the frontal, occipital and parietal bones, where optical measurements, utilizing a non-invasive sensor, would probably take place. Consequently, the calvaria must replicate the optical properties of a real skull, which is not a requirement for the maxilla, as no optical measurements would be performed in this area. The Calvaria was printed using the Form 2 printer from Formlabs (Somerville, MA, USA) in clear resin (RS-F2-GPCL-04) to enable good visibility of the brain. The part took around 11 hours to print, considering a printing resolution of 0.05 mm. After completion, the support structures on the 3-D printed part were removed, washed in isopropyl alcohol for 30 minutes and post-cured in a UV chamber at 60oC for 15 minutes (Figure 60).

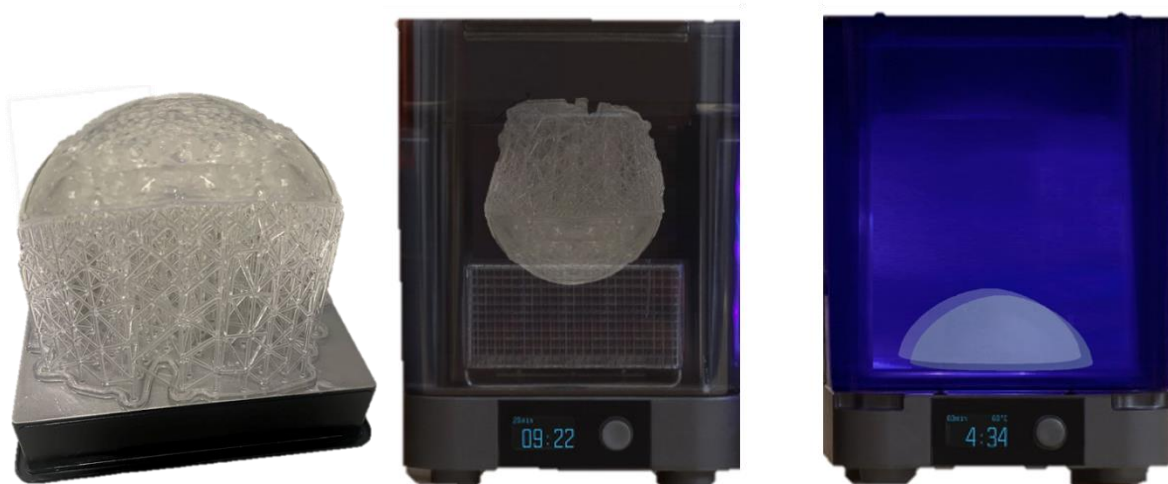


Figure 60: Formlabs post-curing process applied to the calvaria

As the maxilla dimensions exceeded the Form2 printing volume, this part was manufactured in a bigger 3D printer. Hence, the Objt30 Pro (Stratasys, MN, USA) Printer was used to make the maxilla in a transparent PolyJet™ photopolymer called VeroClear™. This part (maxilla) took around 64 hours to print, considering a printing resolution of 0.016 mm. After completion, the gel-like support structures (SUP705) were removed from the printed part. To remove the excess support material surrounding the model, it was soaked in a 1% solution of sodium hydroxide for 1 hour. To improve the material's finish and transparency, it was sanded by hand with dry and wet 200-grit to 1000-grit sandpaper. Some details of the maxilla's complex geometry were sanded with the help of a multi-tool. Finally, the model was exposed to 24 hours of photobleaching, as intense florescent lighting can reduce the yellow tint by over 90%. For the latter process, a house-made chamber was built with aluminium foil and two 45 W, 6500K table lamps. The final result of the maxilla is illustrated in the results section.

On the other hand, a metallic rectangular base (30x20x2 cm) was created in aluminium with four cylindrical legs (Figure 61 in orange colour). Two clamps were designed in Autodesk Netfabb Premium 2019 using operational tools and were 3D printed in VeroClear™ as shown in Figure 91 in grey colour. Each clamp consisted of a two-part structure; one was screwed to the metallic base and supported the bottom of the skull zygomatic arch, while the second part clamped the top of the arch following its geometry. Both parts of each clamp were put together with a nylon screw while holding the zygomatic arch. This design allows for keeping the skull in place, especially when fluids are pumped into the model. The final result of the base and clamps are illustrated in the results section.

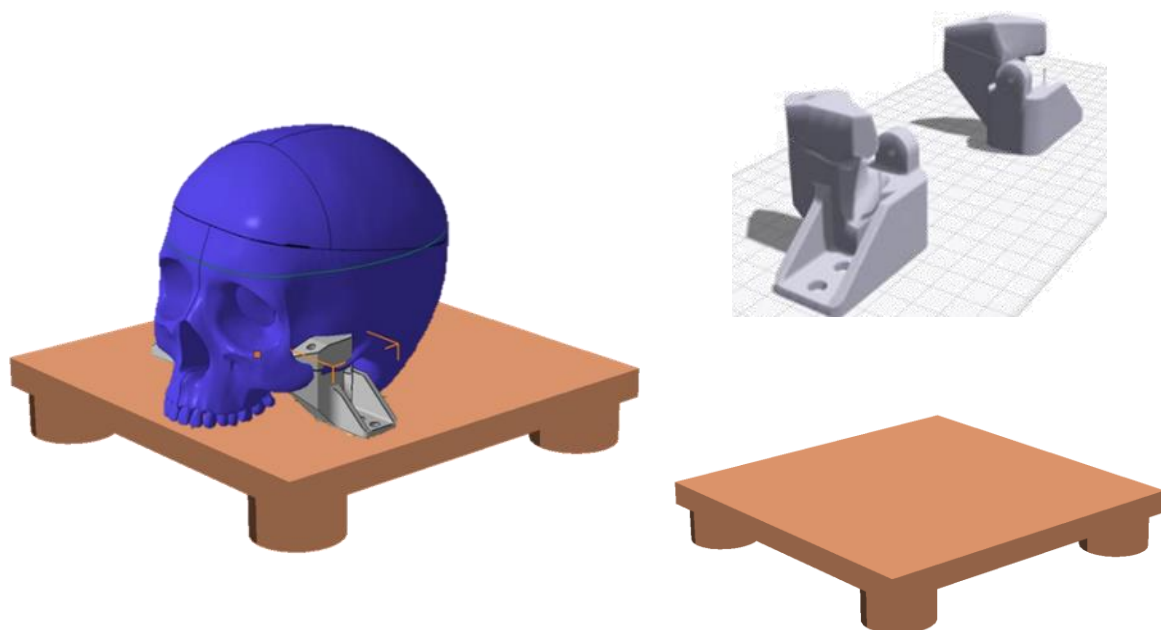


Figure 61: Phantom base and clamps design

As one aim of the phantom is the simulation of haemodynamic events, the insertion of access ports in the calvaria was needed. Initially, some holes were drilled in the calvaria to place plastic commercial connectors (Figure 62). However, this design had two main limitations. Firstly, the presence of leaks due to small gaps between the connectors and the skull due to its convex geometry required the use of a sealant. Secondly, the limited range of tubes or adaptors that could be plugged into the implemented connectors reduced the versatility of the experiments that might be done in the phantom.

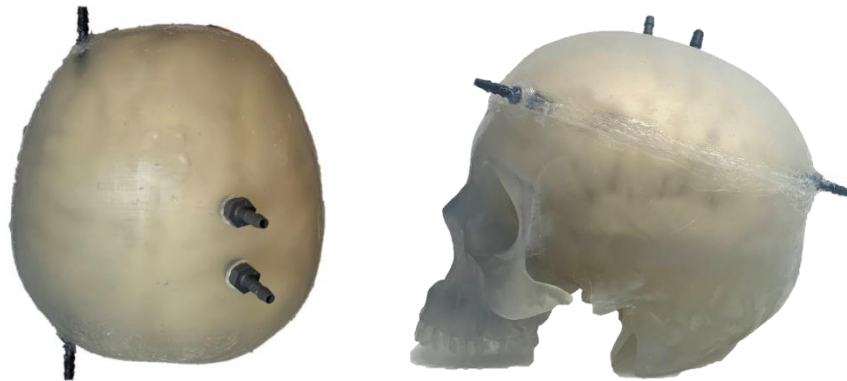


Figure 62: Plastic commercial ports

Therefore, a second calvaria design was created in SolidWorks 2020, as shown in Figure 63. This new model included nine female Luer-ports on the external surface. As a standardised system, Luer-ports allowed leak-free connections between the female and a large range of mating male connectors by rotating one over the other. Additionally, two of the Luer-ports ended as Luer-ports at the interior of the calvaria (Figure 63), where they were connected to the arteries embedded within the brain phantom at the inside of the skull. One was used as the entrance of the circulatory system and the other at the exit. Moreover, two of the ports at the top of the calvaria were placed at the right and left Kocher's points, where external ventricular drains (EVD) are commonly inserted in clinical practice. EVD provides continuous intracranial pressure monitoring and cerebrospinal fluid diversion [251], making Kocher's point the optimal place to insert the invasive ICP sensor in the phantom too. Anatomical measurements were also performed to locate each hemisphere Kocher's point, 11 cm posterior to the phantom nasion, and 3 cm lateral to the midline, equivalent to the mid-pupillary line [252]. Finally, two more ports were placed in the frontal bone, another one at each parietal bone and one more in the higher portion of the occipital lobe over the midline. These final five ports were included for multiple purposes, including the connection to the CSF circulatory system and the future simulation of intracranial haemorrhages (Figure 63). The part took 16 hours to get printed in the Form 2 printer, using a resolution of 0.5 and clear resin (RS-F2-GPCL-04). The post-printing process of this

calvaria was the same as presented in Figure 60. The final version of the calvaria is illustrated in the results section.

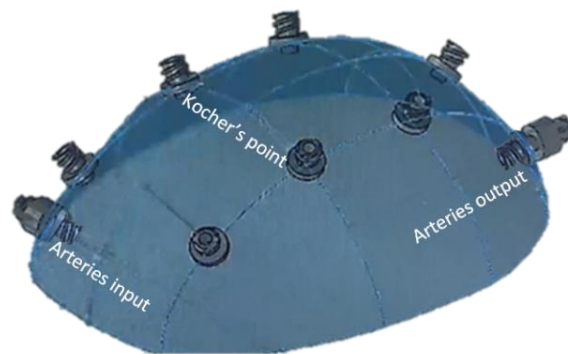


Figure 63: Calvaria with Luer ports to allow the connection of multiple objects

The final step in the skull design and manufacture was the seal between both parts, the calvaria and the maxilla. This process is essential in order to simulate pathological scenarios such as intracranial hypertension. The first approach involved gluing the calvaria to the maxilla using a translucent sealant (UniBond 2078484), creating a hermetic seal in about 24 hours. This non-permanent glue is easy to apply, waterproof and doesn't damage the skull surfaces, which was a good option for preliminary system tests. Next, the seal was tested by injecting water with red ink from a syringe into a scaled version of the model (Figure 64).



Seal test on a scaled version of the model



Translucent sealant glue on the real-size skull

Figure 64: Scaled skull hermeticity test using translucent sealant/ glue

The seal was tested on the real-size skull (Figure 64), pressurized until 40 mmHg, and artificial blood was pumped through the brain arteries in preliminary experiments. As the phantom is a research tool, it should be easy to access the intracranial cavity, brain and cerebral arteries. Furthermore, every time an artery gets disconnected, a haemorrhage occurs, or the CSF needs to be replaced for hygienic

reasons, the skull needs to be opened. Although the glue seal ensured the skull hermeticity during the preliminary tests, it made the process of removing and sealing the skull more time-consuming. Therefore, other strategies were implemented to achieve a hermetic skull that could be opened and sealed in just a few minutes.

The first method consisted of changing the clear silicone for another commercial seal called Plumber's mait (EVO-STIK), which is a non-setting, waterproof putty. The time to seal the skull and to open it back (removing the material) was about 30 minutes; however, the seal didn't bear an ICP over 15 mmHg, probably because of its permanent flexibility. Then, a more elaborated method was proposed, requiring the design and manufacture of a customized gasket, as is shown in Figure 65. This part was 3D printed on the Flexible photopolymer resin in the Form2 printer (Formlabs). Despite this alternative was very fast for opening and closing the skull, it failed to ensure the seal. Also, some cracks on the material appeared after some tests.

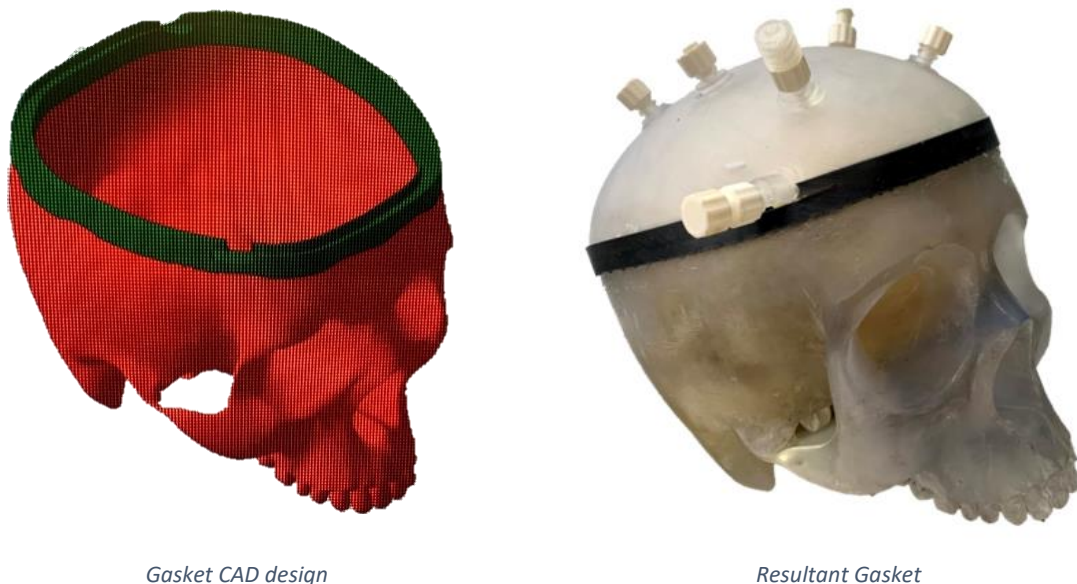


Figure 65: Gasket alternative for the skull seal

A third strategy, inspired by vacuum chambers, involved placing screws from the brim of a new calvaria design into a brim glued to the maxilla and securing them with nuts. The new calvaria had a brim with 20 holes, as shown in Figure 67 and was printed on draft material in the Form2 printer to test this approach. However, due to cost and time limitations, the maxilla couldn't be printed again, so an acrylic customized brim was designed, cut and glued (UniBond 2078484) to the maxilla edge. The later had 20 threaded holes that could be aligned to the calvaria's brim. Finally, a rubber O-ring was cut using the brim shape and placed between the parts before the calvaria's brim was put together with the maxilla's brim by screws (Figure 66).



Calvaria with brim CAD design



Resultant seal

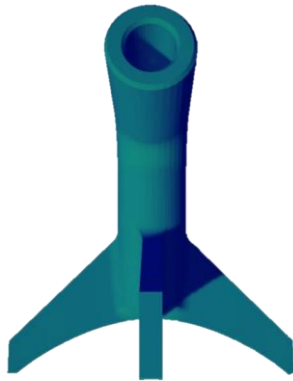
Figure 66: Calvaria with brim and seal using screws

This elaborated strategy failed because the maxilla's brim was glued rather than having it as a whole part as the calvaria was. This limitation led to constant leaks through the maxilla and its brim, probably because the force applied to the screw, the screws broke the glue seal between the maxilla and its brim. There is high confidence that this method could work if the maxilla is designed with a brim as a whole part.

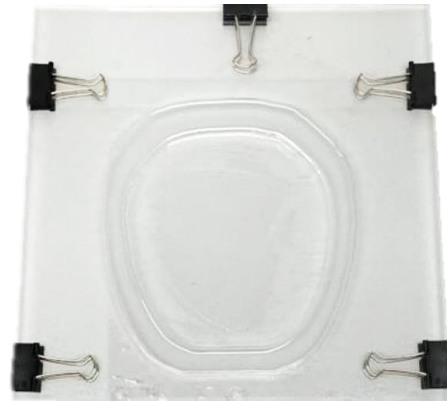
From all the alternatives above, valuable lessons were learned, leading to the design and manufacture of the final seal, which consists of an external compression structure attached to the phantom base. The structure involves a clamp designed from the calvaria's surface and a lead screw, both parts attached by a prisoner's nut. The clamp was printed on the Objt30 Pro in a black colour PolyJet™ photopolymer. The clamp compresses the calvaria against the maxilla to keep both parts together. The clamp's height is set by the position of the lead screw, which is controlled by a thumb nut (Figure 67). The compression is distributed by the clamp through all the calvaria's area in order to ensure a uniform seal. A thick (2mm) silicone gasket was placed between both parts to ensure the seal. A two-layer acrylic mould was manufactured by a laser cutter and is held together by metallic clamps as shown in Figure 67. The material used for the gasket was Sylgard 180, which was mixed by hand with its catalyser in a proportion of 10 to 0.6 grams, respectively. The mix bubbles were removed using a vacuum chamber, where the mix was exposed to -160 psi for twenty minutes. Finally, the mix took 24 hours to set in the mould (Figure 67). The final version of the skull seal is illustrated in the results section.

The seal was tested by increasing the intracranial pressure from 0 to 30 mmHg. The ICP was sensed using an invasive needle tip pressure transducer (Gaeltec Devices Ltd, UK) and its control unit

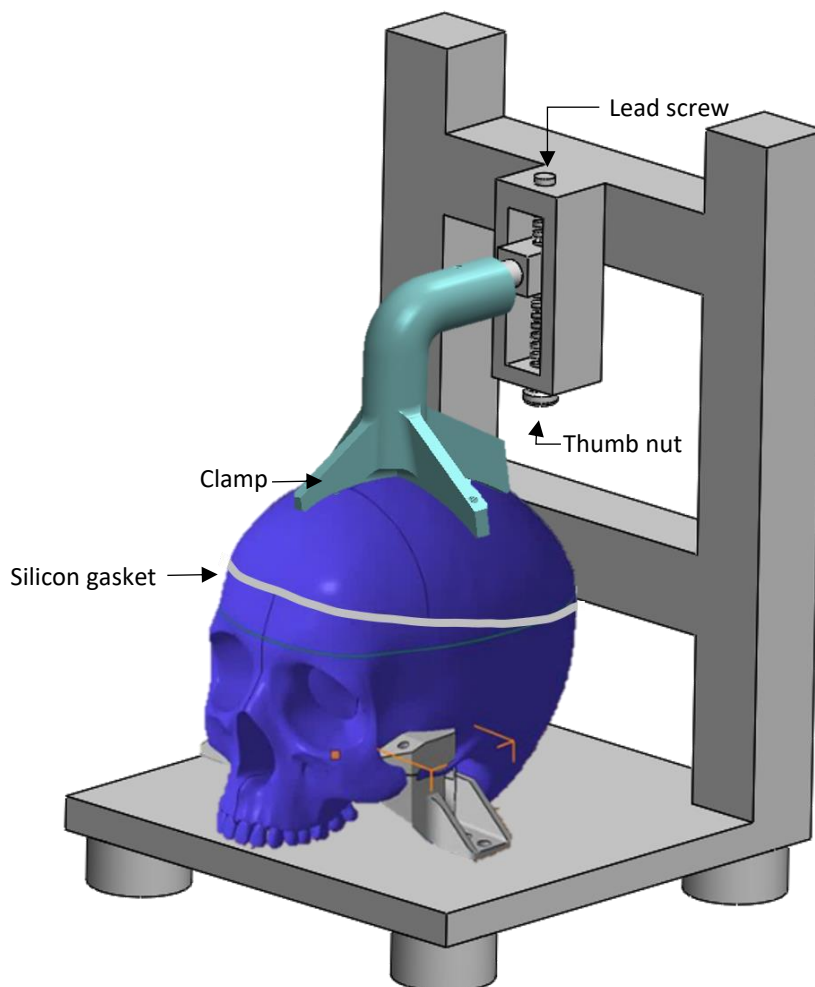
(Neurolog system NL109, Digitimer, USA). The sensor was placed on the right Kocher's point port while the pressure was increased by a syringe through a second port at the top of the calvaria. The presence of leaks was visually checked, and the capacity of the phantom to preserve a stable ICP value for longer than five minutes confirmed a good seal.



Back view of the clamp's CAD



Silicon gasket mould



Compression system to seal the skull

Figure 67: Final seal, compression system

8.2.2.2 Brain

The brain was developed using moulding and casting techniques. The brain mould was developed from a human brain model with arteries (C20 [1017868]) manufactured by 3B Scientific (Hamburg, Germany). According to the information provided by the company, the part was modelled from a healthy specimen in its real size. While the age and sex of the human sample are unknown, the model might belong to an adult man. The latter conclusion was made, given that the model volume is approximately 1250 cm³ and the average adult brain volume is 1260 cm³ for men and 1130 cm³ for women [253]–[255]. Also, the brain model size was used as the reference to scale the skull STL files, as was mentioned before. Therefore, the brain phantom fitted perfectly in the printed skull (Figure 68) and allowed enough space to simulate a CSF intracranial volume of 150 ml, which corresponds to the average volume reported in the literature [256]–[258].



Figure 68: 3B Scientific human brain model with arteries, enclosed into the phantom skull.

A two-part mould of the brain anatomical model was created using Polycraft™ GP-3481-F Silicone Rubber and Polycraft™ GP-3481-F Silicone Clear Catalyst. Initially, a double box of Perspex was designed in SolidWorks 2020 and cut in a laser cutting machine. The design consisted of a tabbed box of 12x15x17 cm that fitted precisely inside a second glued box. The latter had a 5 cm diameter hole at the bottom of the box that served to push the internal box during the demoulding process. Once the box was ready, the brain model was covered with a medium-duty silicone releaser (Ambersil, Formula 6), and it was held from the medulla with a universal clamp attached to a support stand. The brain anatomical model was located in the middle of the box and suspended in the air as shown in Figure 69. Separately a 2.2Kg of Polycraft™ RTV-3481 base was mixed with 220g of Polycraft™ GP-3481-F Silicone Clear Catalyst. The mix was then poured into the box all around the brain model until it was completely covered. After 24h the brain was demoulded by pushing the internal box through the hole of the external one. Once the tabbed box came out, each wall was easily removed, and the silicone mould was ready to be cut. A surgical scalpel was used to split the mould into two halves, following

the cerebral midline. A zigzag cut shape helped to align the mould, as shown in Figure 69. Finally, the mould was tested, creating a brain with 140gr of porcine jelly powder and 900 ml of hot water. After 24h in the fridge, the jelly brain was demoulded (Figure 69), and it was demonstrated the high quality of the mould to copy the brain model.



Figure 69: Brain mould manufacture

Initially, the plan was to include the middle cerebral artery (MCA) in the phantom only, as will be explained in the next section. Therefore, a commercial silicone tube with an inner diameter of 3.2 mm needed to be placed parallel to the temporal lobe at a maximum deep of 3 mm from the parenchyma surface. In order to achieve this aim, a copper cylinder of 3 mm in diameter and 200 mm in length was covered by the silicone tube and placed inside the right hemisphere of the mould as is shown in Figure 70. Then, the inside of the mould was sprayed with a medium-duty silicone releaser (Ambersil, Formula 6) and both parts of the mould were held together using an adjustable stainless-steel baking mould and cooking strings. The mould was put inside an aluminium foil tray before the brain silicone mixture was poured through the hole in the top of the mould (Figure 70).



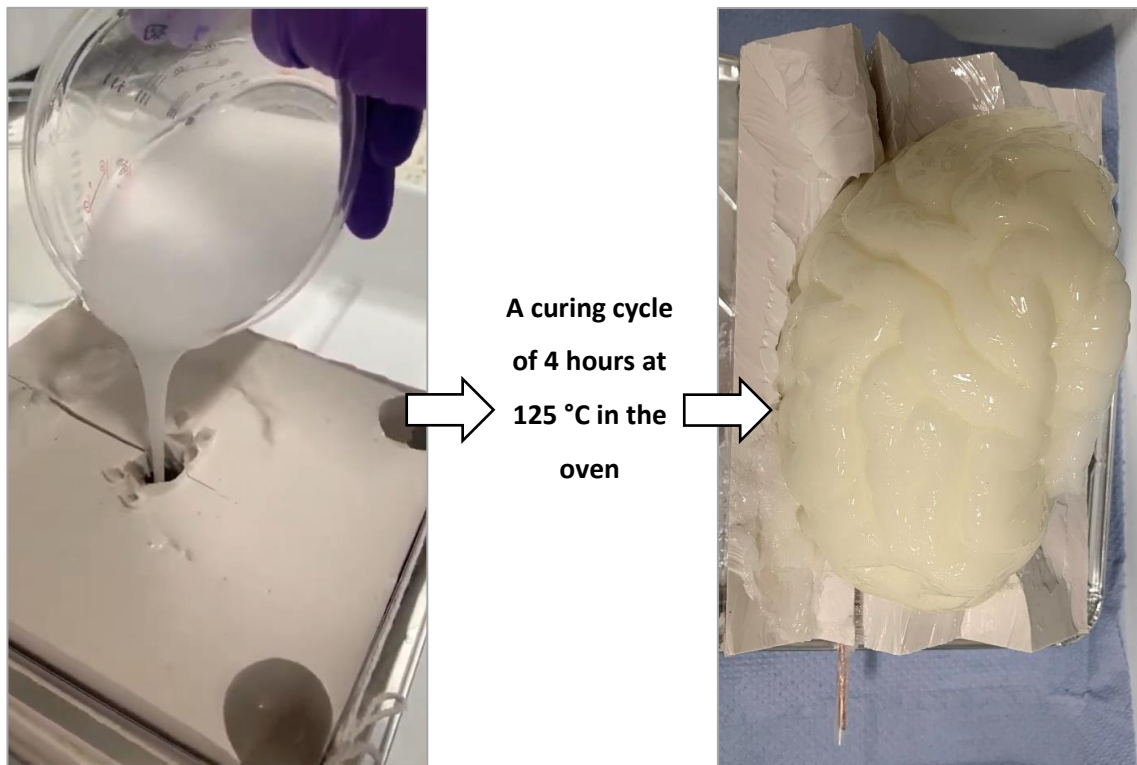
Figure 70: Brain mould with the middle cerebral artery, ready to receive the brain silicone mix.

As it was explained in the materials section, the brain mixture was prepared by adding the two-part silicone dielectric gel (Sylgard 527, DOWSIL – Dow Corning, Michigan, U.S.A) in a ratio of 1:1. Due to the viscosity of the material it was not possible to create the silicone gel mixture, required to fill the brain mould, in just one batch. Hence, it was produced in three batches, two of 300 ml and one of 400 ml, which were mixed by hand in clear plastic mixing cups. Moreover, titanium dioxide (TiO₂) particles with a primary crystal size of 550 nm (Altiris 550, Venator Corporation, Teesside, UK) were added to the mixture in a ratio of (weight/volume) of 0.1 g/100 mL to simulate near-infrared scattering (Figure 71 a). The solution of Sylgard 527 and Titanium Dioxide particles was then mixed and sonicated for ten minutes in a professional ultrasonic cleaner (GT Sonic, Shenzhen, China), as is shown in Figure 71 b. Then, the mix went into three vacuum cycles at -30 inHg in a vacuum degassing chamber (AVE, Bristol, England); at this point, the solution looked homogenous (Figure 71 c). Finally, the mixture underwent a degassing cycle in the ultrasonic cleaner for another 10 minutes (Figure 71 d). Both vacuum and degassing procedures had the aim of removing air bubbles from the silicone mix, which may cause optical heterogeneities within the phantom. The complete procedure described above took less than one hour, which was very important considering the Sylgard 527 working time at 25°C.

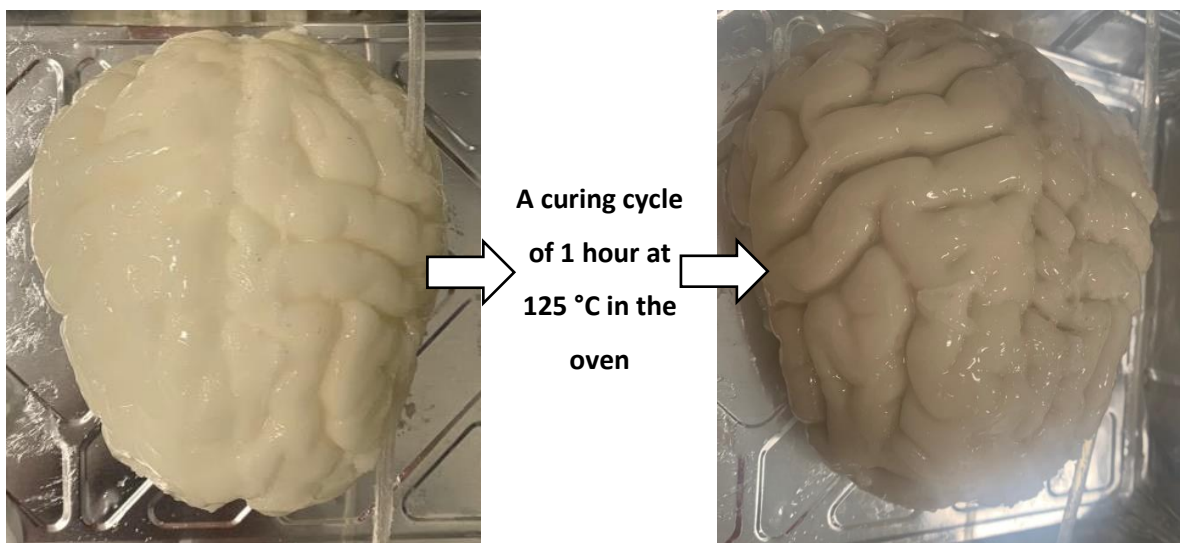


Figure 71: Brain silicone mixture manufacture process

When both, the mould and silicone mixture, were ready, the solution was poured slowly into the mould, and it was taken into the oven for an initial curing cycle of 4 hours at 125 °C temperature (Figure 72a). The oven was preheated, and the temperature was controlled to cool down the part after being cured. Finally, the copper cylinder was pulled out of the MCA tube, the silicone phantom was carefully removed from the casting, and it was taken into the oven at 125 °C for one extra hour on a tray. The latter gave the model the light brown colour that characterizes the human brain (Figure 72b).



a



b

Figure 72: Brain cured in the oven

8.2.2.3 *Blood circulatory system*

8.2.2.3.1 *Brain arteries*

Chapters 5 and 6 explained the two leading technologies, Near-Infrared Spectroscopy (NIRS) and Transcranial Doppler (TCD), used for non-invasive monitoring of brain oxygenation and intracranial pressure in TBI patients. TCD typically interrogates the middle cerebral artery, which is the largest branch of the internal carotid, and mainly supplies the lateral surface of the temporal and parietal lobes (Figure 73). Also, many cerebral imaging evaluations, such as CT scans and MRI, assess the middle cerebral artery to define CBF, flow velocity, and cerebral infarction after trauma [259]. Although the phantom has not been designed for TCD measurements or diagnostic images, it includes the middle cerebral artery in the brain circulation, given its clinical relevance. Considering that this research aims to develop a non-invasive sensor for brain oxygenation and intracranial pressure monitoring in TBI patients using primarily NIRS principles, the phantom should mimic some blood circulation to assess NIRS technology. NIRS technologies do not interrogate a particular artery of the brain; instead, it assesses arterial, venous and capillary blood. However, commercial NIRS devices are usually located on a patient's forehead; hence most of the evidence on this topic is based on frontal lobe measurements. In consequence, the phantom included a representation of the anterior cerebral arteries (ACAs), which are responsible for supplying the frontal lobe (Figure 73).

The phantom's middle cerebral artery consists of a commercial silicone tube with an inner diameter of 3.2 mm, placed at 3 mm from the parenchyma surface. The artery dimension corresponds to the value of 3.1 ± 0.4 mm, measured in 100 patients' MCA by CT angiography in Rai's study [260]. It was included in the phantom's brain manufacturing process; however, once the model was cured, the researcher realized the importance of the frontal lobe supply in NIRS measurements. Therefore, a group of tubes were added to the frontal lobe of the phantom. The ACAs consist of three polydimethylsiloxane (PDMS) vessels fabricated with the novel technique of continuous dip-coating proposed by Nomoni et al. [261]. This technique has shown good results in acquiring photoplethysmographic (PPG) signals from a pulsatile tissue phantom; hence it might be of interest in the comparison of NIRS measurements between the commercial silicone tube (MCA) and the PDMS tube (ACAs). The anterior cerebral artery was fabricated with an internal diameter of 2.2 mm, corresponding with the value reported in the literature of 2.09 mm [262]. Furthermore, to include the ACAs in the already cured brain, a copper cylindrical stick ($D=2$ mm) was put inside the PDMS tube and held at the tip with a small plastic clamp. Then, the stick was pushed from one side to the other of the frontal lobe, leaving 4 mm of parenchymal tissue over the artery. With the artery in place, the clamp and the stick were removed. The ACAs have a two millimetres separation one from the other.

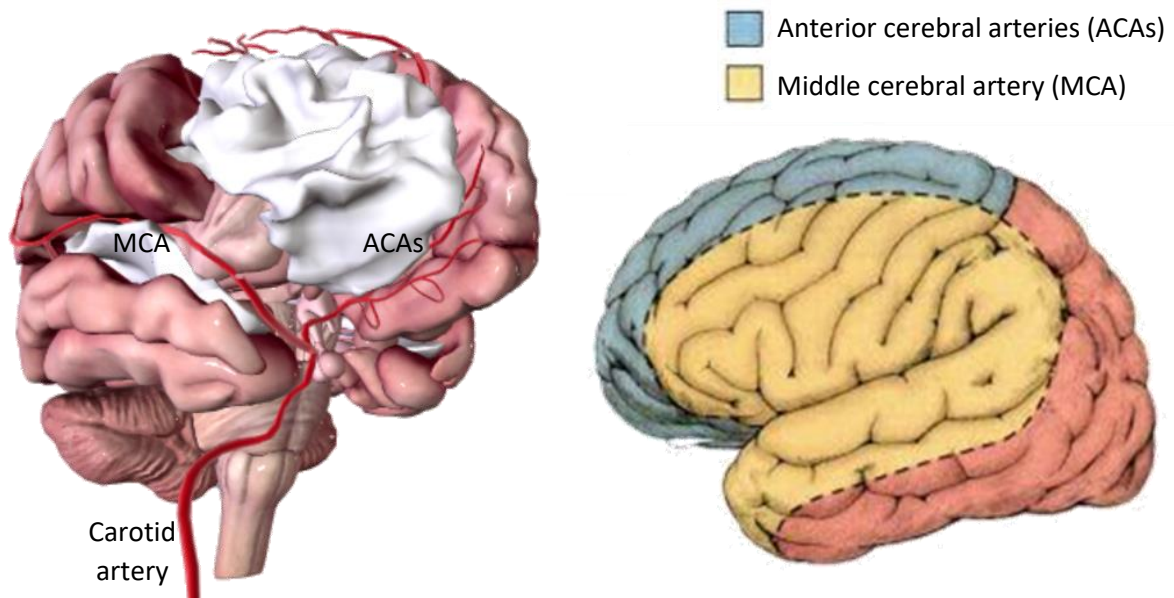


Figure 73: Vascular territories of the cerebral arteries included in the phantom.

8.2.2.3.1.1 Arteries connectors

The cerebral arteries were joined with a 3D-printed barb connector, each connected to the calvaria's internal Luer port. Each connector has an internal reservoir that receives the fluid before it is transferred to the next circulatory step. For example, the connector between the cardiovascular system and the ACAs consists of a female Luer port that is coupled to the calvaria's input port, a reservoir, and on the opposite side are placed three barb connectors to attach the ACAs. Similarly, between the ACAs and the MCA an elbow connector was placed with three barb inputs where the ACAs are attached, and then the fluid flows from the small reservoir to an output port at the lateral side of the connector that supplies the MCA. Figure 74 shows the CAD design of these connectors and an internal view of the reservoir.

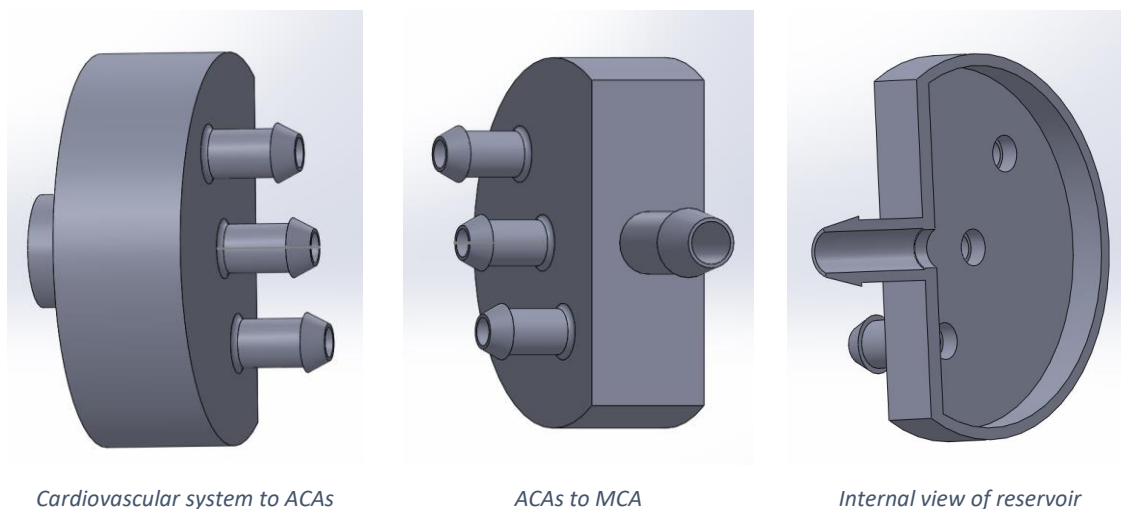


Figure 74: Brain arteries connectors

The connectors were 3D printed on the Objt30 Pro (Stratasys, MN, USA) in a black PolyJet™ photopolymer. After completion, the gel-like support structures (SUP705) were removed from the printed parts by hand, and they were brushed using pressurized cold water.

8.2.2.3.2 Cardiovascular arteries

A cardiovascular close-loop system was designed to create a pulsatile flow through the brain arteries. It consists of a pulsatile pump that simulates the heart and some PVC Clear Vinyl tubes that carry the blood from the heart to the phantom's brain and back. The Harvard Apparatus 55-3305 (Massachusetts, USA) was used to simulate the heart's pumping action [263]. Moreover, Figure 75 shows the vessels that are involved in the cardiovascular circuit, where the pump's outlet feeds the artificial Ascending Aortic vessel (ID = 20 mm, length = 124 mm) [264], [265]. A single tap of the Ascending Aortic vessel feeds the left common carotid artery (ID = 6 mm, length = 136 mm) [266], [267]. Likewise, the common carotid artery is continued by the left internal carotid (ID = 4 mm, length = 86 mm) [266], [267], which is connected to the phantom brain arteries. The outlet of the phantom is plugged into the jugular vein (ID = 14 mm [268]) before returning to a seal cardiotomy/venous reservoir (Affinity pixie, Medtronic, USA). The reservoir has a maximum capacity of 1200 ml and allows a flow rate of up to 7 L/min, which supplies enough artificial blood to the circulatory system.

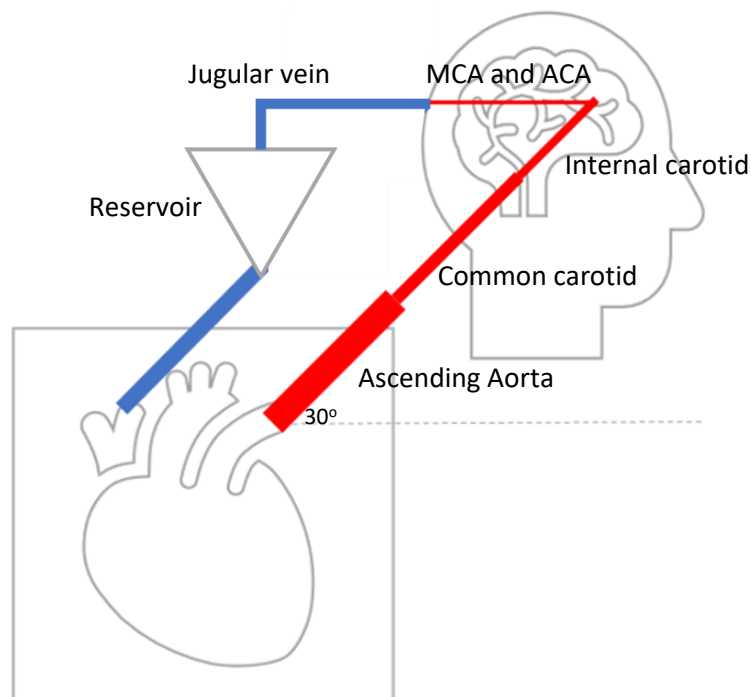


Figure 75: Phantom cardiovascular circulation design

The blood flows from the cardiotomy/venous reservoir to a glass reservoir before it goes back to the pump for recirculation. Additionally, it has also been considered that an angle of 30° and a distance of 346 mm between the head phantom and the heart, as some studies have assessed the effects of head

elevation in the care of head-injured patients [269], [270]. The pump allows changes in stroke volume between 15 to 100 ml and changes in heart rate from 10 to 100 beats per minute. Finally, the systolic phase can be adjusted from 35 to 50% of the total cycle [263]. This pump is specialised for large animal hemodynamic studies using blood.

8.2.2.3.3 Artificial blood

Handling tissue and blood is a complicated, limited process requiring monitoring and controlling multiple variables such as pH, temperature, flow, and gas dilution. This research investigated a new artificial blood recipe to mimic the optical properties of blood to enable a more rapid and replicable evaluation of an optical technology using a phantom. In 2015 Akl et al. reported a dye solution capable of mimicking the extinction spectra of haemoglobin on the NIRS range [271]. The primary dyes of Akl's solution were India ink, Cyan ink and Epolight 2735, which served as absorbers around 700 nm and 950 nm. Unfortunately, Epolight's manufacturer (Epolin, USA) removed the reference '2735' from the market, precluding the exact recipe reproduction.

In order to mimic the blood's optical behaviour, a mix of two solutions with different light absorption at red and infrared wavelengths were needed. The first one should allow more infrared light to pass through and should absorb more red light (660 nm), which can simulate deoxygenated haemoglobin (cyan ink). The second solution should absorb more infrared light (940 nm) and should allow more red light to pass through, mimicking oxygenated haemoglobin (epolight). Consequently, the recipe proposed by Akl et al. for deoxygenated haemoglobin was implemented. A 0.226% v/v of India Ink served as offset and was mixed with 4.17 % v/v of Inkjet Photo Cyan dissolved in Phosphate Buffered Saline (PBS, 0.1 M pH 7.4).

On the other hand, the Epolight reference '2057' was used to replace the Epolight 2735 due to their similar spectra, with a maximum absorption close to 990 nm. The dye reported by Akl et al could be diluted in water, while every other Epolight reference with a peak absorbance in the near-infrared can only be diluted in chemical solvents such as acetone, alcohol, or ether. Therefore, for the oxygenated haemoglobin recipe, the Phosphate Buffered Saline was replaced by 1-Methoxy-2-propanol (98.5%, density = 0.92 g/mL), in which 300 mg/L of Epolight 2057 was diluted. The dye was added slowly into the solvent using magnetic stirring.

Both mixtures (HbO₂/Hb) were mixed in different ratios, starting at low levels (50/50%) and increasing progressively in 5% steps until a ratio of 95/5%. The absorbance spectra of these mixtures were collected using a Lambda 1050 dual-beam spectrophotometer from Perkin Elmer Corp. (Waltham, USA). They were compared to the haemoglobin spectra reported by Prof. Tachtsidis [272], and to the results presented by Akl [271].

8.2.2.4 Blood oxygenation system

The aim of replicating changes in blood oxygenation in the phantom was a considerable challenge; where three different approaches were evaluated in order to achieve it. The first approach consisted of multiple mixtures in various ratios of the artificial deoxygenated and the artificial oxygenated solutions presented above. The mixtures started at low levels (50% artificial HbO₂: 50% artificial Hb) and increased progressively in 5% steps until full saturation (95% artificial HbO₂: 5% artificial Hb), as it is shown on Figure 76.



Figure 76: Artificial blood mixtures

With the aim of mimicking the optical properties of blood in its different oxygenation states, the absorbance spectra of these mixtures were analysed using a Lambda 1050 dual-beam spectrophotometer from Perkin Elmer Corp. (Waltham, USA). Figure 77 shows the light absorption spectra of the different mixtures within the visible and near-infrared range. It was found that the absorbance at 630 nm decreases with increasing oxygenation; at 1000 nm, it increases, while at 780 nm it stays relatively constant, which is the desired behaviour to mimic blood.

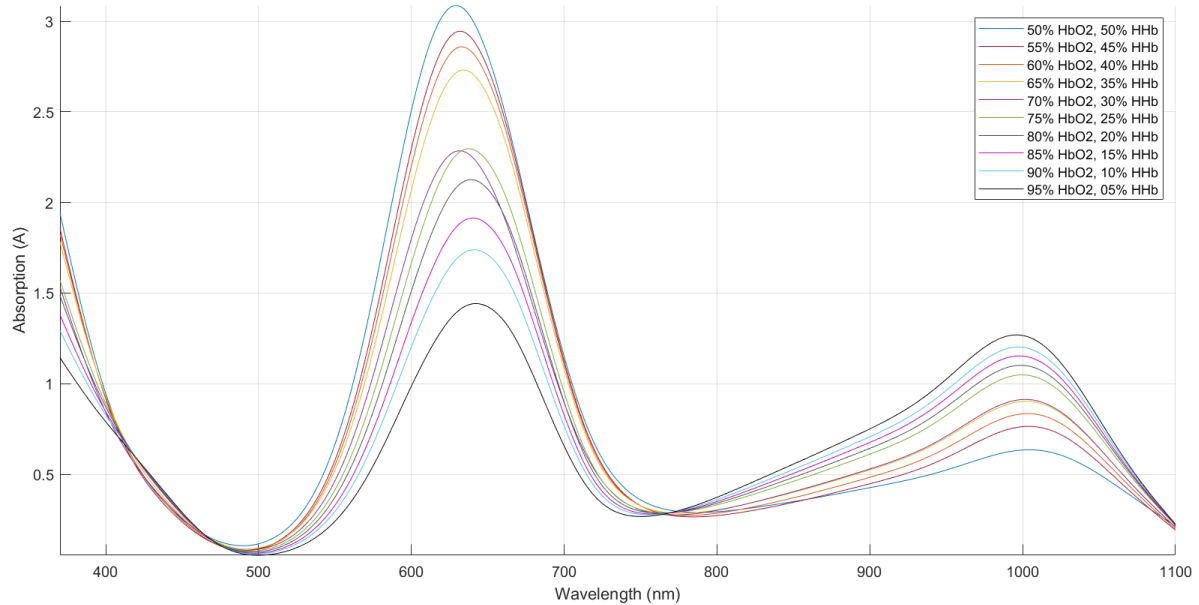


Figure 77: Spectra of the dye mixtures

The spectra of the mixtures suggested the possibility of getting optical measurements related to blood oxygenation changes, such as saturation (photoplethysmography) and tissue oxygenation index (near-infrared spectroscopy). Therefore, a custom-made probe was developed exclusively for testing changes in the optical signals of the different mixtures. The probe consisted of four LEDs (630 nm, 660 nm, 810 nm, and 1020 nm) and three photodiodes placed at 10 mm, 30 mm and 38 mm from the source, respectively. The wavelengths were selected in order to be close to the resultant absorbance peaks presented on the spectra above. PPG signals were acquired from the proximal photodiode, while the remaining two photodiodes were used to find changes in the DC signals needed for NIRS calculations.

A simple “vessel phantom” was developed to simulate the points of measurement of these pulsatile and non-pulsatile signals. The inclusion of the phantom allows a better positioning of optical sensors and a more accurate replication of tissue surrounding the arteries. The phantom involved a clear, hollow cuboid with a length of $L = 60$ mm, a width of 15 mm, a height of $H = 5$ mm, and a wall thickness of $T = 1.5$ mm. This cuboid was 3D printed using clear resin (Formlabs, Somerville, MA, USA) and filled with clear polydimethylsiloxane (PDMS) with a 3% catalyst, which has been shown to replicate mechanical properties of skin [273]. A single custom-made tube was passed through the phantom and was located close to the cuboid’s surface. The inner diameter of the artery had a value of 3 mm and was fabricated following the methodology proposed by Nomoni et al. [261]. The phantom was connected to the internal carotid of the blood circulatory system aforementioned.

Signals from each mixture were recorded using a LabView interface, and the data were processed offline on MATLAB. Firstly, the ratio of ratios (R) and their respective saturation value (SpO_2) was calculated from the AC and DC components of the signals acquired from the different artificial blood mixtures (Figure 78).

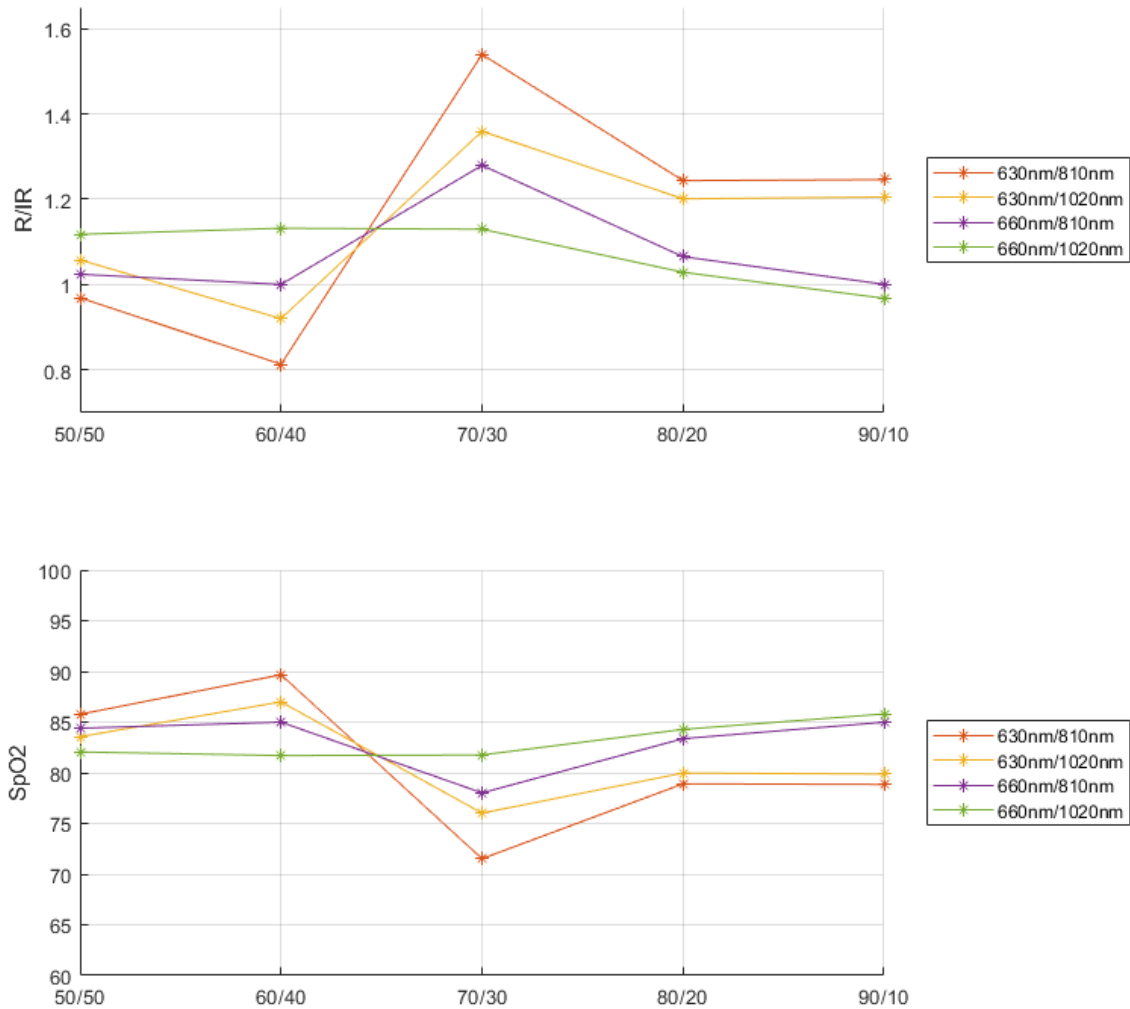


Figure 78: Ratio of ratios and Oxygen saturation at different mixtures concentrations

The calculations using the 660 nm and 1020 nm wavelengths present a reasonable linear trend; however, the difference between low and high concentrations of oxygenated haemoglobin is not representative of the oxygen saturation values. The latter can be explained by non-significant changes in the pulsations' amplitude within the different mixtures' proportions. The table published by Wukitsch (Table 16) describes how differences in the amplitude between red and infrared signals allow the measurement of arterial oxygen saturation [291].

Table 16: Relative plethysmography signals' amplitudes and arterial oxygen saturation (SaO2) values assuming the transmission intensities are equal. R = red; IR = infrared (Copied from [291].).

S _a O ₂	660 nm (R)	940 nm (IR)	R/IR
0%			~3.4
85%			1.0
100%			0.43

With the aim of verifying the absence of changes in the amplitude of the red and infrared signals acquired from the artificial blood, two extreme mixtures (50% and 95% oxygenated) were evaluated. Figure 79 shows changes in DC but not in the PPG's amplitude of the red and infrared signals at both extreme concentrations, leading to an equivalent SpO2 calculation of approx. 85%.

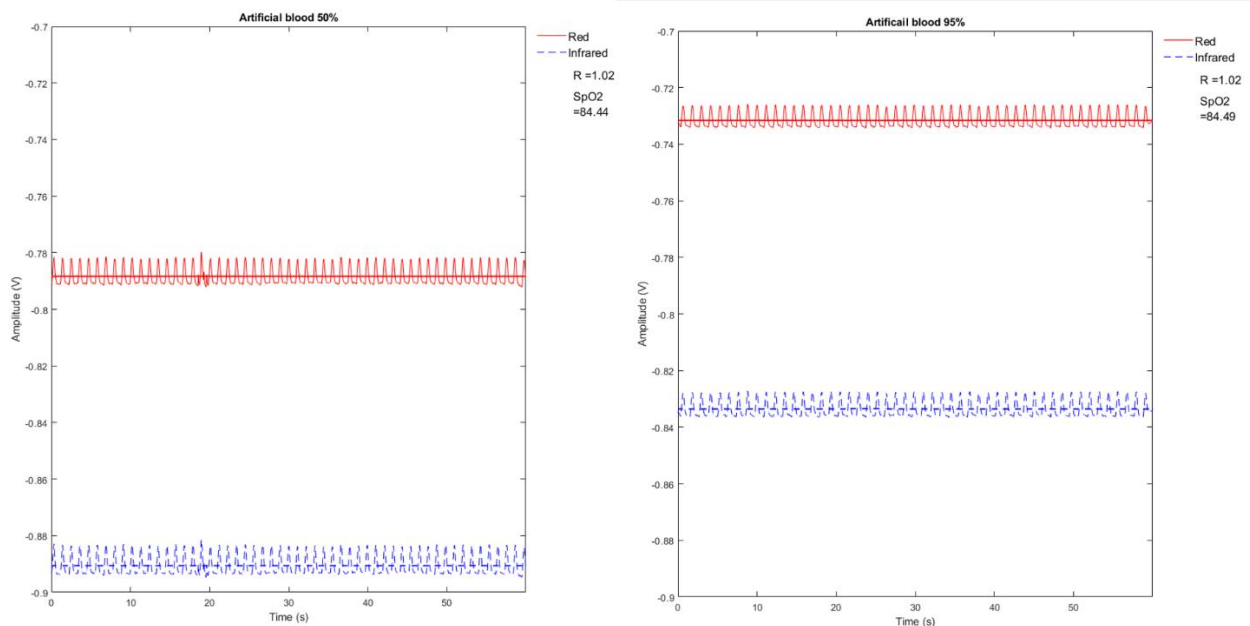


Figure 79: Blood saturation measurement from one extreme concentration (50%) to the other (95%) using artificial blood

Regardless of the lack of changes on the AC component of the proximal photodiode, which denies the simulation of SpO2 changes, a separate analysis was run to evaluate DC changes on the distal photodiodes. The latter was to find reliable changes in the DC signals that correlate to artificial haemoglobin concentrations. This assessment makes sense as NIRS measurements utilise changes in the DC component of the backscattered infrared light. The protocol to acquire the signals from the distal photodiodes used only two extreme mixtures (50% and 95% oxygenated). The recording

initialized with an empty phantom. Then the low oxygenation mixture was added (50% artificial HbO₂: 50% artificial Hb). Once the signal was stable, the fluid was removed. Lastly, the high oxygenation mixture was added (95% artificial HbO₂: 5% artificial Hb), and after the plateau was reached, the phantom was emptied again (Figure 80).

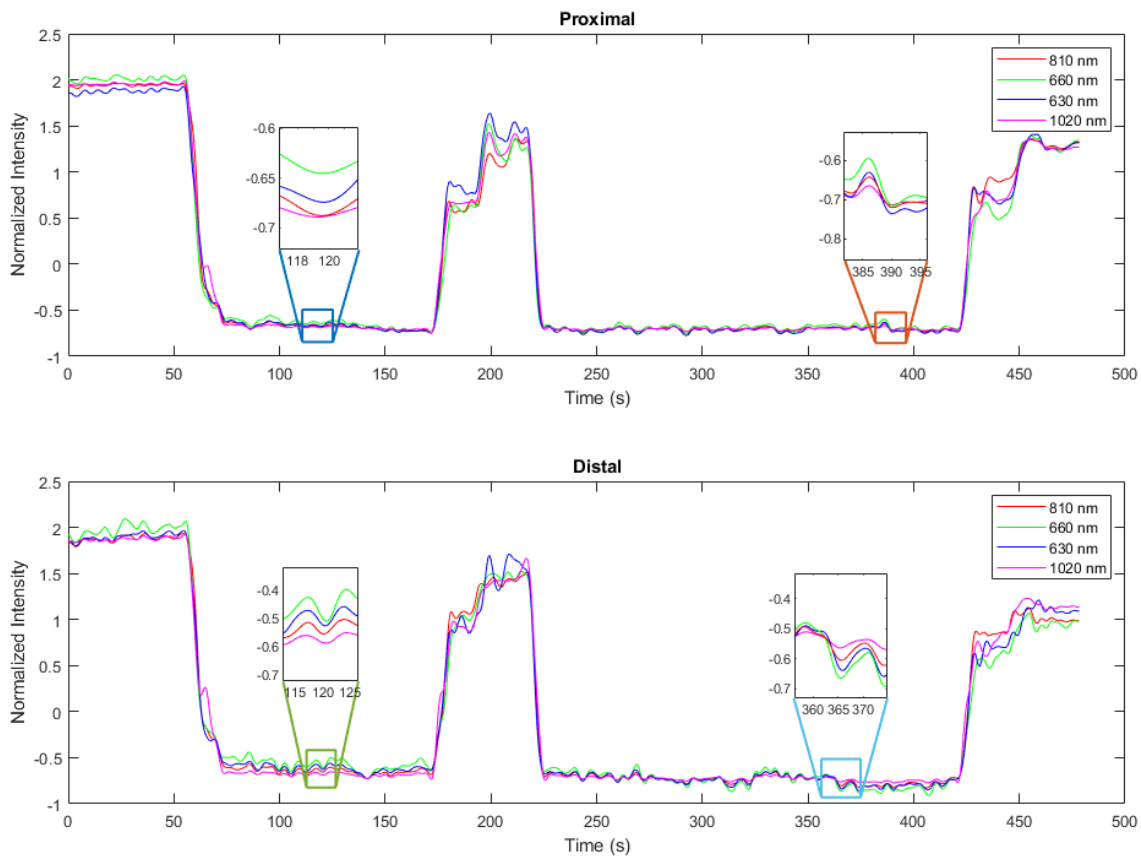


Figure 80: DC changes on artificial blood mixtures, measured by NIRS

Based on the spectral peaks, the intensity of light detected from the artificial deoxygenated mix from the 630 nm wavelength should be lower than the intensity from the 1020 nm wavelength. However, the opposite should have happened when the artificial oxygenated mix is interrogated. The zoom-in view graphs from the oxygenated mixture show that the optical signals vary and cross over (630 nm and 1020 nm) multiple times. Moreover, there is not a significant change between mixtures on the DC signals at any wavelength (Figure 80). Given these points and despite the promising spectral results of the mixtures, the designed artificial blood did not mimic the expected changes in blood oxygenation, measured either with photoplethysmography or near-infrared spectroscopy. Further experimentation is needed to adjust or redesign the oxyhaemoglobin solution, as its absorbance is significantly lower compared to the deoxyhaemoglobin, which could be confounding the results. Moreover, further studies to mimic blood oxygenation using dyes should have into consideration that absorption properties of the dyes change in a mix; and therefore is difficult to predict the mixture final response.

Consequently, this research was moved to a second approach, where animal blood and diluted gases were used to oxygenate haemoglobin. The blood circulatory system mentioned above and a fluorescence oxygen probe (FOSPOR-R, Ocean Insight optical) were implemented in the experiment, which also included a dynamic blood perfusion system. The perfusion system was designed to allow changes in oxygen concentration within the whole saturation range (0-100%) in the circulating blood. The use of real animal blood was needed, as it contains haemoglobin capable of bonding to oxygen molecules. Then, horse blood with ethylenediamine tetra acetic acid (EDTA) was selected due to the volume required by the circulatory system (700 ml) and the anticoagulant benefits of EDTA (TCS Biosciences, UK). The blood was filtered by the cardiotomy/venous reservoir in order to prevent particles, such as clots and blood cell aggregates, from getting into the circulatory system. Filtered blood flowed into the Affinity oxygenator (Medtronic, US), where water and gas continuously circulated, as shown in Figure 81 A.

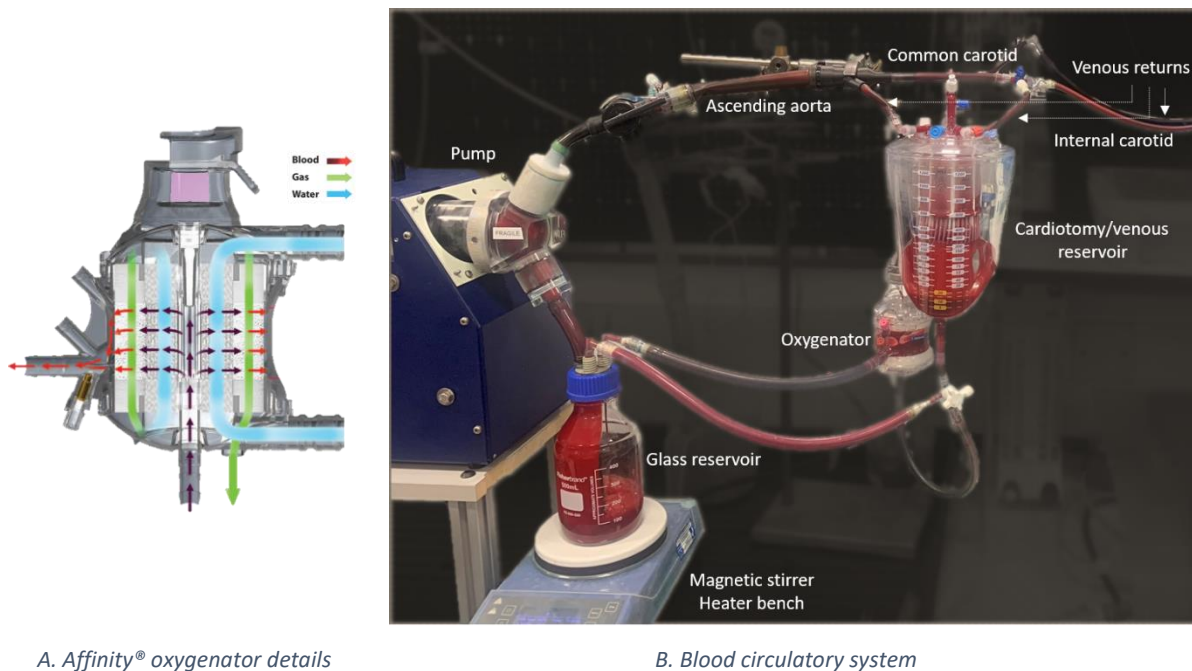
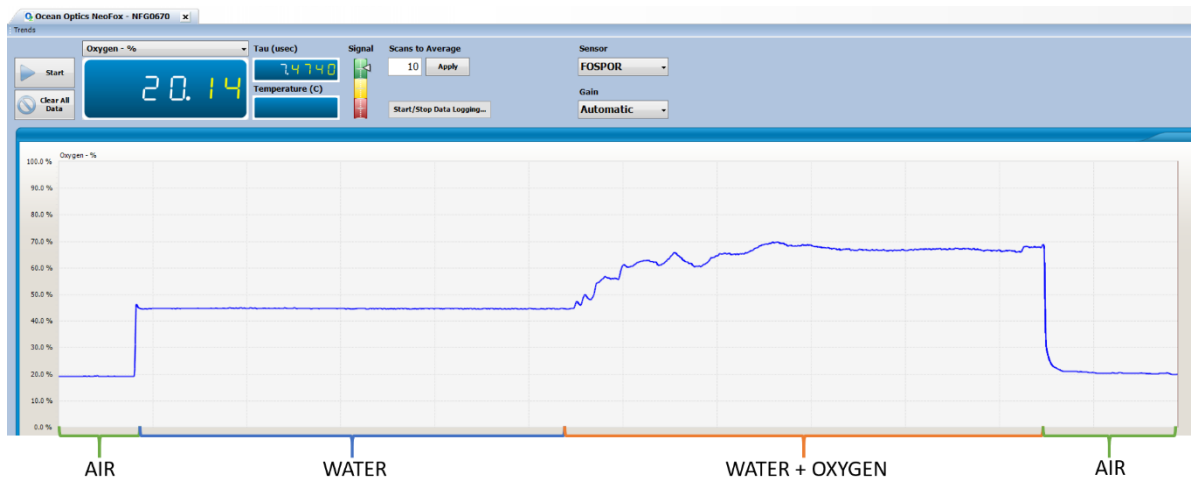


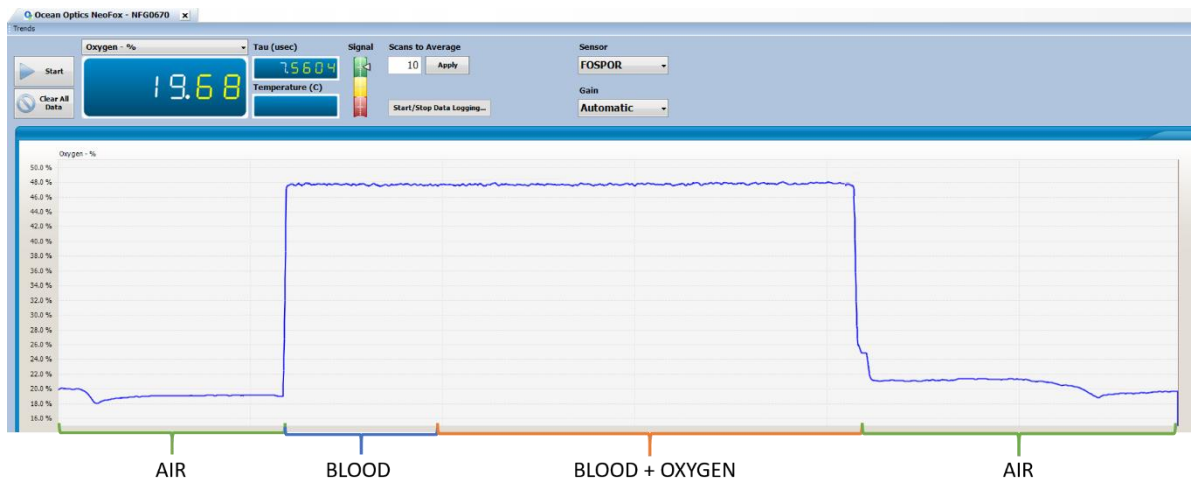
Figure 81: Animal blood oxygenation system

To simulate Earth's atmosphere, where haemoglobin saturation is 100% in healthy people, a ratio of 21% oxygen and 79% nitrogen is needed. The oxygen haemoglobin dissociations curve, which estimates the haemoglobin oxygen saturation based on the O_2 partial pressure in the blood, was used to control blood oxygen saturation in the system (Figure 81 B). Since the partial pressure in the air is the partial pressure in the liquid, by Henry's Law, the associated ratio of oxygen to the total air needed to create the required O_2 partial pressure was calculated by dividing the necessary O_2 partial pressure by 760 mmHg (atmospheric pressure at sea level). A Serinus Cal 1000 dilution calibrator (Acoem Ecotech, Australia) was implemented to dilute oxygen and nitrogen in specific concentrations for a

total flow output of 2L/min. Finally, the animal blood oxygenator system involved a magnetic stirrer, and a heater bench, where the oxygenated blood was preserved continuously in movement at 37 degrees to avoid clot formation. In theory, by adjusting the oxygen and nitrogen concentration rate that flows into the oxygenator, it should have been possible to control the oxygen concentration in the blood pumped into the head phantom, similarly as was proposed by Kurth et al. [227] in their neonatal phantom.



A. Response of the FOSPOR-R probe to diffused oxygen into the water.



B. Response of the FOSPOR-R probe to diffused oxygen into animal blood.

Figure 82: FOSPOR-R response

In this case, the system was tested with the FOSPOR-R. The probe was initially immersed in a glass reservoir with water. Oxygen was diluted in the water to validate the probe response, as shown in Figure 82 A. Then the probe was immersed into the glass reservoir with blood in the animal oxygenation system. However, despite the changes in the gas concentration, the FOSPOR-R did not measure any change in the blood's oxygenation level (Figure 82 B). Moreover, no change in the blood's colour was noticed during the experiment, which visually confirmed that the haemoglobin did not

bind to oxygen. The latter could be due to the blood's working conditions, as this substance is sensitive to pH, temperature, and lifetime. All these factors can lead to clot formation and can speed up cell death. Moreover, the affinity oxygenator has very specific restrictions regarding the gas/flow ratio, the input/output drop pressure and the limitations for reusing this costly part. Therefore, after several failed tests trying to reach functional conditions, and due to the costs associated to this experiment, a third approach was proposed.

The final approach consists of a liquid phantom, which is a replica of the one proposed by Lange *et al.* [274]. The liquid phantom consists of 1500 ml of distilled water mixed with 66 mg of phosphate-buffer (PBSx10) to maintain the pH of the solution at physiological values of pH = 7.4. Moreover, 75 grams of intralipids (20%) were used to introduce scattered centres that match the scattering properties of the tissues. Finally, 15 mL of the horse's blood was added to the mixture (Figure 83). The solution was contained in a vase positioned on a hot stirring plate to keep the temperature and homogeneity of the phantom constant. The temperature of the solution was monitored and kept at 37 °C, and the solution was stirred throughout the whole duration of the experiments.

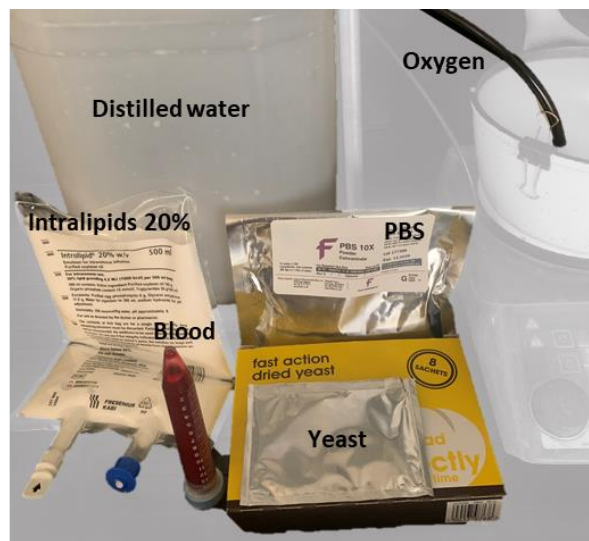


Figure 83: Liquid phantom solutes to mimic changes in blood oxygenation

The basic principle of this liquid phantom is to measure oxyhaemoglobin and deoxyhaemoglobin concentrations over cycles of oxygenation and deoxygenation of the blood. Changes in oxygenation levels, from 0 to 100%, were induced by the diffusion of pure oxygen (100%) into the liquid phantom through an air stone positioned at the bottom of the solution. Typically, the blood is oxygenated by bubbling nano-bubbles of oxygen gas through the liquid. Therefore, deoxygenation can be performed once the blood is fully oxygenated by adding yeast to the liquid phantom. The latter is accomplished due to the fact that yeast consumes oxygen via the same process of aerobic respiration as in human tissue [274].

Changes in the oxygen levels within the liquid phantom were measured with the fluorescence oxygen probe (FOSPOR-R, Ocean Insight optical), and the data was recorded using the NEOFOX Viewer software. The final version of the blood oxygenation system is illustrated in the results section.

8.2.2.5 CSF circulatory system

Additionally, to changes in oxygenation, the phantom simulates changes in intracranial pressure due to its relevance in neuromonitoring. The pressure inside the skull rises when the intracranial volume overcomes the skull capacity due to oedema, haemorrhages or an increase in CSF. In the current phantom design, intracranial volume changes are induced by epidural haemorrhages and alterations in CSF volume. To mimic CSF, this has been implemented by using the artificial CSF KIT produced by EcoCyte Bioscience (Dortmund, Germany). The KIT consists of a two-part solution, part A and part B, to produce 1000 ml of artificial CSF. Part A (50 ml) is mixed with 900 ml of deionised water, then part B (50 ml) is slowly added, and the mix is oxygenated with oxygen at 95%. This commercial recipe of artificial CSF contains NaCl (125 mM), KCl (3 mM), CaCl (22.5 mM), MgSO₄ (1.3 mM), NaH₂PO₄ (1.25 mM), NaHCO₃ (26 mM) and Glucose (13 mM). To preserve the optimal conditions of the artificial CSF, it was kept in constant circulation through a cooler system under 8°C.

The CSF circulatory system (Figure 84) involves a programmable two syringes pump (Legato 180, KD Scientific Inc, MA, USA) that can infuse and withdraw fluid at rates as low as 0.58 pl/min. Considering that normal CSF production has a rate of 0.3 to 0.4 ml/min (500 ml/day) [275], [276], one 20ml syringe is programmed to infuse 18 ml in one hour to mimic real CSF production conditions in the head phantom. Also, CSF is constantly reabsorbed by the arachnoid granulation in the subarachnoid space, which keeps the CSF intracranial volume within 90-150ml. Therefore, the second syringe is programmed to withdraw CSF from the phantom head accordingly with the simulated scenario.

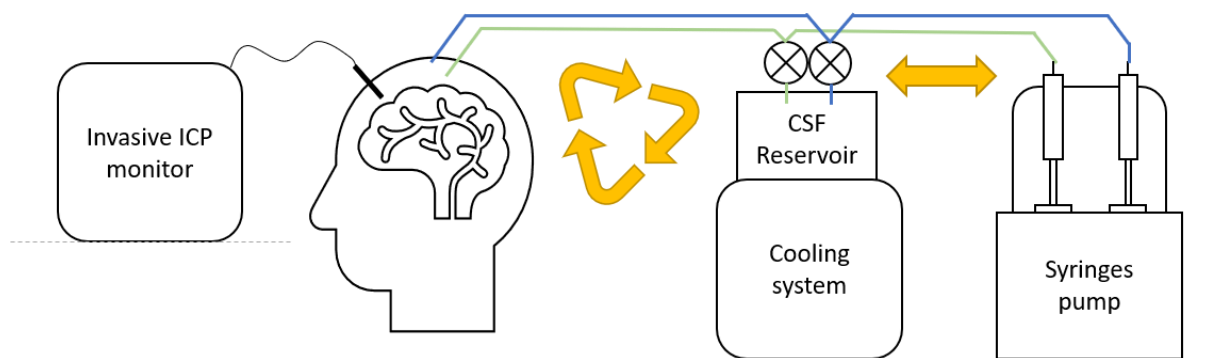


Figure 84: Phantom cerebrospinal fluid circulation design

Finally, the fluid constantly flows in a close circuit to preserve the CSF free from impurities. The pump controls the flow and direction of the fluid, from a cooling reservoir into the head phantom and back. Two 3 ways solenoid valves were synchronised with the pump to allow such circulation. For instance,

one valve at stage 1 connects the reservoir to one syringe to fill it and then changes to state 2 to infuse CSF into the head phantom, increasing ICP. Similarly, the second valve at stage 1 connects the head phantom to the second syringe to fill it and decrease the ICP, while stage 2 infuses the extracted fluid back into the reservoir under 8°C.

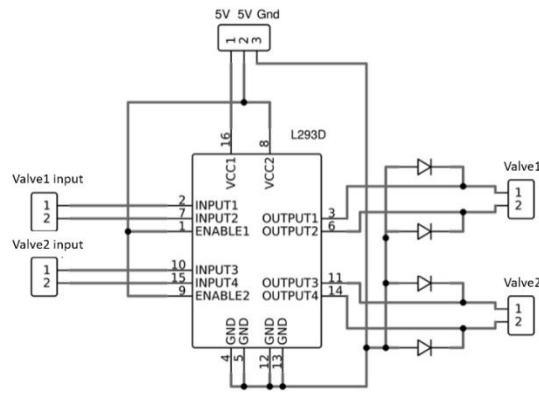


Figure 85: Valves control system

Figure 85 shows the connections of the H-bridge (L293D, STMicroelectronics, Swiss), powered by its own switching adaptor (Pro- elec 5V, 2A). Input pines are toggled automatically by the LabVIEW interface in order to control the flow direction of the solenoid latch valves (LHLA0531111H, The Lee Company, USA). The input pulse is sent through a NI DAQ to the circuit, which lasts at least ten microseconds to change the valve polarity, which requires a very low power to switch (5V, 5.5mJ/switch). As aforementioned, the valves are synchronized to allow changes in the intracranial pressure.

8.2.2.6 LabView interface:

LabVIEW (short for Laboratory Virtual Instrumentation Engineering Workbench) is a system-design platform and development environment from National Instruments used to design tests, perform measurements and data acquisition, and perform instrument control. LabVIEW operates using a graphical language (also known as G language), adopting graphical scripting techniques in a Virtual Environment. In consequence, LabVIEW programs are called visual instruments (VIs). In LabVIEW, the source code is developed graphically in a Block Diagram on which the programmer connects different function-nodes by drawing wires. The VI runs in the Front Panel, where the user can interface with controls and indicators like knobs, dials, graphs, and LEDs. Every Front Panel control or indicator has a corresponding terminal on the Block Diagram, connected to functions and structures from LabVIEW's library to put together the algorithm.

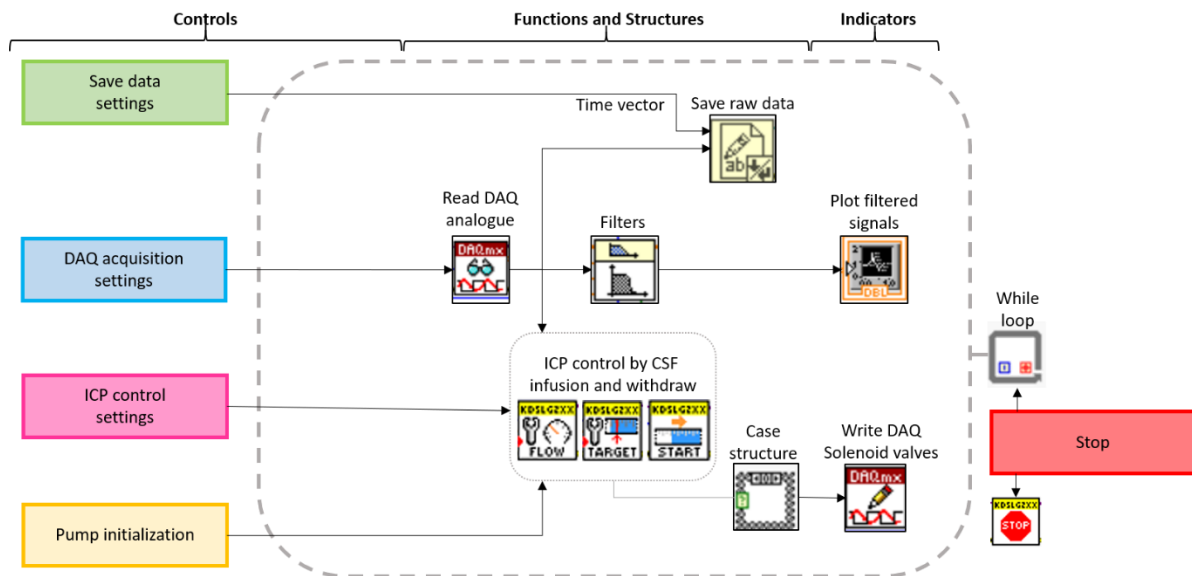


Figure 86: LabVIEW summarized Block Diagram for the phantom

The graphical nature of LabVIEW makes it ideal for the visualization and control of the phantom's parameters. The implementation of multiple functions and conditional structures, as well as the integration of the KD Scientific modules, allowed the automatic control of the CSF system from the interface. Likewise, the interface displays the invasive ICP and ABP signals while they are recorded. Figure 86 is a visual representation of the more significant elements of the phantom's interface code.

8.3 RESULTS AND DISCUSSION

8.3.1 Materials

The spectra from the phantom materials and the animal samples are shown in Figure 87. In all cases, the phantom spectrum lay between the spectra of the animal samples, yet it is important to consider the differences in the samples' thickness. This initial visual inspection of the spectra shows similar trends and the absence of major peaks or changes between the samples within the range of interest. On the transmittance comparisons, there is a closest agreement between the pigs and phantom materials for both tissues.

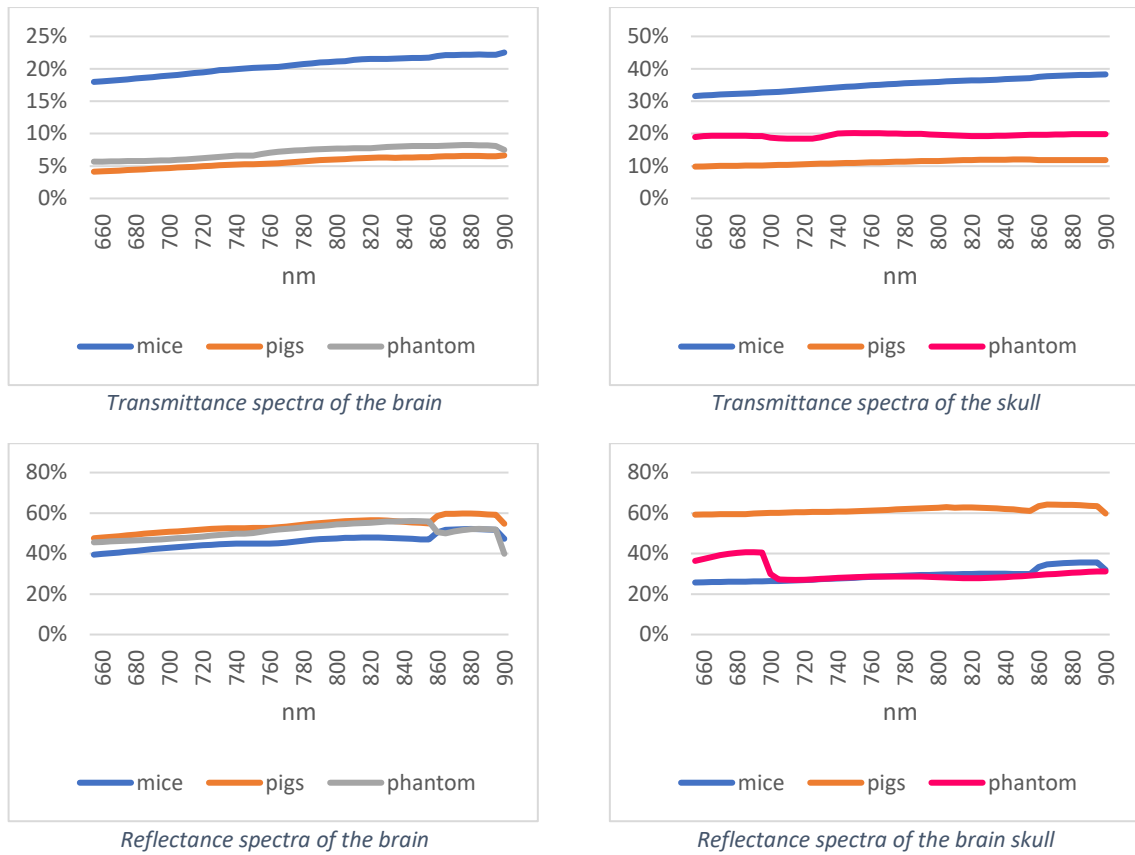


Figure 87: Spectra from the phantom materials and animal samples

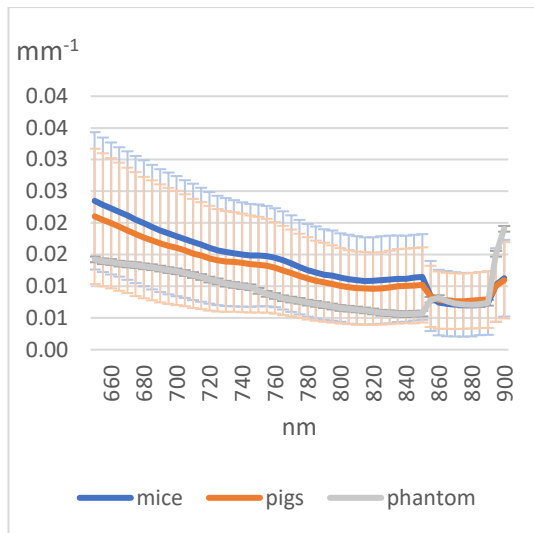
Although on the reflectance analysis, the phantom’s brain is closer to the pigs’ spectrum, the percentage of light reflected by the skull is similar to the amount reflected by the mice’s skulls, especially within the range of 700-900 nm. Moreover, mathematical methods were implemented to compare the spectra point-by-point. The calculated Mahalanobis, Euclidian and Manhattan distances are shown in Table 17.

Table 17: Mahalanobis, Euclidian and Manhattan distances between the phantom materials spectra and animal samples’ spectra.

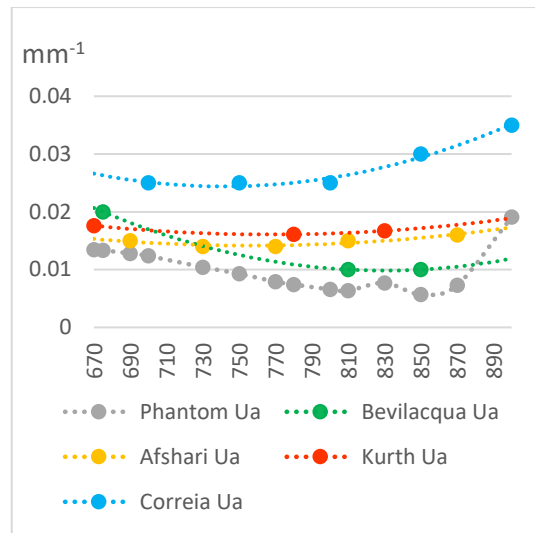
Sample	Measurement	Mahalanobis	Euclidian	Manhattan
Mice brain	Transmittance spectra	1.20	0.95	6.72
Pig brain	Transmittance spectra	1.20	0.11	0.74
Mice skull	Transmittance spectra	3.64	1.12	7.89
Pig skull	Transmittance spectra	2.5	0.59	4.15

Sample	Measurement	Mahalanobis	Euclidian	Manhattan
Mice brain	Reflectance spectra	1.21	0.42	2.66
Pig brain	Reflectance spectra	1.22	0.35	1.76
Mice skull	Reflectance spectra	1.33	0.41	1.77
Pig skull	Reflectance spectra	1.17	2.22	15.5

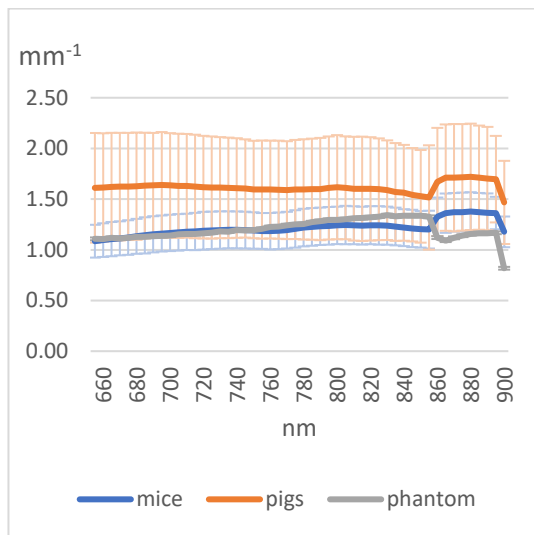
These results corroborate the initial visual inspection, where higher values indicate more considerable differences between the spectra. Then, higher values were found for the mice samples in transmittance mode, while in reflectance mode, the highest value represents the big difference between the phantom's and pigs' skulls. Furthermore, the optical properties were characterized using the IAD approach from the spectra shown in Figure 87, considering the samples' thickness and the integrating sphere specifications. Figure 88 and Figure 89 display the analysis to compare the brain and skull optical coefficients, respectively. Two kinds of comparisons were included. Firstly, the phantom's coefficients were plotted against the animal samples' respective coefficients. Figures 88a and 88c contained the confidence interval calculated from the five animal samples per tissue. Secondly, the phantom's coefficients were compared to values reported in the literature, shown in the figures 88b and 88d. For example, Bevilacqua reported coefficients from the human frontal lobe, while Afshari, Correia and Kurth described the optical properties of their brain and skull phantoms [227], [235], [277], [278]. Unfortunately, Kurth did not report skull coefficients, thus is only included in the brain analysis.



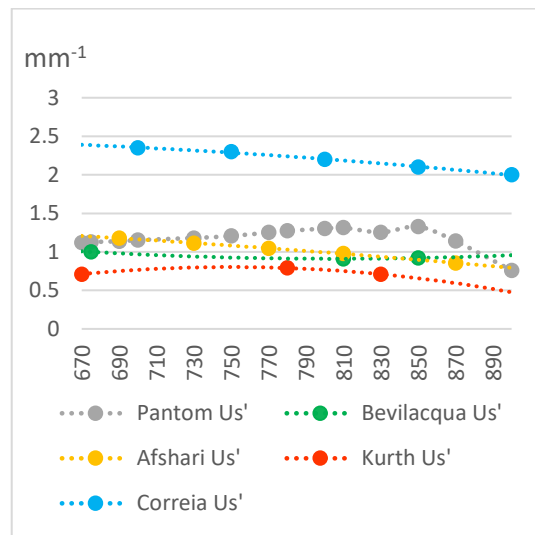
a. Absorbance coefficients, Animal samples comparison



b. Absorbance coefficients, Literature comparison [227], [235], [277], [278]



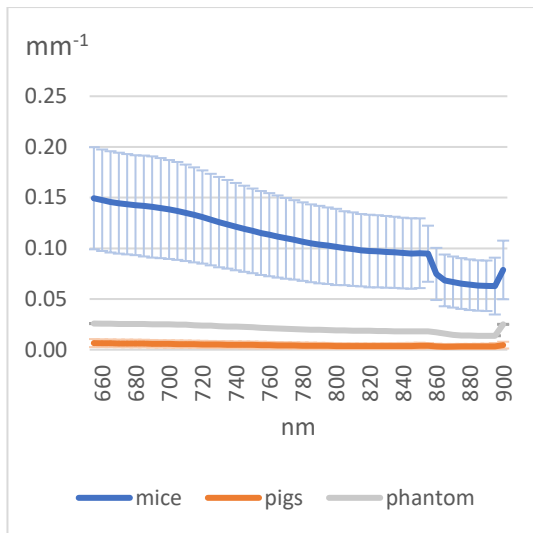
c. Reduced scattering coefficients, Animal samples comparison



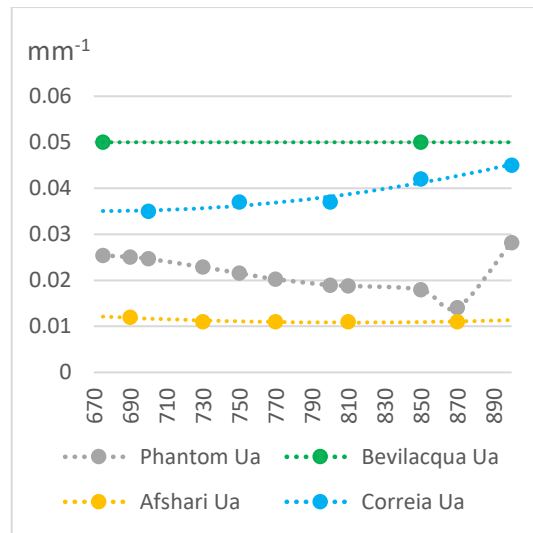
d. Reduced scattering coefficients, Literature comparison [227], [235], [277], [278]

Figure 88: Comparison of the brain's optical properties

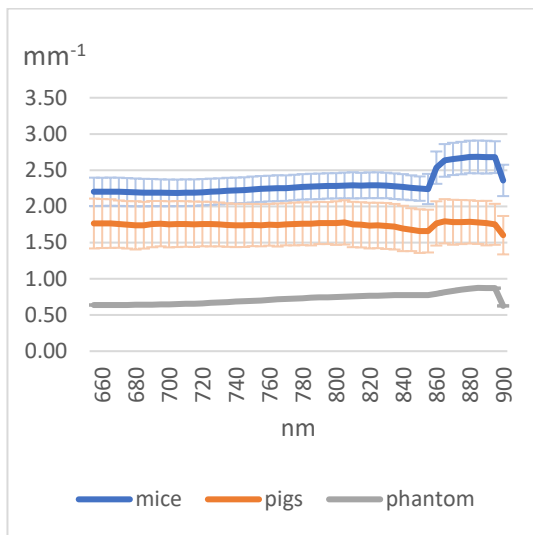
Regarding the absorbance coefficients, the brain phantom material presents lower values than those obtained from the animal samples. Yet, their values are within the 95% confidence interval for both mice and pigs (Figure 88). Similarly, the absorbance coefficients of the phantom's brain are lower than the ones reported by other authors in the literature. Still, they are very close to most authors, presenting lower differences to the values given by Bevilacqua from the human frontal lobe (Figure 88). Likewise, the brain material has a reduced scattering coefficient within the confidence intervals of pigs and mice samples; however, the phantom's scattering decreases at wavelengths above 840 nm. Compared to other authors, the reduced scattering coefficients within the range of interest are very close to the values reported from the most recent phantom published by Afshari in 2022 (error $\pm 0.3 \text{ mm}^{-1}$).



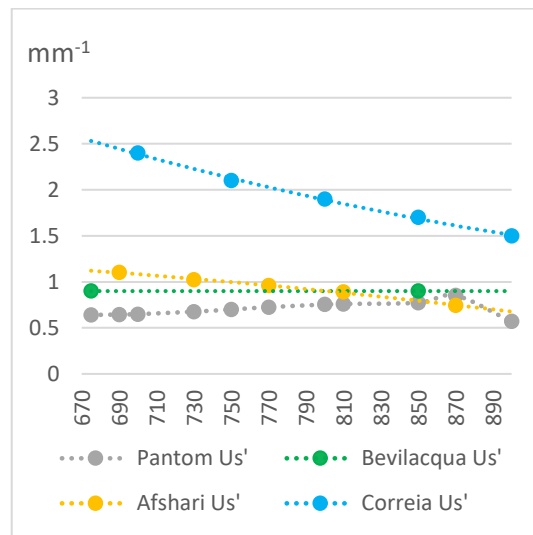
Absorbance coefficients, Animal samples comparison



Absorbance coefficients, Literature comparison [235], [277], [278]



Reduced scattering coefficients, Animal samples comparison



Reduced scattering coefficients, Literature comparison [227], [235], [277], [278]

Figure 89: Comparison of the skull's optical properties

A similar analysis to compare the optical properties of the phantom's skull is shown in Figure 89. Conversely to the brain, the phantom's skull absorption coefficients lay between the calculated coefficients for the animal samples, yet they do not overlap the confidence intervals. Nonetheless, these coefficients are within the ones reported in the literature (error $\pm 0.25 \text{ mm}^{-1}$). Similarly, the phantom skull's scattering coefficients are considerably lower than the ones presented in the animal samples, closer to the pigs' values than the mice's. Even so, within the range of interest, the phantom skull's reduced scattering coefficients are very close to the values reported by Bevilacqua and Afshari, especially at wavelengths over 770 nm. Therefore, there is enough confidence that the phantom materials can replicate the brain's and skull's optical properties.

8.3.2 Design and manufacture

8.3.2.1 Skull

The first column (“before”) of Figure 90 illustrates the maxilla’s initial condition when it came out of the 3D printer, including all the supporting material. Also, this column shows the different views of the maxilla once the support material was removed. The second column (“Post printing process”) of Figure 90 displays all the post-printing steps explained in the methods, which led to the cleaned maxilla faces displayed in the third column (“after”) of this figure. The CAD design, 3D printing and post-printing process resulted in a clear maxilla that mimics the anatomy and dimensions of an adult human man. It needs to be noted that the pictures from “before” and “after” were taken under the same conditions (i.e., camera, type of light, light intensity).



Figure 90: Maxilla's post-printing process

The first version of the calvaria printed on the Form 2 3D printer and the resultant maxilla are illustrated in Figure 91. The figure highlights the clamps that keep the skull in place by holding it from the zygomatic arches. The clamps are screwed into the metallic base, which was later replaced by the platform of the compression structure that keeps the skull sealed.

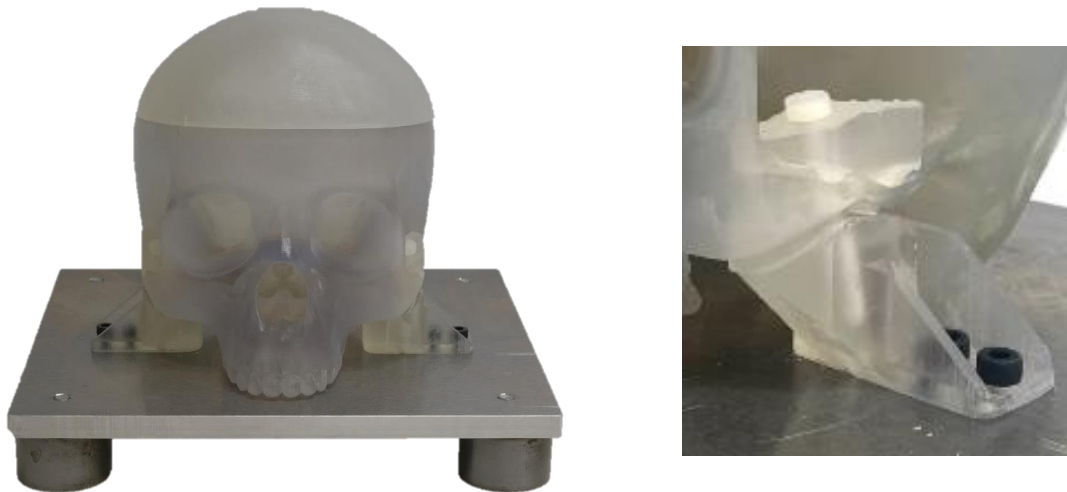


Figure 91: Phantom base and clamps design

In order to allow the simulation of multiple cerebral haemodynamic events, the initial calvaria was modified to include multiple access ports. The implementation of the external Luer ports permits the connection of a large range of commercial adaptors, valves, and syringes, among others (Figure 92). Similarly, luer ports at the calvaria's interior expand the possibility of multiple cerebral arteries, which will be described later. In conclusion, this design of the calvaria increased the versatility of the experiments that can be done in the phantom.



Figure 92: Calvaria with Luer ports allows the connection of multiple objects

Finally, the compression structure to seal the skull is shown in Figure 93. The use of T-slot aluminium extrusions allows an easy assembly of the structure, and the clamp matches the calvaria surface for a uniform pressure distribution. Moreover, the removable and waterproof silicone gasket works as the contact interface between the calvaria and the maxilla, offering extra protection against leaks. It has been noticed that it does not take more than five minutes to open and seal the skull again, which is an incredible sealing-time improvement compared to the first glue seal.

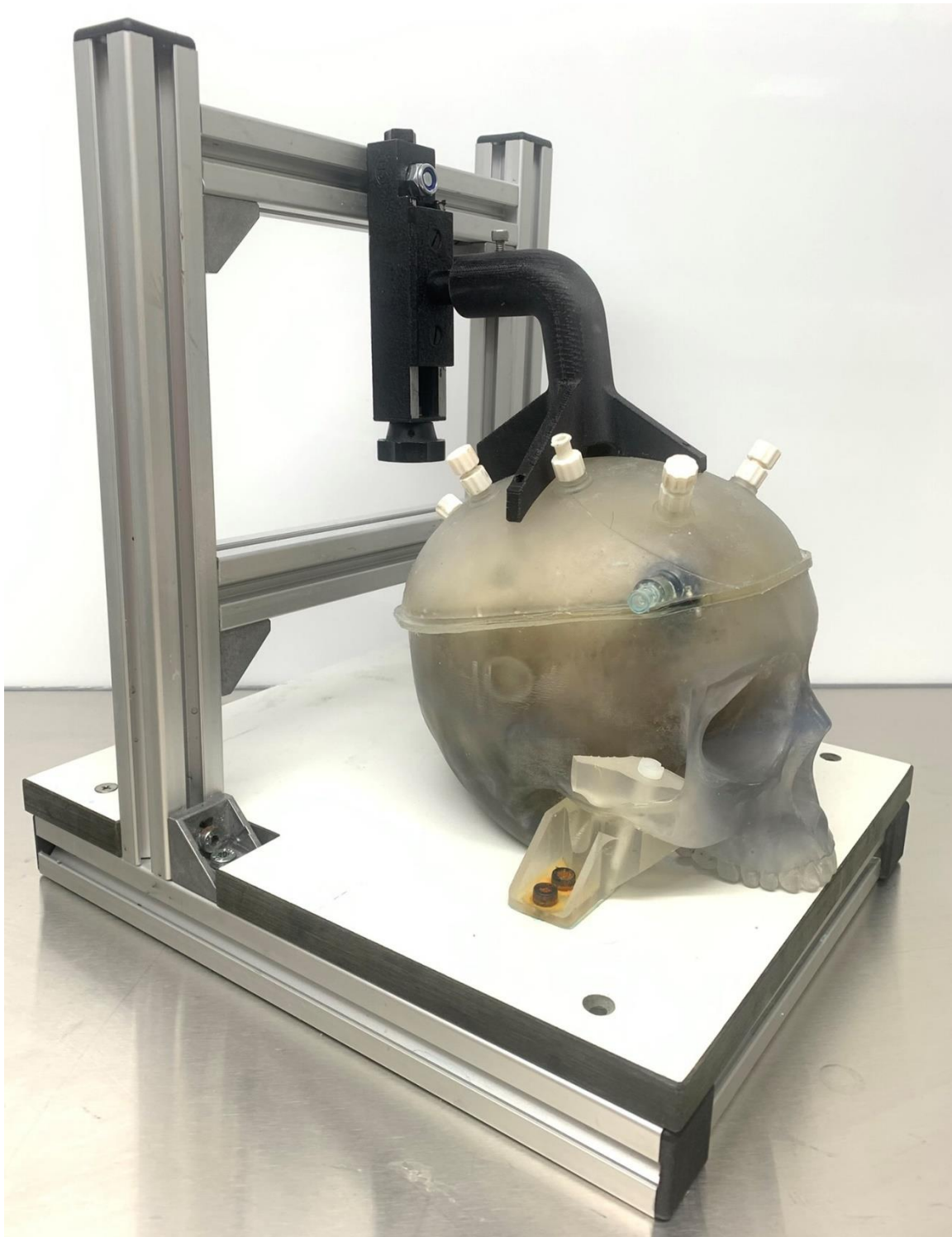


Figure 93: Final seal with compression structure

Finally, the results of the seal test are presented in Figure 94, where the ICP is held for more than five minutes at the different pressure steps from 0 to 30 mmHg. This graphical result, acquired from invasive ICP measurements, demonstrates an adequate seal performance.

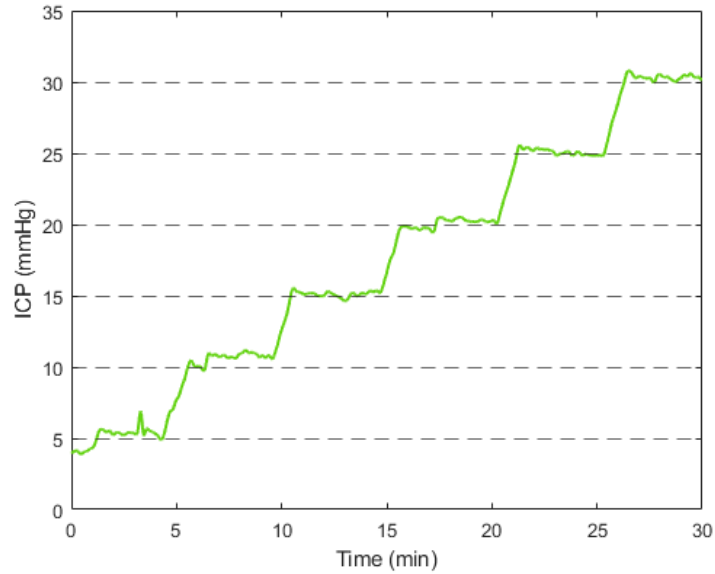
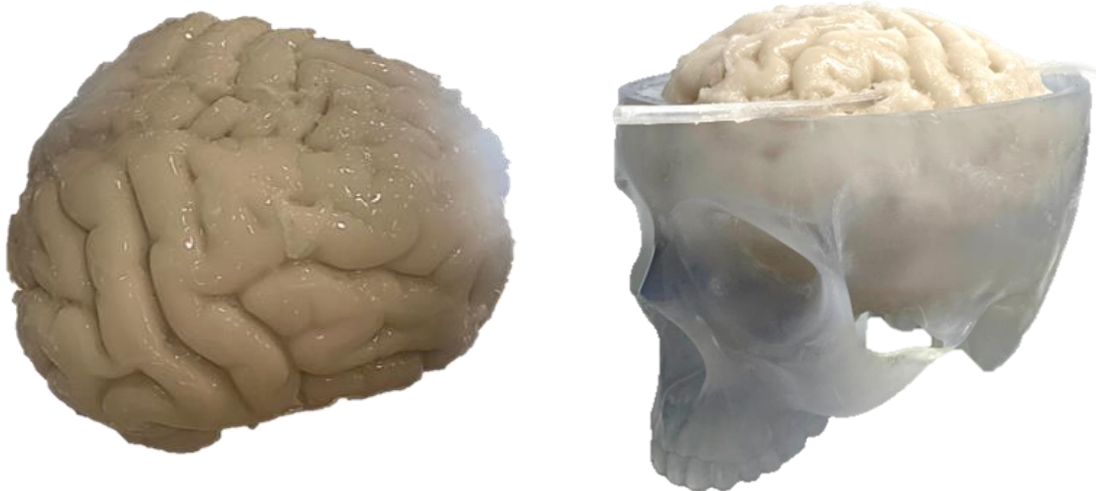


Figure 94: Seal test by increasing the ICP from 0 to 30 mmHg

8.3.2.2 Brain

Figure 95 shows the final brain model manufactured by the casting from an anatomical human brain model (3B scientific). Due to the sticky characteristic of the Sylgard silicone, the model is placed on plastic supports on the maxilla's floor in order to ensure fluid around the brain. It is possible to see the brain floating through the maxilla's walls. Moreover, the brain fits the skull and replicates the mechanical, anatomical, and optical properties as mentioned before.



Later view of the final brain

Maxilla containing the brain inside

Figure 95: Resultant brain

8.3.2.3 Blood circulatory system

8.3.2.3.1 Brain arteries

Figure 96 displays the resultant arteries and the connectors implemented for cerebral blood circulation. The photos show three anterior cerebral arteries and a representation of the middle cerebral artery. Artificial blood was pumped into the system to demonstrate the absence of leaks and regular flow.

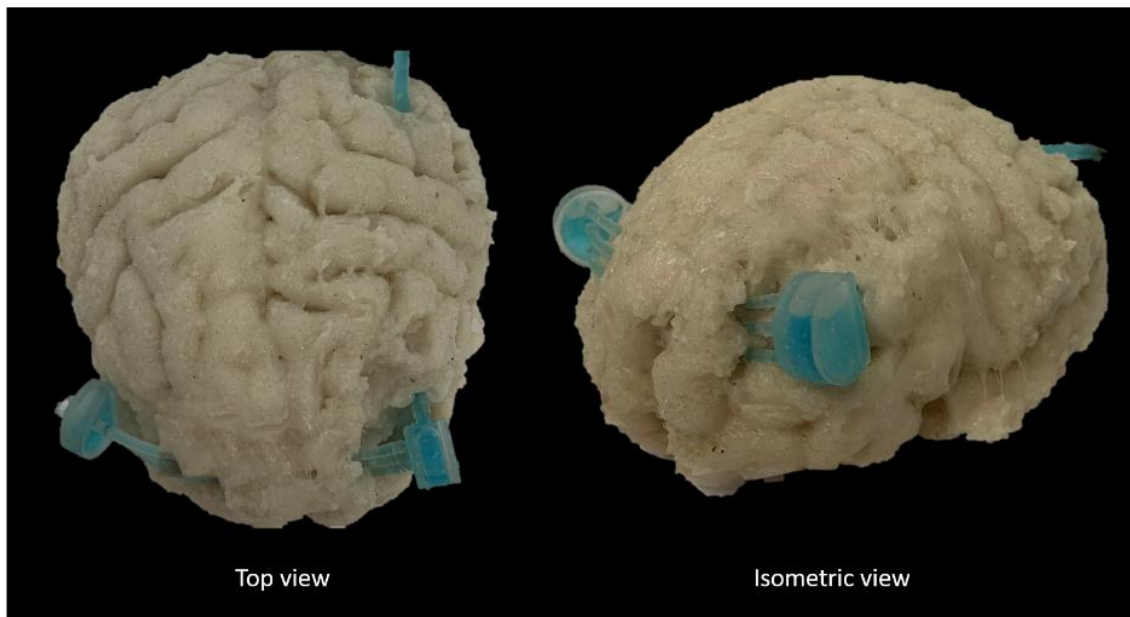


Figure 96: Middle cerebral artery and anterior cerebral arteries of the phantom

More complex and accurate cerebral circulatory structures had been included in previous studies where the aim was to interrogate cerebral blood haemodynamics [231], [279]. However, the simplistic blood circulatory system in this phantom is expected to mimic the brain's pulsatile blood flow.

8.3.2.3.2 Cardiovascular system

The extracerebral circulatory system was assembled following the methods previously described. The tubes were connected using 3D-printed custom-made connectors and commercial couplings, as it is shown in Figure 97. The system included a Harvard apparatus blood pressure sensor at the Aorta's input.

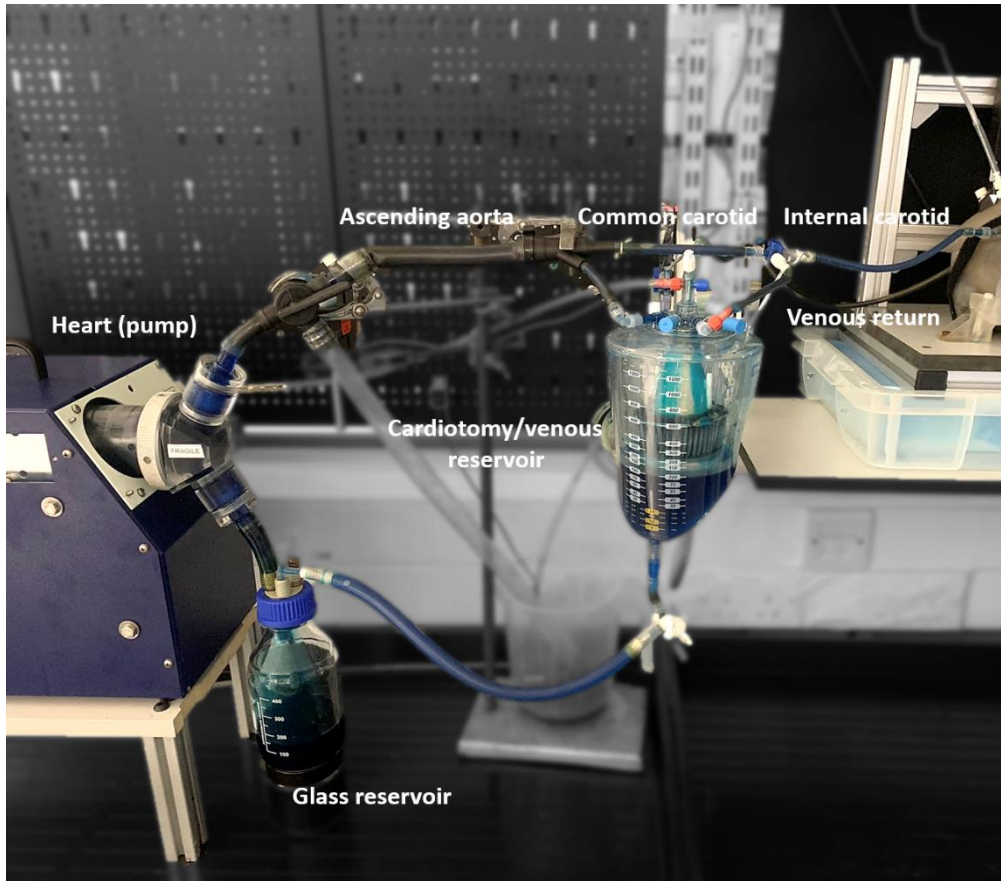


Figure 97: Phantom cardiovascular circulation

The phantom mimicked normal ABP values, with a mean systole value of 118 ± 8.5 mmHg and a diastole of 70 ± 8.5 mmHg. These values were calculated as the mean and standard deviation of the peaks and onsets envelopes (displayed in the zoom-in view in Figure 98). The resultant waveform does not have a clear dichotic notch but corresponds to a stable heart rate of 60 beats per minute. Moreover, peak values of invasive ICP presented the same frequency as ABP pulsations.

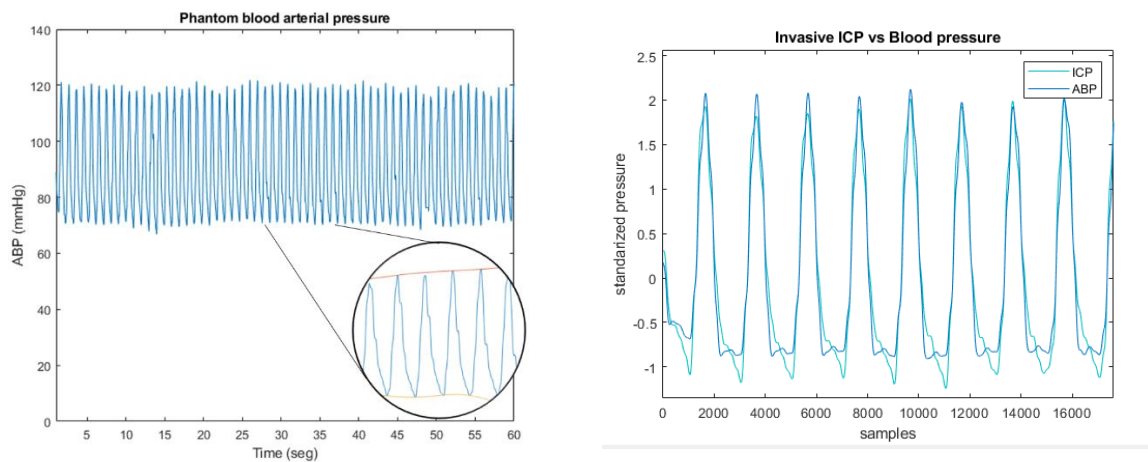
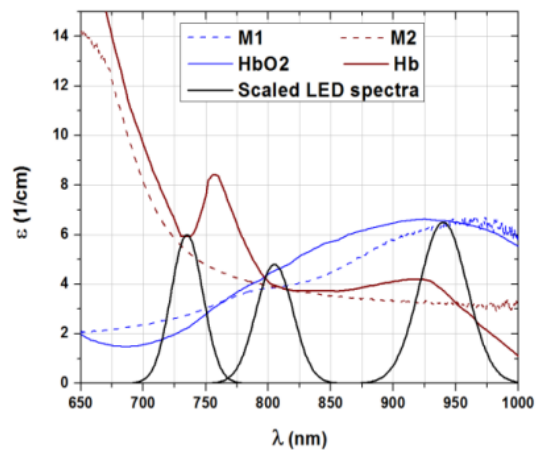


Figure 98: Phantom blood arterial pressure

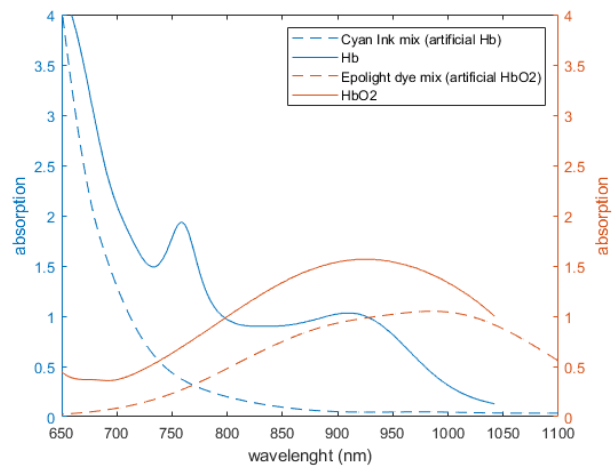
8.3.2.3.3 Artificial blood

In a previous study, Akl *et al.* utilized two mixtures with similar spectra to haemoglobin's spectra (Figure 99 a). Due to some restrictions on reproducing Akl's recipes, new mixtures were designed. The spectra of the cyan mix (artificial Hb) and the Epolight mix (artificial HbO₂) were acquired and compared to the deoxy-haemoglobin and oxyhaemoglobin spectra, respectively (Figure 99 b).



Extinction spectra of the dye mixtures (M1: HbO₂ mixture, M2: Hb mixture) compared to haemoglobin's spectra. Figure copied from AkI's study [271].

a



Absorption spectra of the mixtures (Cyan ink solution: artificial Hb, Epolight solution: artificial HbO₂) compared to haemoglobin's spectra (scaled x5000).

b

Figure 99: Artificial blood spectra comparisons

The trend on the artificial Hb mix's absorbance is similar to the spectrum of deoxyhaemoglobin for wavelengths under the isosbestic point. The latter is shifted to the left by approximately 40 nm in comparison with the isosbestic point of oxy and deoxyhaemoglobin. Similarly, the trend on the artificial HbO₂ mix's absorbance emulates the oxyhaemoglobin spectrum; however, due to the optical properties of the Epolight dye implemented in the mix, the spectrum peak is shifted 100 nm to the right in comparison with the oxyhaemoglobin spectrum peak. Despite the absence of offset in the artificial mixtures' absorbances, as reported by Alk *et al.* The trend on the spectra is close enough. Therefore, it is expected that a mixture of both artificial fluids will mimic blood's absorption peaks, allowing the acquisition of optical signals by using a probe with red and infrared LEDs.

The limitations of the designed artificial blood to mimic changes in oxygenation levels were mentioned before. Nonetheless, implementing these mixtures to acquire pulsatile signals in further ICP analyses avoided the recurrent use of animal blood and all the obstacles related to blood manipulation.

8.3.2.4 Blood oxygenation system

Figure 100A presents the final set-up to change the level of oxyhaemoglobin and deoxyhaemoglobin in blood. Figure 100B shows the response of the FOSFOR-R sensor immersed in the liquid phantom. Initially, the solution was deoxygenated as the resultant effect of the yeast, and then a peak of 100% oxygen was reached by supplying nano-bubbles of oxygen into the liquid phantom. Finally, the oxygen supply was stopped to decrease the oxyhaemoglobin levels in the solution. This change was simulated twice every time the experiment was done.

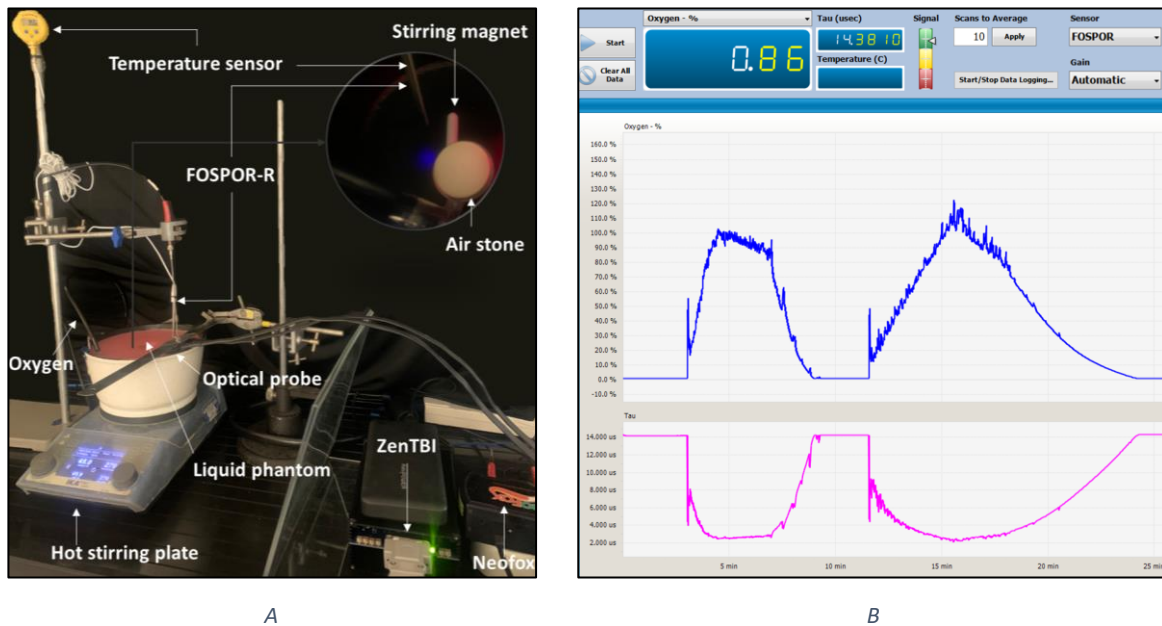


Figure 100: Blood oxygenation system

The response of the optical sensor to changes in oxygenation using the liquid phantom is reported in Chapter 11. Since it was possible to simulate changes in the oxygen concentration using this fluid, then it was implemented in the blood circulatory system of the head phantom (Figure 101). The biggest difference between the liquid phantom setup and the head phantom is the number of layers between the fluid and the sensor, which might affect the optical signals due to scattering and changes in the refraction index. Another relevant difference that affects the experiment logistics is the pressure in the system. The liquid phantom setup is an open system, while the head phantom has a hermetic circulation that allows fluid to be pumped from the reservoir to the head. This characteristic implies an increase in pressure when the oxygen supply is on, making it difficult to control the oxygen level in the head-phantom circuit. As a safety measure, the pressure valve from the cardiotomy venous reservoir remained open to reduce the risk of over pressuring the system.

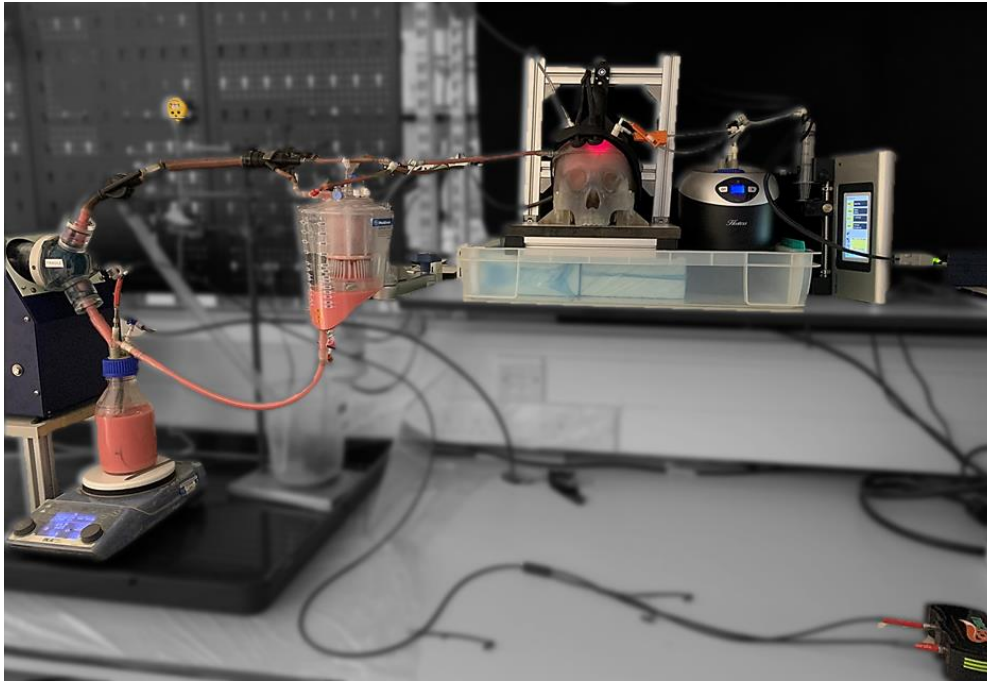
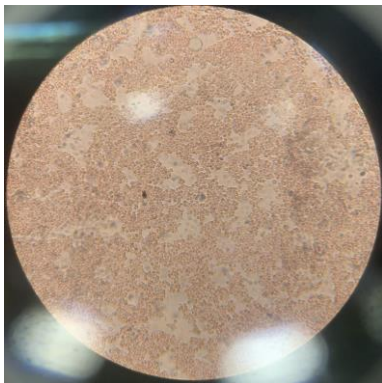
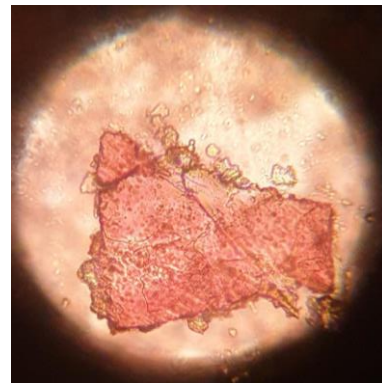


Figure 101: Oxygenation test using the fluid of the liquid phantom in the circulatory system of the head phantom

Due to the restricted availability of the solutes (intralipids, blood) used in the solution, the fluid phantom was exclusively implemented for oxygenation monitoring experiments. The latter also considers the fast detriment on the blood quality within just a couple of hours, for instance, figure 1 shows a microscope picture of a pure-blood sample at the beginning of the day and another picture of a pure-blood sample at the end of the day.



Blood sample before running the experiment



Blood sample after running the experiment

Figure 102: Blood samples quality, before and after experiments

The defibrillated horse blood used in this experiment presented intact blood cells at the beginning of the day; also, some space can be noticed between cells. On the other hand, at the end of the day, the blood sample showed signs of coagulation, where crystal structures of dead blood cells were identified. Accordingly, the experiment was run a few times with fresh blood only to ensure the presence of alive blood cells in the liquid phantom.

8.3.2.5 CSF circulatory system

The close loop control system presented in Figure 103 allows the regulation of the intracranial pressure from a LabVIEW interface. The main advantage of the syringe pump is the no pulsating flow of CSF in both directions (infusion/withdrawal). The latter allows the evaluation of the local effects of blood flow in the CSF oscillations. Nevertheless, the phantom is a simplified representation of the very complex natural system. In particular, simplifications were introduced to handle the anatomic complexity of the CSF circulatory path. The absence of ventricles represents a limitation of the system, as post-trauma ventriculomegaly cannot be simulated. However, the system reproduces the effect that enlarged ventricles lead to in the intracranial pressure by in this case building up cerebrospinal fluid into the subarachnoid space.

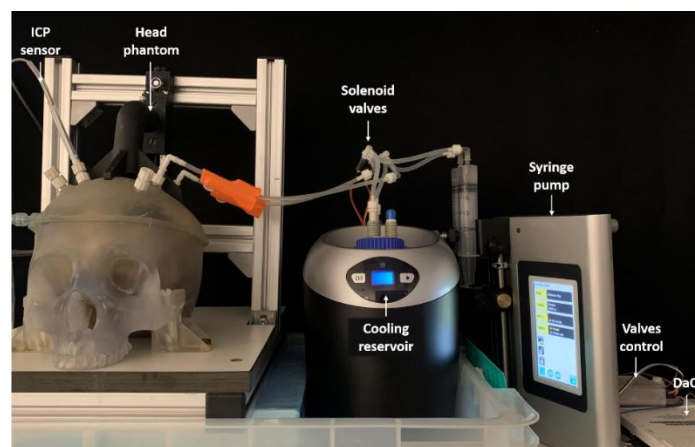


Figure 103: Phantom CSF circulatory system

Although most invasive ICP probes report the mean value for clinical decision-making, ICP is a pulsatile signal affected by arterial blood pressure and cerebral compliance. Therefore, this study has recorded the pulsations of the invasive ICP signals at a normal pressure value (10 mmHg) over several cardiac cycles. Results shown in Figure 104 (A, C) agree with the normal in-vivo conditions simulated on Bottan's phantom (Figure 104 B and D), where pulsations amplitude of approximately 0.4 mmHg were expected [14]. The latter demonstrates the effect of the heart pulsations in the intracranial pressure under normal compliance and healthy conditions.

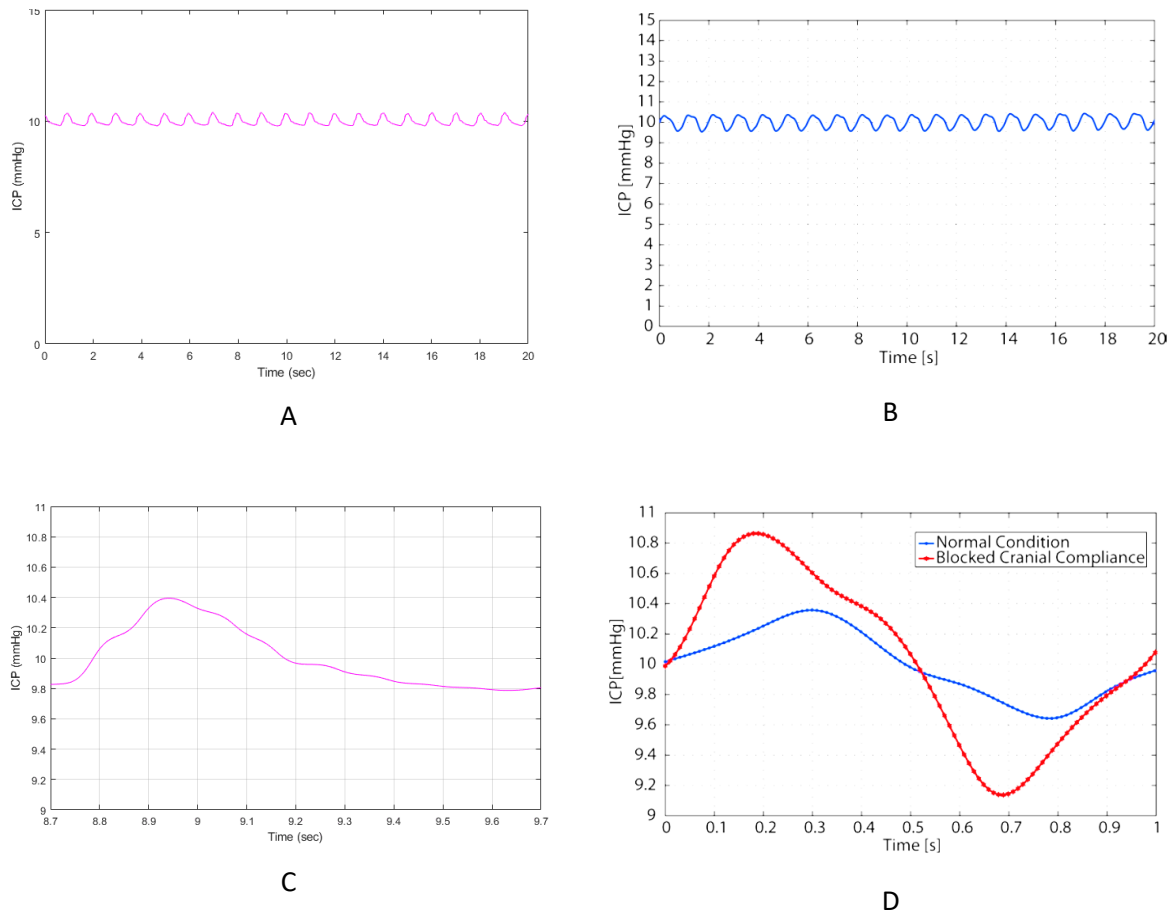


Figure 104: Intracranial ICP oscillation measure in the phantom over several cardiac cycles.

(A) pulsations of the invasive ICP signals at a normal pressure value (10 mmHg) over several cardiac cycles in the phantom. (B) pulsations of the invasive ICP signals at a normal pressure value (10 mmHg) over several cardiac cycles in Bottans' phantom. (C) one pulse of the invasive ICP at a normal pressure value in the phantom. (D) one pulse of the invasive ICP at a normal pressure value in Bottans' phantom.

8.3.2.6 LabView interface:

The interface shown in Figure 105 allows the selection of the DAQ ports for the aforementioned H-bridge and other components of the phantom as the invasive ICP bolt and the ABP transducer. Also, the infusion pump port has to be defined to control the phantom's intracranial pressure from the computer rather than the syringe pump directly. The pump uses UART communication and is usually plugged at COM5. Before running the VI is important to define all the ports and the CSF infusion criteria, such as the flow rate and the target volume. Once the VI is running, the only parameters that can be reprogrammed are the ICP target and the range, which will activate the infusion pump and solenoid valves in order to reach the target intracranial pressure. The close loop control algorithm is based on the continuous invasive measurements read from the invasive bolt through a DAQ analogue port. The mean invasive measurement (blue line) and the defined hysteresis limits (red lines) are shown next to the pump controls. Below, this graph displays the pulsatile invasive ICP, and next to it, the user can find the pulsatile invasive ABP measurement on time.

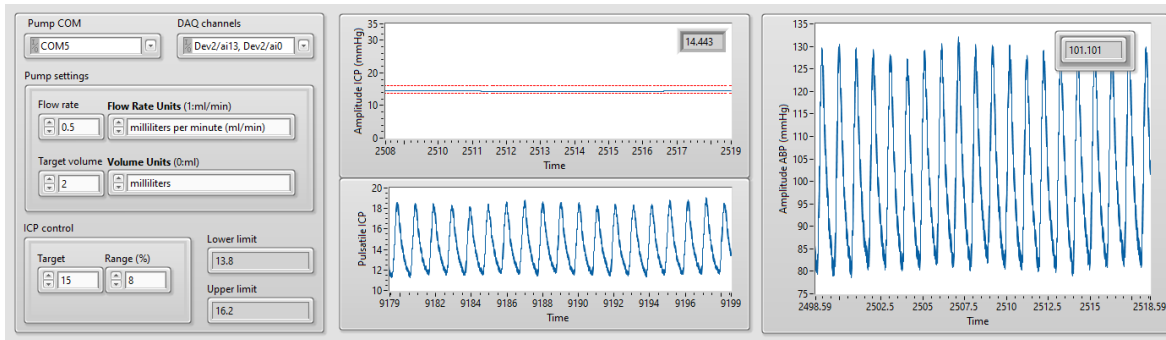


Figure 105: LabVIEW phantom interface

8.4 SUMMARY

In conclusion, the results of this study demonstrated that both phantom materials have similar optical properties to mice and pigs' tissues, where the lowest differences are against the porcine model. It was found that the morphology, which can also be called behaviour, tendency, or geometry, of the phantom's spectra were very similar to the respective animal tissue comparator. Still, there are differences in the amplitude of the absorption coefficients and the percentage of reflected light between the materials and the tissues, but the phantom's measurements are in between the animal samples. Moreover, it was found a good agreement with coefficients from human tissues reported in literature. Therefore, the proposed phantom materials are a good option for the development of a head phantom that works as the ideal platform in the evaluation of an optical multimodal sensor for TBI patients.

Moreover, this chapter reported the design and development of a head phantom with actual anatomical specifications involving a brain and skull with four brain arteries representing the frontal lobe blood supply. Also, the phantom allows measurable changes in physiologic parameters such as intracranial pressure, heart rate, blood pressure, and oxygenation level. Following this thesis aim, the phantom would allow the design and further testing of a multimodal optical sensor capable of providing information about intracranial pressure and cerebral oxygenation changes based on acquired pulsatile and non-pulsatile optical signals from the phantom's cerebral cortex arteries.

9 DESIGN AND DEVELOPMENT OF A MULTIMODAL SENSOR FOR TRAUMATIC BRAIN INJURY MONITORING: ANALOG SYSTEM COUPLED TO AN ACQUISITION LABVIEW INTERFACE

9.1 INTRODUCTION

This thesis explores the capability of NIR signals to provide information about intracranial pressure and cerebral oxygenation changes. In order to investigate this, reflectance pulsatile (AC) and DC signals were acquired from a head phantom, where physiologic changes commonly presented in TBI patients were simulated. This chapter describes the design, development, and manufacturing of a custom-made, multi-parametric sensor to acquire optical signals from the phantom described in the previous chapter. Thus, this chapter is sectioned into three main parts: the probe, an instrumentation system to acquire the analogue signals and a LabView interface to process and record data. This chapter was published in Applied Sciences (DOI: 10.3390/app13085211) [280].

9.2 METHODOLOGY

9.2.1 Probe

As many other optical modalities (i.e., Photoplethysmography (PPG), NIRS, etc.), the sensor's probe design considered light emitters to shine into the tissue and photodetectors to acquire the backscattered light. These optical components' quantity, topology, and placement were defined based on the sensor's application and anatomy location. Firstly, the sensor's application is to interrogate non-invasively the brain and to estimate changes in ICP and cerebral oxygenation. Secondly, the sensor's location is on the right or left side of the forehead, avoiding the midline sinuses. Implementing NIRS principles to PPG measurements opens up great opportunities for extending the capabilities of both techniques. By doing so, the same sensors and technology can be used to obtain parameters relating to tissue oxygenation and intracranial pressure. Therefore, this research utilised four wavelength emitters and three photodetectors in a reflectance mode probe to apply photoplethysmography and NIRS physical principles.

9.2.1.1 Optical parts and operating principles

Four light-emitting diodes (LEDs), also known as sources, were carefully chosen to interrogate specific information from the brain. The wavelengths used are 660 nm, 770 nm, 810 nm and 880 nm. As mentioned before, this research aims to explore the changes in the morphology of the optical pulse, for calculating a computational model, based on quantifiable features of the pulsatile signals to estimate absolute values of intracranial pressure. Therefore, the 810 nm wavelength, also known as the isosbestic wavelength, has the unique characteristic of being absorbed to the same extent by both

oxy and deoxy-haemoglobin [281]. Thus, it is an optimal wavelength to record an optical signal independent of blood oxygenation and could be correlated to intracranial volumetric changes. However, due to the spatial sensitivity profile of a reflectance probe, the signals are likely contaminated by extracerebral information. Therefore, extracerebral volumetric signals are acquired from a proximal photodiode in order to subtract them from the contaminated brain signals. The latter should result in the acquisition of cerebral pulsatile signals. Later, this thesis will illustrate how the feature extraction of these cerebral PPG signals can be used to estimate changes in ICP.

Moreover, wavelengths at 660 nm and 880 nm were also included in order to assess extracerebral oxygen saturation. The utilisation of these wavelengths in pulse oximetry (SpO₂) is widely reported [281]. Pulse oximetry principles rely on light absorbance by different chromophores in blood. For instance, at high blood oxygen saturations (> 80 %), the red light (600 to 750 nm) is absorbed less than the infrared light (750 to 1000 nm), while at low saturations (< 80 %), the absorption is inverted. The pulse oximetry technique utilises the pulsatile (AC) PPG components at both wavelengths to estimate the ratio of absorbances, limiting the use of the DC component for normalisation only. The ratio of ratios (R) is then related to arterial oxygen saturation by empirical curves obtained from controlled hypoxia studies in healthy volunteers. A typical relation of R and SpO₂ is shown in Equation 18 [174], [281].

$$\text{SpO}_2 = 110 - 25 \cdot R, \quad \text{where } R = \frac{\text{AC}_R / \text{DC}_R}{\text{AC}_{IR} / \text{DC}_{IR}}$$

Equation 18: Pulse oximeter calibration as a function of the ratio-of-ratios R

Furthermore, NIRS commercial devices generally use at least two infrared wavelengths (750-1000 nm) to calculate cerebral oxygenation parameters. Also, these two wavelengths are usually selected on opposite sides with respect to the isosbestic point of the haemoglobin absorption spectra (810 nm) [282]. Accordingly, 770 nm and 880 nm LEDs were included in the probe to implement spatially resolved spectroscopy (SRS) measurements.

NIRS does not include the pulsatile component of the signal and focuses on the analysis of the slow-changing DC components. Following the modified Beer-Lambert law ($\Delta A = \mu_a \cdot l$), changes in chromophores absorption coefficients ($\Delta \mu_a$) can be calculated from changes in light attenuation (ΔA) and the differential path length (l). Due to $\mu_a = \epsilon \cdot c$, change in light attenuation allows the calculation of changes in chromophores concentrations once the light travelling path (l) is known.

However, the modified Beer-Lambert law method measures only the changes in concentrations from an arbitrary point. Therefore, spatially resolved spectroscopy (SRS) is implemented to measure an

absolute tissue oxygenation index (Math explanation in Chapter 11). The Tissue Oxygenation Index (TOI) is expressed in percentage and represents the haemoglobin oxygenation saturation of the sampled volume of tissue. This method calculates the relative chromophores concentrations by measuring the relative change in light attenuation (A) along the distance (ρ). Consequently, in NIRS, two distal photodetectors are employed, close together (8 mm), and far from the light source, so the measurement is less affected by the head geometry or surface nonuniformity. Also, due to the small distance between the photodetectors (<10 mm), the change of A along ρ can be assumed linear, which is a prerequisite for SRS. Furthermore, the multi-distance approach makes SRS less susceptible to the superficial structures within the light path.

Previous evaluation of infrared light and cerebral tissue interaction at different source-detector (S-D) separations showed that higher S-D separation increases the penetration depth, but it also causes a decrease in the overall signal quality due to high absorption [220]. Accordingly, the probe design was subdivided into two sub-probes called proximal and distal probes (Figure 106). As this is a research probe, the proposed configuration will enable the flexibility to investigate the effect of S-D on optical signals on demand.

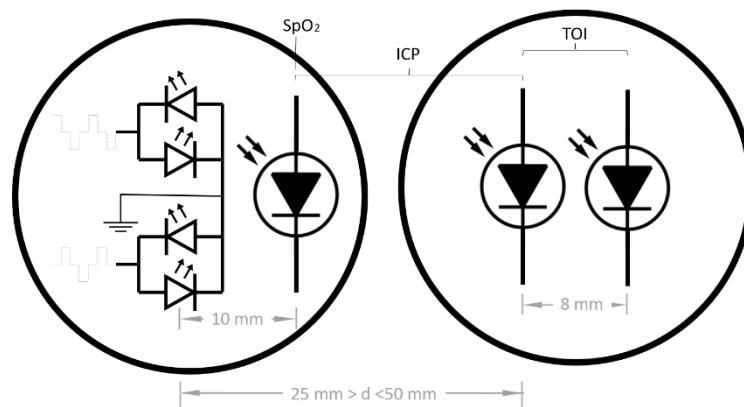


Figure 106: Probe configuration of the optical components

The proximal sub-probe consists of four LEDs (D1-D4) and one photodiode (Ph 0) placed 10 mm from the sources to detect the backscattered light from superficial tissues, which will allow arterial oxygen saturation (SpO_2) measurements. The distal sub-probe includes two photodiodes (Ph 1 and Ph 2) to detect the backscattered light from cerebral tissues, which can be separated from the proximal probe between 25 and 50 mm. The sources and distal photodiodes will allow the evaluation of cerebral oxygenation parameters through SRS.

9.2.1.2 Optical and electrical characteristics

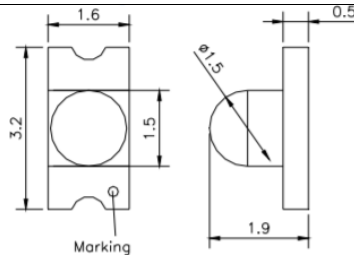
The wavelengths were chosen accordingly to the probe measurements as was explained before (i.e., ICP, SpO_2 , ΔHbO_2 , ΔHHb , TOI...). Also, the acquisition of optical signals from at least two

wavelengths permits the application of the MBL and SRS to estimate the concentration changes of two light absorbers. Moreover, as the probe is in a reflectance configuration, photons that escape outside of that main beam might reach the photodetectors and add noise to the signals. Therefore, the geometry of the selected LEDs (OIS-330, OSA Opto Light GmbH, Germany) is a round shape with a concave-convex cover that narrows the view angle and focuses the emitted light in a tight 40 degrees beam. Similarly, all three photodiodes (VBPW34S, Vishay Intertechnology Inc. USA) were the same reference. A photodiode is operated by absorbing photons and generating a flow of current proportional to the incident light power. The VBPW34S is a high-speed and high-sensitive PIN photodiode that can detect visible and near-infrared radiation with a large active area of 7.5 mm², making it suitable for low-intensity light applications such as PPG signal detection. Table 18 summarizes the optical and electrical characteristics of the light-emitting diodes and photodiodes, respectively, including their mechanical drawings.

Table 18: Optical and electrical characteristics of the LEDs and photodiodes

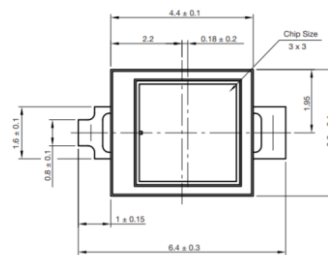
LEDs reference	OIS	OIS	OIS	OIS	Units	Description
Peak wavelength	660	770	810	880	nm	At which the intensity is maximal
Conditions	20	50	30	50	mA	Forward current conditions for the data presented in the table
FWHM	22	24	28	30	nm	Spectral bandwidth at half intensity. $OV < 20$ nm
Forward voltage	1.7	1.6	1.5	1.3	V	Voltage drops across the LED. $2 < OV < 4V$
Radiant intensity	3.5	3.5	12	28	mW/sr	Total amount of optical power emitted in a particular direction. $OV \approx 30$ mW/sr
Viewing angle	40	40	40	40	deg	Degrees from the on-axis where the luminous intensity drops to 50%. $OV \approx 30^\circ$
Forward current	30	50	30	50	mA	Desire current to power on. $OV \approx 20$ mA

Mechanical drawings



Photodiode reference	VBPW34S	Units	Description
Spectral bandwidth	430-1100	nm	Sensitivity to light at different wavelengths
Forward voltage	1	V	Voltage drops across the diode
Reverse dark current	2	nA	Current when there is no incident light. Main source of noise.
Capacitance	25	pF	Determines the speed of response. 1 < OV < 100 pF
Angle of half sensitivity	±65	deg	Defines the detection zone
Rise and fall time	100 each	ns	Equivalent to the response speed
Material and housing	Silicone/planar		Silicon photodiodes are preferred for applications < 1000nm. Planar housing provides smaller dark currents and lower current noise
Area	7.5	mm ²	Sensitive area detecting visible and near-infrared radiation

Mechanical drawings



*OV: optimal value for PPG applications [283].

9.2.1.3 Printed circuit board design

Printed Circuit boards (PCB) are copper-based sheets on which pads and tracks can be customized to distribute and wire up electronic components. The PCBs for the probe and the processing system were designed using an electronic design automation software package known as Altium Designer (Altium Limited, Sydney, Australia) and were manufactured using a Computer Numeric Control machine (Elecrow, Shenzhen City, China). Each sub-probe PCB has a circular shape, with a diameter $d = 21$ mm and boards of 1.6 mm thickness, in order to facilitate good contact with the forehead. A different

shape (i.e., rectangle) or larger diameter could cause difficulties in attaching the probe to the skin, particularly on curved surfaces. The four LEDs were placed in the proximal probe in a two-pairs configuration. At each pair, the LEDs were connected antiparallel; this configuration permits the intermittent switching of the four LEDs when connected to the processing unit. Moreover, the photodiodes were positioned over the middle horizontal axis of the sub-probes, aligned with each other. Both sub-probes included an extra pin to connect the ground plane.

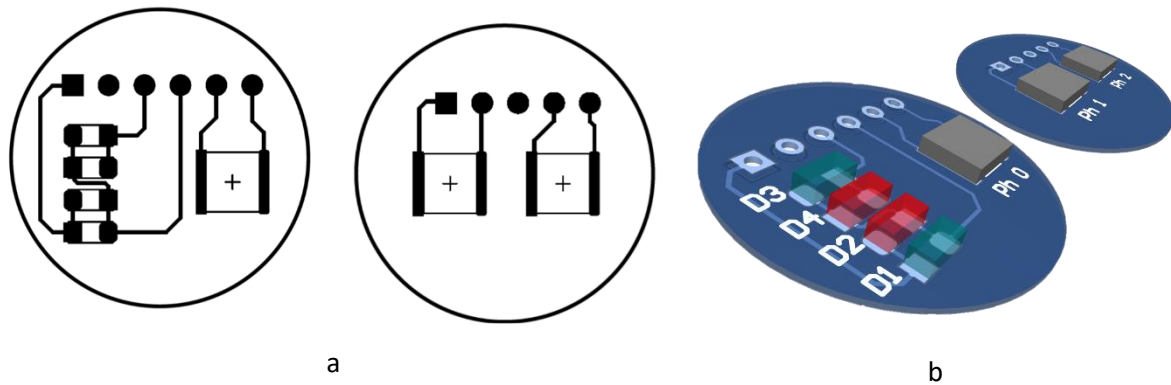


Figure 107: Reflectance probe PCB footprint (a) and PCB's 3D model (b).

In the PCB footprint in (a), the pads are dedicated to placing the optical components. In contrast, the tracks and the through holes connect the components and the processing unit. The 3D model of the PCB in (b) was used to assess the components mounted on the PCB visually. Once the design was ready, CAM files were exported from Altium designer and sent for manufacturing. These single-layer boards were assembled by hand using solder wire and a soldering iron heated to 300 degrees.

9.2.1.4 Case and connection port design

Once the optical components were soldered on the PCBs and all electrical connections checked, five and six pins' connectors were assembled to the through-holes pads of the distal and proximal sub-probes, respectively. The connectors are female, crimp housing, single row, and positive latch. The respective male connector was then pinned to a flat flexible ribbon cable to provide connections from each of the sensor's PCBs to the processing system. On the other end of the 5 and 6 pins' cables, each core was soldered on the corresponding pin of a male D-Sub 15 connector, providing the link with the processing unit (Figure 108, b). Both cables were covered with flat heat shrink tubing to strengthen the connection and avoid cable fractures. Once the PCBs, the optical components, and the cables were assembled, continuity and LEDs/photodiode functionality was verified before proceeding to fabricating the sensor's case.

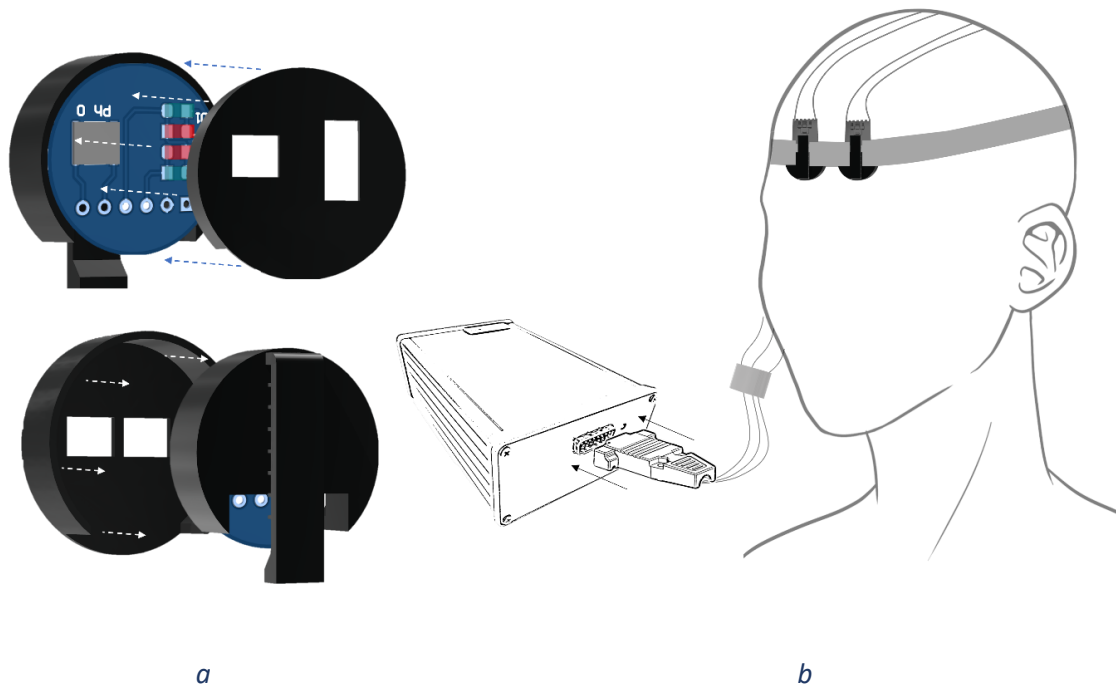


Figure 108: Sensor case 3D model (a) and diagram of the connectors to the processing system (b)

Since the probe needs to be in contact with the skin, the optical components and PCBs are required to be isolated and protected to avoid short circuits, shunting (i.e., the light reaching the photodiode without passing through the tissue), skin burns or causing skin marks. Additionally, without an appropriate case, the photodiodes can be reached by ambient light, increasing dark currents and interference noise. Therefore, the following mechanical structure aimed to shield the optical components and facilitate the contact of the sensor on the skin. The probe case was designed in a 3D CAD design software (Solidworks 2021, Cambridge, UK) and 3D printed using a Formlabs black resin (Somerville, MA, USA). The design of each sub-probe case comprises a compartment and a cover. The two parts were designed and separately manufactured in order to enclose the PCB. Also, the cover of the proximal and the distal probes have different designs in order to accommodate the optical components used in each part.

The case design did not include an optical interface placed on top of the optical components as all the experiments would take place in an in vitro set up. However, it would be possible to include a quartz window or a convex clear silicone interface to cover the LEDs and photodetectors. Such approach should not affect the optical signal. On the contrary, such approach could improve probe-skin contact, reduce losses due to any air gaps and protect the patient's skin. Both type of windows, quartz and silicone, are currently used by commercial NIRS devices as the NIRO (Hamamatsu photonics, Japan) and the O3 (Masimo, USA). The top of Figure 108 (a) shows the 3D model of the proximal probe case, holding the respective PCB. Likewise, the 3D model at the bottom of Figure 108 (a) presents the distal

probe case. A clip system at the back of each sub-probe case allows the sub-probes to attach to a snug-fitting headband (Figure 108, b). The band fits various sizes and has multiple marks to slide the sub-probes to different S-D distances. Both cases are detachable.

The case compartment has a diameter of 23 mm in order to allow the enclosure of the PCB ($d = 21$ mm). Also, the compartment has a rectangular through-cut (dist. from the edge = 2.15 mm) that gives space for the crimp housing connection. The covers' internal diameter is 23.5 mm, and its wall has a thickness of 1 mm, adding to an overall external diameter of 24.5 mm. The case compartment is inserted into the cover, keeping in place the PCB. In addition, the cover provides a wider flat surface for the attachment of the sensor on the skin.

9.2.2 Instrumentation and acquisition system

The processing system described in this section was based on a previous device designed by the Research Centre for Biomedical Engineering at City, University of London. The previous system, ZenPPG, was created to provide a common research tool for optical signal acquisitions [283]. The ZenPPG is a dual-wavelength, dual-channel research PPG system composed of five independent and interchangeable subsystems, each having different functions. ZenPPG is considered an open-source project and provides a common architecture that researchers can modify for specific purposes. Accordingly, for this thesis, three subsystems of the ZenPPG were modified to include two more wavelengths and an extra acquisition channel. Also, this new version allows high-frequency LED switching (1KHz) and the adjustment of all four light intensities from a LabVIEW interface. This new version is called ZenTBI, as the ZenPPG was specifically altered in order to provide a processing system for the TBI probe described above.

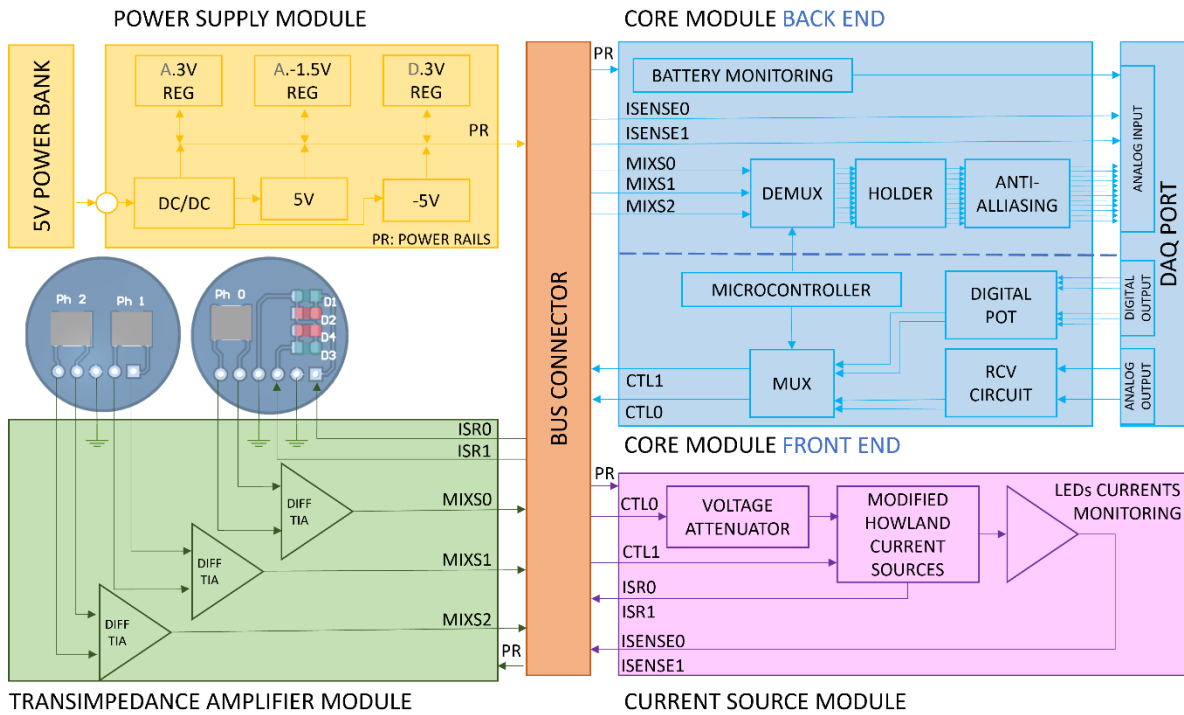


Figure 109: Detailed block diagram showing the architecture of ZenTBI.

Figure 109 shows the architecture of the ZenTBI. The processing system described in this section consists of a four-wavelength, three-channel research PPG system composed of five independent and interchangeable subsystems. Also, three external devices are connected to the ZenTBI, namely: a 5V power bank (RavPower, Shenzhen, China), a NI data acquisition card (DAQ) (National Instruments, Texas, USA) and the probe.

The design of all the modules shown in Figure 109 plays an essential role in the research objectives of this work. The PCBs of the processing system were created using Altium Designer (Altium Limited, Sydney, Australia) and were manufactured using a Computer Numeric Control machine (Elecrow, Shenzhen city, China), as well as the probe's PCBs. The modules' dimensions are 100 × 80 × 1.6 mm, except for the Current source module and the Bus connector. The dimensions of these two boards are 100×60×1.6 mm and 100×48×1.6 mm, respectively. All modules are double-sided copper-clad boards with a HASL surface finish generally preferred for hand-soldering.

9.2.2.1 Bus connector

The Bus board was not modified from the ZenPPG. It allows the connection between a maximum of six modules, three at each layer (Figure 110). The modules are connected to receptacle 50-way surface mount connectors, in which every pin at each connector corresponds to the same pin in all other connectors. Every pin has assigned an unalterable net to ensure the transmission of the voltages and signals between boards.

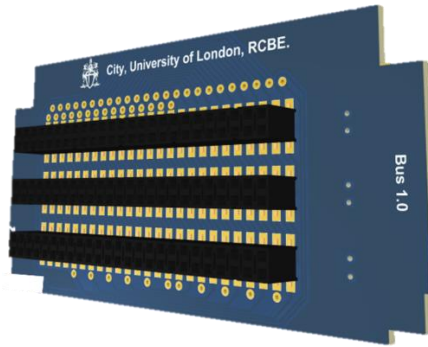


Figure 110: Bus connector 3D model

9.2.2.2 Power supply module

The Power supply module and the bus connector were the only two boards that were not modified from the ZenPPG. The module is connected through a micro-USB port to a 5V power bank with a capacity of 26800 mAh (RavPower, Shenzhen, China). The board comprises the circuitry required to regulate the USB power supply into multiple DC power rails (Figure 111). The initial power bank supply (PS) passes through an isolated point-of-load DC-DC converter (ITX0505S), regulating the initial voltage to IPOS (5V) and INEG (-5V). This dual source powers the microchips on the Current source module and the multiplexers and demultiplexers included in the Core module. The DC power supply from the dual source is regulated down to APOS (3.3V) and ANEG (-1.5V) to power the remaining microchips on the processing system. However, a separate digital power line is regulated down to DPOS (3.3V) from the DC-DC converter output, respecting its own digital ground (DGND). The later power line supplies the microcontroller, avoiding digital noise to corrupt analogue signals.

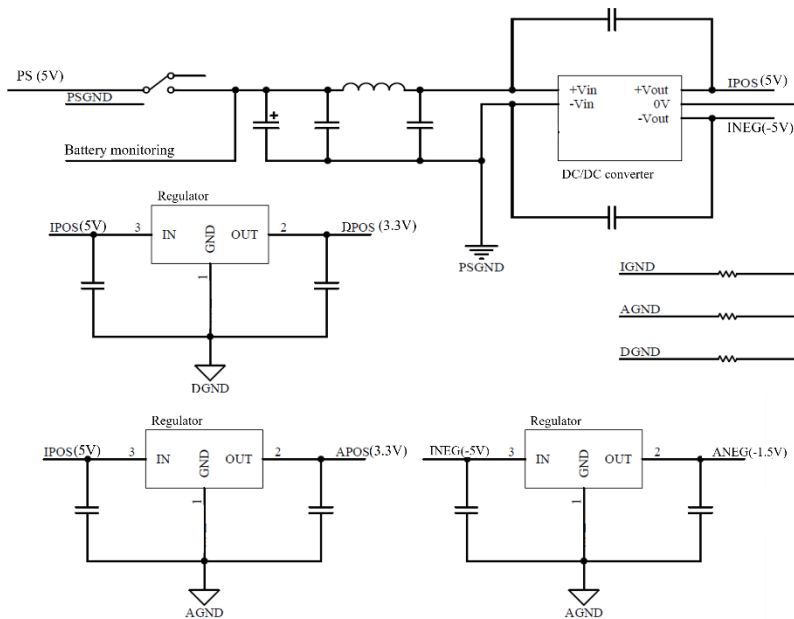


Figure 111: Power supply schematic design

9.2.2.3 Core module front end

The core module is the “brain” of the processing system. It is subdivided into the front end and the back end. The front end is responsible for the intermittent light-switching control that allows simultaneous sampling of four wavelengths. This part of the Core board hosts four independent controls to set the emitters’ currents (Figure 112) and a multiplexing circuit. Previous studies on reflectance PPG demonstrated that acceptable signal quality could be guaranteed without exceeding 50 mA LEDs driving currents [284]. Accordingly, each current control was designed to allow a maximum drive current of 100mA. The first and second control are the DAQ analogue outputs (A0 and A1) connected to voltage attenuator circuits (RCV). Thus, from LabVIEW, A0 is set between 0V and 5V, while A1 can be defined between -5V and 0V. Both outputs were then attenuated down to 0 V to 1 V and -1 V to 0 V, respectively, using voltage dividers and op-amp buffers (Figure 112 a). These controls suffer a second attenuation phase at the beginning of the Current source module to finally get 0 to 100mV and -100mV to 0V, respectively. Moreover, due to the limited number of analogue output channels on the DAQ card, the third and fourth control consist of 10K digital potentiometers (X9C103SIZT1) configured into two independent voltage dividers. One of them is supplied with 3.3V and configured with a fixed resistor of 23K, allowing changes between 0 and 1 V. The other is supplied with -1.5V and configured with a fixed resistor of 5K, creating a last output of -1 to 0mV. Each digital potentiometer is controlled from LabVIEW, where three digital signals are generated to activate (CS) the chip, toggle the INC pin to move the wiper and either increment or decrement the counter in the direction indicated by the logic level on pin U/D (Figure 112 b).

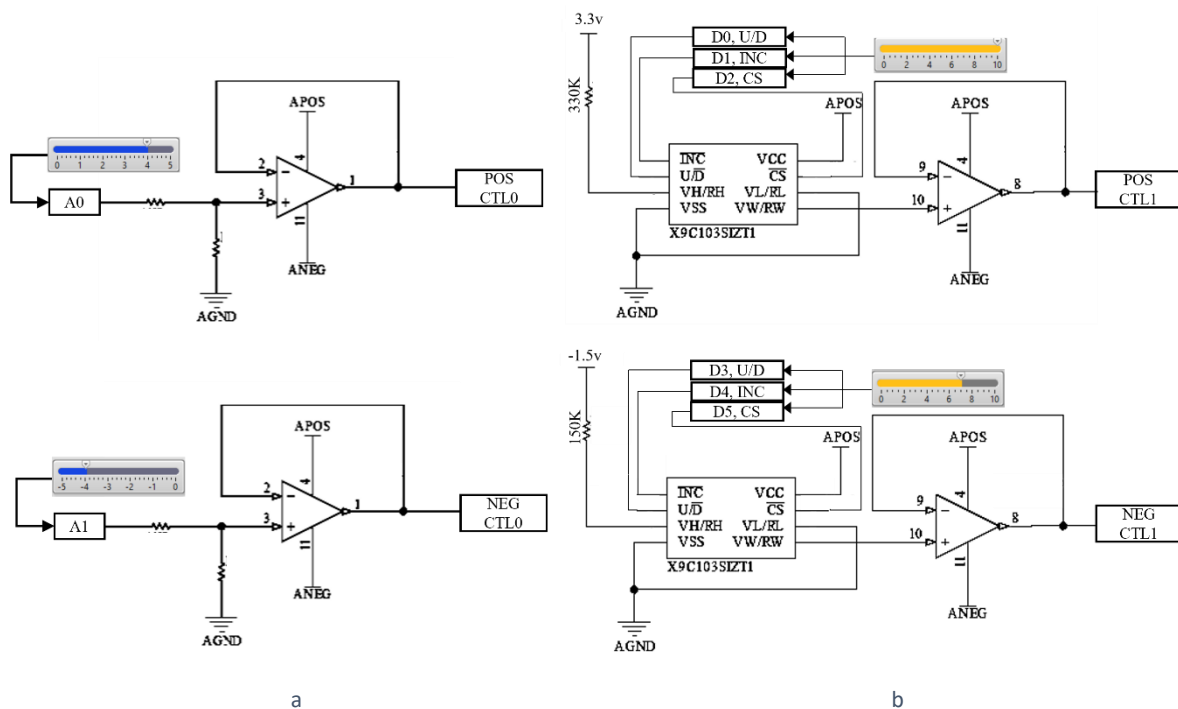


Figure 112: Controls to set the emitters’ currents

The multiplexing circuit generates timed switching signals to turn on one LED at a time, allowing the independent sampling of light at each wavelength by the photodetectors. All four current's controls and the analogue ground (0V) are connected to a double-pole 4-throw multiplexer (MC14052BD). Each multiplexer pole selects one of the three input voltage signals (either positive or negative or ground) and outputs the selected input into a single line, producing two control lines called CTL0 and CTL1. Each control line switches a pair of LEDs. When CTL0 is either positive or negative, CTL1 output in the ground (0V), and vice versa (Figure 113).

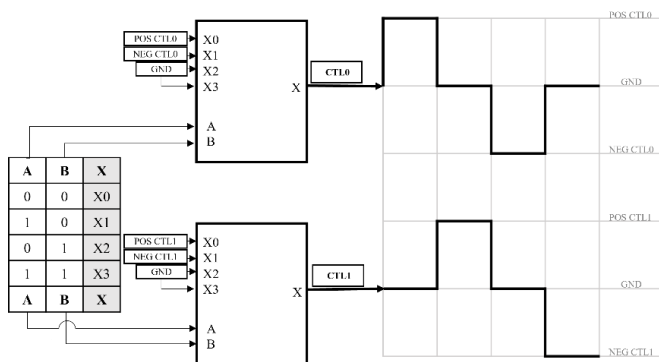


Figure 113: Multiplexing circuit

$$t = \frac{1/F_s}{n_o \cdot \text{photodiodes} * n_o \cdot \text{wavelengths}}$$

$$t = \frac{1/1000}{3 * 4}$$

$$t = 84\mu s$$

Equation 19: Emitter time "ON"

Due to the antiparallel position of the LEDs at each pair, when one of the control lines is positive, only one LED of the pair controlled by that control line is switched "ON," and when negative, the other LED of the same pair is switched "ON." The multiplexer switching time is controlled by an 8-bit Atmel ATtiny 2313-20SU microcontroller unit (MCU) (Atmel Corp, California, USA) at a frequency of 1 KHz. A byte data sequence is created using the multiplexor's truth table and is written on port-D of the MCU.

The two control lines of the multiplexer are passed through the Bus connector into the Current source module, where the voltage is converted into the current required to power the LEDs. The duration time of each LED "ON" is calculated by Equation 19. Thus, each emitter turns "ON" every 2.5ms.

9.2.2.4 Current source module

The Current source module has two main functions: 1) To limit the current driven through the LEDs to a maximum of 100mA, avoiding damages in the probe and skin burns for overheating the emitters. 2) To measure the current across each LED, providing feedback to control the LED currents. In order to accomplish the first function, the module involves two identical and improved Howland current sources followed by a push-pull (npn-pnp) transistor switch (Figure 114). The Howland is unique and interesting because it has both positive and negative feedback paths. When the array of resistance balances the feedback paths ($R2/R1 = R4/R3$), the operational amplifier behaves as a linear voltage-

controlled current source [285]. Thus, the input voltage is proportionally converted into the current to supply the emitters. The amplifier plays a key role in the Howland pump, especially as it is controlled by a high-frequency switching dual input with interleaved grounds (Figure 113). Therefore, unlike the amplifier implemented in the ZenPPG (AD8672, SR: 4V/us), the Zen TBI current source module involved a high slew-rate op-amp (AD8058 SR: 1000 V/us.) to ensure precise emitters' switching. However, op-amps cannot deliver sufficient current to power the LEDs, so a push-pull (nnp-pnp) transistor switch is connected to the output of the Howland operational amplifier.

In this circuit, when the current source driving voltage is positive, the npn transistor is active and switches one emitter "ON" and, when the driving voltage is negative, the pnp transistor is active, switching the other emitter "ON". The maximum current supplied to the LEDs can be limited by resistors R6 and R7 when the transistor is saturated. Finally, the module included two identical instrumentation amplifiers to accomplish the second function of this board, measuring the current across the LEDs. The voltage drop over R5 is measured by the differential input of the instrumentation amplifier (Figure 114). According to Ohm's law, the current that runs over R5 is equal to the voltage divided by the resistance, as R5 has a value of 1 ohm, the current that power the LEDs is equal to the output of the instrumentation amplifier (ISENSE).

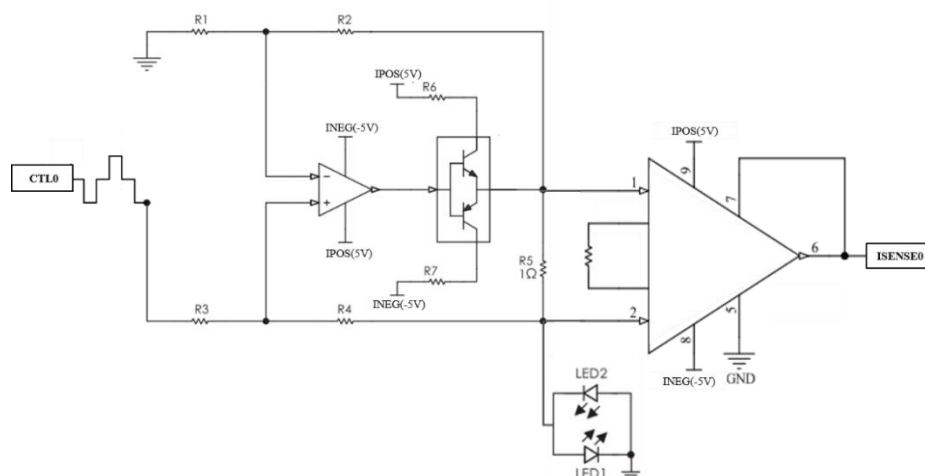


Figure 114: Current source schematic design

9.2.2.5 Transimpedance amplifier module

The transimpedance amplifier (TIA) module converts the photons detected by the photodetectors into mixed voltage signals from multiple wavelengths. The module hosts one female DB15 connector for interfacing with the TBI probe. For the ZenTBI, three identical differential TIA circuits were implemented, one per photodiode. In this particular TIA topology, the photodiode is connected between the negative inputs of two operational amplifiers, each with a gain resistor in a negative feedback configuration. Their outputs are driven into a differential amplifier, allowing the common-

mode rejection of coupled noise. For PPG applications, it is important to use op-amps with large bandwidth and open loop gain and include a phase compensation capacitor to provide stability to the circuit [283]. Accordingly, the TIA circuits use an OPA2380 (bandwidth=90 MHz and open loop gain=130 dB), including a carefully calculated compensation capacitor (Equation 20).

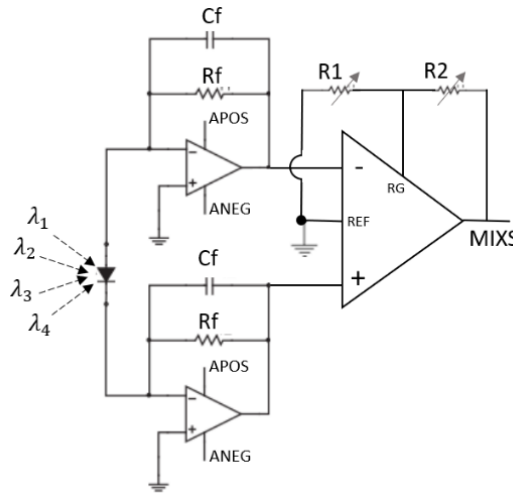


Figure 115: Differential transimpedance amplifier schematic design

$$C_f = \sqrt{\frac{C_i}{2\pi R_f F_c}} \text{ where,}$$

	C _i : photodiode joint capacitance + op amp input capacitance	C _i = 25+ (3+1.1) pF C _i = 2.91 pF
	R _f : feedback resistor value	R _f = 515 ohm
	F _c : amplifier bandwidth gain	F _c = 90MHz
	C _f : phase compensation capacitor	C _f = 10pF

Equation 20: Phase compensation capacitor design

Moreover, the signal amplification is manually adjusted by two external resistors that are connected to the differential amplifier INA331. The gain of this specific op-amp is given by $G=5+5*(R2/R1)$, and since the common noise is cancelled before signal amplification, the detection of small amplitude PPG becomes easily possible. The equal gain of the distal photodiodes transimpedance circuits is key to ensure $\frac{\partial A}{\partial \rho}$ linearity, therefore, R1 and R2 are trimmers that allow a precise gain configuration. The DC outputs of both photodiodes were compared using a homogeneous phantom to set equal gains.

9.2.2.6 Core module back end

The Core module back end is mainly responsible for separating the mixed signals from each TIAs output into four independent raw signals containing information at specified wavelengths. As mentioned earlier, the microcontroller's port-D generates four clocks for multiplexing the LEDs. However, port-B of the MCU is programmed to output another three clocks used for synchronizing

the demultiplexer, that separates the mixed signals into independent wavelength components (Figure 116). Clocks A and B control the internal switches of the demultiplexer to separate the mixed signal into four outputs. As both ports D and B clocks are synchronized, it is possible to sample a specific wavelength at each demux output. However, when a LED is switched from one state to the other (ON/OFF), there is a slight delay between the transitions, called transient response of a diode. Therefore, by sampling the entire LED activation period, the switching noise is also sampled. To overcome this problem, the demultiplexer inhibits control and is activated during these transitions, limiting the sampling period only to the middle of the signal where it is expected that the signal had enough time to settle before sampling.

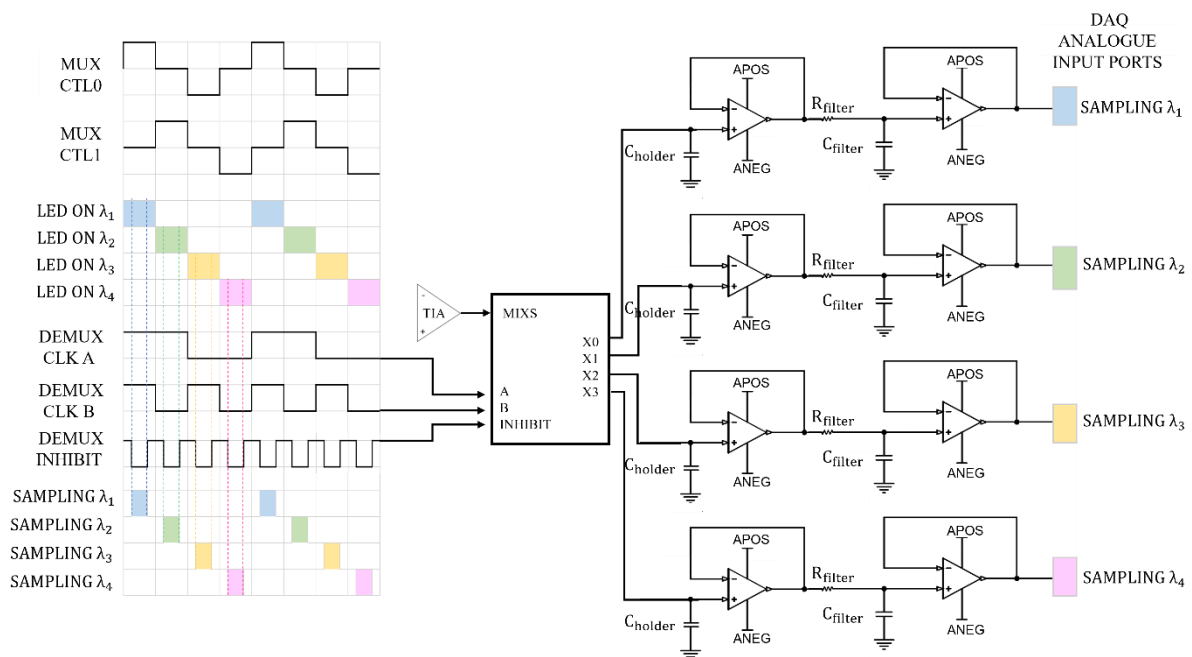


Figure 116: Core module back end schematic design

Moreover, it is necessary to ‘hold’ the sampled voltage until the next clock pulse triggers a new acquisition. Accordingly, a hold capacitor is placed at the output of the demux ports, followed by a buffer circuit that offers a high impedance to the hold capacitor to keep the held voltage from discharging prematurely. Previous studies have tested different hold capacitors for PPG signal sampling, establishing that a 220-nF capacitor provides an optimal performance [283]. After the hold buffer, individual antialiasing filters with a cut-off frequency of 80 Hz were implemented. These passive RC filters limit the bandwidth of the signals and stop the high-frequency switching noise from corrupting them. Every low-pass filter output is the input of an op-amp buffer before the signals are passed onto the NI DAQ card for digitization and further analysis. The raw signals are sampled at 1KHz and contain AC and DC components, which are later separated digitally using LabView digital filters.

Finally, the Core module back end also allows the digitalization of the battery's state and LEDs' currents monitoring, which are displayed on the LabVIEW interface to give the user an indication of the battery's state of charge and to calibrate the LED's intensity.

9.2.2.7 Case

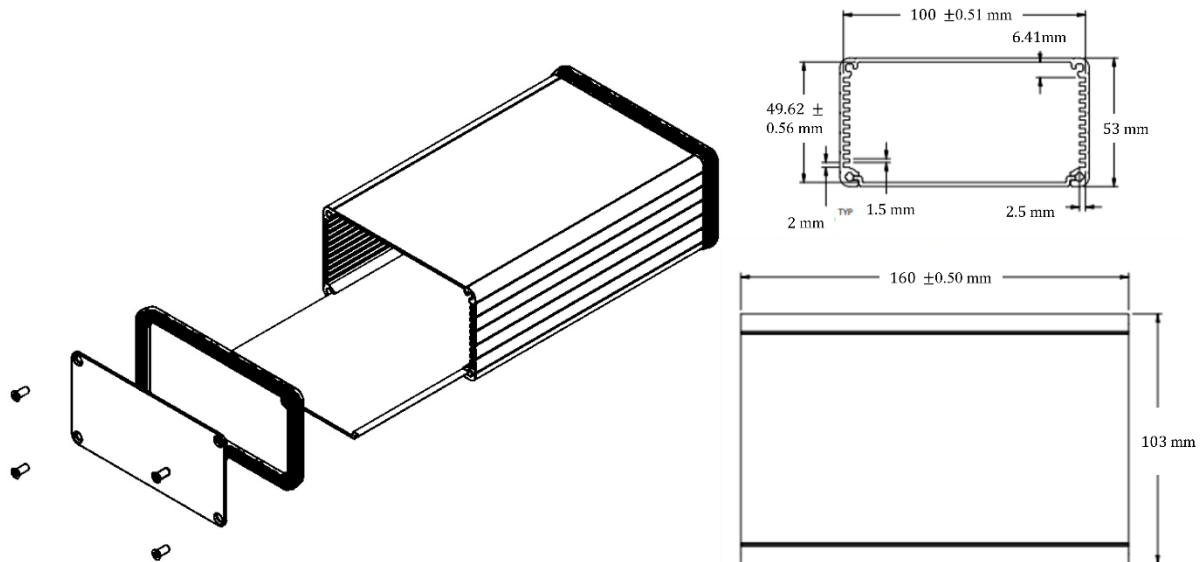


Figure 117: Black Aluminium Enclosure

The portable enclosure was the same one used for the ZenPPG [286]. It consists of a clear anodized aluminium body with a slide removable belly plate and extruded internal slots that are used to mount the PCBs horizontally (Figure 117). The enclosure endplates were designed in SolidWorks to accommodate the connectors and cut on an acrylic material using a laser cutter. The anodized aluminium can be connected to the ground plane, providing better shielding, reducing EMI, and minimizing electrical shock hazards.

9.2.3 LabView interface

The ZenTBI is connected to a NI DAQ for analogue-to-digital conversion and a LabVIEW interface that was exclusively designed to interact with the ZenTBI. Furthermore, the graphical nature of LabVIEW makes it ideal for data acquisition of digitised signals, data analysis, instrument control, test and measurements, displaying signals in real-time, and saving them for post-acquisition analysis. For these reasons, LabVIEW was chosen as the programming language for controlling the probe LEDs' intensities and acquiring the output signals of the ZenTBI.

The DAQ acquisition settings are the list of parameters needed to acquire data from the DAQ system. The signals are acquired from the analogue income ports (A0:A11, A13:A15) of the DAQ using a referenced single-ended (RSE) measurement system, which means that every input voltage is measured with respect to the ground. Parameters as the sampling mode are fixed on the Block

Diagram, so the user cannot change this value from continuous sampling to any other mode. However, as a research tool, some settings, such as the sampling frequency (F_s), can be adjusted by the user from the Front Panel, yet it is recommended to use a 1KHz F_s .

Similarly, some settings are required to save the data. A file icon control was placed on the Frontal Panel, so the user can define the path file to save the data. A new txt file is created every time the VI runs; if the path file has been used before, the new file will replace the existing one.

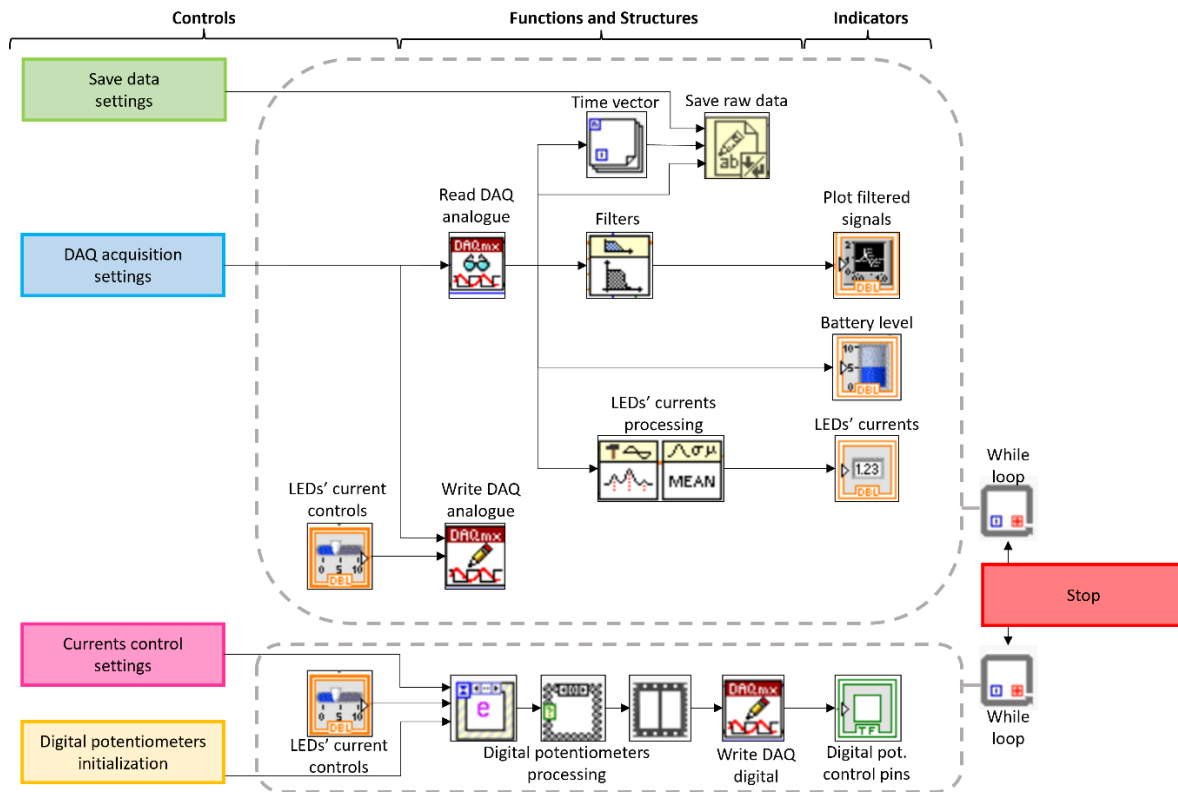


Figure 118: LabVIEW summarized Block Diagram for the TBI sensor

Multiple math, logical and array operations are included in the algorithm. However, Figure 118 is a visual representation of the bigger code elements.

Inside the while loop, the DAQmx driver reads ten samples of each analogue input port per loop iteration. The resultant n-dimension array is later divided into sub-arrays corresponding to each input signal. Since all three photodiodes sample light from the four LEDs, twelve optical signals are recorded by analogue ports from A0 to A11. The algorithm creates a time vector by implementing a for loop and some mathematical operation to the sample frequency. The raw optical signals and the time vector are saved on a .txt file for offline data post-processing. However, these were digitally filtered to display the AC and DC components of the optical signals. A bandpass Butterworth filter order 10 was implemented with cut-off frequencies of 0.4 and 6 Hz to separate the AC from the DC component

at each signal. Likewise, the DC signal was extracted using a lowpass Butterworth filter order 10 with a cut-off frequency of 0.4 Hz.

Moreover, signals recorded by analogue ports A13, A14 and A15, correspond to the ZenTBI battery level, ISENSE1 and ISENSE2, respectively. A tank indicator shows the battery level of the processing system. Furthermore, the currents across the LEDs are monitored by the signals ISENSE. Each has information from two LEDs, thus, positive voltages correspond to the current across one of the LEDs and are extracted by calculating the mean value of the peaks. Similarly, the negative voltages of ISENSE correspond to the second LED current and are separated by finding the mean value of the valleys. All four LEDs' currents are visualized in the Front Panel as numeric indicators.

In addition to acquiring, displaying and saving the data, the VI has the key task of allowing digital control of the LEDs' light intensities by adjusting the current across them. In the previous section two mechanisms were explained to control the currents. The first one requires the DAQ analogue outputs, which are controlled by two independent step sliders from 0 to ± 5 V. The values set on the sliders are the actual positive, and negative voltage at the DAQ analogue outputs A0 and A1, respectively. The second mechanism consists of two digital potentiometers, one for the positive voltage and another for the negative voltage, used to generate CTL1. Each digital potentiometer is controlled from LabVIEW using a step slider from 0 to 30 steps. Multiple cases and mathematical operations were implemented to control the digital outputs as follows: When the interface is running, the digital output (D2/D5) switches to HIGH to enable the potentiometer (CS). If the value on the slider is increased from the current position, the digital output (D0/D3) switches to HIGH to increase the resistance value (U/D) and vice versa. The difference between the slider's new value and the previous one, defines the resistance change by sending the same number of logical pulses to the digital output (D1/D4) that controls the pin INC of the potentiometer.

9.2.4 Technical evaluation

The technical evaluation consisted of three sections. Firstly, the input and output of each of the ZenTBI modules were evaluated using an Oscilloscope. Secondly, the power consumption was calculated by measuring the voltage over a 1-ohm resistor placed in series between the battery and the ZenTBI supply input. According to Ohm law, the voltage measured with a digital multimeter corresponded with the current consumption ($I=V/R$). Finally, a quality evaluation of the pulsatile signals was done with the aim of finding the best combination of source-detector distance and wavelength to acquire good-quality PPG signals. The signals from the proximal probe (S-D = 1 cm) and the proximal photodiode of the distal probe at different S-D distances (S-D = 2.5,3.0,4.0,5.0 cm) were assessed. The parameters of the quality evaluation set-up are presented in Table 19. The analysis included a pre-processing step, where the signals from all wavelengths and both proximal and distal photodetectors

were filtered using a Butterworth bandpass filter of order 3 (f_c :0.5 to 12 Hz). Then the 60-second record was segmented into 5-second windows, where nine different signal quality indexes were calculated based on literature [287], [288]. The list of indexes is perfusion, kurtosis, skewness, kurtosis in the frequency domain, skewness in the frequency domain, entropy, zero-crossing rate, noise ratio and relative power. Outliers were replaced by the mean in all the indexes using the `filloutliers` function of Matlab. Finally, the comparison of all wavelength signals' quality at the different source-detector separations was done by a non-parametric Anova (Kruskal Wallis), considering a confidence level of 95%.

Table 19: Quality evaluation set-up parameters

Protocol/Sensor/Phantom	Parameter	Value	Units
Protocol	Recording time	60	Sec
Sensor	LEDs currents	30	mA
	Sample frequency	1000	Hz
	Probes distance	0, 5, 15, 25	mm
	Location	Phantom's forehead	
Phantom	Circulating fluid	Artificial blood	65%
	Heart rate	60	bpm
	Stroke	15	cc/stroke
	Intracranial pressure	15	mmHg

9.3 RESULTS AND DISCUSSION

Correspondingly to the methods, the results are sub-divided in four sections to show the final probe, ZenTBI, interface and the technical evaluation of the functioning system.

9.3.1 Probe

Figure 119 illustrates multiple photos of the resultant probe. Figure A shows the PCB with all the assembled components. The labels from D1 to D4 correspond to the four LEDs, which jointly with the photodiode Ph0 and the latch connector, make the proximal probe. Similarly, the distal probe consists of the photodiodes Ph1 and Ph2 and the latch connector. Both PCBs are protected and covered by the cases shown in Figure B; each was customized for the components' position and dimensions, which helps to minimize the penumbra effect or optical shunting. Also, the cases avoid direct contact between the electronic components and the skin (Figure C). Moreover, the probes latch connectors can be connected and disconnected from the sensor's cable when needed (Figure D), as well this type of connector also ensures a strong connection once it is in place. Finally, Figures E and F show how the

hooks at the back of the probes help to place them in the right position on top of the phantom's forehead.

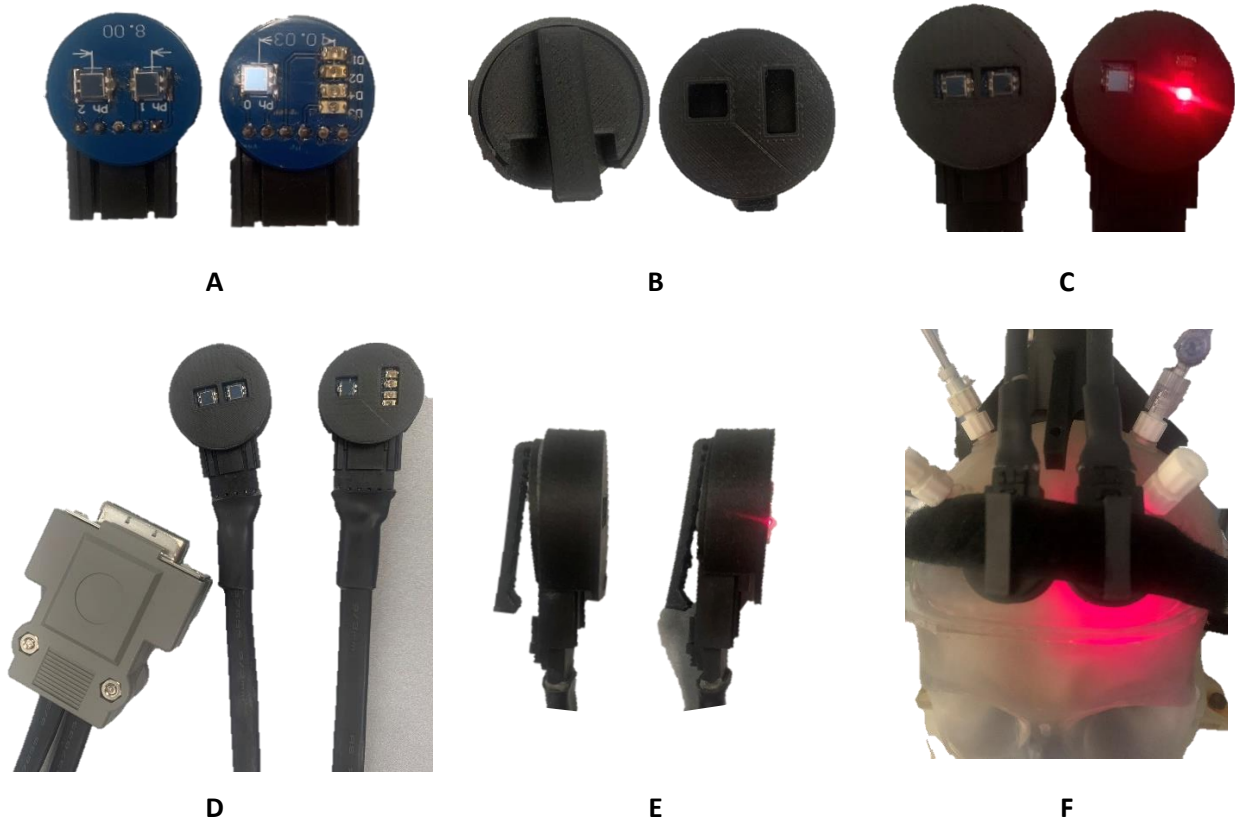
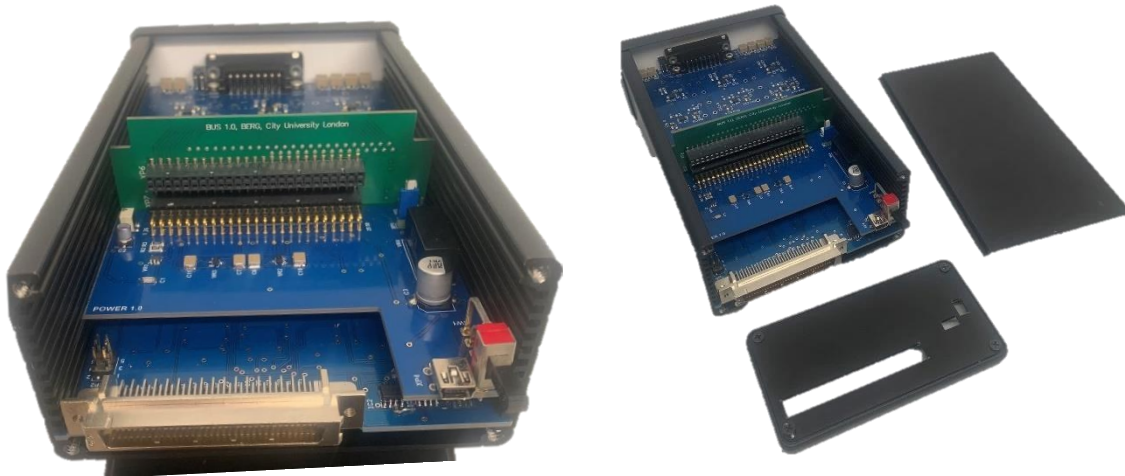


Figure 119: Multimodal probe for TBI monitoring of ICP and oxygenation

9.3.2 Instrumentation and acquisition system

The ZenTBI, described in detail in the methods, has the aim of controlling the LEDs' switching and intensity, while its instrumentation circuit allows the synchronized acquisition of optical signals using four wavelengths and three photodiodes. This modular system consists of 4 modules (blue PCBs) interconnected by a bus board (green PCB), as shown in Figure 120 A. The boards slide into the slots of a commercial metallic box. The ZenTBI has three ports, a power switch and its respective green light for power indication (Figure 120 B). In addition, the probe, the external battery and the NI DAQ card are connected to the ZenTBI, as illustrated in Figure 120 C.



A



B



C

Figure 120: ZenTBI instrumentation system

9.3.3 LabVIEW interface

To complete the system, a LabVIEW Interface was developed. The program is divided into the TBI sensor and the phantom control (Figure 121). In part A, both systems can be activated by clicking in the “TBI sensor” and the “Phantom” buttons. Defining the ports before running the VI is important to avoid any error. The interface has two separate physical channels control to state the DAQ ports of the ZenTBI (A) as well as the ports that the phantom’s DAQ utilizes (B) to record the invasive ICP, and ABP and to control the solenoid valves. Other parameters that should be initialised before running the VI are the sampling frequency (Hz) and the file path where the data will be recorded if the “Record” bottom (A) is activated at any point. On the TBI sensor section, the user can visualize the battery level and can slide the horizontal pointer sliders to control the current of each LED. Values of the LEDs’ currents are displayed next on boxes next to the slider controls and can be seen graphically on a red and blue plot below the controls. The current control is very important to ensure the quality of the signals and for the further calculation of SpO₂ measurements.

Moreover, part A contains multiple valuable graphs during experiments; for instance, the pulsatile signals from the proximal (PPG) and the distal (Pulsatile NIRS proximal) probes are displayed at each wavelength. Additionally, the DC component of the signals acquired from the distal probe (NIRS proximal and NIRS distal) is also plotted at the wavelengths of interest for the future analysis of cerebral oxygenation parameters. At the end of section A, the raw signals of all three photodiodes can be visualised. Section B was previously described on 8.

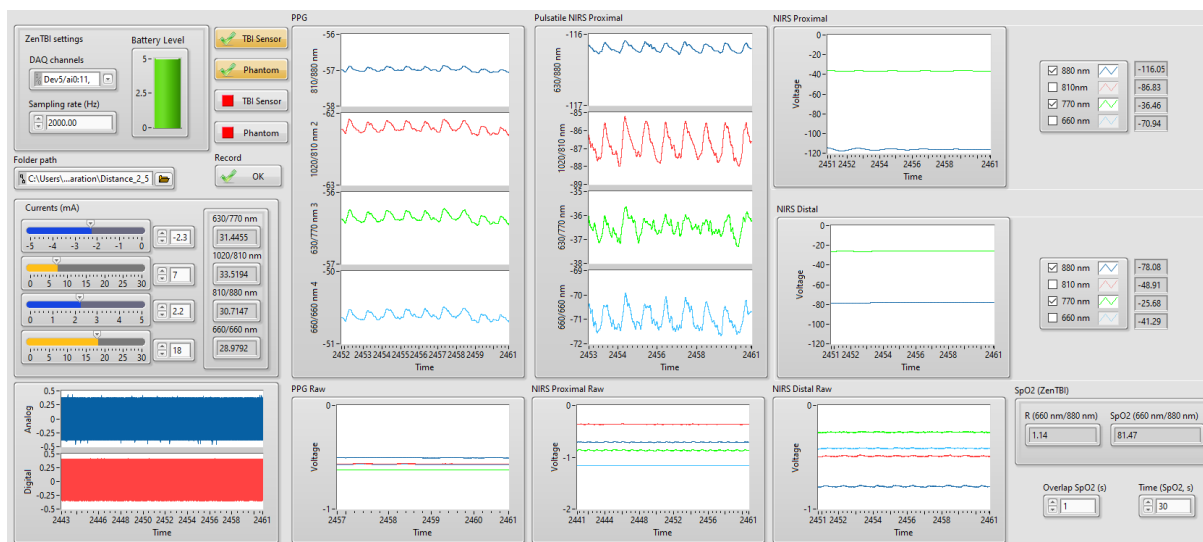
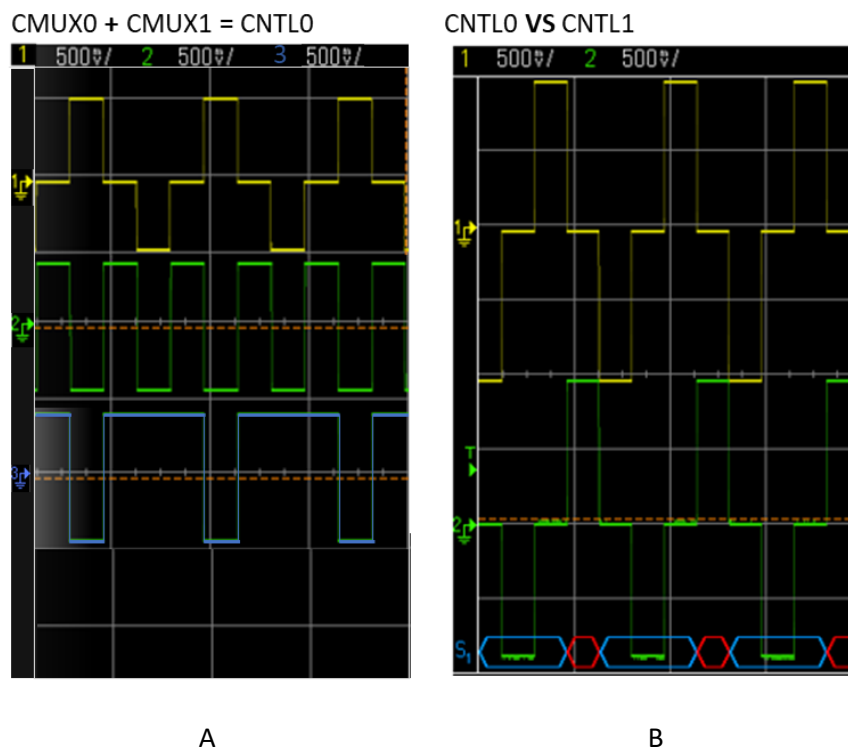


Figure 121: LabVIEW sensor interface

9.3.4 Technical evaluation

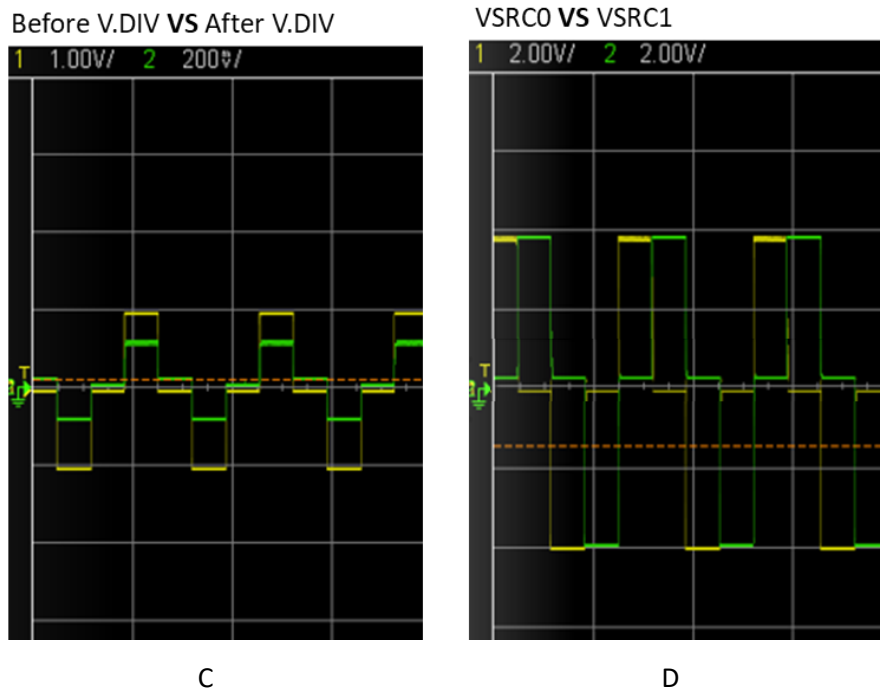
9.3.4.1 Oscilloscope debug

The methods presented different figures to explain how the instrumentation system switches the LEDs and controls their currents. In addition to the multiplexer for the switching and the current source control for the currents' regulation, some figures were included the describe the transimpedance circuit and the demultiplexing stage. This section of the results presents the signals measured directly from the pins on the PCB using an oscilloscope, which demonstrates the agreement with the previous diagrams and the ZenTBI correct operation at all the stages mentioned above. Firstly, Figure 122 (A) shows the outputs of the microcontroller CMUX0 in blue and CMUX1 in green, which following the multiplexer's truth table, produces the output CNTL0 shown in yellow. The positive and negative amplitudes of the yellow signal are defined by the DAQ analogue outputs and the digital potentiometers previously described, which could allow a maximum amplitude of 1 V, as is shown in Figure 100 (B). This figure visualizes both controls, CNTL0 and CNTL1, at their maximum amplitude. It is crucial to identify that one positive or negative pulse occurs only when the other control is OFF (ground), which warrants that only one LED is ON at a time.



As mentioned before, reflectance PPG demonstrated that acceptable signal quality could be guaranteed without exceeding 50 mA LEDs driving currents; therefore, each current control was designed to allow a maximum drive current of 100 mA. Figure 100 (C) illustrates the voltage attenuation of CNTL0 from 1V to 100 mA and -1V to -100 mA. This pulse of 100 mA amplitude is the input of the Howland pump. Moreover, as the operational amplifiers of the Howland pump cannot

deliver sufficient current to power the LEDs, a push-pull (npn-pnp) transistor switch was connected to the output of the Howland operational amplifier; see the voltage output in Figure 100 (D).



Besides the LEDs supply, the response of each photodiode was tested at the output of the transimpedance amplifier. An impulse response is shown in Figure 100 (E), where the photodiode was covered from light and exposed again very fast.

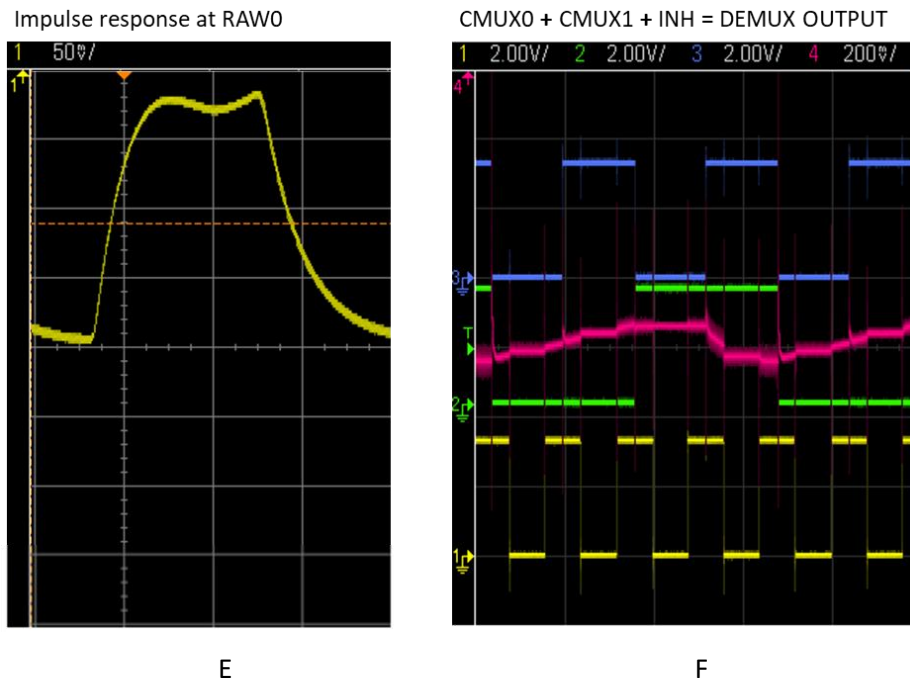


Figure 122: Oscilloscope debug sequence

Finally, the demultiplexer was evaluated to ensure the decomposition of the mixed signal (from all four wavelengths) into four independent signals. Figure 100 (F) displays the demux controls generated by the microcontroller, CMUX0 as the green line, CMUX1 as the purple line and the INHIBIT as the yellow line. The output of the demultiplexer is the pink signal that becomes erratic every time the INHIBIT is ON; then, a constant voltage can be seen at the different demux combinations according to its true table. The presented debug sequence demonstrates the right operation of the main ZenTBI stages.

9.3.4.2 Power consumption

During the power consumption assessment, two measurements occurred, one without the probe and the second with the probe connected to the system. The LEDs in the second measurement were driven by 40 mA of current. The load current calculated using Ohms Law was 360 mA without the probe and 420 mA with the system complete. From the second measured load current, the battery life of the entire system can be calculated and is given as:

$$\text{Battery life} = \frac{\text{Battery capacity}}{\text{Load current}} \times 0.7$$

$$\text{Battery life} = \frac{26800 \text{ mAh}}{420 \text{ mA}} \times 0.7$$

$$\text{Battery life} = 45 \text{ hours}$$



Figure 123: TBI system ready for use

9.3.4.3 Signal quality

The system's performance was validated by the quality assessment of the pulsatile signals acquired from the proximal detector (proximal probe S-D = 1 cm) and the distal detector (proximal photodiode of the distal probe) at different source-detector distances (S-D = 2.5,3.0,4.0,5.0 cm). The evaluation of the DC signals from both photodiodes at the distal probe will be explored in future chapters to calculate NIRS parameters. Figure 124 A displays the raw PPG signals from the distal detectors at all

the wavelengths, while Figure 124 B shows the Raw PPG at 810 nm from all the S-D distances. A random window from the one-minute recording was plotted to show the pulsations quality.

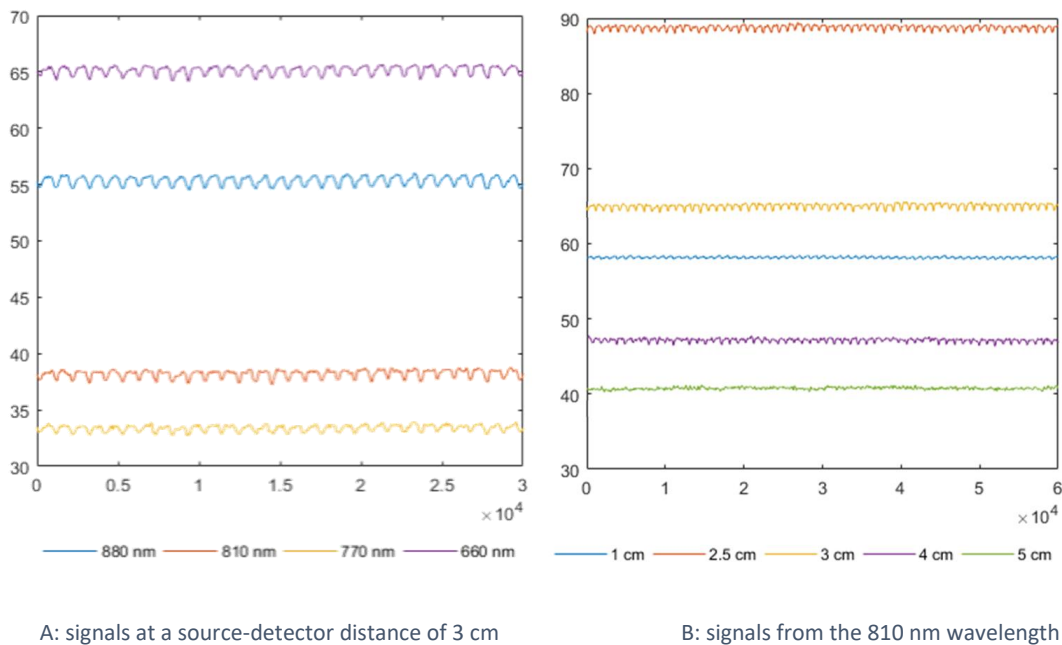


Figure 124: Raw PPG signals

From the raw signals, it is interesting to identify the different DC levels of the wavelengths at a specific source-detector distance. Later in this analysis will be shown how the quality of the 810 nm signal is better than the other wavelengths despite its DC level is not the highest or the lowest. On visual inspection, as can be appreciated in Figure 124 A, it seems reasonable to suggest that the signals from 810 nm have a greater raw pulsatile morphological quality than the other wavelengths. Therefore, the signals from this wavelength were compared between the different S-D distances, showing a significant difference in the DC and amplitude of the AC signals between the proximal (1 cm) and distal photodiodes (2.5,3.0,4.0,5.0 cm). The latter, bearing in mind that each photodiode has its own instrumentation system and gain, which is why the proximal signal (1 cm) is in between the other signals and its peaks are smaller (Figure 124 B).

Nonetheless, the DC of the distal photodiode decreases while the S-D separation increases, which shows how light intensity is reduced when the detector gets farther from the source (Figure 124 B). This change in DC has an effect on the perfusion index ($PI = AC/DC * 100$), which is the gold standard for assessing PPG signal quality, and it is calculated as the ratio of the pulsatile blood flow to the non-pulsatile (DC) [287]. Therefore, this index is the only one from the list of quality indexes assessed in this study that cannot be compared between photodetectors' positions. Yet, it was compared between wavelengths at a fixed source-detector distance of 3 cm.

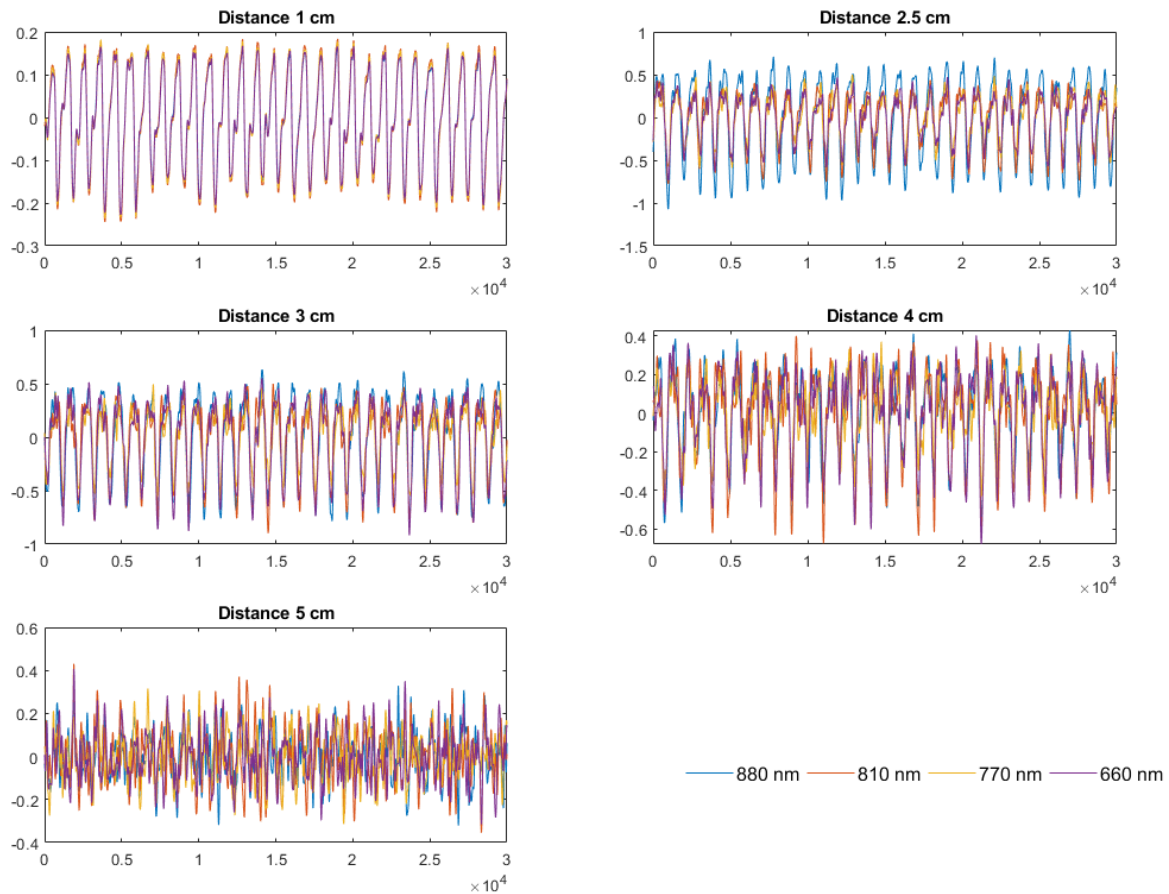


Figure 125: Filtered signals from all wavelengths at different source-detector distances

Figure 125 shows a zoom-in view of the filtered signals recorded at different distances from the light source. From visual inspection, the amplitude of the PPG signal at the proximal photodiode (1 cm) is significantly smaller than the pulses acquire from the distal photodiode at different S-D separations. The calibration of both photodiodes' gain resulted in a similar DC level when the S-D distance was around 3 cm. Therefore, this noteworthy difference in the AC component could only be explained by the lack of extracerebral circulation. Moreover, a greater distortion is seen in the signals at a higher S-D separation, increasing the variability between wavelengths. The latter was expected and corroborated the results obtained from the Monte Carlo simulation in Chapter 7.

Nine quality indexes were calculated from the PPG signals. A factorial analysis was considered to evaluate the effect of the wavelengths and the S-D separation on the quality indexes. However, the Anova residuals did not follow a normal distribution (p -value Kolmogorov Smirnov > 0.05), so the evaluation was limited to a non-parametric analysis. Figure 126 displays the median value for all the indexes at the different separations and for all the wavelengths. The Kruskal-Wallis analysis showed significant differences in the distribution of at least one S-D distance for all the indexes ($p < 0.05$).

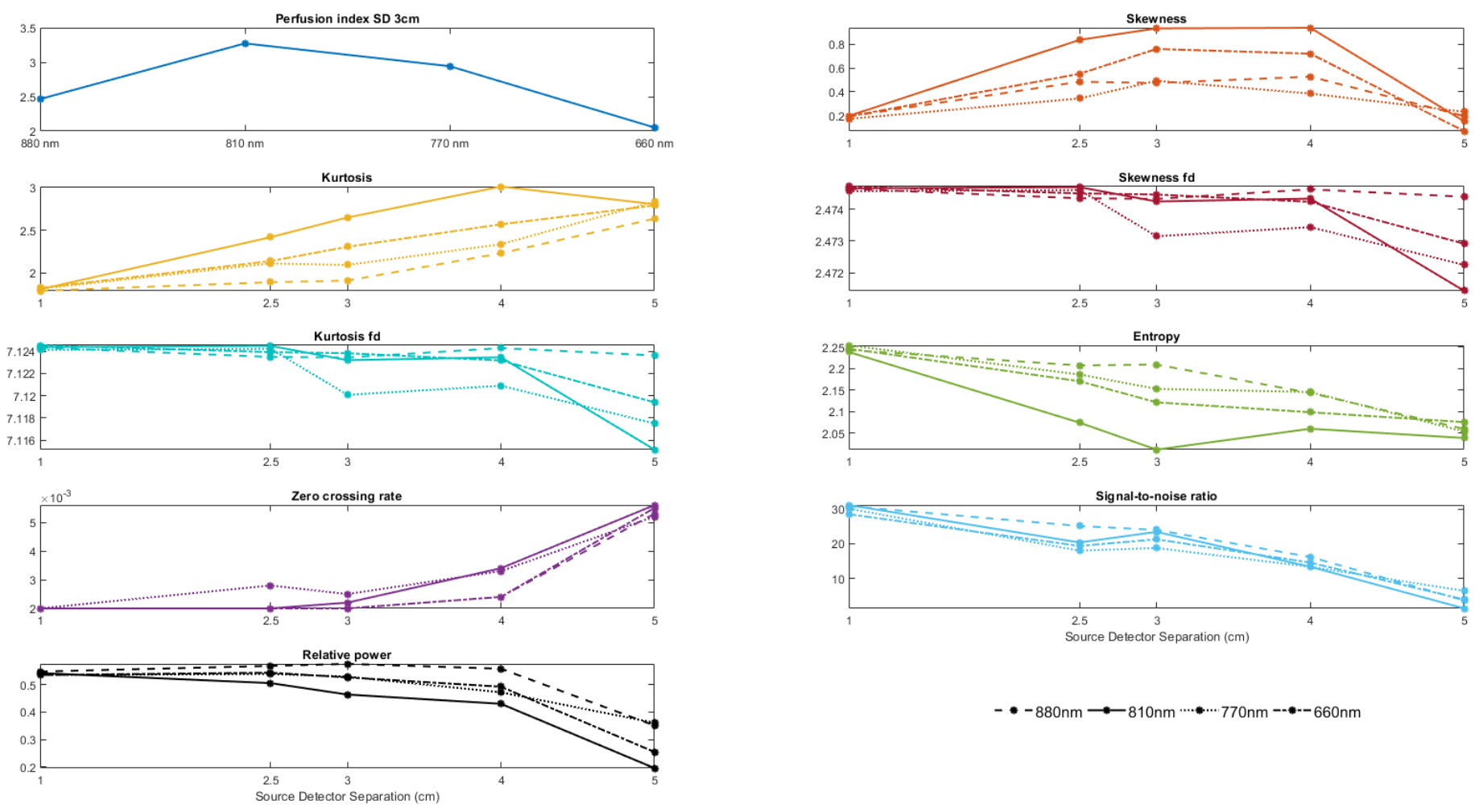


Figure 126: Median value of the quality indexes at each S-D distance for all the wavelength

The perfusion index is the ratio between the pulsatile blood flow and non-pulsatile blood flow in peripheral tissue that serves as a gold standard for assessing PPG signals. The perfusion indexes calculated for a fixed S-D distance of 3 cm are all above 0.4%, showing strong pulse strength, yet the 810 nm wavelength presents the higher PI value.

Moreover, skewness measures how symmetric the signal's distribution is, and kurtosis measures how sharp the peak of the signal's distribution is. A distribution with many outliers will have low skewness and kurtosis values since its probability distribution will be asymmetric, flatter and will approach zero slower [289]. Hence, there are more erratic peaks on the distal signals than the proximal, with a statistically significant difference. Also, the wavelength with higher skew and kurtosis is 810 nm at all the S-D separations. Similarly, the skew and kurtosis on the frequency domain are higher in the proximal detectors ($S-D < 3$ cm), yet there are no significant differences between the wavelengths (p -value > 0.05).

Furthermore, Shannon entropy provides a quantitative measure of the uncertainty present in a signal on the basis that the presence of noise adds uncertainty to the system [287], [288]. Then lower values ($E < 5$) correlate to low noise, which is the case for all signals despite the S-D separation or the wavelengths. However, the 810 nm wavelength at an S-D distance of 3 cm presents the lower entropy values.

Another important index on pulsatile signals quality is the Zero crossing rate, which on PPG signals is calculated as the rate of sign changes with the signal mean as the reference. On a window of 5 seconds (5000 samples) and simulating a heart rate of 60bpm, the results of the proximal detectors ($S-D < 3$ cm) show a zero-crossing rate of 0.0020, correlated to the absence of erratic peaks crossing the mean signal. The zero-crossing index of the 770 nm wavelength is significantly different to the other wavelengths at S-D separations lower than 3 cm.

The signal-to-noise ratio is a well-used measure that compares the desired signal level to the background noise level [287]. The higher the ratio, the lower the noise. The resultant median ratios over 22 dB indicate the low proportion of the noise against the PPGs signals. Better ratios are reported from the proximal (1 cm) and the distal (3 cm) photodetectors, where slightly higher median values correspond to the 880 nm and 810 nm wavelengths. A substantial decrease in the signal-to-noise ratio is proportional to a higher S-D separation.

Finally, it has been found that most of the energy of the systolic and diastolic waves is concentrated within the 1–2.5 Hz frequency band, then the ratio of the power spectral density (PSD) in this band

compared to the PSD in the overall signal 0–8 Hz provides a measure of the signal quality (<0.5 expected value > 0.8) [288], [290]. This index is around 0.55 in the signals from closer photodetectors ($S-D < 3$ cm), yet the PSD drops substantially when the $S-D$ distance becomes higher than 3 cm.

In conclusion, this quality analysis compared indexes between different $S-D$ separations and wavelengths. It is reasonable to think that, excluding the signals from the proximal photodiode (1 cm), the best distance to acquire PPG signals from a distal photodiode in the head phantom is 3 cm. Also, the best quality index values were acquired from the 810 nm wavelength, although there are no significant differences between the wavelengths at all the evaluated indexes.

9.4 SUMMARY

This chapter presented the design and manufacture of an optical sensor, acquisition system and user interface that would allow the identification of changes in cerebral oxygenation and the estimation of intracranial pressure by the analysis of the pulsatile and non-pulsatile signals acquired from cerebral tissue. The sensor can acquire both types of signals (AC/DC) from the photodiodes in a reasonable quality for their implementation in further computational analysis. Although NIRS has been implemented before for cerebral oxygenation, further analyses of the pulsatile signals' features, using this sensor and the phantom, would open the possibility to estimate ICP non-invasively.

10 IN-VITRO ASSESSMENT OF A NON-INVASIVE ICP SENSOR IN A HEAD PHANTOM

10.1 INTRODUCTION

After trauma, intracranial volume changes, among others, due to oedema, haemorrhages, and impaired CSF circulation. At some point, the excessive intracranial volume increases the pressure around the brain and the vessels on the cerebral cortex surface. The latter affects these vessels' morphology and “squeezes” their volume, which could yield a different shape of the optical signal backscattered from the cerebral tissue. Therefore, this research hypothesises that the morphological features of the PPG signals from the backscattered light of the forehead could correlate to changes in ICP. In order to test the aforementioned hypothesis, this chapter presents a rigorous analysis of quantifiable features of pulsatile signals acquired with the ZenTBI from the head phantom under different ICP levels, which enables the development of a computational model that estimates absolute values of intracranial pressure from the optical signals. This work was presented at the SPIE conference 2023 [291].

10.2 METHODOLOGY

10.2.1 Phantom set up

The head phantom previously described in Chapter 8 was used to mimic intracranial hydrodynamic changes. Changes in the intracranial pressure (ICP) from 5 mmHg to 30 mmHg were induced by a programmable two syringes pump (Legato 180, KD Scientific Inc, MA, USA) that infused and withdrew fluid at a normal CSF production rate of 0.3 ml/min (500 ml/day) [275], [276]. The pump pressurizes the water surrounding the brain in the intracranial compartment according to an ICP set-point value that is controlled through a LabVIEW interface (National Instruments, Texas, USA).

A linear-drive-based pulsatile pump (Harvard Apparatus 55-3305, Massachusetts, USA) was used to supply the phantom with a continuous blood pressure-mimicking waveform [263]. Healthy circulatory parameters (Table 20) were simulated and controlled during the whole experiment. The system continuously pumps artificial blood, previously described in Chapter 8, through the blood circulatory system during data acquisition.

Table 20: Phantom circulatory parameters

Parameter	Phantom value
CSF bulk flow	0.3 ml/min
Basal heart rate	50 bpm
Blood stroke	15 cc/stroke
Heart phase ratio (%Systole/%Diastole)	40%/60%

10.2.2 Acquisition system

Blood pressure and intracranial pressure were monitored at selected locations in the phantom. The blood pressure was monitored with a research-grade blood pressure transducer (Harvard Apparatus, Massachusetts, USA) at the inlet of the phantom's aorta. The intracranial pressure was recorded in the epidural/subarachnoid space, which is the same on the phantom due to the lack of meninges. Following the gold standard for clinical ICP monitoring, a needle tip pressure transducer (Gaeltec Devices Ltd, UK) and a corresponding control unit were used to acquire invasive ICP measurements (Neurolog system NL109, Digitimer, USA). Measured data were transferred to a NI data acquisition card (DAQ) (National Instruments, Texas, USA), processed in LabVIEW and recorded on a desktop computer.

The custom-made, multi-parametric sensor described in Chapter 9 was placed on the phantom's forehead directly above the vessel. The sensor consists of a proximal and distal probe, placed next to the other with a 5mm separation between them. The probe was connected to the ZenTBI (Chapter 9) and plugged into a NI DAQ for analogue-to-digital conversion. The LabVIEW interface explained in Chapter 9 allowed signals visualization and interaction with the ZenTBI. LED's currents were set at 30 mA, and signals were recorded with a sampling frequency of 1000 Hz for five minutes after each ICP step was stable.

10.2.3 Experiment Protocol

To investigate the effect of varying intracranial pressure on the PPG signal features, a blood-mimicking fluid (artificial blood) was continuously pulsed through a cardiovascular close-loop system, including a branching circuit from a simplified human cerebral arterial network (Chapter 8). Simultaneously, changes in the intracranial pressure were induced from 5 mmHg to 30 mmHg in steps of 5 mmHg. The infusion pump controlled the pressure through the user interface, which kept the desired pressure stable according to the invasive probe measurements (Figure 127). The range was defined according to the typical adult ICP values (5 to 15 mmHg), the ICP values in which treatment is required (20 to

25 mmHg), and the ICP values that indicate severe, life-threatening intracranial hypertension (>30 mmHg). The experiment was replicated 16 times in order to have good results resolution and generate a good amount of data to develop an estimation model further. Between the replicates, the intracranial pressure was set at 5mmHg, and the heart rate was reduced. When the pressure decreased from 30mmHg to 5 mmHg, the heart rate increased to 50 bpm, and the protocol was run again.

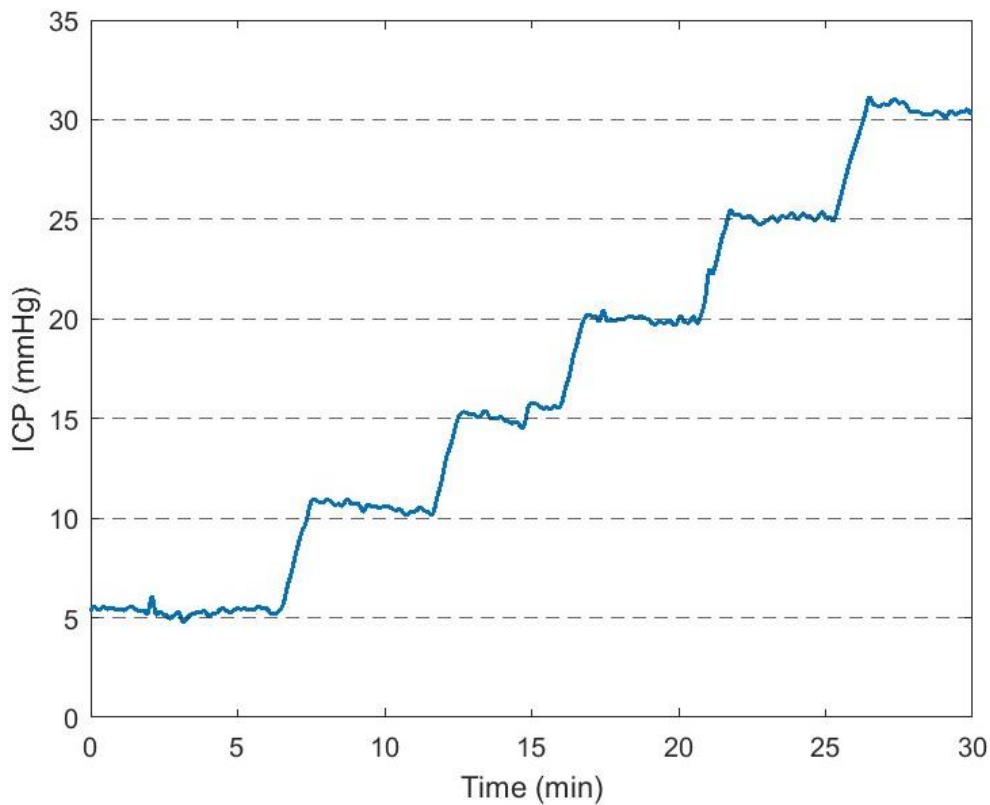


Figure 127: Experimental protocol where ICP changes were induced on the phantom

10.2.4 Analysis Protocol

MATLAB (version 2018b) processed and analysed the recorded signals. First, the signals were filtered using a Butterworth filter to separate the AC component from the DC. A second-order bandpass filter was applied with 0.5 and 12 Hz cut-off frequencies to get the pulsations. Similarly, a third-order, lowpass filter with a cut-off frequency of 0.2 Hz was used to obtain the DC component. Then, the signals were normalised by dividing the AC part of the signal by its DC, followed by a 10-factor multiplication.

Several features have been extracted and investigated in the literature to characterise pulsating signals, such as PPG [292], [293]. In this study, ten time-domain features were extracted from the optical signals. Figure 128 shows a graphical representation of the features extracted. These features were: the amplitude (F1), pulse width (F2), upslope (F3), decay time (F4), rise time (F5), area under

the curve (F6), area of the systolic period (F7), area of the diastolic period (F8), the ratio between both systolic and diastolic areas (F9), and the ratio of the maximum and minimum point of the second derivative pulse (F10). Due to ICP rises as a consequence of an intracranial volume change (swelling, bleeding, increased cerebrospinal fluid), the morphology and other characteristics of the optical pulse (PPGs) are affected, and they correlate to ICP. Therefore, the features were selected according to their correlation with different physiological changes in the human body, as is summarised in Table 21.

From the five minutes of cerebral PPG signals acquired at each ICP step, the median value of each feature was calculated in a signal window of 5 seconds. The features from each ICP step were compared using the following statistical analysis.

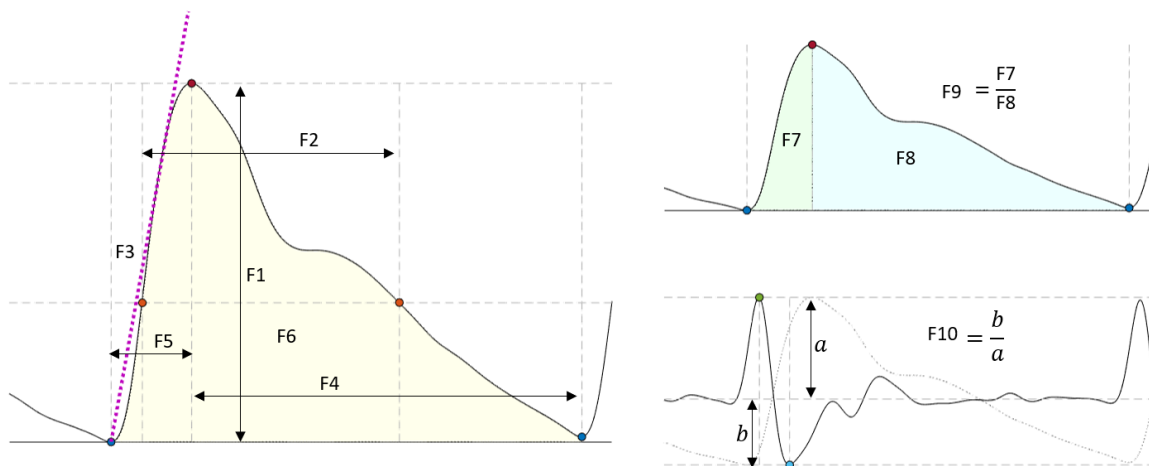


Figure 128: Features extracted from the optical signals

The first analysis consisted of evaluating significant median differences at each feature of the pulsatile signals when the phantom's intracranial pressure was increased. Therefore, the mean arrays of the extracted features for all 16 replicates were calculated. Then, a Kruskal Wallis analysis was run considering a significant level of 95% ($\alpha=0.05$). Only signals from the 810nm wavelength were included in this non-parametric analysis, as this wavelength has the particular characteristic of being absorbed to the same extent by oxy and deoxy-haemoglobin. Thus, it is the ideal point to record optical signals independent of blood oxygenation, such as ICP. Also, only the signals from the proximal photodiode of the distal probe were included in the analysis. As was explained before (Chapter 9), higher source-detector distance allows light to travel deeper into the tissue; hence, only the pulsatile signals from the proximal photodiode of the distal probe were included in the current analysis, expecting to get volumetric changes information from the brain.

Table 21: Description of photoplethysmogram (PPG) features extracted and their clinical relationship

Feature	Definition	Description	Correlation to physiological changes	Reference
F1	Amplitude	Measured as the amplitude difference between the onset of the pulse and its systolic peak	Stroke volume Local vasodilatation Microvascular expansion Vascular compliance	[293], [273]
F2	Pulse width	Represented as a time interval between the 50% of the maximum systolic amplitude of PPG	Systemic vascular resistance	[293]
F3	Up slope	Amplitude of the maximum slope point, measured from the onset of the pulse	Stroke volume Vascular compliance	[293]
F4	Decay time	Time between the location of the systolic peak and the onset of the next pulse	Blood pressure	[292]
F5	Rise time	Time between the onset of the pulse and the location of the systolic peak	Blood pressure	[292]
F6	Area under the curve	The total area of the PPG in a pulsation	Total peripheral resistance	[292], [293]
F7	Area of the systolic period	Area of the systolic phase, measured from the onset of the pulse and the location of the systolic peak	Vasoconstriction Vasodilation Venous function	[273]
F8	Area of the diastolic period	Area of the diastolic phase, measured from the location of the systolic peak and the onset of the next pulse	Vasoconstriction Vasodilation Venous function	[273]
F9	Systole and diastole ratio	Ratio between both systolic and diastolic areas	Properties of the cardiovascular system	[292]
F10	Second derivative ratio	Ratio of the maximum and minimum point of the second derivative pulse	Arterial distensibility Evaluation of vasoactive agents	[292]

In order to identify if there were significant changes between the features at the different ICP values, including all four wavelengths, a factorial analysis was run, considering a significant level of 95% ($\alpha=0.05$). The factors were the ICP value (levels 5,10,15,20,25, and 30 mmHg) and the wavelengths (levels 660,770,810 and 880 nm). The ANOVA's assumptions were evaluated using multiple statistic tests. The Kolmogorov-Smirnoff test was used to evaluate if each feature followed a normal distribution for each factor. Bartlett's test was used to evaluate each factor's variance homogeneity. Graphical methods assessed data independence. Box-Cox transformations using an optimal lambda were applied to go forward with the factorial analysis when the assumptions did not comply with the assumptions of normality, heteroscedasticity and independence. After the transformation, both factors were included in a linear model to identify their possible interaction effect on the feature changes.

The extracted features from the 810 nm wavelength signals were used to estimate the mean invasive ICP value using a 5-second window on all 16 replicates signals pool. Next, regressive support vector machine (SVM) models were applied using a linear kernel, radial-basis kernels with varying scales, and polynomial kernels with varying orders. The models aim to estimate intracranial pressure values from changes in the PPG features extracted from the proximal photodiode of the distal probe. Two different partitioning techniques were evaluated; in the first one, the pool data of all 16 replicates were randomly partitioned into training and testing groups by the Pareto 80/20 law [294]. The second approach splits the data into k-folds, where the number of folds (k) equals the number of replicates (16). A fold is constituted of the entirety of the data of one replicate. Then the same nine models were tested on the data of the fold and trained on the remaining data. Finally, the performance of the SVM models was evaluated per partitioning approach, using accuracy selection criteria, such as the mean absolute error, sensibility, specificity, area under the curve, determination coefficient, root mean square error and correlation coefficient. The best performance algorithm was then applied to the test data set to assess the model's accuracy. For instance, the agreement between invasive and estimated values was assessed using a Bland-Altman analysis.

Finally, the selected model per partition approach was tested for its future application in an embedded system. The optical signal at 810 nm from the distal photodiode was sectioned in 5 seconds windows for all the replicates. Each segment of raw data went through the same pre-processing method and feature extraction used to train the model. First, the features of each segment were standardised using the mean and standard deviation previously calculated from the features of the training set. Next, the model was fed with standardized features to estimate an ICP value

corresponding to the measurement window. The mean absolute error (MAE) of the model was established as follows:

$$\text{MAE} = \frac{\sum_1^n |\text{Predicted ICP}_{5 \text{ sec}} - \text{Invasive ICP}_{\text{mean } 5 \text{ sec}}|}{n}$$

Equation 21: Mean absolute error

Where n is the number of segments evaluated from all the replicates.

10.3 RESULTS AND DISCUSSION

The sensor consists of four LEDs of different wavelengths (660 nm, 770nm, 810 nm and 880 nm) and three photodiodes located at different distances from the source. The sensor has two probes, the proximal and distal probe. The proximal probe contains the LEDs and the first detector, which is fixed at 1 cm from the source, and its aim is to sense the pulsatile signals from extracerebral tissues. The distal probe has the remaining two photodiodes, which will allow the assessment of oxygenation parameters by NIRS principles (DC signals only). The larger distance of these photodiodes from the source allows the interrogation of cerebral tissue, as was explained in chapter 7. In addition, to identify changes in the DC signal of backscattered light, the proximal photodetector of the distal probe also detects the pulsatile components (AC signal or PPG) of the brain. As the current analysis is for ICP measurements only, the distal photodetector of the distal probe was not included in the analysis. Therefore, in this chapter, the signals from the proximal photodetector of the distal probe are called distal PPGs.

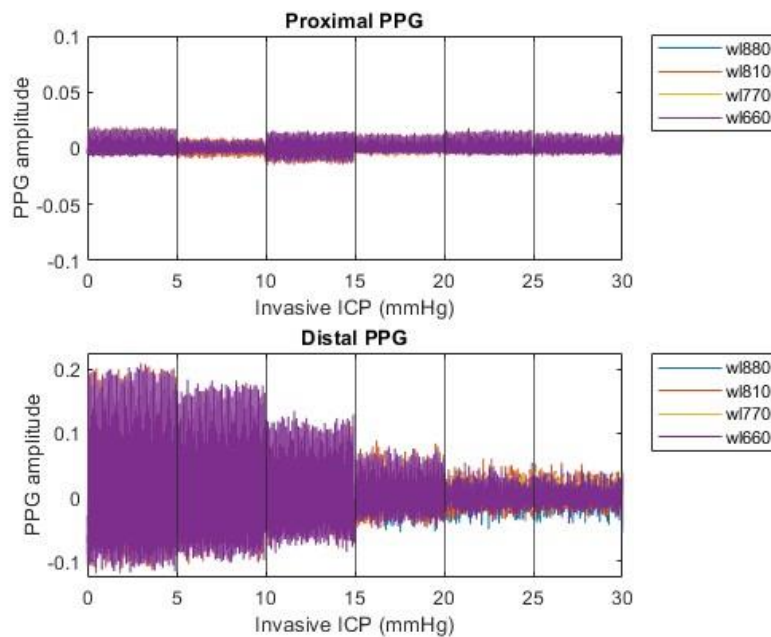


Figure 129: Normalized PPG signals from both proximal and distal detectors, full record of one replicate

Figure 129 shows the full record of one of the sixteen replicates, where no apparent changes in the amplitude of the proximal PPG signals occurred when ICP raised at all wavelengths. This could be explained by the lack of extracerebral circulation and tissue layers on the phantom. On the other hand, the amplitude of the distal PPG signals decreases as ICP increases. This behaviour could be related to a lower blood volume due to the partial occlusion of the vessels by the surrounding intracranial pressure. This condition of the phantom simulates clinical scenarios where the brain is compressed due to intracranial hypertension, reducing perfusion and blood flow to the cerebral tissue. Then, if the brain vessels' volume is reduced, the amplitude of PPG signals and quality will decrease.

Figure 130 is a zoom-in view on a 10-second window of the normalised PPG signals at each ICP level from both proximal and distal detectors of one replicate. By amplifying the signal is possible to see the pulsations and the difference between proximal and distal signals quality. Unsurprisingly, proximal PPGs amplitude and quality are significantly lower than the distal PPGs, as the phantom lacks from a scalp with its extracerebral circulation. A previous Monte Carlo simulation (7) demonstrated that light could penetrate a 10 mm distance using a source-detector separation of 1 cm; therefore, due to the lack of scalp (average thickness 3 mm) on the phantom, the proximal detector is sensing some scattered light from the brain vessels (10 mm deep from the skull surface).

The difference between distal and proximal signals graphically evaluated the effect of the extracerebral signals in the ICP measurements. To calculate this difference, the AC component of the proximal signal was subtracted from the AC component of the distal signal and divided by the average of both distal and proximal DC signals. Figure 131 shows zoom-in views of a 10-second window of the normalised PPG signals at the extreme values (5 mmHg and 30 mmHg) from both proximal and distal detectors of one replicate, including the difference between the detector's signals. The latter illustrates the minimum effect of proximal signals in the distal PPGs on the current in-vitro set-up. Consequently, all further analysis will be done only considering distal PPG signals.

Nonetheless, for a better understanding of extracerebral signals during intracranial hypertension, this research recommends the future development of a scalp with its own circulatory system. Likewise, the current method to set the phantom's intracranial pressure doesn't allow the scenario of hypertension due to brain swelling (oedema) or cerebral ventricles dilation (ventriculomegaly), in which cases, the brain suffers enlargement and compression. This research suggests the future implementation of strategies to simulate these conditions on the head phantom in order to evaluate its effects on both proximal and distal pulsatile signals.

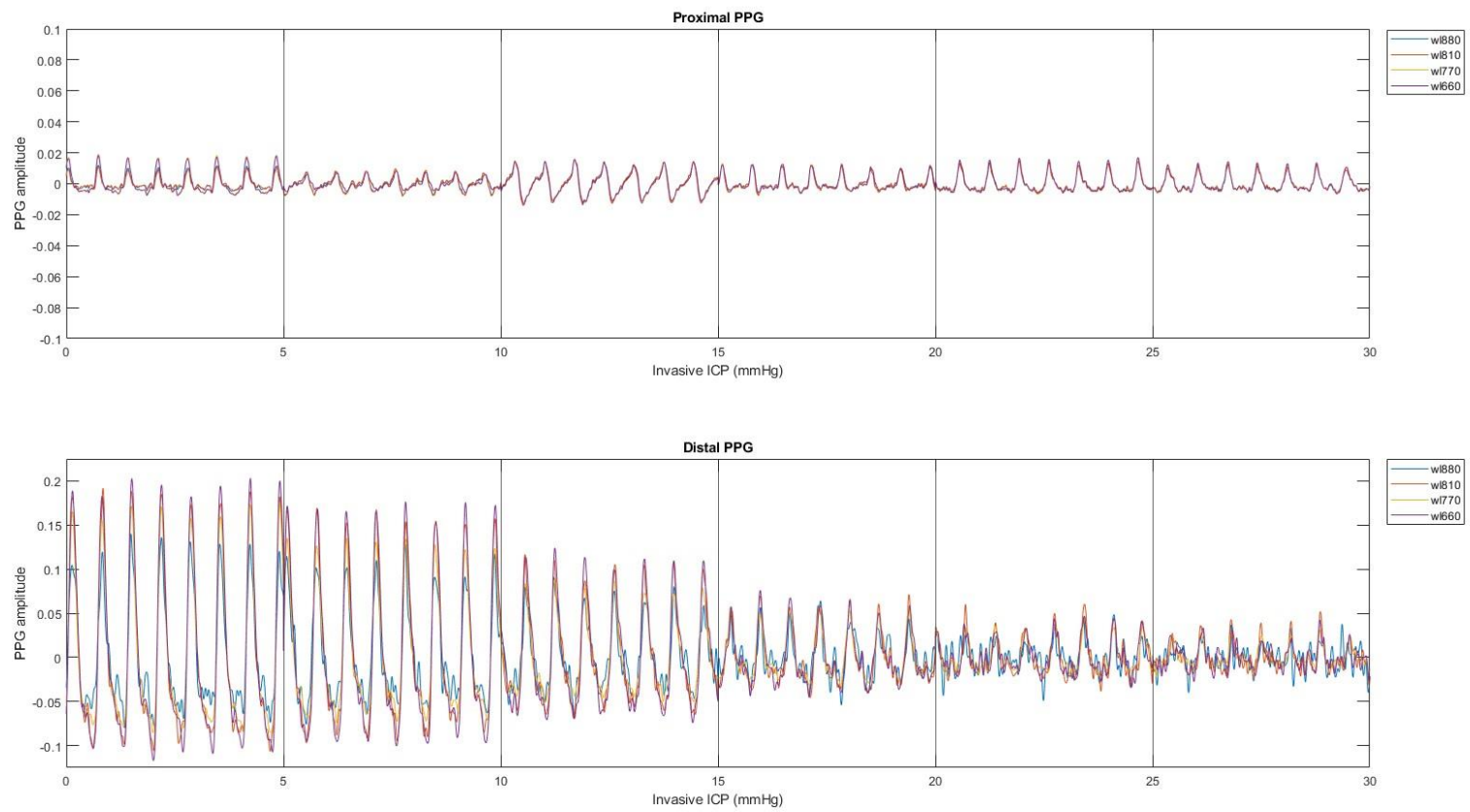


Figure 130: Zoom in view on a 10 second window of the normalized PPG signals from both proximal and distal detectors of one replicate

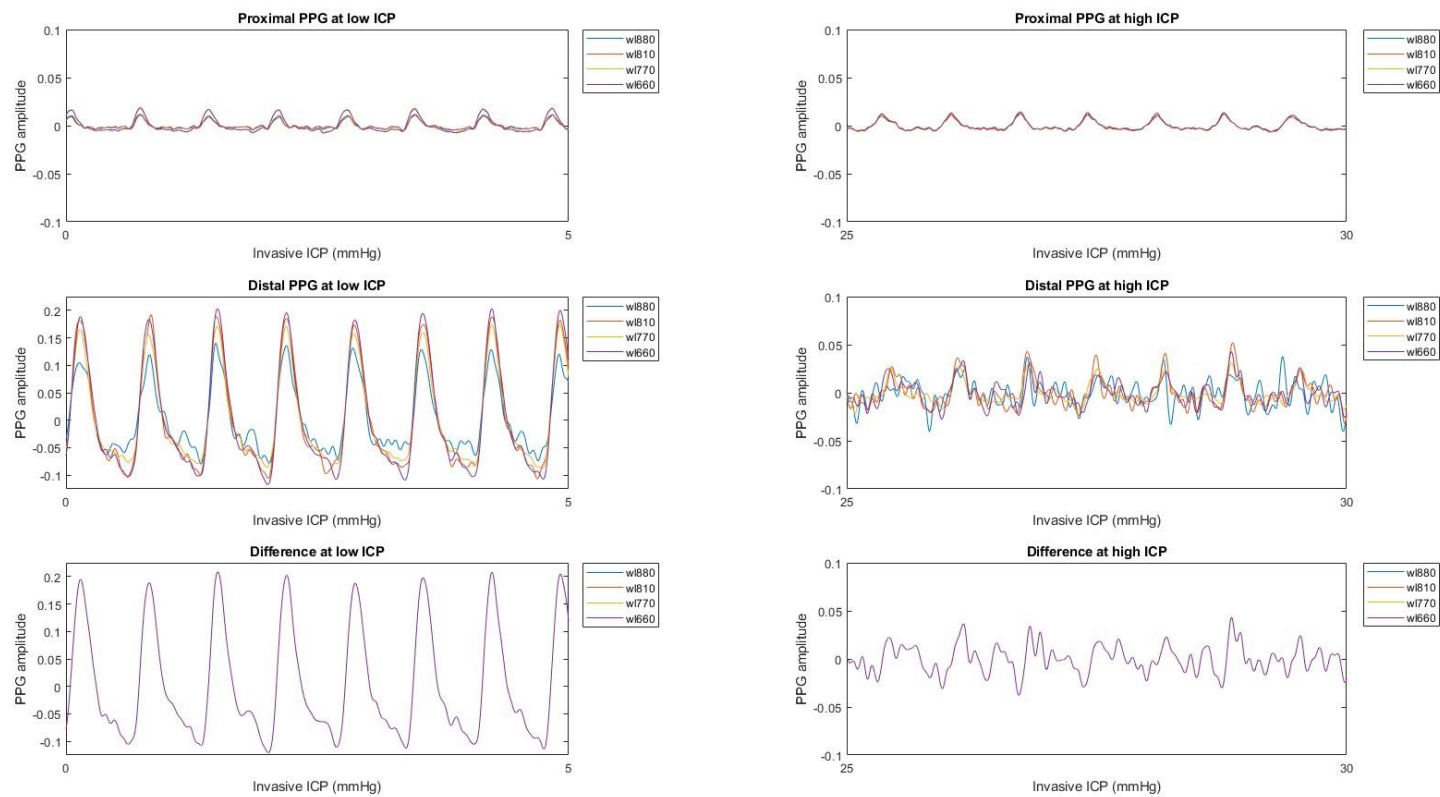
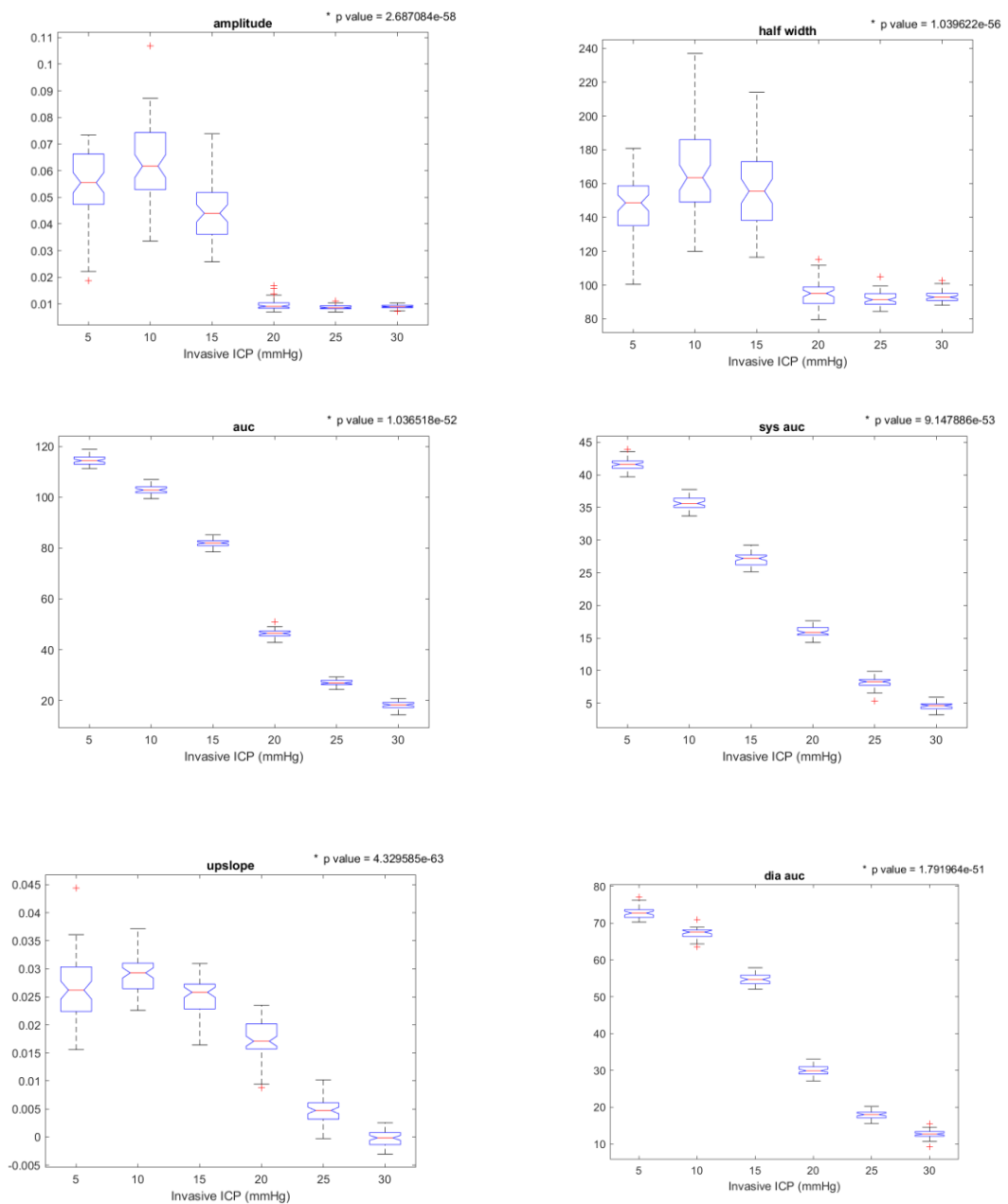
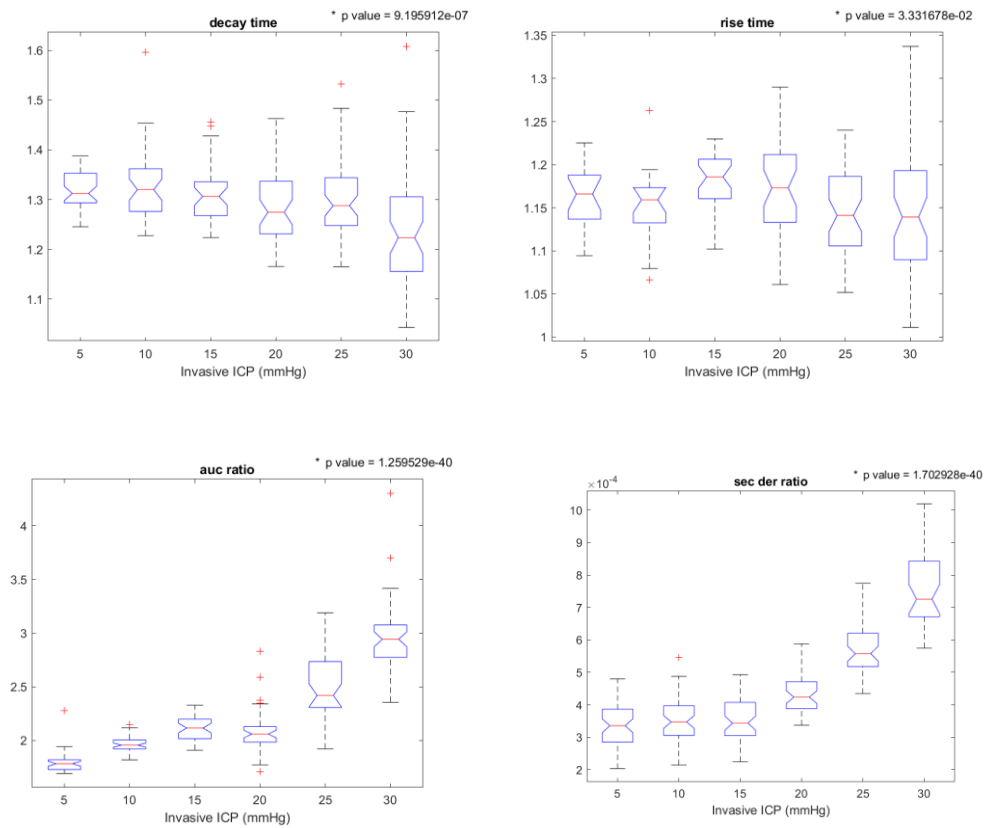


Figure 131: Zoom-in views of a 10 second window of the normalised PPG signals at the extreme values (5 mmHg and 30 mmHg) from both proximal and distal detectors of one replicate, including the difference between the detector's signals

From Figure 130 and Figure 131 it is possible to identify changes in the pulses' morphology, from a clear PPG signal at low ICP values to a noisy, poor signal at 30 mmHg. Accordingly, a Kruskal-Wallis analysis allowed the comparison of multiple features of the PPG signals while the ICP was increased. The following boxplot graphs show each feature's median and interquartile range per pressure level [5:5:30 mmHg]. The p-value of the non-parametric test is presented on top of each graph. A star next to the p-value represents a significant difference ($\alpha < 0.05$) for at least one of the features' medians at one level of ICP. All the features presented significant changes by ICP raising, with a significant p-value for the Kruskal Wallis test.





This non-parametric analysis was done only for the 810 nm wavelength, as this one has meant to be the wavelength for ICP measurements. However, the following factorial analysis (Figure 132) demonstrated a significant effect of the different wavelengths at all the features of the pulsatile signals. In order to fulfil the Anova primary assumptions, a Box cox transformation was run. It was verified that the residuals fitted a normal distribution after the transformation. The results of the ANOVA showed a significant effect of both factors in all the features of the pulsatile signals and a significant interaction between the wavelengths and the ICP level.

Nonetheless, the trend at all wavelengths is the same when the ICP is increased. Therefore, this research will keep analysing the isosbestic point as the optimal wavelength to estimate ICP without any oxygenation contribution. Following the non-parametric and parametric test results, all the features were used to train the following regression vector machine models.

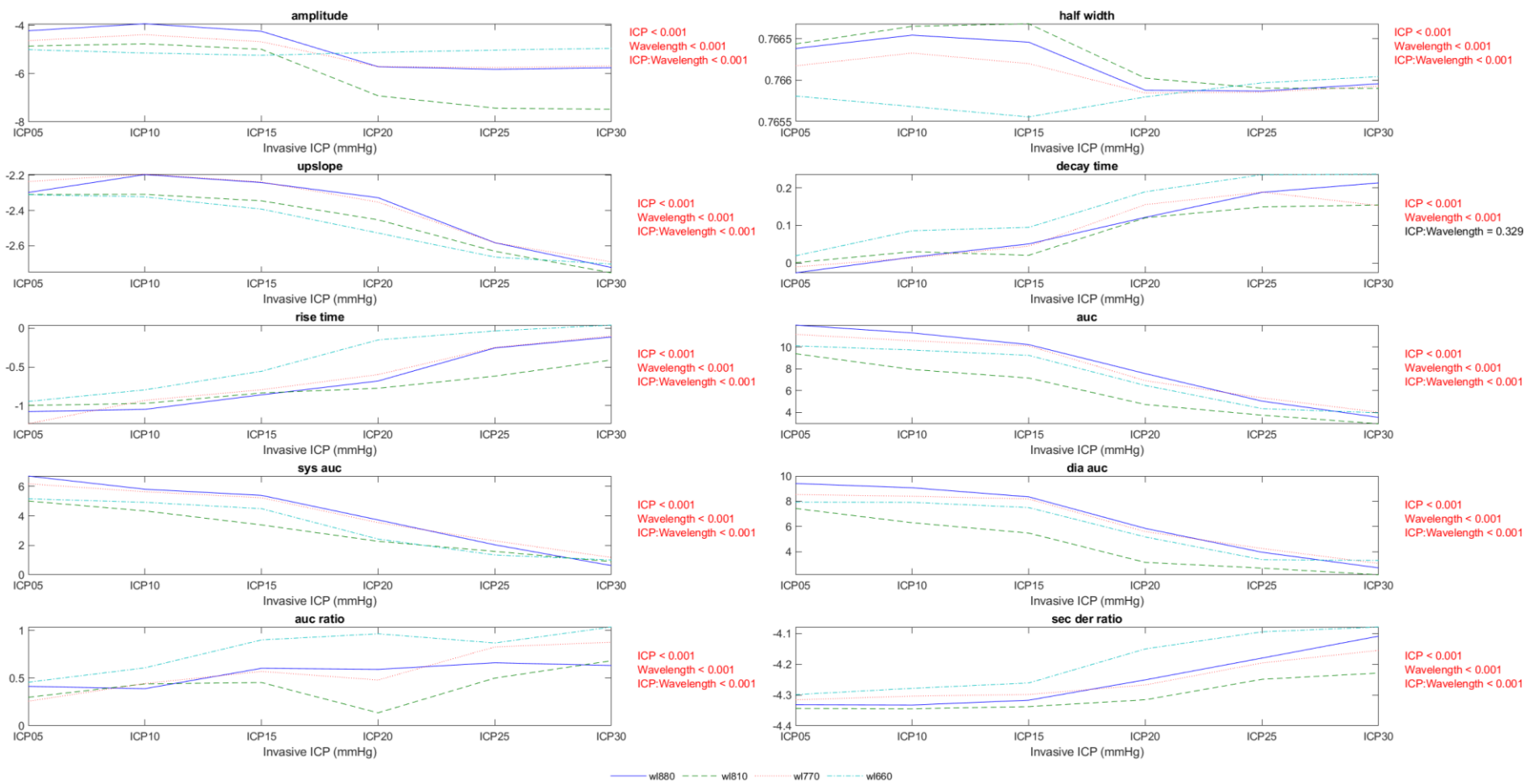


Figure 132: Factorial analysis of the ICP levels and wavelengths effect in the features of the PPG signals, including factors interaction

10.3.1 Resultant model of the first partition approach, Pareto 20/80:

The accuracy parameters to compare the estimated ICP values against the invasive ICP measurements on the testing group (20% data) are displayed in Table 22. Each column presents the results of a model. Thus, at each row the best values were highlighted for the respective accuracy parameter; for instance, the values closer to zero were highlighted at the row where the average error for each model was reported. The radial basis Kernel model of scale 1.5 was highlighted for its good performance in estimating ICP based on brain PPG signal features. The graphical representation of this model's accuracy is presented in Figure 133.

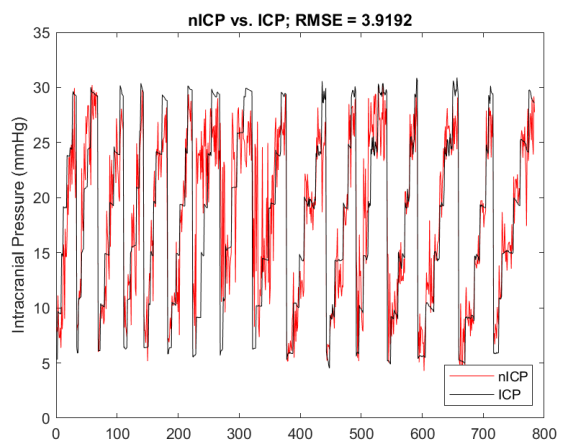
Table 22: Models accuracy comparison

Accuracy	linear	rbf_0_5	rbf_1	rbf_1_5	rbf_2	poly_2	poly_3	poly_4	poly_5
Error	0.22	0.19	0.12	0.11	0.13	0.82	0.52	166.05	10416.84
Sensitivity	0.68	0.76	0.81	0.84	0.83	0.72	0.01	0.77	0.11
Specificity	0.96	0.98	0.99	0.98	0.96	0.97	1.00	0.83	0.97
AUC	0.87	0.94	0.94	0.94	0.94	0.92	0.08	0.83	0.55
Determination	-1.68	0.74	0.81	0.80	0.80	-742	-682	-5E+7	-2E+8
RMSE	0.77	0.43	0.37	0.31	0.28	14.44	13.57	3762.9	128445
Correlation	0.39	0.87	0.90	0.90	0.90	0.06	0.00	0.03	0.03
P value	0.00	0.00	0.00	0.00	0.00	0.37	0.96	0.64	0.66

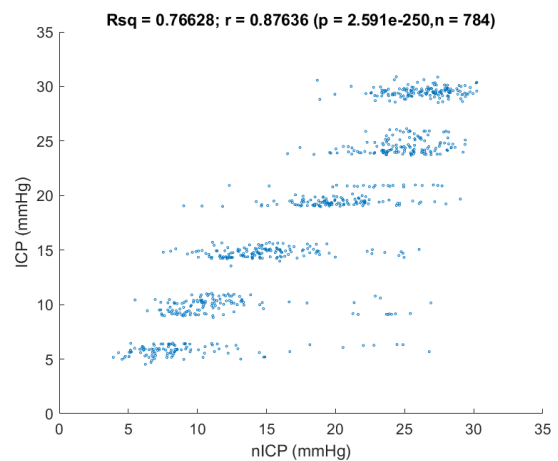
Figure 133 (a) illustrates how the estimated values of ICP (red lines) follow the trend of the invasive measurements on all 16 replicates (each peak). From this graph the quality of the optical signals at each replicate can be deduced; for example, the estimation at replicates seven to nine is lower than the others; this could be because of the quality of the optical signals acquired at those three replicates. Moreover, the root-mean-square error was 3.9 mmHg, which is a good RMSE considering the clinical error of invasive probes (± 2 mmHg) [295]. Figure 133 (b) shows an uphill pattern from lower to higher ICP values; this indicates a positive relationship between the estimated ICP (nICP) and the invasive measurement (ICP). Having a determination coefficient of 0.766 indicates that 76.62 % of the variation in the intracranial pressure is explained by variation in the estimated ICP values. Because the coefficient of determination can't exceed 100 %, a value of 76.62 % indicates that the regression line closely matches the actual sample data. Moreover, the estimated and invasive data have a strong correlation of 0.876 (p-value < 0.05), meaning that an increase in nICP corresponds to an increase in invasive measurement.

The Bland Altman analysis shown in Figure 133 (c) indicates an average bias between the invasive and non-invasive methods of 0.13, which is very close to zero. However, having a normal distribution for the differences (Kolmogorov Smirnov test, p -value > 0.05), it is expected that 95% of the differences between the two monitoring methods are within the range (± 5.3 mmHg). These limits of agreement ($Z=1.96$) are still wide for ICP monitoring, where clinical guidelines recommend a maximum difference of 2 mmHg. Moreover, the variability of the bias is consistent across the graph, and in accordance with the trend line, the estimated values at low ICP values (<18 mmHg) are higher than the gold standard, while at high ICP (>18 mmHg) are lower.

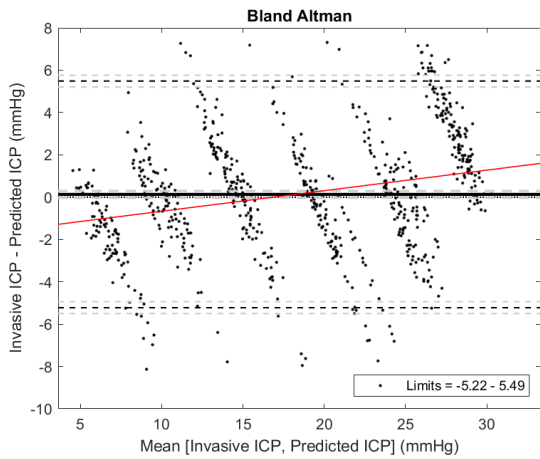
The residuals graph in Figure 133 (d) corroborates the normal distribution of the residuals as well as their random allocation, which suggests that the regression model is a 'good fit' for ICP estimation based on the features of the pulsatile optical signals. Finally, the ROC curve presented in Figure 133 (e) shows the diagnostic capacity of the model to estimate hypertension cases (ICP > 20 mmHg). The model presented a sensitivity of 0.898, which means that it has a high true positive rate of 89.8%. Similarly, the model has an optimal specificity value of 0.923; then, it can identify 92.3% of observations below the hypertension threshold of 20 mmHg. Ultimately, an area under the curve of 0.96 indicates the outstanding capacity of the model to classify normal and hypertensive observations.



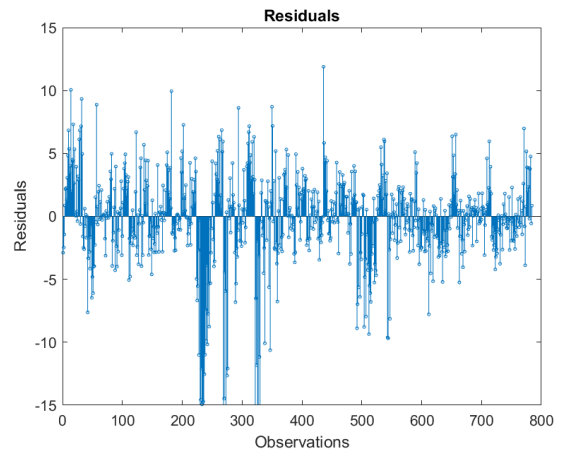
(a)



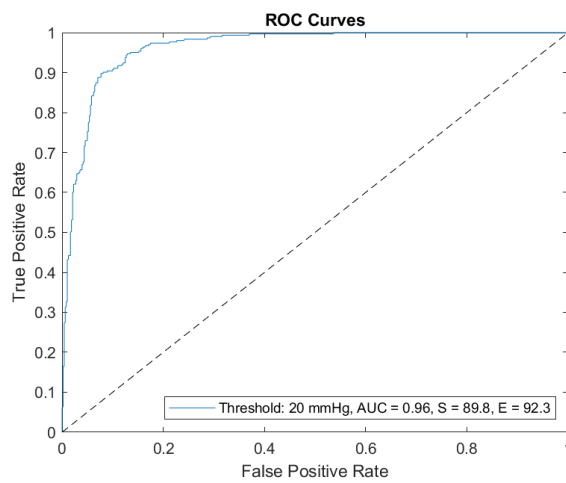
(b)



(c)



(d)



(e)

Figure 133: Model performance graphs from Pareto partition

Finally, using the data of all 16 replicates on small segments of 5 seconds, the model presented a mean absolute error of 3.72 mmHg, which supports the trend displayed on Figure 134 where the estimated data follows the changes in the intracranial pressure. The latter simulated the model performance in real time acquisition.

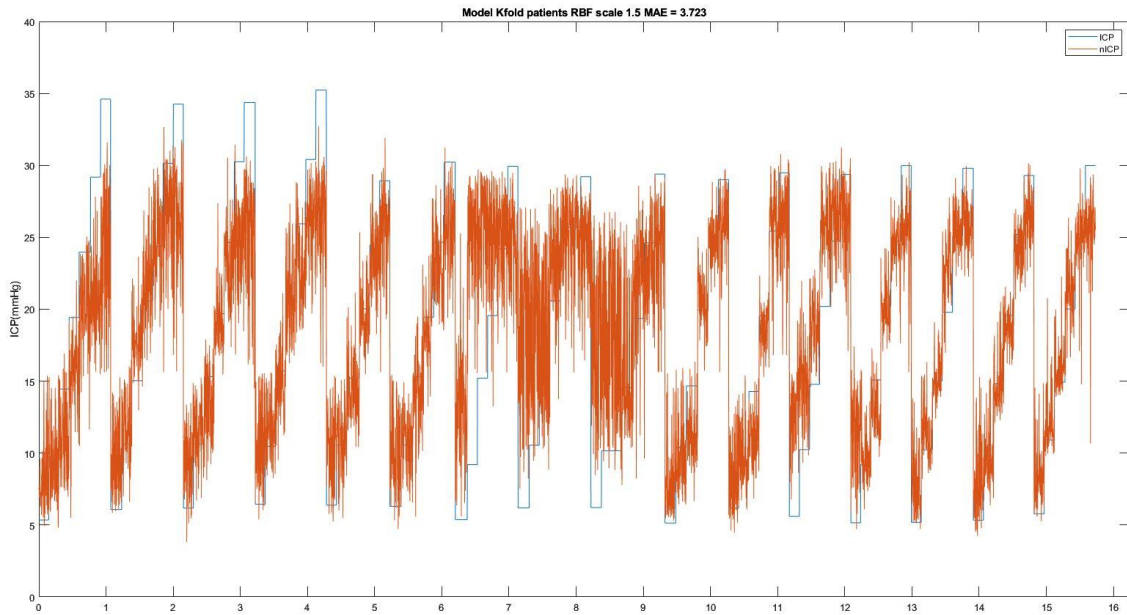


Figure 134: Online estimation of ICP from 5 seconds windows

10.3.2 Resultant model of the second partition approach, k-folds by replicate:

The same nine models were calculated per fold partition. As there were 16 folds, a total of 144 models were calculated for this k-fold approach. The best model from each fold was selected based on the accuracy parameters shown in Table 23. The top three models were selected from the sixteen resultant models. Figure 135 shows the behaviour of all three models using the aforementioned online method.

Table 23: Accuracy of the best model for each fold

Fold	Model	Scale	Error	Sensitivity	Specificity	AUC	Rsq	RMSE	Correl Coeff	P value correl
1	linear		0.43	0.97	0.99	1.00	0.09	7.55	0.97	<0.01
2	linear		0.02	0.99	0.95	0.99	0.88	2.89	0.95	<0.01
3	linear		0.07	0.96	0.94	0.98	0.82	3.48	0.96	<0.01
4	linear		0.08	0.97	1.00	1.00	0.88	2.87	0.96	<0.01
5	rbf	2	0.00	0.96	0.98	0.99	0.86	3.09	0.93	<0.01
6	rbf	2	0.05	0.89	0.99	0.99	0.83	3.55	0.93	<0.01
7	rbf	0.5	0.52	0.53	0.68	0.66	0.05	8.31	0.41	<0.01
8	rbf	1	0.40	0.99	0.66	0.85	0.18	7.54	0.54	<0.01
9	rbf	0.5	0.25	0.88	0.64	0.78	0.04	6.99	0.44	<0.01
10	linear		0.04	0.95	0.97	0.99	0.87	2.80	0.94	<0.01
11	linear		0.04	0.97	0.99	1.00	0.84	3.30	0.94	<0.01
12	rbf	2	0.30	0.99	0.74	0.90	0.63	5.07	0.89	<0.01
13	rbf	2	0.10	0.93	0.99	1.00	0.85	3.23	0.93	<0.01
14	rbf	2	0.13	0.94	0.96	0.99	0.89	2.77	0.96	<0.01
15	rbf	2	0.08	0.98	0.99	0.99	0.91	2.39	0.97	<0.01
16	rbf	2	0.12	0.94	0.96	0.98	0.88	2.74	0.95	<0.01

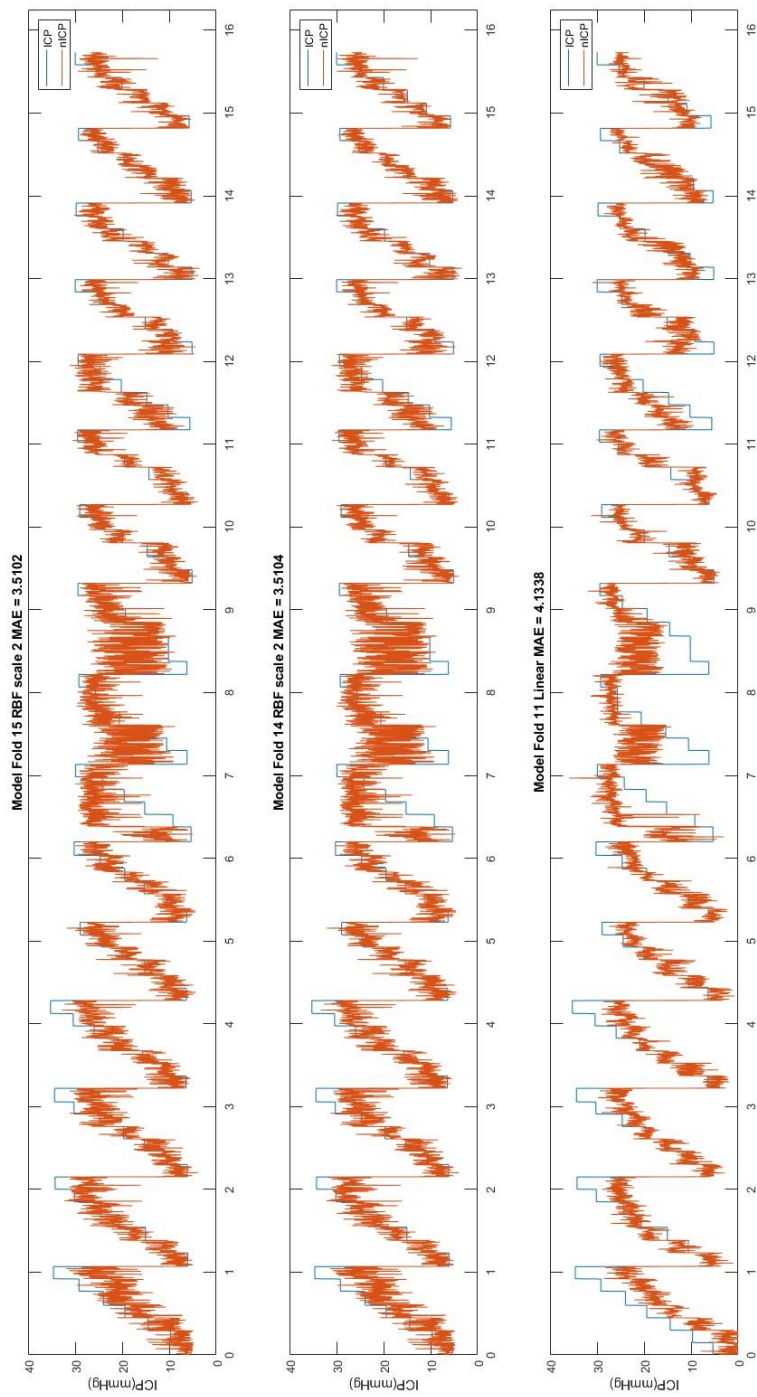


Figure 135: Online estimation of ICP from 5 seconds windows using the selected k-fold models

The best result from this analysis was presented by the RBF model with scale 2, which was calculated using fold 15 as the test data. This model has an online mean absolute error of 3.51 mmHg and shows a particularly good fit to the replicates.

The performance analysis shown in Figure 136 exhibited the response of the RBF scale 2 models when it was tested with all the data of the replicate number 15 (fold). In this analysis, the segments were randomized, so the intracranial pressure values are not sorted from low to high, as seen in (a). Also, figure (b) displays an uphill pattern from lower to higher ICP values; this indicates a positive relationship between the estimated ICP (nICP) and the invasive measurement (ICP). Moreover, this analysis depicts a high determination coefficient of 0.92, meaning that the estimated ICP values explain 92.79 % of the intracranial pressure variation. Similarly, a significant correlation coefficient of 0.97 (p-value < 0.05) implies that an increase in nICP corresponds to an increase in invasive measurement.

Moreover, the Bland Altman analysis plotted in figure (c) indicates an average bias between the invasive and non-invasive methods of -0.54, which is close enough to zero. However, having a normal distribution for the differences (Kolmogorov Smirnov test, p-value > 0.05), 95% of the differences between the two monitoring methods are expected to be within the approximate range of ± 4 mmHg. These limits of agreement ($Z=1.96$) are very good for non-invasive ICP monitoring, considering the maximum difference recommended by clinical guidelines (± 2 mmHg). Moreover, the variability of the bias is consistent across the graph, and accordingly, with the trend line, the estimated values at low ICP values (<17 mmHg) are higher than the gold standard, while at high ICP (>17 mmHg) are lower.

The residuals graph on (d) corroborates the normal distribution of the residuals and their random allocation, suggesting that the regression model is a 'good fit' for ICP estimation based on the features of the pulsatile optical signals. Finally, the ROC curve presented in (e) shows the diagnostic capacity of the model to estimate hypertension cases (ICP > 20 mmHg). The model presented a sensitivity of 0.93, which means that it has a high true positive rate of 93.1%. Similarly, the model has an optimal specificity value of 0.98; then, it can identify 98.4% of observations below the hypertension threshold of 20 mmHg. Ultimately, an area under the curve of 0.99 indicates the outstanding capacity of the model to classify normal and hypertensive observations.

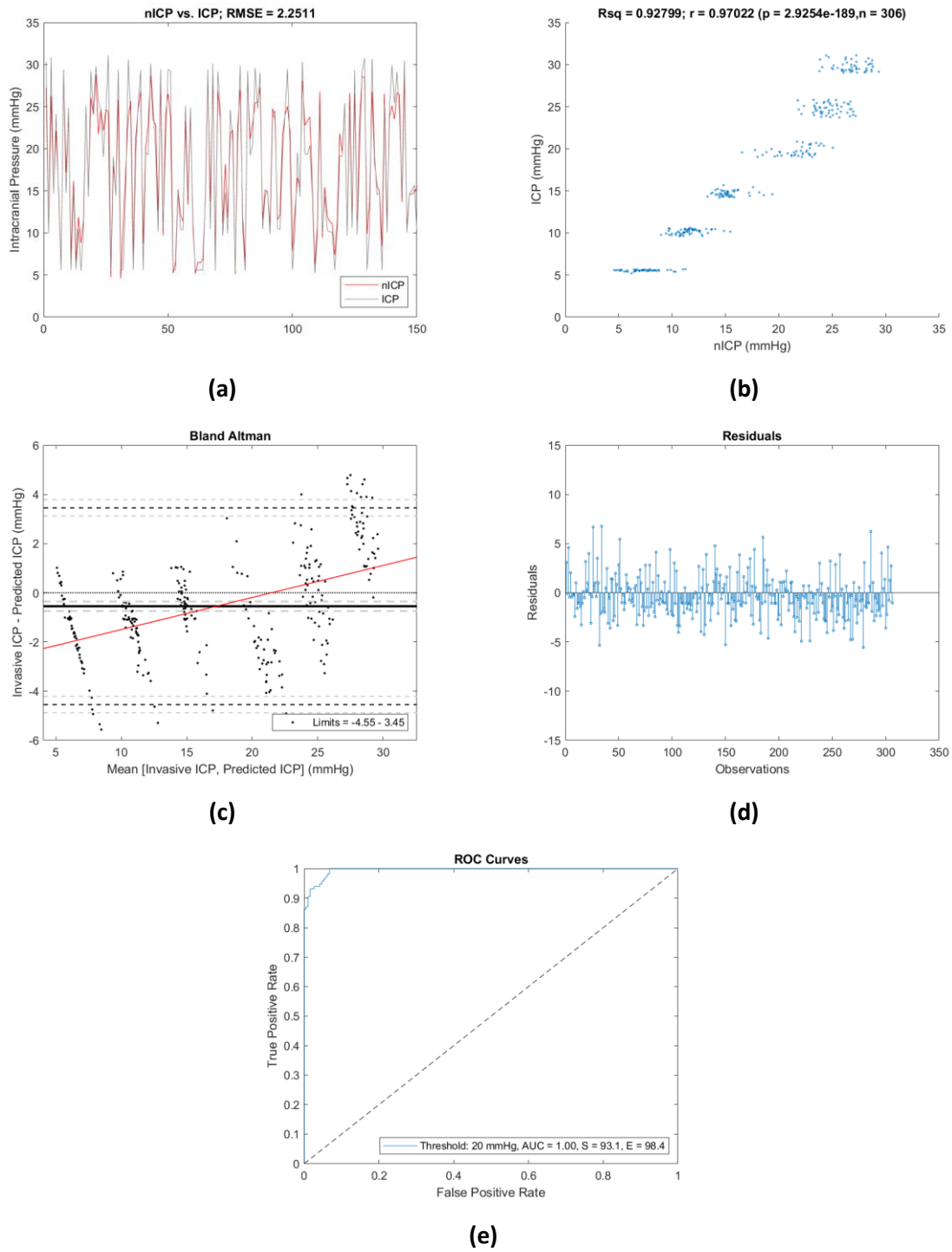


Figure 136: Model performance graphs from 15-fold partition

The results presented from both partition approaches ended in selecting RBF models as the best options for estimating ICP using the features of optical pulsatile signals. As the data were recorded using a phantom technology, the Pareto approach is valid to split the data, as every replicate occurred under the same simulated conditions. However, the k-fold approach is the most appropriate method for the future use of this technology in TBI patients, where each replicate emulates a different patient. Also, this partitioning method allowed the computation of the mean and standard deviation of the different accuracy parameters that resulted from testing RBF with scale 2 models at each fold. Table

24 presents an accuracy comparison between the RBF with scale 1.5 from the Pareto partition and the RBF with scale 2 from the k-fold.

Table 24: Comparison of the models selected from both partitioning methods

Accuracy parameter	RBF scale 1.5 pareto partition	RBF scale 2 k-folds partition	
	Absolute value	Mean	± sd
Error	0.09	0.17	± 0.18
Sensitivity	0.90	0.86	± 0.23
Specificity	0.92	0.94	± 0.09
AUC	0.96	0.94	± 0.10
Determination Coefficient	0.77	0.67	± 0.32
RMSE	3.92	4.43	± 2.39
Correlation Coefficient	0.88	0.86	± 0.15
P value correlation	0.00	0.00	

10.4 SUMMARY

In conclusion, the results of this study demonstrated that the features extracted from the pulsatile signals acquired with the ZenTBI are correlated to changes in the intracranial pressure within normal and pathological ranges. The simulation of both normal and pathological levels of ICP using the head phantom allowed the acquisition of a significant pool of data needed for the quantitative analysis of the PPG features and the development of multiple models for estimating absolute values of intracranial pressure. The accuracy of these non-invasive ICP measurements in real-time could enable the combination of this technique with NIRS for the multimodal assessment of ICP and oxygenation in TBI cases. Consequently, the next chapter demonstrates ZenTBI's capacity to measure oxygenation changes in a phantom-based technology.

11 IN-VITRO ASSESSMENT OF A NON-INVASIVE OXYGENATION SENSOR IN A PHANTOM

11.1 INTRODUCTION

This chapter aims to demonstrate the sensor's capability to measure changes in oxygenation by implementing a homogeneous phantom, and the SRS algorithms explained below.

11.2 METHODOLOGY

11.2.1 Phantom set up

A metallic cylindrical recipient was filled to the top with the liquid phantom solution described in the *blood oxygenation system* section of Chapter 8. The inner surface of the container was covered in black absorbing material to satisfy the semi-infinite boundary approximation (reflectance from a single layer system). A hot stirring bench controlled the temperature and the homogeneity of the solution.

A second oxygenation test was carried out in the head phantom, where the same recipe of the liquid phantom was used as blood in the circulatory system. The mixture was constantly heated and mixed in a glass reservoir that was connected to the oxygen supply. The intracranial pressure and the heart rate were set at 15mmHg and 50 pulses per minute, respectively.

11.2.2 Acquisition system

The custom-made, multi-parametric sensor described in Chapter 9 was placed on top of the liquid phantom. The sensor was protected by a clear film layer between the probe and the liquid phantom, and no gap of air was left between the sensor and the fluid. The separation between the proximal and distal probes was 5 mm and was continuously measured by the ruler that held the probe in place (Figure 137). Likewise, the optical sensor was located on the forehead in the head phantom test, and the probes' separation remained at 5 mm (Figure 137).

The probe was connected to the ZenTBI (Chapter 9), which was connected to a NI DAQ for analogue-to-digital conversion. The LabVIEW interface explained in Chapter 9 allowed signals visualization and interaction with the ZenTBI. In addition, LEDs' currents were calibrated to get a similar DC value at initial conditions. Finally, the signals were recorded with a sampling frequency of 2000Hz and recorded during the whole experiment without interruption.

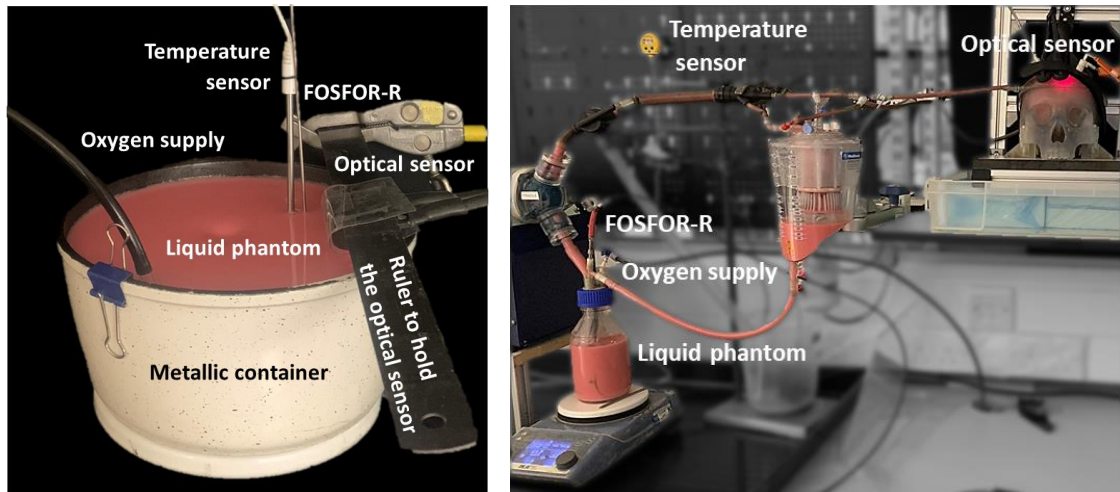


Figure 137: Phantom set up for non-invasive oxygenation measurements

The FOSFOR-R sensor from Ocean Insight optical, is an oxygen sensor that utilizes both ruthenium and platinum-based fluorescent molecules whose fluorescence is quenched by the presence of molecular oxygen. This probe is compatible with the NeoFox unit and the NeoFox Viewer software application (Ocean Insight optical, FL, USA). Accordingly, to its manufacturer, the NeoFox is a device for measuring fluorescence lifetime, phase and intensity. Therefore, quantification of oxygen was performed using the fluorescence-based O_2 sensor (Neofox; Ocean Optics FOSFOR-R probe), which was implemented in the setup as the reference measurement. The FOSFOR -R probe was submerged into the liquid phantom, leaving 2 cm from the container's bottom.

11.2.3 Experimental protocol

The measurements on the liquid phantom started after the temperature stabilized. One continuous record of the experiment was acquired per replicate. The initial baseline was measured from the liquid phantom before adding blood, oxygen, or yeast to the mixture. After 30 seconds, the blood was added steps of 5 ml to the mixture. The latter was to see the active response of both invasive and non-invasive sensors. The next step involved deoxygenating the phantom from its initial condition by adding 2 g of yeast. Once the <10% oxygen plateau was reached, the oxygen supply was turned on to record data until the FOSFOR-R probe showed an oxygenation level of 100%. The following deoxygenated and oxygenated cycles were controlled by only turning off and on the oxygen supply.

11.2.4 Analysis Protocol

MATLAB (version 2018b) processed and analysed the recorded signals. The signals were filtered using a fourth-order, lowpass filter with a cut-off frequency of 0.2 Hz to obtain the DC component. Then, the signals from distal and proximal detectors at both 770 nm and 880 nm were used to calculate the attenuation slope. The value of $\frac{\partial A}{\partial \rho}$ was measured by the probe as the change of light attenuation along

the photodetectors' distance. Light attenuation was related to light intensity (voltage measurements) by applying Beer Lamber Law as follows:

$$\frac{\partial A(\lambda_j)}{\partial \rho} = \frac{\log\left(\frac{I_{\text{photodiode (proximal)}}(\lambda_j)}{I_{\text{photodiode (distal)}}(\lambda_j)}\right)}{\rho_{\text{photodiode (distal)}} - \rho_{\text{photodiode (proxial)}}$$

By solving the diffusion approximation for a highly scattering medium ($\mu_a \gg \mu_s$), the value of $\frac{\partial A}{\partial \rho}$ was related to the relative absorption coefficient of the specific wavelength as follows:

$$K * \mu_a(\lambda_j) = \frac{1}{3 * (1 - h * \lambda_j)} * \left[\ln * \left(10 * \frac{\partial A(\lambda_j)}{\partial \rho} \right) - \frac{2}{\rho} \right]^2$$

Where K represents an unknown constant for scattering in the near-infrared region, $\rho = 3\text{cm}$ is the mean emitter-detectors distance, and h is the normalized slope of μ_s along λ , which is invariable among tissues and subjects, then $h = 6.3 \times 10^{-4}$ (mm^{-1}/nm) is used [296]. Furthermore, it was possible to calculate the relative concentrations of both chromophores by solving the following equations system for at least two wavelengths (770 nm and 880 nm). Where $\varepsilon_{i,j}$ are the extinction coefficients of $i = [\text{HbO}_2]$, $[\text{HHb}]$ and $j = \lambda_1, \lambda_2$.

$$\begin{bmatrix} K * \text{HbO}_2 \\ K * \text{HHb} \end{bmatrix} = [\varepsilon_{ij}]^{-1} * \begin{bmatrix} K * \mu_a(\lambda_1) \\ K * \mu_a(\lambda_2) \end{bmatrix}$$

Moreover, these concentrations were used to find the tissue oxygenation index (TOI).

$$\text{TOI} = \frac{K * [\text{HbO}_2]}{K * [\text{HbO}_2] + K * [\text{HHb}]}$$

11.3 RESULTS

11.3.1 Liquid phantom setup

The liquid phantom was manufactured with the aim of testing the TBI probe's capability to detect changes in oxygenation levels. Initially, the baseline of the solution without any blood was measured. The active response of the isosbestic wavelength (810 nm) to the addition of blood by steps of 5 ml is displayed in Figure 138.

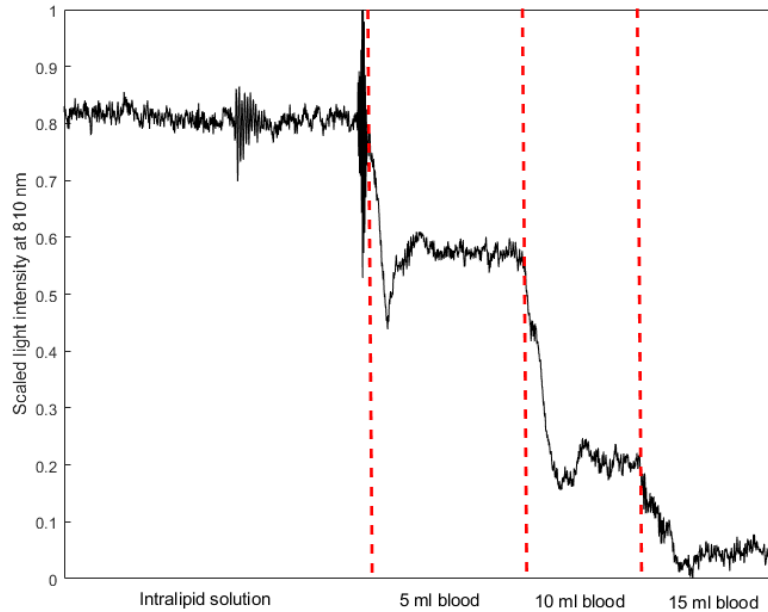


Figure 138: Sensor response to the presence of blood

The experiment was run a couple of times. One replica was selected to illustrate the sensor's response and subsequent calculation of the Tissue oxygenation index.

Figure 139 displays the raw optical signals from both photodiodes of the distal probe at 770 nm and 880 nm. The normalized values of the light intensity measured by the detectors behave as expected. The light intensity at 770 nm is higher when the phantom is oxygenated due to less light being absorbed by haemoglobin at this wavelength in comparison to the light absorbed by haemoglobin at 880 nm (Figure 140). The opposite occurs when the phantom is deoxygenated, as a higher concentration of deoxyhaemoglobin absorbs more light at 700 nm and less light at 880 nm, leading to a drop in light intensity at 770 nm and an increase in the detected light intensity at 880 nm wavelength. Also, the light intensity from the proximal photodetector was always higher than the light intensity from the distal photodetector, which guaranteed the correct acquisition of the optical signals and the subsequent calculation of positive slopes for both wavelengths.

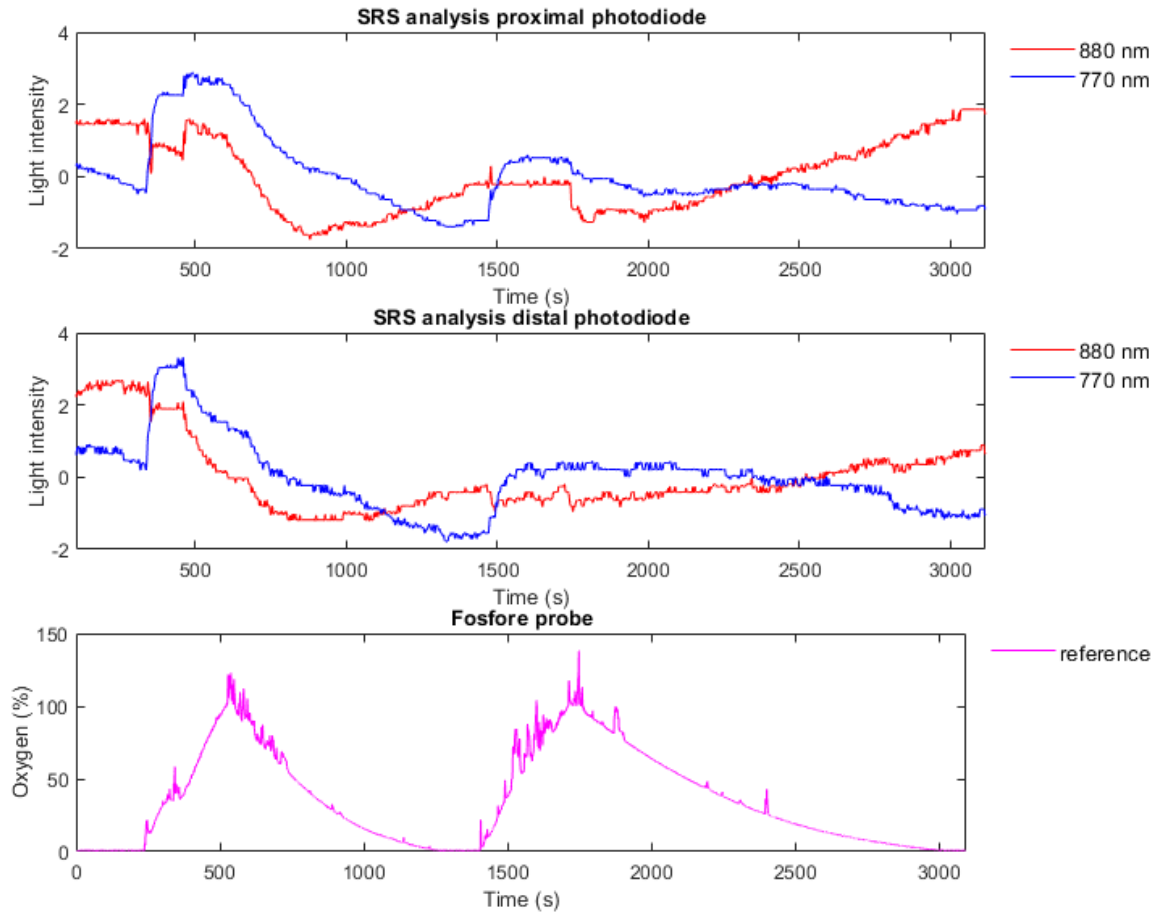


Figure 139: Normalized optical signals at 770 nm and 880 nm in comparison with the FOSFOR-R probe measurement

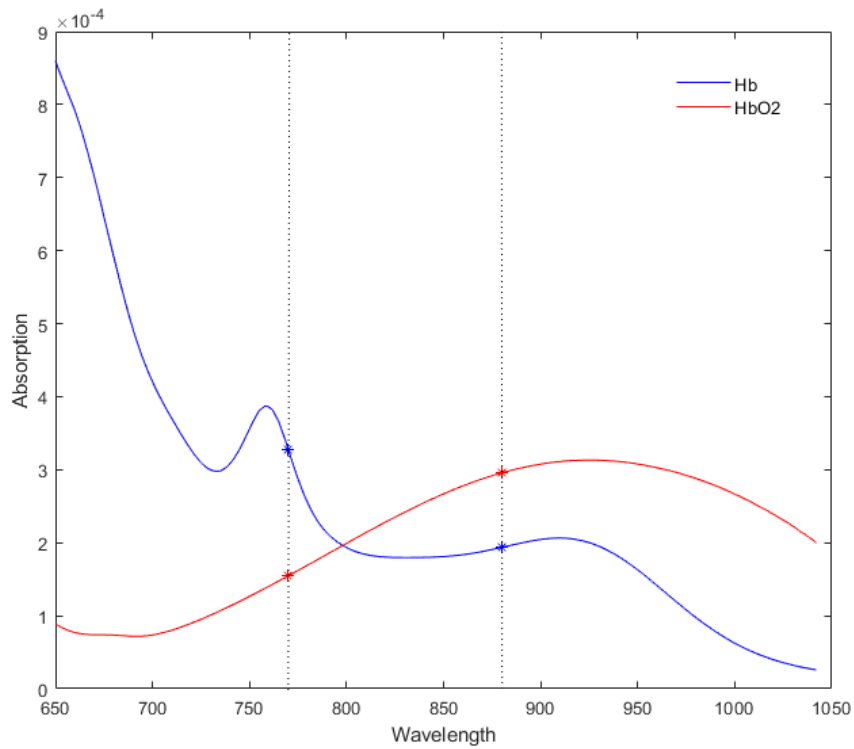


Figure 140: Haemoglobin absorption spectra

The Tissue oxygenation index was calculated from the acquired optical signals using the SRS algorithm previously explained in the methods section. The resultant TOI can be compared to changes in the oxygen levels in Figure 141.

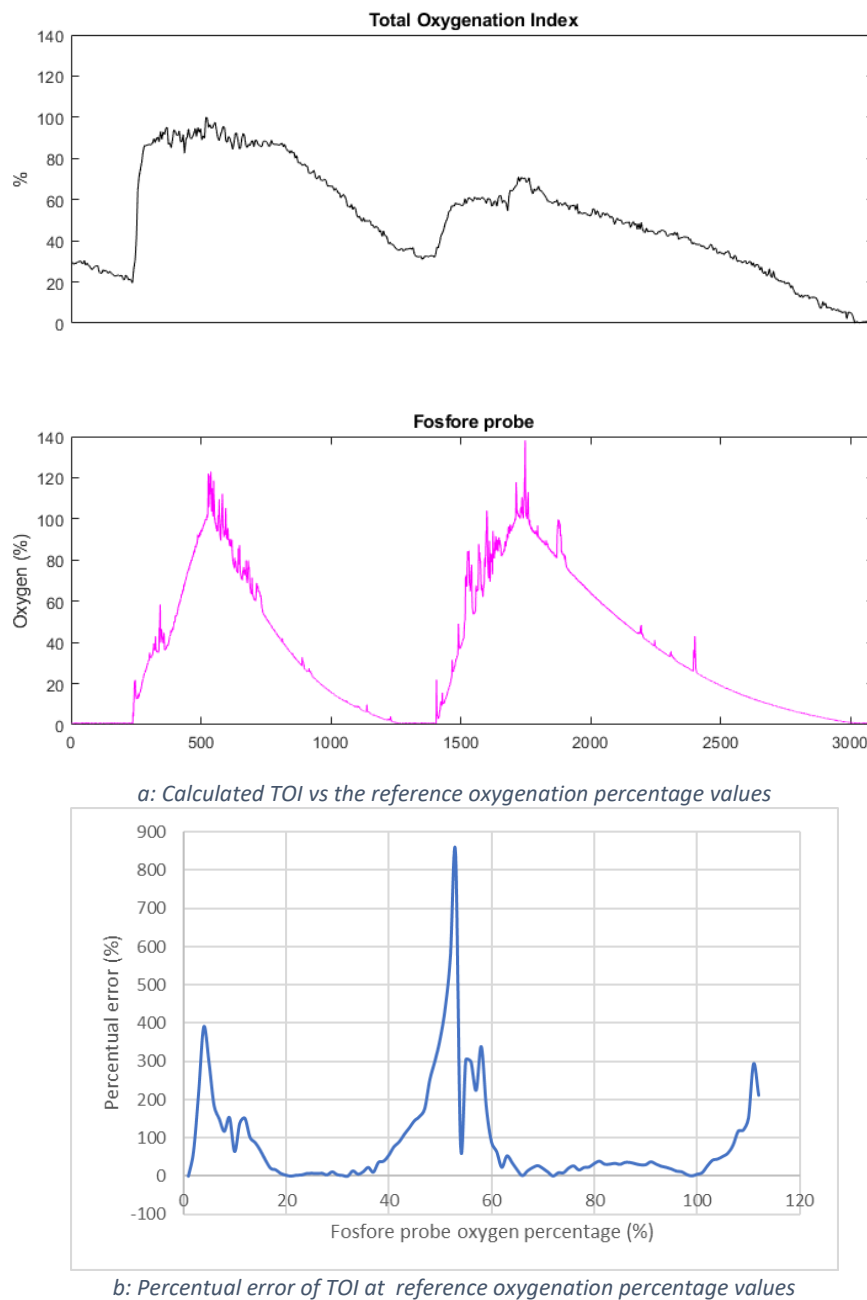


Figure 141: Calculated Tissue oxygenation index (TOI) in comparison with the FOSFOR-R probe measurement

Only after the offline analysis of TOI was completed opportunities to improve the protocol were identified. For instance, it can be noticed that the zero value on the reference does not agree with the lowest value of TOI. The latter could be explained by the fact that the experiment had run before this illustrative replica, and then a low haemoglobin concentration remained on the fluid. Moreover, the default calibration curve of the FOSFOR-R measures the oxygen level in the liquid phantom, which

correlates to changes in oxygenated haemoglobin. However, it was observed that the absence of oxygen did not imply an instant drop in haemoglobin concentration. For instance, after the first cycle, the percentage of haemoglobin per total haemoglobin had not dropped completely before the oxygen was turned on again. Only at the end of the second cycle, where the oxygen was left off for longer, a skewer drop in TOI was observed. A similar effect occurs with the oxygen peaks, where an increased TOI correspond with the FOSFORE peaks, yet their changes in magnitude are not the same. The percentage error shows that the biggest differences are at values close to zero, which could be a calibration error and at values around 50% oxygenation. The latter is evident in the skewer slopes of the reference in comparison to the calculated TOI. Nonetheless, the percentual error is low within the 20 to 40% range and 60 to 100% oxygenation values. It was found that half of the measurements had an error against the reference under 33.8%.

The calibration curve provided by the manufacture of the FOSFORE-R was calculated from free oxygen particles in water, which is why the percentage of oxygen measured by the FOSFOR probe is correlated to changes in TOI yet does not correspond to the absolute concentration of oxyhaemoglobin in the liquid phantom. It is reasonable to think that more time of exposure to oxygen is needed to get higher changes in the tissue oxygenation index, as no complete saturation (100%) of this parameter was evidenced during the experiment. As explained in previous chapters, NIRS technology is sensitive to variations in room temperature, outside light, and movement artefacts that critically affect the TOI calculation.

11.3.2 Head phantom using the liquid phantom fluid as blood

Since the deoxygenation process in the head phantom took twice the time in comparison to the liquid phantom setup, the signals register started with the blood fully oxygenated. Then, the yeast was dissolved in 50 ml of the solution and injected into the cardiotomy venous reservoir. The oxygen supply was turned on when the FORFORE oxygen measurement was below 10%. Unlike the liquid phantom's protocol, the oxygen flow was not constant in the head phantom setup to avoid overpressuring the system. The variation in the oxygen level (40 % to 100 %) can be observed in Figure 142. The behaviour of the optical signals at both photodetectors was as expected. The light intensity at 770 nm is higher when the phantom is oxygenated and lower when the oxygen level is reduced, which is the opposite that occurs to the light intensity at 880 nm. Therefore, the normalized optical signals cross each other when there is a change in the haemoglobin concentration. This represents the possibility of measuring changes in oxygenation using the optical sensor and the head phantom.

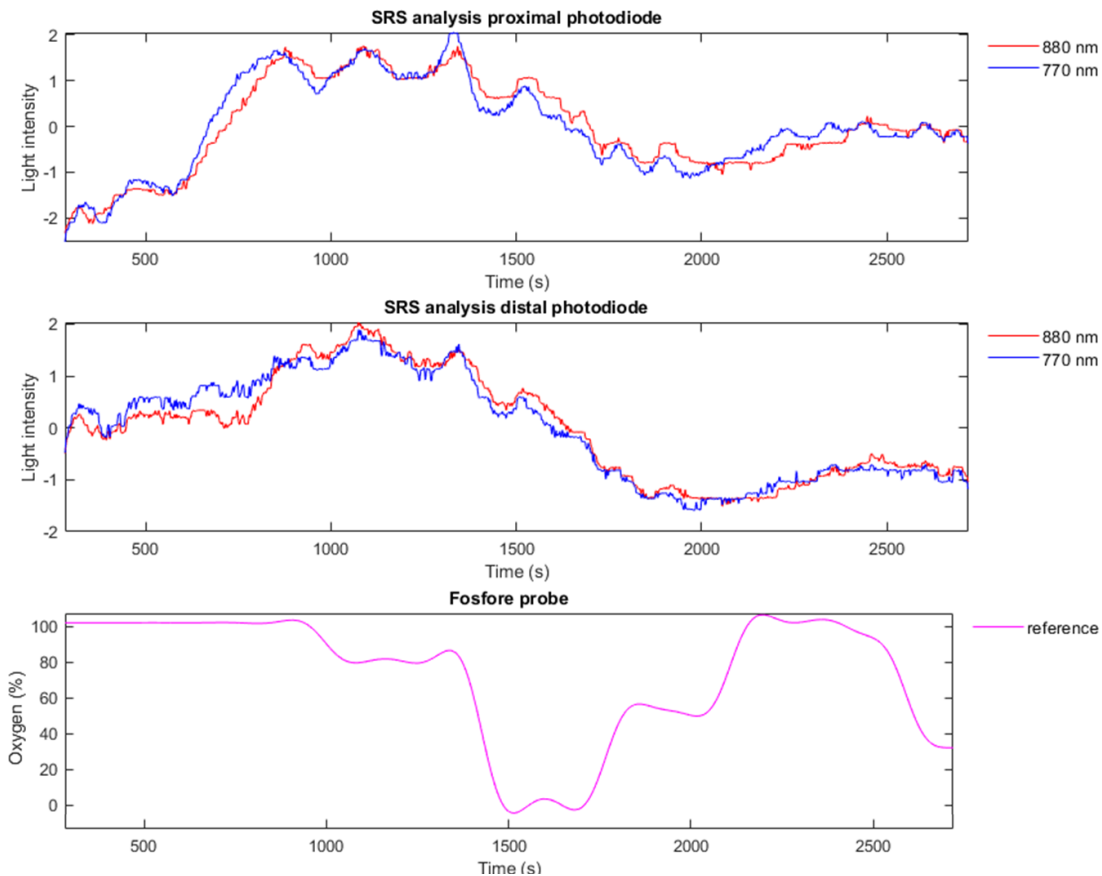


Figure 142: Normalized optical signals at 770 nm and 880 nm in comparison with the FOSFOR-R probe measurement, acquired from the head phantom using the liquid phantom fluid as blood

Nonetheless, the trend of both wavelengths is too similar, which has a restrictive effect on the subsequent TOI calculation. This behaviour might be related to the presence of multiple layers in the phantom, which increase photons loss, leading to a smaller change in light intensity from both wavelengths. Specific calibration of the optical system gain to obtain signals from the head phantom might magnify these differences in light intensity.

Finally, pulsatile signals from the closest distal photodiode were collected using the liquid phantom fluid. Less noisy pulsatile signals at 810 nm and 880 nm can be observed with the naked eye. Even though the quality of the signals can be improved by increasing the system pressure, heart frequency and stroke volume, these results are a sample of the future implementation of this setup to evaluate both ICP and oxygenation changes at the same time in the head phantom. Also, these findings open the door to further in vitro analysis of oxygen saturation (SpO₂).

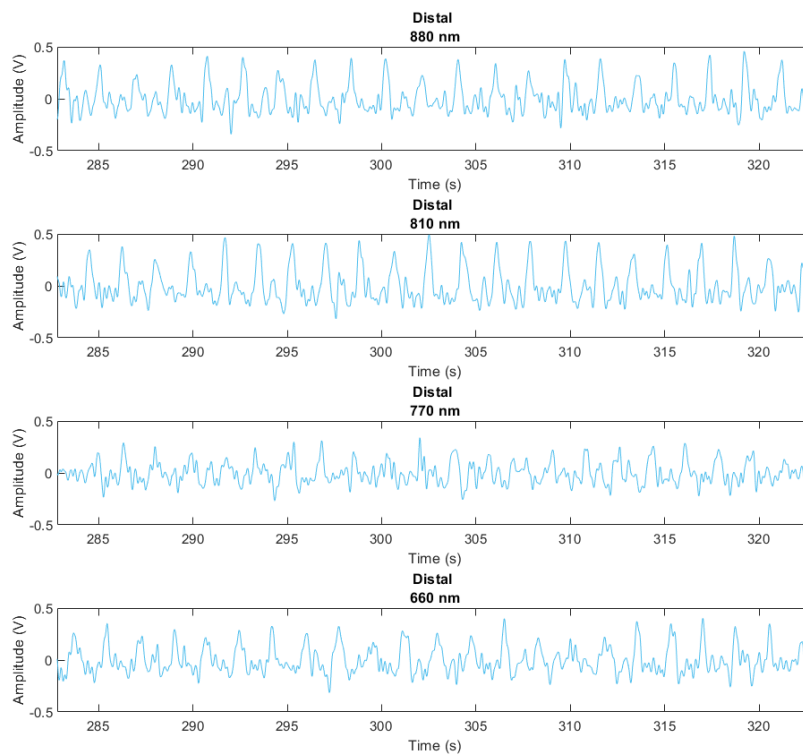


Figure 143: Pulsatile signals acquired from the head phantom using the liquid phantom fluid as blood

11.4 SUMMARY

In conclusion, the in-vitro experiment presented in this chapter is a proof-of-concept capability of the ZenTBI to measure changes in oxygenation level. The simulation of both normal and ischaemic oxygenation levels using the fluid phantom allowed the acquisition of optical signals at 770nm and 880 nm, needed for the quantitative calculation of the tissue oxygenation index. Implementing these non-invasive oxygenation measurements in the head phantom could enable the combination of this technique with the aforementioned ICP estimation for the multimodal assessment of ICP and oxygenation in TBI cases.

12 DISCUSSION

12.1 SUMMARY OF THE CURRENT NON-INVASIVE MULTIMODAL MONITORING TECHNIQUES TO ASSESS ICP AND CEREBRAL OXYGENATION IN TBI PATIENTS

The literature has shown the importance of multimodal monitoring in diagnosing, prognosis, and treating patients with TBI [32]. However, no cohort study in the last decade has compared the correlation or accuracy of a non-invasive multimodal monitoring technique with their respective (invasive) reference measurement in TBI patients. The later bearing in mind that there is not gold standard for invasive oxygenation monitoring that is comparable with NIRS principles. This research presented a systematic review that identified non-invasive techniques which might be used for the multimodal, non-invasive, and continuous monitoring of brain oxygenation and ICP. Although this review identified NIRS and TCD as the current prominent non-invasive techniques for monitoring brain oxygenation and ICP, significant research is still required to collect sufficient evidence for implementing multimodal monitoring technologies for TBI patients.

Despite the inconclusive results of the systematic review regarding oxygenation monitoring in TBI patients, evidence suggests that NIRS might be the most promising non-invasive technology to develop a multimodal sensor for TBI monitoring, as it can investigate multiple parameters of cerebral haemodynamics [158]. Therefore, this research involved a literature review to rigorously investigate the utilisation of NIRS in TBI and synthesise the available evidence of the association between NIRS-based measurements and commonly monitored neurophysiological parameters, such as oxygenation and cerebral autoregulation.

The physical principles of NIRS allow the interrogation of deep tissue layers and the calculation of blood chromophores concentrations, such as haemoglobin and deoxyhaemoglobin. The two most common approaches are the modified beer lambert law in CW-NIRS and the diffusion equation in SRS, which have provided valuable information regarding cerebral oxygenation in TBI monitoring. Despite the intrinsic limitations of this optical technology and the absence of a valid invasive reference that measures the same parameters, heterogenic evidence has found a correlation between NIRS measurements and invasive values of P_{btO_2} and S_{jvO_2} , as well as with oxygenation interventions and other cerebral physiological parameters, such as CBF, ICP and CPP.

Furthermore, this tool suggests the alteration of intracranial conditions at both extremes of autoregulation failure, as haemoglobin concentration and total haemoglobin increase during hyperemia and decrease at hypoxia or ischaemic conditions. The latter stands by the correlation between traditional autoregulation indexes and those calculated from NIRS measurements. Therefore, it is sensible to consider NIRS as a valuable source of cerebral information that could be

implemented in addition to cerebral oxygenation monitoring to assess other physiological parameters within the skull, leading to a multimodal monitoring tool.

12.2 SUMMARY OF THESIS AND FINDINGS

This research designed, manufactured and tested a novel optical sensor to provide a non-invasive, continuous monitoring tool that evaluates changes in intracranial pressure and oxygenation after a traumatic brain injury. An essential work package presented in this thesis is the in-vitro setup developed to test the sensor. The resultant novel head phantom mimics tissues' optical properties, the skull and brain anatomies, and some physiological variables (i.e., ICP, heart rate, stroke, blood oxygen level) can be controlled.

Most phantoms reported in the literature mimic up to two of the abovementioned requirements. The head phantom presented in this work matches the optical properties of the actual brain and the skull, which was tested by a materials characterization and comparison with animal samples and reported values in previous literature. At the wavelengths of interest, the silicone and resin implemented to mimic the brain and skull presented closer optical properties to the respective pig tissues. Yet, even fewer differences were found when the absorbance and reduced scattering coefficients were compared to the optical coefficients reported by other authors [227], [236], [277], [278].

Moreover, the phantom was designed to replicate the anatomical structures of an adult man, bearing in mind that men have twice the risk of head injury than women. Although the model is a simplified version of a very complex anatomy, the phantom includes the main structures to test this thesis hypothesis (brain and skull), simulating their anatomical measurements. Furthermore, the blood circulatory system perfuses the silicone cerebral vessels leading to blood pulsations within these vessels and the further acquisition of cerebral PPG signals.

Considering that this phantom is a tool for testing a multimodal optical sensor for ICP and cerebral oxygenation monitoring, features were included to mimic related physiological changes. For instance, the skull was adequately sealed, and a controlled CSF circulatory system was developed to allow controlled changes in the intracranial pressure. Likewise, a liquid phantom based on intralipids and animal blood was tested to induce changes in oxygenation levels. As demonstrated, the resultant head phantom fit the design requirements and helped with the design, development and testing process of the developed ZenTBI system.

The ZenTBI sensor involves a reflectance probe with a four-wavelength light source and three photodetectors. The sensor enables the detection of backscatter photons from cerebral and extracerebral layers. Although literature and commercial NIRS devices have defined optimal source-detector ranges to interrogate the brain using near-infrared light, this research applied its own Monte

Carlo simulation in a healthy head model to test the sensor's geometry. This study indicated that source-detector separations above 3 cm would allow the sensor to assess brain tissue with less interference from extracerebral tissues. Furthermore, 3 to 5 cm separations showed optical penetration depths from 11 to 15 mm. Finally, was noted the parabolic banana-shaped transcranial pathway of the reflectance configuration.

In addition to the sensor geometry, the LED's wavelengths and the multiple photodetector's positions were defined by the parameters to measure. Firstly, the probe design proposes the use of red (660 nm) and infrared light (880 nm) measured by a proximal photodetector (S-D=10 mm) to calculate arterial oxygen saturation using traditional pulse oximetry methods. Although the phantom lacks a perfused scalp, the artificial blood analysis showed PPG signals with their DC component collected with the proximal photodetector. Therefore, it is reasonable that the proximal sub-probe would work as a pulse oximeter probe.

Secondly, the probe incorporates two different infrared light wavelengths (770 nm and 880 nm) that penetrate deeply into the head tissues and discriminate between the unique absorption spectra of oxyhemoglobin and deoxyhemoglobin. The DC signals from the backscattered light of these NIR wavelengths were detected by two distal photodetectors placed within a 3 to 4 cm distance from the source. This specific configuration enabled the evaluation of relative changes in cerebral oxygenation using well-known SRS-NIRS algorithms. Such in-vitro evaluation required developing a blood oxygenation system that mimicked oxygen level changes in a liquid phantom. Results displayed similar trends of TOI against the reference (FOSFOR-R) while oxygen was diluted into the liquid. Therefore, it is reasonable that the source and distal sub-probe would work as an SRS-NIRS probe for cerebral oxygenation monitoring.

Unlike PPG, NIRS considers artery pulsations as noise; consequently, these systems eliminate the AC component with temporal and spatial filters[297]. However, these oscillations can be used to extract meaningful information about cerebral physiology. As explained in the first chapters of this thesis, under normal physiological conditions, the transmural intracranial pressure (ICP, the pressure within the skull) has little effect on the cerebral perfusion pressure (the gradient of pressure to perfuse the brain) due to cerebral autoregulation. However, when ICP becomes dangerously high (such as after a head injury), the transmural pressure constricts the vessels at flexible sites, such as vessels on the brain's surface and arterioles [64]. The latter leads to morphological changes in the cerebral PPG signals that could be rigorously analysed through quantifiable features to enable the development of a computational model to estimate absolute values of intracranial pressure non-invasively. Under this rationale, the ZenTBI sensor utilises one of the distal photodetectors to acquire PPG signals from the cerebral surface vessels at the isosbestic point (810 nm).

In vitro experiments for data acquisition at different ICP values resulted in the evaluation of PPG features and further evaluation of ML models to estimate ICP non-invasively. This work demonstrated for the first time that computational models based on cerebral PPG features could estimate the intracranial pressure with a mean absolute error of 3.7 mmHg. Although all the findings mentioned above result from methodical and rigorous in-vitro work, as was expected within the frame of this doctoral thesis, the multimodal sensor proposed here could have a massive impact on patients' lives and healthcare costs if it would make its way to the market.

This technology will enable earlier and better detection and, thus, earlier diagnosis of raised ICP and impaired cerebral oxygenation, leading to better patient outcomes. In addition, this non-invasive device could reduce secondary brain injury caused by too few patients receiving monitoring due to the high costs, risks and logistic challenges of invasive monitoring. Moreover, it has the potential to transform healthcare delivery by allowing neuromonitoring in new patient populations (patients with moderate TBI or TBI contraindicated for invasive monitoring because of blood-clotting disorders, and patients with other neurological conditions such as hydrocephalus, meningitis, brain tumour, stroke) and in new settings (at the accident scene or during triage). In addition, a future ZenTBI commercial device could drastically reduce financial costs (invasive monitoring costs for the NHS on average £9,050 per patient) and patient risks, including risks from patients being left unmonitored.

12.3 COMPARISONS WITH OTHER RELATED WORKS

12.3.1 Head phantom

Biomedical in-vitro models aim to replicate different characteristics and processes of the human body. Mainly, this research designed and manufactured a novel NIRS-compatible head phantom where ICP and blood oxygenation can be controlled. To date, multiple phantoms have been developed to test cerebral oxygenation measurements with NIRS devices, which involve hundreds of small vessels (≈ 0.6 mm) to represent the cerebral vascular network [227], [235]. The phantom presented in this research only included four intracranial arteries, the MCA and three ACAs. The optical signals were measured from the ACAs, which each has an internal diameter of 2.2 mm, corresponding with the value reported in the literature of 2.09 mm [260], yet much bigger than the vessels simulated in other NIRS phantoms [227], [235]. The box-shape systems reported in the literature ease the involvement of so many small vessels but neglect the effect of vessels' compliance to acquire pulsatile optical signals and the human anatomy.

The developed phantom simplified the intracerebral network in order to mimic the brain and skull anatomy. The 3D-printed skull was scaled from a pre-existing CAD model, and the brain was cast from an anatomical training model. The resultant geometry fits the literature's normal values for

intracranial and parenchymal volumes [253]–[258]. Moreover, similar manufacturing resources have been used by other researchers to mimic human anatomy; for instance, Bonnet et al. used a plastic human skull model from 3B Scientific and cast a human brain [231]. Nonetheless, more accurate anatomical models have been created from healthy adult magnetic resonance images [229], especially for developing MRI-compatible or CT-scan-compatible phantoms [230], [233], [238]. Also, additional anatomical structures have been included by other authors, such as ventricles, the circle of Willis, meninges, scalp, skin and hair [231], [237], [238]. All these anatomical structures play crucial roles in cerebral fluid dynamics and optics measurements; then, they should be incorporated into a future version of the phantom in order to get closer to reality.

A literature review has indicated the optimal set of phantoms' composition and properties for specific applications [242]. The reviewers highlighted the use of silicone and resins as durable phantom matrixes to mimic complex geometries [242]. The materials and manufacturing techniques described in this research are not significantly different to the methods reported by other authors. For example, multiple authors have created life-sized silicone brains using Sylgard 527 to mimic cerebral mechanics [231], [237]. Others have used agar gel and silica dioxide to create optical-compatible intracranial phantoms [232] or a clear polyester plastic resin mixed with titanium dioxide to replicate optical but not mechanical properties [227]. Therefore, this work utilized TiO₂ to mimic tissue scattering in a silicone brain model that could emulate both mechanical and optical properties.

Likewise, this is not the first study where the human skull anatomy has been replicated, though it is the first time that NIRS measurements have been tested directly from the phantom's forehead. Most studies utilized polyester and polyurethane resin phantoms, and in some cases, the resin was mixed with scattering additives such as TiO₂, microspheres, and Indian ink, among others [231],[234],[237],[242]. The Formlabs resin implemented to 3D print the calvaria of the phantom's skull is a polyurethane resin, which has been suggested to match the tissues' absorbing molecules better [242]. The materials spectra analyses presented in this thesis showed that the brain and skull's optical properties are comparable to the animal samples and literature.

Furthermore, liquid solutions have been used with great success in conjunction with solid phantoms, where holes or channels have been left in the solid phantom to replicate optical properties heterogeneity [242]. Accordingly, two aqueous suspension phantoms were developed in this research with the aim of mimicking blood's optical properties and oxygenation changes. The first ink-based approach successfully imitated blood's spectra trend within the NIR range, allowing the acquisition of PPG signals from the phantom's cerebral vessels. This fluid is durable and can be reused multiple times, yet it does not mimic changes in oxygen concentrations. However, a previous study reported ink-based artificial blood that replicates changes in oxygen concentration [271], which could

not be reproduced in this work but would be most valuable for further in-vitro research. Considering the facts, this research had to implement a liquid phantom based on intralipids and erythrocytes from whole animal blood. This recipe was proposed by Lange et al. [274] and has been implemented in several studies to assess NIRS technology response to changes in oxygenation level [274], [298].

This research tested multiple oxygenation approaches, as oxygen saturation is not easily changed. The final liquid phantom involved distilled water with PBS, which contains sodium chloride to maintain the pH and has similar osmolarity and ion concentration to the human body to avoid blood cells lyse and heme dissociation from the haemoglobin molecule [242].

Intralipids are highly used in liquid phantoms as they are biologically similar to what is thought to cause scattering in human tissues [242]. Conversely to titanium dioxide (TiO₂), the most common choice for scattering in science and engineering, intralipids do not settle, making them a better option for aqueous phantoms [242]. In accordance, this research utilized intralipids for the liquid phantom while TiO₂ particles were dissolved in the silicone mix used to build the phantom brain. The main consequences of this scatterer choices are 1) the durability of the liquid phantom (days) in comparison to the brain (years) [242], and 2) the differences in the index of refraction (IR) between the fluid (IR = 1.45) and the brain (IR = 2.4).

Finally, the addition of whole blood into the liquid phantom provides realistic tissue spectra where oxygen can bind to the haemoglobin of the red blood cells [242]. Multiple authors have implemented oxygen diffusion methods to change oxygen saturation [227], [235]. The most common techniques are changing oxygen and nitrogen concentrations or adding oxygen and yeast into the solution [274]. Nonetheless, the nitrogen method is relatively slow and sensitive to gas exchange between the phantom and the ambient air. In contrast, the yeast method is simpler to implement and deoxygenates the blood faster [274].

The phantom performance regarding the oxygenation setup was tested by a fluorescence probe comparable to the clinical invasive technique called tissue oxygen tension (PbtO₂). The raw optical signals acquired from the distal photodetectors in the liquid phantom agreed with the optical signals trend reported in an in-vivo study where momentaneous ischemia was induced in healthy volunteers' arms [299]. Moreover, the agreement between oxygen levels and light intensity for different wavelengths allows the calculation of relative haemoglobin concentrations. However, it was hard to identify a complete deoxygenated and oxygenated status in the liquid phantom using the Fosfore R probe; therefore, future experiments should create a calibration curve of the reference for this application or replace it with another reference sensor. For instance, Afshari's study showed a good

relationship between oxygen concentration and StO₂ level measured by a whole-blood-CO-oximeter [235].

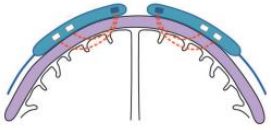
In addition to the oxygenation setup, the head phantom consists of a CSF circulatory system that allows controlled intracranial pressure changes. The constant infusion of fluid into the subarachnoid space was the main contributor to the change in the intracranial volume, leading to a subsequent increase in the intracranial pressure. Other studies have reported phantoms designed for replicating CSF dynamics, which describe the exponential relationship between volume and ICP [231]. Although the current work did not run several infusion tests to assess V/P association, the resultant ICP trends from the constant pressure infusion test shown in chapters 8 and 10 are similar to the results presented by Bottan [231].

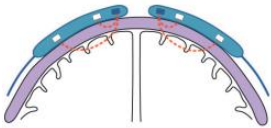
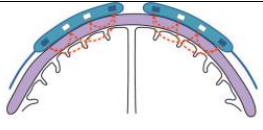
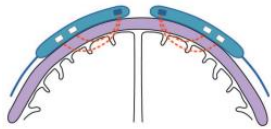
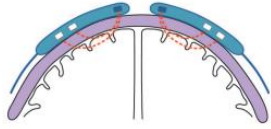
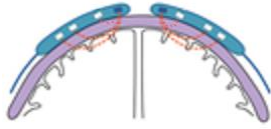
12.3.2 Probe and instrumentation design

Similar to the comparison with the literature presented above for the head phantom, this section compares the probe and instrumentation design with other optical systems for neurocritical monitoring.

Even though the Montecarlo simulation results presented in this study were obtained from a healthy head model, the maximum penetration depth was 1.5 cm at an S-D separation of 5cm. However, the quality assessment of the PPG signals acquired from the phantom showed poor quality at such a big separation (5 cm), concluding that an optimal S-D separation to reach the cerebral tissue, as well as good PPG signals, is within 3 cm to 4 cm. Controversially, most NIRS commercial devices placed the distal detectors within the range of 4 and 5 cm [300]–[303], and they report higher depths of penetration (40% more) assessed by functional NIRS [300]. In particular, the Foresight elite (Casmed, UK) is the only NIRS system that has a large distal S-D distance of 5 cm and a proximal detector S-D separation of 1.5 cm, for this system, the depth of penetration (DOP) is 2.5 cm (60% more) [302]. Nonetheless, an in-vitro evaluation of NIRS depth of penetration in a liquid phantom shows a maximum of 1.5 cm depth using an S-D separation of 4 cm, which is closer to the results obtained in the Montecarlo simulation [304].

Table 25: Comparison of commercial NIRS probes with the ZenTBI probe

NIRST System	Manufacturer	λs	Photodiode S-D separations	Design
INVOS	Medtronic	730 and 810 nm [302]	30 mm and 40 mm [303]	

FORE-SIGHT ELITE	Casmed	685, 730, 770, 805, and 870 nm [302]	15 mm and 50 mm [303]	
EQUANOX	Nonin Medical Inc	725, 760, 810 and 870 nm [305]	20 mm and 40 mm [303]	
NIRO	Hamamatsu	735, 810, 850 nm [306]		
O3	Masimo	4 different λ s, not found in literature [307]	30 mm and 40 mm	
ZenTBI	In-house	660, 770, 810 and 880 nm	10 mm, 30 mm and 38 mm	

In addition to the differences in S-D separations, commercial NIRS systems interrogate multiple wavelengths. Mathematically, the same number of wavelengths are needed per chromophore analysed; therefore, only two wavelengths are required to calculate HbO₂ and HHb concentrations. However, Table 25 shows that four of five NIRS manufacturers interrogate more than two wavelengths within the near-infrared spectra. These extra wavelengths aim to compensate for tissue background optical properties such as skin pigmentation, hydration and deep tissue optical characteristics, which are highly variable among patients [302]. Although compensation algorithms for water concentration or skin pigmentation were not included in this thesis, the DC signals from the 810 nm in addition to the 770 nm and 880 nm, might allow the future enhancement of the current SRS algorithm used in this thesis.

Moreover, the designed and manufactured instrumentation system allowed the acquisition of NIRS and PPG signals from the in-vitro setup. Multiple graphs within this thesis show the morphology of the pulsations, as some quality indexes were calculated to evaluate the signals. Even though the signals' quality depends on the subject (in vitro/in vivo), the PPG signals acquired from the phantom using artificial blood successfully led to the extraction of features. Still, there is always room for improvement in the acquisition system design. Other authors have reported techniques to reduce the impact of ambient light, signal saturation, and movement artefacts in pulsatile signals [293], [308], which could be added to the current ZenTBI system to reduce common noise sources.

12.3.3 Cerebral NIRS systems in multimodal monitoring

Similar to the comparison with the literature presented above for the head phantom and probe design, this section compares the ZenTBI with other NIRS systems that utilise “any type” of pulsation for ICP monitoring.

Themelis et al. 2007, described NIRS pulsations as heartbeat oscillations produced at the very dense cerebral arterial network [297]. They calculated changes in cerebral blood flow and volume from the morphology of the optical oscillations. Their algorithm assumes that the peak of the pulse derivative represents the magnitude of the pulsatile flow, which follows: $\left(\frac{\partial I}{\partial t} \propto \frac{\partial V}{\partial t} = Q\right)$. Themelis et al. tested the algorithm using a commercial CW-NIRS system in eight piglets and found a correlation coefficient of 0.93 against laser doppler flow measurements. Although this research focused on CBF, it supports the hypothesis presented in this thesis where cerebral parameters (i.e., ICP) are estimated from the morphology of NIRS pulsatile signals. The maximum peak of the PPG derivative could be added to the pool of features presented in this research to estimate ICP, considering the physiological relationship between CBF and intracranial pressure. Lastly, Themelis et al. work provided a method that could be easily incorporated into a NIRS system, including the sensor presented in this thesis, which would provide a robust multimodal monitoring tool to evaluate CBF, ICP and cerebral oxygenation.

A new supplementary strategy to conventional NIRS is in development, diffuse correlation spectroscopy (DCS), a near-infrared diffuse optical technique that measures a blood flow index (BFI) instead of cerebral oxygenation by quantifying laser speckle statistics. Some authors have proposed that ICP can be estimated from the pulsatile behaviour of blood flow due to the cardiac cycle. Below are presented some studies that used DCS to estimate ICP non-invasively:

Fischer et al. 2020, acquired DCS signals from six children with external hydrocephalus and six adults with a moderate or severe TBI that required ICP monitoring [309]. A recurrent neural network (RNN) model was trained using the time series of the pulsatile CBF as an input, generating an ICP estimate. Neural networks are a powerful algorithm in the sense of engineering because they can discover patterns from data without prior analysis through feature engineering. The issue with applying neural networks to raw data in this way is its complexity and the very large dataset needed for the algorithm to develop to the point where it generalises successfully [309]. Moreover, the reported accuracy of ± 4 mmHg in the random sample splitting method (50% training, 50% testing) may be deceptively good because the training set partially contains information about all subjects used [309]. Nonetheless, the interesting results presented by Fischer et al. open the possibility of exploring recurrent neural networks using the time series of the pulsatile NIRS as an input to estimate ICP rather than by feature extraction. The latter is considering that RNN models need large datasets that can be generated using

the head phantom. Likewise, this work expands the options for multimodal non-invasive monitoring, where blood flow can be involved as an additional parameter of a multimodal optical probe.

Ruesch et al. have been working with NIRS and DCS technologies to estimate ICP non-invasively. The authors present a recompilation of studies where ICP changes were induced incrementally (from about 3-10 mmHg up to 40 mmHg in steps of 10mmHg) through fluid infusion in non-human primates (n=5 to 8) as it is shown in Figure 144 [310]–[313]. A traditional intraparenchymal probe recorded invasive ICP values. Additionally, the OxiplexTS was the frequency domain NIRS system implemented by the researchers to estimate changes in oxy- and deoxy-haemoglobin. This NIRS probe consists of two wavelengths (690 nm and 830 nm) and four S-D separations, yet haemoglobin concentrations were calculated at an S-D distance of 1.66 cm. In 2020 Ruesch et al. developed a transfer function to translate HbO_2 changes measured with NIRS into ICP changes [310]. The transfer function considered magnitude and phase changes in haemoglobin concentrations while ICP oscillations were induced over long periods of time. The estimated ICP from the transfer function presented a correlation range with invasive ICP of 0.57 to 0.89 [310]. The function presented in Ruesch’s work showed a relevant correlation between changes in the haemoglobin concentrations and changes in ICP, yet the function cannot estimate absolute values of ICP, and the authors report limitations due to cerebral autoregulation. Unlike the ZenTBI, this transfer function analyses the oscillations of the changes in haemoglobin concentration rather than the AC pulsation from the NIRS signal. Nonetheless, considering that the ZenTBI probe can also estimate changes in oxy and deoxy-haemoglobin concentrations, based on Ruesch’s results, the magnitudes and phases of these parameters could be evaluated as additional features into the ZenTBI nICP model.

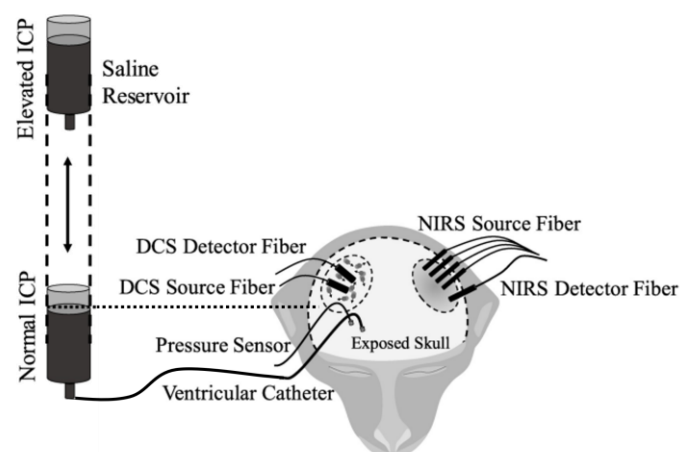


Figure 144: Experimental setup from Ruesch studies [310]–[313]

Later, in 2020, Ruesch’s team published another paper on the same experiment. This time they expand the idea of using hemodynamic changes to measure ICP and demonstrate that absolute values of ICP extraction are possible. Similarly to Fischer et al. [309], this study extracted features from the cardiac

pulsation of cerebral blood flow measured by DCS and implemented advanced machine learning algorithms to correlate the morphological changes in the CBF waveform with the ICP baselines [314]. The DCS system utilises a single long-coherence length laser at $\lambda = 850$ nm wavelength and an S-D distance of 2 cm. The QRS complex of an EKG allowed the detection of a cardiac pulse in the cerebral blood flow signal, which typically presents three distinct peaks: the percussion peak, derived from the systolic pulse; the tidal peak, produced when the percussion peak bounces back due to intracranial compliance; and the dicrotic peak, which results from the closure of the aortic valve [314]. After normalization and filtering, the following morphological features were extracted from the cardiac pulse: peak height, prominence, full width at half maximum, and the time point of the peak relative to the prior diastolic minimum. Each of the features was calculated per pulse peak (percussion, tidal and dicrotic). Moreover, peak-to-peak differences were calculated, as well as the area under the curve [314]. An additional feature added to the algorithm was the averaged mean arterial pressure (MAP) over the time span of the 120 averaged pulses [314]. The available feature sets were split using the Pareto approach (80%-20%) to build a regression forest model only with data below 30 mmHg. The researchers reported accuracy parameters like correlation (0.91), mean square error (3.3 mmHg) and limits of agreement for a 95% CI of ± 3.7 mmHg. Also, the authors reported that AUC and MAP were the most important features in estimating ICP. The results, therefore, indicate the possibility of reliable estimation of ICP in absolute numbers based on MAP (Invasive arterial line), Δ CBF and EKG measurements [314].

This remarkable study utilises the cardiac pulse acquired by DCS in a similar way to how this thesis used the PPG signals acquired from the AC component of NIRS (ZenTBI). Interestingly, as explained by Themelis et al., flow and volume are closely correlated [297]. Then it is not surprising that morphological features from the flow pulsations change when ICP increases, as the volume signals from NIRS-PPGs do. Nonetheless, Ruesh's approach relies on incorporating EKG measurements for pulse detection in the DCS signals, which is not needed by the ZenTBI method as PPG signals are synchronized to the heart cycle. Moreover, their model needs to be tested using a k-fold, online approach, as their current results come from a model that might be biased because it was trained and tested with data from all subjects. Finally, this study confirms once again the relevance of MAP in cerebral monitoring. At the moment, Ruesh's method is not completely non-invasive, as it utilizes MAP measurements from an arterial line to estimate ICP. However, this variable should be considered for robust cerebral multimodal monitoring; thus, non-invasive methods based on PPG signals could be implemented in future versions of the ZenTBI [292].

To wrap up Ruesh's research, the last published analysis (2022) made on non-human primates aimed to explore non-invasive ICP estimation using cardiac waveform features extracted from relative

haemoglobin concentration changes (HbO₂ and HbT), measured with NIRS device [312]. Unlike the previous study, the relative haemoglobin concentration changes do not present the three distinct peaks involved in the cardiac pulse of the flow measurements, conversely, it involves only one peak per cardiac cycle. Therefore, the features extracted in this analysis were the peak height, prominence, full width at half maximum, the time point of the peak relative to the prior diastolic minimum, AUC, MAP, and x- and y-coordinates of the centre of mass of the normalized pulse. Similarly, forest modelling was implemented for the haemoglobin concentration features and for an equal set of features extracted from DCS flow measurements [312]. The results reported for both haemoglobin changes and flow pulsations are very good, even when MAP is not included as a feature in the model. The performance of the ΔHbO_2 model showed a correlation with invasive ICP of 0.838, an MSE of 6.971 mmHg, and limits of agreement for 95% CI of -4.960 to 4.984 mmHg. Also, this set of features increased the performance of the DCS model when MAP was removed, presenting a correlation coefficient of 0.916, MSE of 3.778 mmHg, and 95% CI of -3.785 to 3.756 mmHg [312]. Although the results presented by Ruesh in this analysis support the hypothesis that feature extraction from optical pulsatile signals of cerebral parameters correlates to absolute changes in the intracranial pressure, all animals were represented in both the training and the testing sets (Figure 145). The latter diminish the generalizability of the model to unseen data.

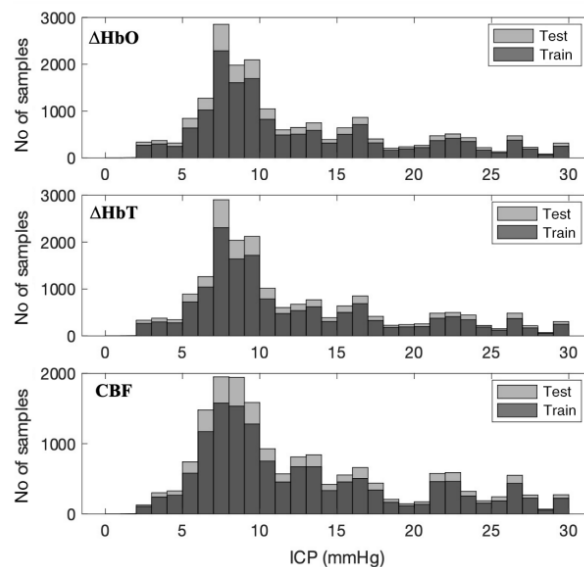


Figure 145: Histogram of ICP distribution for both train and test sets following a Pareto approach in Ruesh et al study [312].

In comparison to the ZenTBI analysis, a leave-one-out or k-fold approach was implemented to train and test the model. The resultant correlation coefficient of 0.86, mean absolute error of 3.7 mmHg, and limits of agreement of ± 4 mmHg suggest that NIRS-PPG signals could estimate ICP similarly to the DCS-based method, yet this would be known with certainty when the ZenTBI is tested on a comparable

in-vivo experiment. Nonetheless, the possibility of including haemoglobin concentration pulses in the analysis of the ZenTBI is viable due to the multimodality of the designed probe.

Similarly, Baker et al 2017 and Wu et al 2021, hypothesized that the combination of waveforms of pulsatile cerebral blood flow and concurrent pulsatile ABP waveforms analysis can provide an accurate estimate of critical closing pressure (CrCP), which depends on both ICP and small arterioles compliance (actual CPP=ABP-CrCP) [315], [316]. Baker et al. acquired DCS signals from the forehead and continuous non-invasive arterial blood pressure (ABP) measured with a finger plethysmograph system. Data were recorded from 20 healthy volunteers lying in a supine body position, and transcranial doppler ultrasound was implemented as the reference measurement to calculate the critical closing pressure [315]. Even promising, this methodology would require access to two different systems (DCS and Finometer Pro) and the accuracy in comparison to the critical closing pressure calculated from TCD is still limited (95% CI limits of agreement of -13 to 9 mmHg) [315]. Likewise, Wu et al included 14 acute ischemic stroke patients in a study that simultaneously measured DCS, non-invasive ABP and TCD to estimate the critical closing pressure ($R^2 = 0.74$) [306]. However, unlike the ZenTBI, these two DCS-based technologies do not estimate ICP values and require arterial blood pressure measurements to provide an estimated value, involving strategies for signal alignment. Nonetheless, the authors introduced and demonstrated a novel optical technique for continuous, non-invasive monitoring of the critical closing pressure with near-infrared light, a parameter that the authors believe has to be validated as a proxy for ICP [315], [316].

Although some of the aforementioned optical systems interrogate haemoglobin concentrations and estimate ICP non-invasively, the author of this thesis could not find in the literature any multimodal NIRS device that measures absolute ICP and cerebral oxygenation non-invasively. Additionally, any of the systems mentioned in this discussion utilises cerebral PPG signals to estimate ICP, while the DC component of NIRS is implemented in cerebral oxygenation calculations.

12.4 STRENGTHS AND LIMITATIONS OF THIS STUDY

12.4.1 Strengths

This thesis presented a comprehensive synthesis of cerebral physiologic changes after traumatic brain injury, including the clinical practice guidelines for patients' evaluation and monitoring, their limitations and the leap to multimodal monitoring. Likewise, this study produced a systematic review of non-invasive techniques that monitor intracranial pressure and oxygenation in TBI patients, comprising a detailed description of NIRS clinical applications for cerebral oxygenation and autoregulation monitoring.

The proposed Monte Carlo Simulation in a healthy multi-layer head model helped optimize the source-detector distance and provided a better understanding of light tissue interaction with NIR light. The ZenTBI system fulfilled the design requirements for acquiring PPG and NIRS signals, which were methodically evaluated on an in-vitro setup. Despite lacking an established quality guideline to evaluate PPG signals, the quality of the acquired signals was compared at different S-D separations, reinforcing Monte Carlo results. The implementation of multiple wavelengths, photodetectors at different S-D separations and analysis of both pulsatile and non-pulsatile components of the reflected signals allowed the assessment of multiple physiological parameters simultaneously.

Although SRS is a well-known NIRS technique for cerebral oxygenation monitoring, this thesis proposed the analysis of features from the pulsatile component of the NIRS signal. This analysis demonstrated that the photoplethysmography signals acquired from the phantom brain surface correlated to changes in the intracranial pressure, allowing the calculation of regression models to estimate ICP non-invasively.

A simple but plausible pool of features was successfully extracted from cerebral PPG signals produced in a controlled environment. The latter led to the implementation of nine types of ML models, evaluated and compared using the most common regression metrics and graphical analytical tools. The online simulation used to test the models established the potential of this novel analysis to estimate ICP non-invasively from the PPG signals hidden in NIRS records. In addition, SRS algorithms were successfully implemented to provide a cerebral oxygenation measurement, defining the ZenTBI system as a multimodal monitoring tool.

Finally, a novel head phantom that mimics the optical properties, the anatomy and some pathological changes within the brain permitted the first proof of concept of this multimodal optical sensor for TBI. Furthermore, the optical characterisation of the materials and detailed manufacture process presented in this study could allow the reproduction of this in-vitro tool by other researchers for multiple applications. Moreover, the phantom could mimic changes in heart rate, stroke, intracranial pressure and blood oxygen level even at extreme values, which are impossible to induce in healthy volunteers or rarely happen in medicated patients.

12.4.2 Limitations

The intrinsic limitations of an in-vitro set-up confine the results presented in this thesis. Despite the efforts to create a head model close to the actual anatomy and tissue's optical properties, the developed phantom lacks critical structures that greatly impact cerebral hemodynamics and autoregulation. For example, the lack of ventricles, compliant vessels, capillary bed, meninges, subarachnoidal space circulation, and venous sinuses, among others. Hence, the future addition of

these structures would allow the simulation of more realistic changes in cerebral physiology and provide optical signals closer to those acquired from human foreheads.

One critical example of the later limitation is the lack of extracerebral circulation and a scalp on the phantom, which only limited the analysis to cerebral signals. Therefore, this study could not evaluate the optical subtraction of normalized proximal PPGs from normalized distal PPGs. Yet, the researcher noticed that a direct signals subtraction would result in a distorted PPG signal. The latter is because the distance between the distal and proximal photodiodes is greater than 1 cm; thus, light attenuation is not linear between these detectors. Once the extracerebral component is removed, the integrity of the cerebral PPG signal is key to estimating ICP by feature extraction.

Consequently, two probe design modifications are proposed to avoid alterations in the morphology of the PPG brain signals without extracerebral contamination. Firstly, a Montecarlo simulation using both distal and proximal photodetectors could evaluate the difference in the number of photons received by these detectors at specific positions (i.e. $P=1$ cm, $D=3$ cm) to find the optimal detecting area size that ensures a linear attenuation between the photodiodes despite the separation between them. Secondly, ICP estimation could use the two distal photodetectors rather than the proximal detector. This modification would avoid problems with the subtraction as light attenuation is linear and known between these two detectors.

The assessment of non-invasive cerebral oxygenation parameters remains technically challenging. Clinically, the current invasive references ($SjvO_2$ and $PbtO_2$) utilize distinct physical principles and measure distinct physiological parameters. Some NIRS manufacturers and the FDA have adopted a proxy called field saturation, which is the sum of an empirically estimated percentage of arterial oxygen saturation (SaO_2) and jugular bulb venous oxygen saturation ($SjvO_2$). However, on the phantom, it is impossible to differentiate between arterial and venous blood due to the absence of gas exchange in the phantom's brain. Then, it does not make sense to utilise any of the invasive clinical references. Moreover, the use of commercial SRS devices as a reference during the oxygenation tests was not viable in this research, yet it is known that oxygen values and trending characteristics are machine specific, then they are not interchangeable among different commercial brands [300]. In spite of all this, this study has shown similar trends between the TOI calculations and the direct measurement of oxygen concentration in the liquid phantom using the FOSFORE R probe.

13 CONCLUSION AND FUTURE WORK

This thesis identified three broad sections; the first is the theoretical framework in cerebral physiology, and TBI is explained in chapters 2 and 3. The second section comprised chapters 4 and 5 and presented a literature review of non-invasive monitoring techniques emphasized in near-infrared spectroscopy. These sections were the theoretical foundations for the subsequent applied work presented in section three. Finally, this last section included chapters 6 to 11 and described the development of the in-vitro setup and the optical sensor, from which it was possible to simulate and assess ICP and cerebral oxygenation non-invasively. As this thesis concludes, this chapter summarises the key findings and links them to the original aims and objectives. Moreover, whereas some suggestions for improving the methodologies used have been given throughout the last section, final recommendations on the direction of future work are given in this chapter.

This thesis aimed to develop a non-invasive multimodal monitoring sensor to assess ICP and cerebral oxygenation in TBI patients. In order to do so, the reflectance ZenTBI sensor was designed and manufactured for the acquisition of pulsatile and non-pulsatile signals from different source-detector (S-D) separations. Additionally, in vitro investigations in a head phantom were carried out, which required the creation of a model that followed real anatomical specifications, mimicked optical tissue properties and allowed changes in physiological parameters. The developed probe was successfully coupled to a processing system, and it demonstrated to be able to acquire good quality PPG signals using four different wavelengths. By inducing changes in the phantom's physiological parameters and acquiring signals from different S-D separations, the in-vitro studies in the head phantom allowed the investigation of the intracranial pressure and cerebral oxygenation non-invasively.

The extraction of features from the pulsatile signals acquired from the head phantom at different ICP levels led to the effective implementation of multiple machine-learning algorithms. The accuracy of such models to estimate ICP non-invasively is the first indicator, known by the author that changes in the cerebral PPG morphologies correlate to changes in the intracranial pressure. Likewise, Beer-Lambert law and the diffusion approximation for a highly scattering medium were successfully applied to the non-pulsatile signals acquired from the distal probe photodiodes, allowing the calculation of absolute changes in cerebral oxygenation. It is hoped that future studies will contribute to determining the performance of the ZenTBI sensor in-vivo, whereas the application of more sophisticated features and algorithms may be investigated as well.

The ZenTBI sensor wavelengths were selected accordingly to the probe application, yet within the range of 660 nm and 880 nm, there are two other competing absorbers (water and pigment melanin) that have the potential to influence NIRS-based ICP and oxygen measurement. The effect of these

absorbers could be evaluated by Monte Carlo simulations changing the water content in different head tissue layers, as well as changing the melanin concentration in the forehead skin. Previous Monte Carlo studies have evaluated these two parameters on the finger and epidermis [317]–[319].

Additionally, future work could include the simulation, using Monte Carlo techniques, of physiopathological changes associated with TBI in order to understand light-tissue interaction under a sick scenario. Similarly, further modelling research regarding the incident angle of the sensor's source and detector could lead to optimal values at which more photons are reflected from the cerebral tissue and are captured by the photodetectors. Another valuable Monte Carlo simulation could assess the use of multiple photodiodes with a more extensive area at higher source-detector distances, which could equal the number of photons collected at different S-D separations. The simulated information could then be utilized to improve the sensor design.

This research found the optimal S-D range to acquire cerebral signals using Monte Carlo simulation and in vitro analysis; hence, there is no point in having two separate probes (proximal and distal) rather than a single flexible probe containing all four wavelengths and three photodiodes. An integrated probe would ensure the detector's alignment and facilitate the sensor's attachment to the forehead. In addition to the band system, a new design of the probe may also include an adhesive layer that sticks the sensor to both the human skin and the surface of the phantom. In other improvements to the probes, a lighter cable with an electromagnetic shielding layer should be considered to reduce signals' noise by movement artefacts and electromagnetic fields.

Likewise, further improvements in the instrumentation system could reduce the negative impact of different noise sources in the optical signals. For instance, an ambient light cancellation circuit would avoid signal saturation due to high levels of ambient light or small gaps between the sensor and the measuring surface. Moreover, the separation of the AC and DC components using analogue filters could allow higher amplification of the pulsatile signals to improve the quality of these signals, as well as the implementation of an offset cancelling circuit to reduce the movement artefacts in the pulsatile signals.

Furthermore, this research ran a first proof of concept successfully using a limited set of morphological features; however, there is plenty of room for exploring features in the frequency domain as well as additional parameters from the second derivative. This process could be optimised using hyperparameter turning. In addition to a feature-based model, it would be interesting to evaluate the accuracy of time series modelling to estimate ICP. Also, the acquisition of a bigger dataset from the head phantom could allow the implementation of unsupervised algorithms such as neural networks,

which in comparison to the support vector machine models described in this thesis, might present higher classification accuracy for intracranial hypertension.

Although this research presented a good performance of the model in an online evaluation, the immediate next step to this investigation would be testing the model in real-time while pulsatile signals are being acquired from the head phantom. One possible approach would be to convert the Matlab file comprising the feature extraction and the model that estimates ICP into a .NET file that communicates to LabVIEW in real time.

The range of algorithms that can be evaluated using the optical signals and the phantom may be successfully extended beyond its current limits. The further addition of improvements to the phantom may allow the simulation of other pathological effects, such as haemorrhages, swelling, ventriculomegaly, compliance changes and others, enabling the development of robust algorithms closer to the clinical reality of TBI patients.

From this group of improvements to the phantom, the most relevant one might be the inclusion of a scalp with extracerebral circulation. The latter would need to consider the effect that changes in the intracranial pressure have on extracerebral circulation. For instance, cerebral autoregulation alters the arterial pressure and blood flow supply to the brain, which is partially shared with extracerebral arteries that supply blood to the forehead, such as the supratrochlear, supraorbital and superficial temporal arteries. Therefore, adding the scalp to the head phantom should be considered an ambitious challenge, especially if the effects of skin pigmentation and a capillary bed are included in the scalp design.

All the aspects mentioned above of the scalp will allow further development of an algorithm to subtract extracerebral signals from the distal photodiode signals to get only cerebral information. Such subtraction should consider that light attenuation is not linear when the source-detector separation is significant (>10 mm). Then, as mentioned in the discussion limitations section, a modification in the photodetectors area size could equal the number of photons between proximal and distal diodes, which might compensate for the nonlinear behaviour of light attenuation. Likewise, the algorithm could use distal photodiodes only to subtract extracerebral contamination from the cerebral PPG signals rather than using the proximal photodiode.

On the other hand, there are plenty of improvement opportunities regarding the oxygenation in-vitro setup. This research presented multiple methods that were not successful yet that have a lot of potentials. For instance, using ink to generate an artificial blood fluid mimics different haemoglobin concentrations. Further investigation in spectroscopy and chemistry could improve the proposed recipe to fulfil the research expectations, cutting the inconveniences of working with real blood.

Nonetheless, it would be helpful to understand better the medical oxygenator apparatus, which could oxygenate animal blood or the liquid phantom fluid in the head phantom without increasing the risk of pressurizing the system.

The possibility of changing oxygen levels within a close pulsatile system, with fewer limitations, would enable the possibility to deeply evaluate pulsatile signals related to oxygenation changes such as oxygen saturation. Current NIRS measurements are always lower than arterial oxygen saturation measured by pulse oximetry (SpO_2) because NIRS cannot discriminate between arterial blood, capillaries, and venous blood [171]. Consequently, the DC signals measured by NIRS represent a mixed saturation between arterial and venous blood, with a predominant venous component, as approximately 75% of cerebral blood is venous [61]. However, using the pulsatile and non-pulsatile NIRS signals from cerebral tissue, the developed sensor could measure SaO_2 in the same way as pulse oximeters but directly on the head.

All efforts, methods, finding and knowledge presented in this work are proof of the developed non-invasive multimodal monitoring sensor to assess ICP and cerebral oxygenation in TBI patients, which was conceived since the beginning as a healthcare tool that will provide early information to healthcare professionals to treat patients timely, reducing the risk of secondary injuries that lead to disability and mortality. Within the group of multimodal monitoring parameters, ICP and oxygenation are crucial, yet future implementation of blood pressure using PPG features [292] could allow the assessment of cerebral autoregulation non-invasively. For instance, the calculation of non-invasive PRx, as the moving correlation on ICP and MAP, as well as the possible estimation of TOx, which represents the moving correlation of TOI and CPP. The latter bearing in mind that cerebral perfusion pressure (CPP) is key in cerebral autoregulation monitoring and that it would be possible to calculate it once ICP and MAP can be estimated.

Concluding, the novel results presented in this thesis demonstrate that the full capabilities of the optical signals in cerebral monitoring are still not fully exploited, yet this promising technique could lead to an accurate non-invasive tool for multimodal monitoring in TBI patients.

14 REFERENCES

- [1] T. Vanderah, D. Gould, and J. Nolte, "Introduction to the nervous system," in *Nolte's the human brain : an introduction to its functional anatomy.*, 7th ed. Philadelphia: ELSEVIER, 2016, pp. 1–38.
- [2] G. J. Tortora and B. Derrickson, "The brain and cranial nerves," in *Principles of Anatomy & Physiology*, 14th ed. Wiley, 2014.
- [3] T. "Vanderah, D. Gould, and J. Nolte, "Electrical signaling by neurons," in *Nolte's the human brain : an introduction to its functional anatomy.*, 7th ed. Philadelphia: ELSEVIER, 2016, pp. 154–181.
- [4] P. P. Urone and R. Hinrichs, "Nerve Conduction–Electrocardiograms," in *College Physics*, OpenStax, College Physics, 2012, p. 159.
- [5] T. "Vanderah, D. Gould, and J. Nolte, "Synaptic transmission between neurons," in *Nolte's the human brain : an introduction to its functional anatomy.*, 7th ed. Philadelphia: ELSEVIER, 2016, pp. 182–206.
- [6] Picfair, "Nerve synapse, illustration," *3d illustration of a synapse*. Accessed: Apr. 16, 2020. [Online]. Available: <https://www.picfair.com/pics/08436127-nerve-synapse-illustration>
- [7] E. D. Bigler, "Pathophysiology," in *Textbook of Traumatic Brain Injury*, J. M. Silver, T. W. McAllister, and D. B. Arciniegas, Eds., Third. Washington: American Psychiatric Association Publishing, 2018, pp. 41–60.
- [8] T. R. Olson and W. Pawlina, "Head and neck," in *A.D.A.M. Student Atlas of Anatomy*, Cambridge University Press, 2015, pp. 347–444.
- [9] G. J. Tortora and B. Derrickson, "The skeletal system: the axial skeleton," in *Principles of Anatomy & Physiology*, 2014.
- [10] T. "Vanderah, D. Gould, and J. Nolte, "Meningeal coverings of the brain and spinal cord," in *Nolte's the human brain : an introduction to its functional anatomy.*, 7th ed. Philadelphia: ELSEVIER, 2016, pp. 88–103.
- [11] P. K. Y. Kan, M. H. M. Chu, E. G. Y. Koo, and M. T. V. Chan, "Brain Herniation," in *Complications in Neuroanesthesia*, Elsevier Inc., 2016, pp. 3–13. doi: 10.1016/B978-0-12-804075-1.00001-8.
- [12] A. C. Guyton and J. E. Hall, "Contributions of the Cerebellum and Basal Ganglia to Overall Motor Control," in *GUYTON AND HALL Textbook of Medical Physiology*, 12th ed. Philadelphia: Saunders, 2011, pp. 681–695.
- [13] N. V. Watson and S. M. Breedlove, "The Cerebellum Has Three Divisions with Distinct Functions," in *The Mind's Machine*, 2nd ed. Sinauer Associates, 2015.
- [14] A. C. Guyton and J. E. Hall, "Regulation of respiration," in *GUYTON AND HALL Textbook of Medical Physiology*, 12th ed. Philadelphia: Saunders, 2011, pp. 505–523.
- [15] T. Vanderah, D. Gould, and J. Nolte, "The thalamus and internal capsule," in *Nolte's the human brain : an introduction to its functional anatomy*, 7th ed. Philadelphia: ELSEVIER, 2016. doi: 978-1-4557-2859-6.
- [16] E. J. Grossman and M. Inglese, "The role of thalamic damage in mild traumatic brain injury," *J. Neurotrauma*, vol. 33, no. 2, pp. 163–167, Jan. 2016, doi: 10.1089/neu.2015.3965.

- [17] T. "Vanderah, D. Gould, and J. Nolte, "The hypothalamus and limbic system," in *Nolte's the human brain : an introduction to its functional anatomy.*, 7th ed.Philadelphia: ELSEVIER, 2016, pp. 579–604.
- [18] W. H. Williams *et al.*, "Traumatic brain injury: a potential cause of violent crime?," *The Lancet Psychiatry*, vol. 5, no. 10. Elsevier Ltd, pp. 836–844, Oct. 01, 2018. doi: 10.1016/S2215-0366(18)30062-2.
- [19] G. J. Tortora and B. Derrickson, "The endocrine system," in *Principles of Anatomy & Physiology*, 14th ed.2014, pp. 615–692.
- [20] T. "Vanderah, D. Gould, and J. Nolte, "Cerebral cortex," in *Nolte's the human brain : an introduction to its functional anatomy.*, 7th ed.Philadelphia: ELSEVIER, 2016, pp. 541–578.
- [21] K. M. Van de Graaff, R. W. Rhees, and S. L. Palmer, "Cardiovascular System: Blood," in *Human Anatomy and Physiology*, 4th ed.McGraw-Hill Education, 2013.
- [22] G. J. Tortora and B. Derrickson, "The cardiovascular system: the blood," in *Principles of Anatomy & Physiology*, 14th ed.Wiley, 2014, pp. 693–719.
- [23] G. J. Tortora and B. Derrickson, "The cardiovascular system: the heart," in *Principles of Anatomy & Physiology*, 14th ed.Wiley, 2014, pp. 720–760.
- [24] T. "Vanderah, D. Gould, and J. Nolte, "Blood supply of the brain," in *Nolte's the human brain : an introduction to its functional anatomy.*, 7th ed.Philadelphia: ELSEVIER, 2016, pp. 126–153.
- [25] J. Graves, C. Betrus, and J. A. Rafols, "Situating cerebral blood flow in the pathotrajectory of head trauma," in *Cerebral Blood Flow, Metabolism, and Head Trauma: The Pathotrajectory of Traumatic Brain Injury*, New York: Springer, 2013, pp. 29–51. doi: 10.1007/978-1-4614-4148-9_2.
- [26] A. Chodobski, B. J. Zink, and J. Szmydynger-Chodobska, "Blood-Brain Barrier Pathophysiology in Traumatic Brain Injury," *Transl. Stroke Res.*, vol. 2, no. 4, pp. 492–516, 2012, doi: 10.1007/s12975-011-0125-x.
- [27] scyrus 3D Models, "Neuron Astrocyte Blood Vessel Erythrocyte." Turbosquid, 2011. [Online]. Available: <https://www.turbosquid.com/3d-models/blood-vessel-astrocyte-neuronal-3d-model/711317>
- [28] G. J. Tortora and B. Derrickson, "The Chemical Level of Organization," in *Principles of Anatomy & Physiology*, 14th ed.Wiley, 2014, pp. 59–90.
- [29] G. J. Tortora and B. Derrickson, "Fluid, Electrolyte, and Acid–Base Homeostasis," in *Principles of Anatomy & Physiology*, 14th ed.Wiley, 2014, pp. 1055–1073.
- [30] G. J. Tortora and B. Derrickson, "The respiratory system," in *Principles of Anatomy & Physiology*, 14th ed.Wiley, 2014, pp. 840–917.
- [31] I. Jalloh, K. L. H. Carpenter, A. Helmy, T. A. Carpenter, D. K. Menon, and P. J. Hutchinson, "Glucose metabolism following human traumatic brain injury: methods of assessment and pathophysiological findings," *Metabolic Brain Disease*, vol. 30, no. 3. Springer New York LLC, pp. 615–632, Jun. 01, 2015. doi: 10.1007/s11011-014-9628-y.
- [32] A. T. Mazzeo and D. Gupta, "Monitoring the injured brain," *J. Neurosurg. Sci.*, vol. 62, no. 5, pp. 549–562, 2018, doi: 10.23736/S0390-5616.18.04465-X.
- [33] J. J. Casaletto, "Differential diagnosis of metabolic acidosis," *Emergency Medicine Clinics of North America*, vol. 23, no. 3 SPEC. ISS. W.B. Saunders, pp. 771–787, 2005. doi: 10.1016/j.emc.2005.03.007.

- [34] G. J. Tortora and B. Derrickson, "The cardiovascular system: blood vessels and hemodynamics," in *Principles of Anatomy & Physiology*, Wiley, Ed., 14th ed. 2014, pp. 761–830.
- [35] E. MEANEY, F. ALVA, R. MOGUEL, A. MEANEY, J. ALVA, and R. WEBEL, "Formula and nomogram for the sphygmomanometric calculation of the mean arterial pressure," *Heart*, vol. 84, no. 64, 2000.
- [36] C. Berry *et al.*, "Redefining hypotension in traumatic brain injury," *Injury*, vol. 43, no. 11, pp. 1833–1837, Nov. 2012, doi: 10.1016/j.injury.2011.08.014.
- [37] R. A. Stocker, "Intensive Care in Traumatic Brain Injury Including Multi-Modal Monitoring and Neuroprotection," *Med. Sci.*, vol. 7, no. 3, p. 37, Feb. 2019, doi: 10.3390/medsci7030037.
- [38] E. J. Mahoney, W. L. Biffl, D. T. Harrington, and W. G. Cioffi, "Isolated brain injury as a cause of hypotension in the blunt trauma patient," *J. Trauma*, vol. 55, no. 6, pp. 1065–1069, Dec. 2003, doi: 10.1097/01.TA.0000100381.89107.93.
- [39] T. Lin, "Physiology of the circulation," in *Fundamentals of Anaesthesia*, T. S. Lin and C. Pinnock, Eds., Cambridge: Cambridge University Press, 2016, pp. 315–341. doi: 10.1017/9781139626798.019.
- [40] A. C. Guyton and J. E. Hall, *GUYTON AND HALL Textbook of Medical Physiology*, 12th ed. Philadelphia: Saunders, 2011.
- [41] C. W. Kreipke and J. A. Rafols, "Situating Cerebral Blood Flow in the Pathotrajectory of Head Trauma," in *Cerebral Blood Flow, Metabolism, and Head Trauma: The Pathotrajectory of Traumatic Brain Injury*, Springer New York, 2013, pp. 29–51. doi: 10.1007/978-1-4614-4148-9.
- [42] K. Kinoshita, "Traumatic brain injury: Pathophysiology for neurocritical care," *Journal of Intensive Care*, vol. 4, no. 1. BioMed Central Ltd., p. 10, 2016. doi: 10.1186/s40560-016-0138-3.
- [43] MeSH Database, "Intracranial Pressure - MeSH - NCBI," *NCBI*. NCBI, 2020. doi: D007427.
- [44] A. Tameem and H. Krovvidi, "Cerebral physiology," *Contin. Educ. Anaesthesia, Crit. Care Pain*, vol. 13, no. 4, pp. 113–118, 2013, doi: 10.1093/bjaceaccp/mkt001.
- [45] N. Stocchetti *et al.*, "Time course of intracranial hypertension after traumatic brain injury," *J. Neurotrauma*, vol. 24, no. 8, pp. 1339–1346, 2007, doi: 10.1089/neu.2007.0300.
- [46] J. C. Kienzler, R. Zakelis, S. Bäbler, E. Remonda, J. Fandino, and J. Kienzler, "Validation of Noninvasive Absolute Intracranial Pressure Measurements in Traumatic Brain Injury and Intracranial Hemorrhage Arminas Ragauskas, DSc ‡," *Oper. Neurosurg.*, vol. 16, pp. 186–196, 2019, doi: 10.1093/ons/opy088.
- [47] R. Aaslid and K. F. Lindegaard, "Cerebral Hemodynamics," *Anesthesiology*, vol. 18, no. 2, p. 355, 1957, doi: 10.1097/00000542-195703000-00071.
- [48] I. H. Johnston and J. O. Rowan, "Raised intracranial pressure and cerebral blood flow. 3. Venous outflow tract pressures and vascular resistances in experimental intracranial hypertension," *J. Neurol. Neurosurg. Psychiatry*, vol. 37, no. 4, pp. 392–402, Apr. 1974, doi: 10.1136/jnnp.37.4.392.
- [49] N. Carney *et al.*, "Guidelines for the Management of Severe Traumatic Brain Injury, Fourth Edition," 2017. doi: 10.1227/NEU.0000000000001432.
- [50] A. Marmarou, K. Shulman, and R. M. Rosende, "A nonlinear analysis of the cerebrospinal fluid system and intracranial pressure dynamics," *J. Neurosurg.*, vol. 48, no. 3, pp. 332–344, 1978,

doi: 10.3171/jns.1978.48.3.0332.

- [51] G. Portella *et al.*, "Continuous cerebral compliance monitoring in severe head injury: Its relationship with intracranial pressure and cerebral perfusion pressure," *Acta Neurochir. (Wien)*, vol. 147, no. 7, pp. 707–713, 2005, doi: 10.1007/s00701-005-0537-z.
- [52] M. Harary, R. G. F. Dolmans, and W. B. Gormley, "Intracranial pressure monitoring—review and avenues for development," *Sensors (Switzerland)*, vol. 18, no. 2. MDPI AG, Feb. 05, 2018. doi: 10.3390/s18020465.
- [53] Z. Messina and H. Patrick, *Partial Pressure of Carbon Dioxide (PCO2)*. StatPearls Publishing, 2019. Accessed: Jun. 16, 2020. [Online]. Available: <http://www.ncbi.nlm.nih.gov/pubmed/31869112>
- [54] N. Fabregas and J. Fernández-Candil, "Hypercapnia," in *Complications in Neuroanesthesia*, Elsevier, 2016, pp. 157–168. doi: 10.1016/B978-0-12-804075-1.00020-1.
- [55] J. A. C. Suazo, A. I. R. Maas, W. A. Van Den Brink, H. Van Santbrink, E. W. Steyerberg, and C. J. J. Avezaat, "CO₂ reactivity and brain oxygen pressure monitoring in severe head injury," *Crit. Care Med.*, vol. 28, no. 9, pp. 3268–3274, Sep. 2000, doi: 10.1097/00003246-200009000-00024.
- [56] E. W. Lang and M. Jaeger, "Systematic and Comprehensive Literature Review of Publications on Direct Cerebral Oxygenation Monitoring," *Open Crit. Care Med. J.*, vol. 6, pp. 1–24, 2013.
- [57] L. B. Ngwenya, J. F. Burke, and G. T. Manley, "Brain Tissue Oxygen Monitoring and the Intersection of Brain and Lung," 2016, doi: 10.4187/respcare.04962.
- [58] G. Rosenthal *et al.*, "Brain tissue oxygen tension is more indicative of oxygen diffusion than oxygen delivery and metabolism in patients with traumatic brain injury," *Crit. Care Med.*, vol. 36, no. 6, pp. 1917–1924, 2008, doi: 10.1097/CCM.0b013e3181743d77.
- [59] M. Oddo *et al.*, "Monitoring of Brain and Systemic Oxygenation in Neurocritical Care Patients," *Neurocrit. Care*, vol. 21, no. 2, pp. 103–120, Oct. 2014, doi: 10.1007/s12028-014-0024-6.
- [60] A. Ercole and A. K. Gupta, "Cerebral oxygenation," in *Core Topics in Neuroanaesthesia and Neurointensive Care*, B. F. Matta, D. K. Menon, and M. Smith, Eds., Cambridge University Press, 2011, pp. 72–84. doi: 10.1017/CBO9780511977558.007.
- [61] C. Sokoloff *et al.*, "Clinical Usefulness of Transcranial Doppler as a Screening Tool for Early Cerebral Hypoxic Episodes in Patients with Moderate and Severe Traumatic Brain Injury," *Neurocrit. Care*, 2019, doi: 10.1007/s12028-019-00763-y.
- [62] A. Bhardwaj, H. Bhagat, and V. Grover, "Jugular venous oximetry," *J. Neuroanaesth. Crit. Care*, vol. 02, no. 03, pp. 225–231, Dec. 2015, doi: 10.4103/2348-0548.165046.
- [63] J. A. Gomes and A. Bhardwaj, "Normal Intracranial Pressure Physiology," in *Cerebrospinal Fluid in Clinical Practice*, B. M. Morrison, Ed., Elsevier Inc, 2009, pp. 19–25. doi: 10.1016/B978-1-4160-2908-3.X0001-6.
- [64] A. C. Guyton and J. E. Hall, "Cerebral Blood Flow, Cerebrospinal Fluid, and Brain Metabolism," in *GUYTON AND HALL Textbook of Medical Physiology*, 12th ed. Philadelphia: Saunders, 2011, pp. 764–771.
- [65] T. Vanderah, D. Gould, and J. Nolte, "Ventricles and CSF," in *Nolte's the human brain : an introduction to its functional anatomy*, 7th ed. Philadelphia: ELSEVIER, 2016.
- [66] S. Grubb and M. Lauritzen, "Deep sleep drives brain fluid oscillations," *Science (80-.)*, vol.

- 366, no. 6465, pp. 572–573, Nov. 2019, doi: 10.1126/science.aaz5191.
- [67] M. Elwishi and J. Dinsmore, “Monitoring the brain,” *BJA Educ.*, vol. 19, pp. 54–59, 2019, doi: 10.1016/j.bjae.2018.12.001.
- [68] N. Lundberg, H. Troupp, and H. Lorin, “Continuous recording of the ventricular-fluid pressure in patients with severe acute traumatic brain injury. A preliminary report.,” *J. Neurosurg.*, vol. 22, no. 6, pp. 581–590, Jun. 1965, doi: 10.3171/jns.1965.22.6.0581.
- [69] L. Cox, B. Ramakers, and W. Abdo, “Plateau Waves, Intracranial Hypertension and Prognosis. How Identical Waves Can Lead to Different Outcomes in Two Patients with Traumatic Brain Injury.,” *Enliven J Anesth. Crit Care Med*, vol. 1, no. 1, 2014, Accessed: Jun. 28, 2020. [Online]. Available: <http://www.enlivenarchive.org/articles/plateau-waves-intracranial-hypertension-and-prognosis-how-identical-waves-can-lead-to-different-outcomes-in-two-patients-with-trau.html>
- [70] G. Castellani *et al.*, “Plateau waves in head injured patients requiring neurocritical care,” *Neurocrit. Care*, vol. 11, no. 2, pp. 143–150, Oct. 2009, doi: 10.1007/s12028-009-9235-7.
- [71] A. Spiegelberg, M. Preuß, and V. Kurtcuoglu, “B-waves revisited,” *Interdiscip. Neurosurg. Adv. Tech. Case Manag.*, vol. 6, pp. 13–17, Dec. 2016, doi: 10.1016/j.inat.2016.03.004.
- [72] L. A. Calviello, J. Donnelly, F. A. Zeiler, E. P. Thelin, P. Smielewski, and M. Czosnyka, “Cerebral autoregulation monitoring in acute traumatic brain injury: What’s the evidence?,” *Minerva Anesthesiol.*, vol. 83, no. 8, pp. 844–857, 2017, doi: 10.23736/S0375-9393.17.12043-2.
- [73] E. Bor-Seng-Shu *et al.*, “Cerebral hemodynamics: Concepts of clinical importance,” *Arq. Neuropsychiatr.*, vol. 70, no. 5, pp. 357–365, 2012, doi: 10.1590/S0004-282X2012000500010.
- [74] C. Beynon, L. Wessels, and A. W. Unterberg, “Point-of-Care Testing in Neurosurgery,” *Semin. Thromb. Hemost.*, vol. 43, no. 4, pp. 416–422, Jun. 2017, doi: 10.1055/s-0037-1599159.
- [75] B. I. A. of America, “ABI vs. TBI: What is the difference?,” 2021. <https://www.biausa.org/brain-injury/about-brain-injury/nbiic/what-is-the-difference-between-an-acquired-brain-injury-and-a-traumatic-brain-injury> (accessed Jan. 08, 2021).
- [76] Headway, “Types of brain injury | Headway,” Jan. 08, 2021. <https://www.headway.org.uk/about-brain-injury/individuals/types-of-brain-injury/> (accessed Jan. 08, 2021).
- [77] A. Brazinova *et al.*, “Epidemiology of Traumatic Brain Injury in Europe: A Living Systematic Review,” *J. Neurotrauma*, Dec. 2018, doi: 10.1089/neu.2015.4126.
- [78] B. D. Greenwald, D. M. Burnett, and M. A. Miller, “Congenital and Acquired Brain Injury. 1. Brain Injury: Epidemiology and Pathophysiology,” *Arch Phys Med Rehabil*, vol. 84, no. 1, 2003, doi: 10.1053/apmr.2003.50052.
- [79] K. O’Phelan, “Traumatic Brain Injury: Definitions and Nomenclature,” in *Manual of Traumatic Brain Injury*, F. S. Zollman, Ed., 2nd ed. Chicago: demosMedical, 2017, pp. E59–E60. doi: 10.1097/HTR.0000000000000346.
- [80] G. Teasdale and B. Jennett, “ASSESSMENT OF COMA AND IMPAIRED CONSCIOUSNESS. A Practical Scale,” *Lancet*, vol. 304, no. 7872, pp. 81–84, Jul. 1974, doi: 10.1016/S0140-6736(74)91639-0.
- [81] J. J. Tepas, D. L. Mollitt, J. L. Talbert, and M. Bryant, “The pediatric trauma score as a predictor of injury severity in the injured child,” *J. Pediatr. Surg.*, vol. 22, no. 1, pp. 14–18, 1987, doi: 10.1016/S0022-3468(87)80006-4.

- [82] H. R. Champion, W. J. Sacco, W. S. Copes, D. S. Gann, T. A. Gennarelli, and M. E. Flanagan, "A revision of the trauma score," *J. Trauma - Inj. Infect. Crit. Care*, vol. 29, no. 5, pp. 623–629, 1989, doi: 10.1097/00005373-198905000-00017.
- [83] S. P. Baker, B. O'Neill, W. Haddon, and W. B. Long, "The injury severity score: a method for describing patients with multiple injuries and evaluating emergency care," *J. Trauma*, vol. 14, no. 3, pp. 187–196, 1974, doi: 10.1097/00005373-197403000-00001.
- [84] R. Åstrand and B. Romner, "Classification of Head Injury," in *Management of Severe Traumatic Brain Injury*, T. Sundstrøm, Ed., Berlin, Heidelberg: Springer Berlin Heidelberg, 2012, pp. 11–16. doi: 10.1007/978-3-642-28126-6_2.
- [85] T. W. McAllister, "Overview of Mild Brain Injury," in *Textbook of Traumatic Brain Injury*, J. M. Silver, T. W. McAllister, and D. B. Arciniegas, Eds., Third. Washington: American Psychiatric Association Publishing, 2018, pp. 583–605.
- [86] K. M. Helmick, C. A. Spells, S. Z. Malik, C. A. Davies, D. W. Marion, and S. R. Hinds, "Traumatic brain injury in the US military: epidemiology and key clinical and research programs," *Brain Imaging Behav.*, vol. 9, no. 3, pp. 358–366, Sep. 2015, doi: 10.1007/s11682-015-9399-z.
- [87] N. Carney *et al.*, "Concussion guidelines step 1: Systematic review of prevalent indicators," *Neurosurgery*, vol. 75, no. SUPPL. 1. Lippincott Williams and Wilkins, 2014. doi: 10.1227/NEU.0000000000000433.
- [88] M. N. Haider *et al.*, "Intracranial pressure changes after mild traumatic brain injury: a systematic review," *Brain Inj.*, vol. 32, no. 7, pp. 809–815, 2018, doi: 10.1080/02699052.2018.1469045.
- [89] J. E. Roseberry and M. McCrea, "Assessment of Sports-Related Concussion," in *Textbook of Traumatic Brain Injury*, J. M. Silver, T. W. McAllister, and D. B. Arciniegas, Eds., Third. Washington: American Psychiatric Association Publishing, 2018, pp. 623–634.
- [90] T. R. Frieden, D. Houry, and G. Baldwin, "Traumatic Brain Injury In the United States: Epidemiology and Rehabilitation."
- [91] A. I. R. Maas *et al.*, "The Lancet Neurology Commission Traumatic brain injury: integrated approaches to improve prevention, clinical care, and research Executive summary The Lancet Neurology Commission," *Lancet Neurol*, vol. 16, pp. 987–1048, 2017, doi: 10.1016/S1474-4422(17)30371-X.
- [92] A. I. R. Maas *et al.*, "Traumatic brain injury: integrated approaches to improve prevention, clinical care, and research," *Lancet Neurol.*, vol. 16, no. 12, pp. 987–1048, 2017, doi: 10.1016/S1474-4422(17)30371-X.
- [93] O. Lasry *et al.*, "VIEWS & REVIEWS Epidemiology of recurrent traumatic brain injury in the general population A systematic review From the Department of Epidemiology," 2017.
- [94] T. Lawrence, A. Helmy, O. Bouamra, M. Woodford, F. Lecky, and P. J. Hutchinson, "Traumatic brain injury in England and Wales: prospective audit of epidemiology, complications and standardised mortality," *BMJ Open*, vol. 6, p. 12197, 2016, doi: 10.1136/bmjopen-2016.
- [95] D. S. Wijayatilake, C. Talati, and S. Panchatsharam, "The Monitoring and Management of Severe Traumatic Brain Injury in the United Kingdom: Is there a Consensus?: A National Survey," *J. Neurosurg. Anesthesiol.*, vol. 27, no. 3, pp. 241–245, 2015, Accessed: Oct. 17, 2019. [Online]. Available: www.jnsa.com
- [96] J. D. Corrigan, C. Harrison-Felix, and J. Haarbauer-Krupa, "Epidemiology of Traumatic Brain Injury," in *Textbook of Traumatic Brain Injury*, J. M. Silver, T. W. McAllister, and D. B.

- Arciniegas, Eds., Third. Washington: American Psychiatric Association Publishing, 2018, pp. 3–24.
- [97] M. Majdan *et al.*, “Epidemiology of traumatic brain injuries in Europe: a cross-sectional analysis,” 2016. doi: 10.1016/S2468-2667(16)30017-2.
- [98] A. J. Belinda Gabbe *et al.*, “Comparison of Mortality Following Hospitalisation for Isolated Head Injury in England and”, doi: 10.1371/journal.pone.0020545.
- [99] G. Fuller, M. Woodford, T. Lawrence, T. Coats, and F. Lecky, “Do prolonged primary transport times for traumatic brain injury patients result in deteriorating physiology? A Cohort study,” *Prehospital Emerg. Care*, vol. 18, no. 1, pp. 60–67, Jan. 2014, doi: 10.3109/10903127.2013.831507.
- [100] S. L. James *et al.*, “Global, regional, and national burden of traumatic brain injury and spinal cord injury, 1990–2016: a systematic analysis for the Global Burden of Disease Study 2016,” 2019, doi: 10.1016/S1474-4422(18)30415-0.
- [101] V. C. Chang, E. Niki Guerriero, and A. Colantonio, “Epidemiology of Work-related Traumatic Brain Injury: A Systematic Review,” *J. Ind. Med.*, vol. 58, pp. 353–377, 2015, doi: 10.1002/ajim.22418.
- [102] M. Mian *et al.*, “Shaken baby syndrome: A review,” *Fetal and Pediatric Pathology*, vol. 34, no. 3. Informa Healthcare, pp. 169–175, Jun. 01, 2015. doi: 10.3109/15513815.2014.999394.
- [103] HSCIS, “Accident and Emergency Attendances in England 2014-2015,” England, 2015.
- [104] J. M. Nemeth, C. Mengo, E. Kulow, A. Brown, and R. Ramirez, “Provider Perceptions and Domestic Violence (DV) Survivor Experiences of Traumatic and Anoxic-Hypoxic Brain Injury: Implications for DV Advocacy Service Provision,” *J. Aggress. Maltreat. Trauma*, vol. 28, no. 6, pp. 744–763, 2019, doi: 10.1080/10926771.2019.1591562.
- [105] A. K. Wagner, H. C. Sasser, F. M. C. Hammond, D. Wiercisiewski, and J. Alexander, “Intentional traumatic brain injury: Epidemiology, risk factors, and associations with injury severity and mortality,” *J. Trauma - Inj. Infect. Crit. Care*, vol. 49, no. 3, pp. 404–410, 2000, doi: 10.1097/00005373-200009000-00004.
- [106] J. T. J. M. van Dijck, M. D. Dijkman, R. H. Ophuis, G. C. W. de Ruiter, W. C. Peul, and S. Polinder, “In-hospital costs after severe traumatic brain injury: A systematic review and quality assessment,” *PLoS ONE*, vol. 14, no. 5. Public Library of Science, May 01, 2019. doi: 10.1371/journal.pone.0216743.
- [107] C. E. Dismuke, R. J. Walker, and L. E. Egede, “Utilization and Cost of Health Services in Individuals With Traumatic Brain Injury,” *Global journal of health science*, vol. 7, no. 6. pp. 156–169, Nov. 01, 2015. doi: 10.5539/gjhs.v7n6p156.
- [108] T. Ahmad, S. Horton, E. Worthington, and R. Morris, *The effects of brain injury*, 5th ed. Nottingham: Headway – the brain injury association, 2018. Accessed: Feb. 25, 2021. [Online]. Available: http://www.thepsychologist.org.uk/archive/archive_home.cfm/volumeID_19-editionID_134-ArticleID_1011-getfile_getPDF/thepsychologist%5C0406why.pdf
- [109] J. D. Alarcon *et al.*, “Clinical practice guidelines for the care of patients with severe traumatic brain injury: A systematic evaluation of their quality,” *Journal of Trauma and Acute Care Surgery*, vol. 75, no. 2. pp. 311–319, Aug. 2013. doi: 10.1097/TA.0b013e3182924bf8.
- [110] B. S. Di *et al.*, “A critical review to traumatic brain injury clinical practice guidelines,” *Medicine (Baltimore)*, vol. 98, no. 9, p. e14592, Mar. 2019, doi: 10.1097/MD.00000000000014592.

- [111] Maiti and Bidinger, *Traumatic Brain Injury*, 2nd ed., vol. 53, no. 9. Cambridge: Cambridge University Press, 2020. doi: 10.1017/9781108355247.
- [112] E. A. Wilde and D. Little, "Clinical Imaging," in *Textbook of Traumatic Brain Injury*, J. M. Silver, T. W. McAllister, and D. B. Arciniegas, Eds., Third. Washington: American Psychiatric Association Publishing, 2018, pp. 89–126.
- [113] S.-B. Ko, "Multimodality Monitoring in the Neurointensive Care Unit: A Special Perspective for Patients with Stroke," *J. Stroke*, vol. 15, no. 2, p. 99, 2013, doi: 10.5853/jos.2013.15.2.99.
- [114] V. Petkus *et al.*, "Non-invasive Cerebrovascular Autoregulation Assessment Using the Volumetric Reactivity Index: Prospective Study," *Neurocrit. Care*, vol. 30, no. 1, pp. 42–50, Feb. 2019, doi: 10.1007/s12028-018-0569-x.
- [115] E. Needham, C. McFadyen, V. Newcombe, A. J. Synnot, M. Czosnyka, and D. Menon, "Cerebral Perfusion Pressure Targets Individualized to Pressure-Reactivity Index in Moderate to Severe Traumatic Brain Injury: A Systematic Review," *J. Neurotrauma*, vol. 34, no. 5, pp. 963–970, Mar. 2017, doi: 10.1089/neu.2016.4450.
- [116] C. Wen-Ta, S. Ching-Shuan, L. Jia-Wei, and H. Sheng-Jean, "Application of brain tissue oxygen monitoring in traumatic brain injury.," *Int. Brain Inj. Assoc.*, no. 2, 2009, Accessed: Feb. 25, 2020. [Online]. Available: <https://www.internationalbrain.org/articles/application-of-brain-tissue-oxygen-monitoring-in-traumatic-brain-injury/>
- [117] P. J. D. Andrews, N. M. Dearden, and J. D. Miller, "Jugular bulb cannulation: Description of a cannulation technique and validation of a new continuous monitor," *Br. J. Anaesth.*, vol. 67, no. 5, pp. 553–558, 1991, doi: 10.1093/bja/67.5.553.
- [118] Y. Wei, Y. Jiao, D. An, D. Li, W. Li, and Q. Wei, "Review of dissolved oxygen detection technology: From laboratory analysis to online intelligent detection," *Sensors (Switzerland)*, vol. 19, no. 18. MDPI AG, Sep. 02, 2019. doi: 10.3390/s19183995.
- [119] Hach, "Medición óptica de oxígeno disuelto en centrales eléctricas y en calderas," 2015, [Online]. Available: https://www.google.com.co/url?sa=t&rct=j&q=&esrc=s&source=web&cd=3&cad=rja&uact=8&ved=0ahUKewiXzMj8rKzQAhXSZiYKHdfPATcQFggnMAI&url=http%3A%2F%2Fes.hach.com%2Fasset-get.download.jsa%3Ffid%3D41917005556&usg=AFQjCNEUXm8BG2n7TyHqW4_zbyDEaL39sA&sig2=pWyH28XmJp-
- [120] M. Roldan and P. A. Kyriacou, "Near-Infrared Spectroscopy (NIRS) in Traumatic Brain Injury (TBI)," *Sensors*, vol. 21, no. 1586, p. 30, 2021, doi: 10.3390/s21051586.
- [121] W. N. McDicken and T. Anderson, "Basic physics of medical ultrasound," in *Clinical Ultrasound*, Elsevier Ltd, 2011, pp. 3–15. doi: 10.1016/B978-0-7020-3131-1.00001-8.
- [122] T. national institute of biomedical imaging and Bioengineering, *How Ultrasound Works*, (2015). [Online]. Available: <https://www.youtube.com/watch?v=I1Bdp2tMFsY>
- [123] S. Purkayastha and F. Sorond, "Transcranial doppler ultrasound: Technique and application," *Semin. Neurol.*, vol. 32, no. 4, pp. 411–420, 2012, doi: 10.1055/s-0032-1331812.
- [124] M. Roldan, T. Y. Abay, and P. A. Kyriacou, "Non-invasive techniques for multimodal monitoring in Traumatic Brain Injury (TBI): systematic review and meta-analysis," *J. Neurotrauma*, p. neu.2020.7266, Aug. 2020, doi: 10.1089/neu.2020.7266.
- [125] B. MATTHEWS and N. VONGSAVAN, "Advantages and limitations of laser Doppler flow meters," *Int. Endod. J.*, vol. 26, no. 1, pp. 9–9, 1993, doi: 10.1111/j.1365-

2591.1993.tb00531.x.

- [126] E. K. S. Louis and L. C. Frey, *Electroencephalography - An introductory text*. American Epilepsy Society, 2016. Accessed: Mar. 04, 2021. [Online]. Available: <https://www.ncbi.nlm.nih.gov/books/NBK390354/>
- [127] M. Gura, I. ElMacl, R. Sarl, and N. CoSkun, "Correlation of Pulsatility Index with Intracranial Pressure in TBI," *Turk. Neurosurg.*, pp. 210–215, 2011.
- [128] D. J. Davies *et al.*, "Cerebral oxygenation in traumatic brain injury: Can a non-invasive frequency domain near-infrared spectroscopy device detect changes in brain tissue oxygen tension as well as the established invasive monitor?," *J. Neurotrauma*, vol. 36, no. 7, pp. 1175–1183, Apr. 2019, doi: 10.1089/neu.2018.5667.
- [129] L. Vinciguerra and J. Bösel, "Noninvasive Neuromonitoring: Current Utility in Subarachnoid Hemorrhage, Traumatic Brain Injury, and Stroke," *Neurocrit. Care*, vol. 27, no. 1, pp. 122–140, 2017, doi: 10.1007/s12028-016-0361-8.
- [130] A. Mejía, "Traumatic brain injury: a practical vision," Medellin, Colombia, 2019.
- [131] M. W. Herklots *et al.*, "Prospective Evaluation of Noninvasive HeadSense Intracranial Pressure Monitor in Traumatic Brain Injury Patients Undergoing Invasive Intracranial Pressure Monitoring," *World Neurosurg.*, vol. 106, pp. 557–562, 2017, doi: 10.1016/j.wneu.2017.07.022.
- [132] M. Martin *et al.*, "Prediction of Early Intracranial Hypertension After Severe Traumatic Brain Injury: A Prospective Study," *World Neurosurg.*, vol. 127, pp. e1242–e1248, 2019, doi: 10.1016/j.wneu.2019.04.121.
- [133] U. Kawoos, R. M. McCarron, C. R. Auken, and M. Chavko, "Advances in intracranial pressure monitoring and its significance in managing traumatic brain injury," *Int. J. Mol. Sci.*, vol. 16, no. 12, pp. 28979–28997, Dec. 2015, doi: 10.3390/ijms161226146.
- [134] H. Kristiansson, E. Nissborg, J. Bartek, M. Andresen, P. Reinstrup, and B. Romner, "Measuring elevated intracranial pressure through noninvasive methods: A review of the literature," *Journal of Neurosurgical Anesthesiology*, vol. 25, no. 4, pp. 372–385, Oct. 2013. doi: 10.1097/ANA.0b013e31829795ce.
- [135] D. S. Nag, S. Sahu, A. Swain, and S. Kant, "Intracranial pressure monitoring: Gold standard and recent innovations," *World Journal of Clinical Cases*, vol. 7, no. 13, Baishideng Publishing Group Co, pp. 1535–1553, Jul. 01, 2019. doi: 10.12998/wjcc.v7.i13.1535.
- [136] D. Moher, A. Liberati, J. Tetzlaff, and D. G. Altman, "Guidelines and Guidance Preferred Reporting Items for Systematic Reviews and Meta-Analyses: The PRISMA Statement", doi: 10.1371/journal.pmed.1000097.
- [137] Cochrane, *Cochrane Handbook for Systematic Reviews of Interventions*, 6.0. Cochrane, 2019. [Online]. Available: www.training.cochrane.org/handbook.
- [138] GA Wells *et al.*, "The Newcastle-Ottawa Scale (NOS) for assessing the quality of nonrandomised studies in meta-analyses." Accessed: Jan. 09, 2020. [Online]. Available: http://www.ohri.ca/programs/clinical_epidemiology/oxford.asp
- [139] R. A. Fisher, "Statistical Methods for Research Workers.," in *Breakthroughs in statistics*, Oliver and Boyd, Eds., 6th ed. New York: Springer, 1936, pp. 66–70.
- [140] S. IBM Support, "Confidence intervals for correlations," 2018. <https://www.ibm.com/support/pages/confidence-intervals-correlations> (accessed Jan. 10,

- 2020).
- [141] L. A. Calviello *et al.*, "Relationship Between Brain Pulsatility and Cerebral Perfusion Pressure: Replicated Validation Using Different Drivers of CPP Change," *Neurocrit. Care*, vol. 27, no. 3, pp. 392–400, 2017, doi: 10.1007/s12028-017-0404-9.
 - [142] D. Cardim *et al.*, "Transcranial Doppler Monitoring of Intracranial Pressure Plateau Waves," *Neurocrit. Care*, vol. 26, no. 3, pp. 330–338, 2017, doi: 10.1007/s12028-016-0356-5.
 - [143] G. Rosenthal, A. Furmanov, E. Itshayek, Y. Shoshan, and V. Singh, "Assessment of a noninvasive cerebral oxygenation monitor in patients with severe traumatic brain injury: Clinical article," *J. Neurosurg.*, vol. 120, no. 4, pp. 901–907, 2014, doi: 10.3171/2013.12.JNS131089.
 - [144] S. R. Leal-Noval *et al.*, "Invasive and noninvasive assessment of cerebral oxygenation in patients with severe traumatic brain injury," *Intensive Care Med.*, vol. 36, no. 8, pp. 1309–1317, 2010, doi: 10.1007/s00134-010-1920-7.
 - [145] I. Soliman *et al.*, "New Optic Nerve Sonography Quality Criteria in the Diagnostic Evaluation of Traumatic Brain Injury," *Crit. Care Res. Pract.*, vol. 2018, 2018, doi: 10.1155/2018/3589762.
 - [146] G. Huang *et al.*, "Clinical value of non-invasive monitoring of cerebral hemodynamics for evaluating intracranial pressure and cerebral perfusion pressure in patients with moderate to severe traumatic brain injury," *Neurol. Asia*, vol. 17, no. 2, pp. 133–140, 2012.
 - [147] K. P. Budohoski *et al.*, "Non-Invasively Estimated ICP Pulse Amplitude Strongly Correlates with," *Acta Neurochir. Suppl.*, vol. 114, 2012, doi: 10.1007/978-3-7091-0956-4.
 - [148] J. R. T. Melo *et al.*, "Transcranial Doppler can predict intracranial hypertension in children with severe traumatic brain injuries," *Child's Nerv. Syst.*, vol. 27, no. 6, pp. 979–984, 2011, doi: 10.1007/s00381-010-1367-8.
 - [149] G. Brandi, M. Béchir, S. Sailer, C. Haberthür, R. Stocker, and J. F. Stover, "Transcranial color-coded duplex sonography allows to assess cerebral perfusion pressure noninvasively following severe traumatic brain injury," *Acta Neurochir. (Wien)*, vol. 152, no. 6, pp. 965–972, 2010, doi: 10.1007/s00701-010-0643-4.
 - [150] F. A. Rasulo *et al.*, "The accuracy of transcranial Doppler in excluding intracranial hypertension following acute brain injury: A multicenter prospective pilot study," *Crit. Care*, vol. 21, no. 1, pp. 1–8, 2017, doi: 10.1186/s13054-017-1632-2.
 - [151] B. Schmidt *et al.*, "Noninvasive Assessment of ICP: Evaluation of New TBI Data Bernhard," *Intracranial Press. brain Monit.* xv, vol. 122, p. 351, 2016, doi: 10.1007/978-3-319-22533-3.
 - [152] N. F. O'Brien, T. Maa, and K. Reuter-Rice, "Noninvasive screening for intracranial hypertension in children with acute, severe traumatic brain injury," *J. Neurosurg. Pediatr.*, vol. 16, no. 4, pp. 420–425, 2015, doi: 10.3171/2015.3.PEDS14521.
 - [153] O. Ganslandt, S. Mourtzoukos, A. Stadlbauer, B. Sommer, and R. Rammensee, "Evaluation of a novel noninvasive ICP monitoring device in patients undergoing invasive ICP monitoring: Preliminary results," *J. Neurosurg.*, vol. 128, no. 6, pp. 1653–1660, 2018, doi: 10.3171/2016.11.JNS152268.
 - [154] C. Robba *et al.*, "Non-invasive intracranial pressure assessment in brain injured patients using ultrasound-based methods," *Acta Neurochir. Suppl.*, vol. 126, pp. 69–73, 2018, doi: 10.1007/978-3-319-65798-1_15.
 - [155] OxiplexTS, "A non-invasive, real-time monitor of precise tissue oxygenation and hemoglobin

- concentration," *Newton Drive*, 2001.
<http://www.iss.com/biomedical/instruments/oxiplexTS.html> (accessed Feb. 24, 2020).
- [156] M. INVOS, "Overview: Reflect site-specific tissue perfusion noninvasively."
<https://www.medtronic.com/covidien/en-us/products/cerebral-somatic-oximetry/invos-technology.html> (accessed Feb. 25, 2020).
- [157] J. Bellner, B. Romner, P. Reinstrup, K. A. Kristiansson, E. Ryding, and L. Brandt, "Transcranial Doppler sonography pulsatility index (PI) reflects intracranial pressure (ICP)," *Surg. Neurol.*, vol. 62, no. 1, pp. 45–51, Jul. 2004, doi: 10.1016/j.surneu.2003.12.007.
- [158] W. Weigl *et al.*, "Application of optical methods in the monitoring of traumatic brain injury: A review," *J. Cereb. Blood Flow Metab.*, vol. 36, no. 11, pp. 1825–1843, 2016, doi: 10.1177/0271678X16667953.
- [159] F. F. Jöbsis, "Noninvasive, Infrared Monitoring of Cerebral and Myocardial Oxygen Sufficiency and Circulatory Parameters," *Science (80-.)*, vol. 23, no. 4323, pp. 1264–1267, 1977.
- [160] F. Mathieu, A. Khellaf, J. C. Ku, J. Donnelly, E. P. Thelin, and F. A. Zeiler, "Continuous Near-Infrared Spectroscopy Monitoring in Adult Traumatic Brain Injury," *J. Neurosurg. Anesthesiol.*, p. 1, Jul. 2019, doi: 10.1097/ana.0000000000000620.
- [161] N. Karamzadeh *et al.*, "A machine learning approach to identify functional biomarkers in human prefrontal cortex for individuals with traumatic brain injury using functional near-infrared spectroscopy," *Brain Behav.*, vol. 6, no. 11, Nov. 2016, doi: 10.1002/brb3.541.
- [162] C. S. Robertson, S. P. Gopinath, and B. Chance, "A New Application for Near-Infrared Spectroscopy: Detection of Delayed Intracranial Hematomas after Head Injury," *J. Neurotrauma*, vol. 12, no. 4, pp. 591–600, Aug. 1995, doi: 10.1089/neu.1995.12.591.
- [163] S. P. Gopinath, C. S. Robertson, C. F. Contant, R. K. Narayan, R. G. Grossman, and B. Chance, "Early detection of delayed traumatic intracranial hematomas using near-infrared spectroscopy," *J. Neurosurg.*, vol. 83, no. 3, pp. 438–444, Sep. 1995, doi: 10.3171/jns.1995.83.3.0438.
- [164] S. P. Gopinath, C. S. Robertson, R. G. Grossman, and B. Chance, "Near-infrared spectroscopic localization of intracranial hematomas," *J. Neurosurg.*, vol. 79, no. 1, pp. 43–47, Jul. 1993, doi: 10.3171/jns.1993.79.1.0043.
- [165] S. H. Haddad and Y. M. Arabi, "Critical care management of severe traumatic brain injury in adults," *Scandinavian Journal of Trauma, Resuscitation and Emergency Medicine*, vol. 20, no. 1. BioMed Central, pp. 1–15, Feb. 03, 2012. doi: 10.1186/1757-7241-20-12.
- [166] M. Nitzan, I. Nitzan, and Y. Arieli, "The various oximetric techniques used for the evaluation of blood oxygenation," *Sensors (Switzerland)*, vol. 20, no. 17. MDPI AG, pp. 1–28, Sep. 01, 2020. doi: 10.3390/s20174844.
- [167] F. F. Jöbsis, "Noninvasive, infrared monitoring of cerebral and myocardial oxygen sufficiency and circulatory parameters," *Science (80-.)*, vol. 198, no. 4323, pp. 1264–1266, 1977, doi: 10.1126/science.929199.
- [168] A. N. Sen, S. P. Gopinath, and C. S. Robertson, "Clinical application of near-infrared spectroscopy in patients with traumatic brain injury: a review of the progress of the field," *Neurophotonics*, vol. 3, no. 3, p. 031409, Apr. 2016, doi: 10.1117/1.nph.3.3.031409.
- [169] J. M. Murkin and M. Arango, "Near-infrared spectroscopy as an index of brain and tissue oxygenation," *Br. J. Anaesth.*, vol. 103, no. SUPPL.1, pp. i3–i13, 2009, doi: 10.1093/bja/aep299.

- [170] Y. Yamashita and M. Niwayama, "Principles and Instrumentation," in *Application of Near Infrared Spectroscopy in Biomedicine*, T. Jue and K. Masuda, Eds., Boston, MA: Springer US, 2013, pp. 1–19. doi: 10.1007/978-1-4614-6252-1_1.
- [171] H. Owen-Reece, M. Smith, C. E. Elwell, and J. C. Goldstone, "Near infrared spectroscopy," *Br. J. Anaesth.*, vol. 82, no. 3, pp. 418–444, 1999.
- [172] P. Van der Zee *et al.*, "Experimentally measured optical pathlengths for the adult head, calf and forearm and the head of the newborn infant as a function of inter optode spacing," in *Advances in Experimental Medicine and Biology*, Springer, Boston, MA, 1992, pp. 143–153. doi: 10.1007/978-1-4615-3404-4_17.
- [173] J. K. Choi, J. M. Kim, G. Hwang, J. Yang, M. G. Choi, and H. M. Bae, "Time-Divided Spread-Spectrum Code-Based 400 fW-Detectable Multichannel fNIRS IC for Portable Functional Brain Imaging," *IEEE J. Solid-State Circuits*, vol. 51, no. 2, pp. 484–495, Feb. 2016, doi: 10.1109/JSSC.2015.2504412.
- [174] T. Ysehak Abay, "Reflectance photoplethysmography for non-invasive monitoring of tissue perfusion," 2016. [Online]. Available: <http://openaccess.city.ac.uk/16923/>
- [175] P. Rolfe, "In vivo near-infrared spectroscopy," *Annu. Rev. Biomed. engi neering*, vol. 2, no. 1, pp. 715–754, 2000.
- [176] J. McNulty, M. Born, and R. S. Pozos, "Near-Infrared Spectroscopy (NIRS)," in *Springer Handbook of Medical Technology*, Berlin, Heidelberg: Springer Berlin Heidelberg, 2011, pp. 423–438. doi: 10.1007/978-3-540-74658-4_22.
- [177] R. E. Gagnon, A. J. Macnab, F. A. Gagnon, D. Blackstock, and J. G. LeBlanc, "Comparison of two spatially resolved NIRS oxygenation indices," *J. Clin. Monit. Comput.*, vol. 17, no. 7–8, pp. 385–391, 2002, doi: 10.1023/A:1026274124837.
- [178] F. Lange and I. Tachtsidis, "Clinical brain monitoring with time domain NIRS: A review and future perspectives," *Applied Sciences (Switzerland)*, vol. 9, no. 8. MDPI AG, p. 1612, Apr. 01, 2019. doi: 10.3390/app9081612.
- [179] M. Ferrari and V. Quaresima, "Review: Near infrared brain and muscle oximetry: From the discovery to current applications," *J. Near Infrared Spectrosc.*, vol. 20, no. 1, pp. 1–14, 2012, doi: 10.1255/jnirs.973.
- [180] T. Van Essen *et al.*, "Comparison of frequency-domain and continuous-wave near-infrared spectroscopy devices during the immediate transition," *BMC Pediatr.*, vol. 20, no. 1, p. 94, Feb. 2020, doi: 10.1186/s12887-020-1987-4.
- [181] J. D. Veesa, H. Dehghani, and C. D. Joshua Veesa, "Functional near infrared spectroscopy using spatially resolved data to account for tissue scattering: A numerical study and arm-cuff experiment," *J. Biophotonics*, vol. 12, p. 201900064, 2019, doi: 10.1002/jbio.201900064.
- [182] E. Okada, "Photon migration in NIRS brain imaging," in *Application of Near Infrared Spectroscopy in Biomedicine*, Springer US, 2013, pp. 37–58. doi: 10.1007/978-1-4614-6252-1_3.
- [183] H. M. Watzman, C. D. Kurth, L. M. Montenegro, J. Rome, and J. M. Steven, "Arterial and Venous Contributions to Near-infrared Cerebral Oximetry | Anesthesiology | ASA Publications," *Anesthesiology*, vol. 93, no. 10, pp. 947–953, 2000, Accessed: Jul. 31, 2020. [Online]. Available: <https://anesthesiology.pubs.asahq.org/Article.aspx?articleid=1945335>
- [184] A. Tateishi *et al.*, "Qualitative comparison of carbon dioxide-induced change in cerebral near-infrared spectroscopy versus jugular venous oxygen saturation in adults with acute brain

- disease | Ovid," *Neurol. Crit. CARE*, vol. 23, no. 10, pp. 1734–1738, 1995, Accessed: Jul. 05, 2020. [Online]. Available: <https://0-oce-ovid-com.wam.city.ac.uk/article/00003246-199510000-00019/HTML>
- [185] P. J. Kirkpatrick, P. Smielewski, M. Czosnyka, D. K. Menon, and J. D. Pickard, "Near-infrared spectroscopy use in patients with head injury," *J. Neurosurg.*, vol. 83, no. 6, pp. 963–970, 1995, doi: 10.3171/jns.1995.83.6.0963.
- [186] S. B. Lewis, J. A. Myburgh, E. L. Thornton, and P. L. Reilly, "Cerebral oxygenation monitoring by near-infrared spectroscopy is not clinically useful in patients with severe closed-head injury: A comparison with jugular venous bulb oximetry | Ovid," *Clin. Investig. (Lond).*, vol. 24, no. 8, pp. 1334–1338, 1996, Accessed: Jul. 05, 2020. [Online]. Available: <https://0-oce-ovid-com.wam.city.ac.uk/article/00003246-199608000-00011/HTML>
- [187] A. Kampfl, B. Pfausler, D. Denchev, H. P. Jaring, and E. Schmutzhard, "Near Infrared Spectroscopy (NIRS) in Patients with Severe Brain Injury and Elevated Intracranial Pressure: A Pilot Study," *Acta Neurochir. Suppl.*, vol. 1997, no. 70, pp. 112–114, 1997, doi: 10.1007/978-3-7091-6837-0_35.
- [188] M. E. Kerr, D. Marion, P. A. Orndoff, B. B. Weber, and S. M. Sereika, "Evaluation of near infrared spectroscopy in patients with traumatic brain injury," *Adv. Exp. Med. Biol.*, vol. 454, pp. 131–137, 1998, doi: 10.1007/978-1-4615-4863-8_16.
- [189] A. Ter Minassian *et al.*, "Correlation between cerebral oxygen saturation measured by near-infrared spectroscopy and jugular oxygen saturation in patients with severe closed head injury," *Anesthesiology*, vol. 91, no. 4, pp. 985–990, 1999, doi: 10.1097/00000542-199910000-00018.
- [190] O. S. K. Cheng, S. Prowse, and A. J. Strong, "Oscillations in the near-infrared signal in patients with severe head injury," *Acta Neurochir. Suppl.*, vol. 81, pp. 135–137, 2002, doi: 10.1007/978-3-7091-6738-0_35.
- [191] A. Brawanski, R. Faltermeier, R. D. Rothoerl, and C. Woertgen, "Comparison of Near-Infrared Spectroscopy and Tissue Po₂ Time Series in Patients after Severe Head Injury and Aneurysmal Subarachnoid Hemorrhage," *J. Cereb. Blood Flow Metab.*, vol. 22, no. 5, pp. 605–611, May 2002, doi: 10.1097/00004647-200205000-00012.
- [192] A. D. McLeod, F. Igielman, C. Elwell, M. Cope, and M. Smith, "Measuring cerebral oxygenation during normobaric hyperoxia: A comparison of tissue microprobes, near-infrared spectroscopy, and jugular venous oximetry in head injury," *Anesth. Analg.*, vol. 97, no. 3, pp. 851–856, Sep. 2003, doi: 10.1213/01.ANE.0000072541.57132.BA.
- [193] M. N. Kim *et al.*, "Noninvasive Measurement of Cerebral Blood Flow and Blood Oxygenation Using Near-Infrared and Diffuse Correlation Spectroscopies in Critically Brain-Injured Adults," *Neurocrit Care*, vol. 12, pp. 173–180, 2010, doi: 10.1007/s12028-009-9305-x.
- [194] I. Tachtsidis *et al.*, "Analysis of the changes in the oxidation of brain tissue cytochrome-c-oxidase in traumatic brain injury patients during hypercapnoea: A broadband NIRS study," *Adv. Exp. Med. Biol.*, vol. 701, pp. 9–14, 2011, doi: 10.1007/978-1-4419-7756-4_2.
- [195] A. Ghosh, I. Tachtsidis, C. Kolyva, D. Highton, C. Elwell, and M. Smith, "Normobaric Hyperoxia Does Not Change Optical Scattering or Pathlength but Does Increase Oxidised Cytochrome c Oxidase Concentration in Patients with Brain Injury," *Adv. Exp. Med. Biol.*, vol. 765, pp. 67–72, 2013, doi: 10.1007/978-1-4614-4989-8_10.
- [196] A. Vilke *et al.*, "Predictive value of early near-infrared spectroscopy monitoring of patients with traumatic brain injury," 2014, doi: 10.1016/j.medic.2014.10.001.

- [197] V. Durnev, V. Filipce, A. G. Brzanov, M. M. Mijovska, and M. T. Stevanovska, "CEREBRAL OXYGENATION NON INVASIVE MONITORING IN TRAUMATIC BRAIN INJURY-A PILOT STUDY ," *Mac Med Rev.*, vol. 71, no. 2, pp. 113–118, 2017, doi: 10.1515/mmr-2017-0019.
- [198] S. Fantini and A. Sassaroli, "Frequency-Domain Techniques for Cerebral and Functional Near-Infrared Spectroscopy," *Frontiers in Neuroscience*, vol. 14. Frontiers Media S.A., Apr. 07, 2020. doi: 10.3389/fnins.2020.00300.
- [199] P. D. Adelson, E. Nemoto, A. Colak, and M. Painter, "The Use of Near Infrared Spectroscopy (NIRS) in Children after Traumatic Brain Injury: A Preliminary Report," *Acta Neurochir. Suppl.*, vol. 1998, no. SUPPL. 71, pp. 250–254, 1998, doi: 10.1007/978-3-7091-6475-4_72.
- [200] C. M. Dunham, C. Sosnowski, J. M. Porter, J. Siegal, and C. Kohli, "Correlation of noninvasive cerebral oximetry with cerebral perfusion in the severe head injured patient: a pilot study," *J. Trauma*, vol. 52, no. 1, pp. 40–46, 2002, doi: 10.1097/00005373-200201000-00009.
- [201] C. Zweifel *et al.*, "Noninvasive monitoring of cerebrovascular reactivity with near infrared spectroscopy in head-injured patients," *J. Neurotrauma*, vol. 27, no. 11, pp. 1951–1958, 2010, doi: 10.1089/neu.2010.1388.
- [202] R. Shafer, A. Brown, and C. Taylor, "Correlation between cerebral blood flow and oxygen saturation in patients with subarachnoid hemorrhage and traumatic brain injury," 2010, doi: 10.1136/jnis.2010.004184.
- [203] J. Diedler *et al.*, "The limitations of near-infrared spectroscopy to assess cerebrovascular reactivity: The role of slow frequency oscillations," *Anesth. Analg.*, vol. 113, no. 4, pp. 849–857, 2011, doi: 10.1213/ANE.0b013e3182285dc0.
- [204] P. Taussky *et al.*, "Validation of frontal near-infrared spectroscopy as noninvasive bedside monitoring for regional cerebral blood flow in brain-injured patients," *Neurosurg. Focus*, vol. 32, no. 2, pp. 1–6, 2012, doi: 10.3171/2011.12.FOCUS11280.
- [205] M. N. Kim *et al.*, "Continuous Optical Monitoring of Cerebral Hemodynamics During Head-of-Bed Manipulation in Brain-Injured Adults," 2014, doi: 10.1007/s12028-013-9849-7.
- [206] D. Highton, A. Ghosh, I. Tachtsidis, J. Panovska-Griffiths, C. E. Elwell, and M. Smith, "Monitoring Cerebral Autoregulation After Brain Injury: Multimodal Assessment of Cerebral Slow-Wave Oscillations Using Near-Infrared Spectroscopy," *Anesth Analg.*, 2015, doi: 10.1213/ANE.0000000000000790.
- [207] J. Bindra, • Paul Pham, • Anders Aneman, A. Chuan, and M. Jaeger, "Non-invasive Monitoring of Dynamic Cerebrovascular Autoregulation Using Near Infrared Spectroscopy and the Finometer Photoplethysmograph," *Neurocrit Care*, 2016, doi: 10.1007/s12028-015-0200-3.
- [208] N. Ö. Doğan, "Bland-Altman analysis: A paradigm to understand correlation and agreement," *Turkish Journal of Emergency Medicine*, vol. 18, no. 4. Emergency Medicine Association of Turkey, pp. 139–141, Dec. 01, 2018. doi: 10.1016/j.tjem.2018.09.001.
- [209] R. S. Samraj and L. Nicolas, "Near infrared spectroscopy (NIRS) derived tissue oxygenation in critical illness," *Clin. Investig. Med.*, vol. 38, no. 5, pp. E285–E295, 2015, doi: 10.25011/cim.v38i5.25685.
- [210] T. Li, Y. Li, Y. Sun, M. Duan, and L. Peng, "Effect of head model on Monte Carlo modeling of spatial sensitivity distribution for functional near-infrared spectroscopy," *J. Innov. Opt. Health Sci.*, vol. 8, no. 5, p. 8, Sep. 2015, doi: 10.1142/S1793545815500248.
- [211] J. Selb, T. M. Ogden, J. Dubb, Q. Fang, and D. A. Boas, "Comparison of a layered slab and an atlas head model for Monte Carlo fitting of time-domain near-infrared spectroscopy data of

- the adult head," *J. Biomed. Opt.*, vol. 19, no. 1, p. 016010, 2014, doi: 10.1117/1.jbo.19.1.016010.
- [212] M. Dehaes *et al.*, "Assessment of the frequency-domain multi-distance method to evaluate the brain optical properties: Monte Carlo simulations from neonate to adult," *Biomed. Opt. Express*, vol. 2, no. 3, p. 552, 2011, doi: 10.1364/boe.2.000552.
- [213] T. Li, H. Gong, and Q. Luo, "Visualization of light propagation in visible Chinese human head for functional near-infrared spectroscopy," *J. Biomed. Opt.*, vol. 16, no. 4, p. 045001, 2011, doi: 10.1117/1.3567085.
- [214] S. Mahmoodkalayeh and M. A. Ansari, "A subject-specific layered head model for monte carlo fitting in time-domain near-infrared spectroscopy," *Proc. - Int. Conf. Laser Opt. 2018, ICLO 2018*, vol. 19, p. 518, 2018, doi: 10.1109/LO.2018.8435810.
- [215] R. Mudra, A. Nadler, E. Keller, and P. Niederer, "Analysis of near-infrared spectroscopy and indocyanine green dye dilution with Monte Carlo simulation of light propagation in the adult brain," *J. Biomed. Opt.*, vol. 11, no. 4, p. 044009, 2006, doi: 10.1117/1.2341652.
- [216] L. Wu, Y. Lin, and T. Li, "Effect of Human Brain Edema on Light Propagation: A Monte Carlo Modeling Based on the Visible Chinese Human Dataset," *IEEE Photonics J.*, vol. 9, no. 5, 2017, doi: 10.1109/JPHOT.2017.2743048.
- [217] Q. Zhang, E. N. Brown, and G. E. Strangman, "Adaptive filtering for global interference cancellation and real-time recovery of evoked brain activity: a Monte Carlo simulation study," *J. Biomed. Opt.*, vol. 12, no. 4, p. 044014, 2007, doi: 10.1117/1.2754714.
- [218] Y. Zhang, J. W. Sun, and P. Rolfe, "RLS adaptive filtering for physiological interference reduction in NIRS brain activity measurement: A Monte Carlo study," *Physiol. Meas.*, vol. 33, no. 6, pp. 925–942, Jun. 2012, doi: 10.1088/0967-3334/33/6/925.
- [219] E. Okada, M. Firbank, M. Schweiger, S. R. Arridge, M. Cope, and D. T. Delpy, "Theoretical and experimental investigation of near-infrared light propagation in a model of the adult head," *Appl. Opt.*, vol. 36, no. 1, p. 21, 1997, doi: 10.1364/ao.36.000021.
- [220] Roldan M., Chatterjee S., and Kyriacou P.A., "Light-Tissue Interaction Modelling of Human Brain towards the Optical Sensing of Traumatic Brain Injury," in *43rd Annual International Conference of the IEEE Engineering in Medicine & Biology Society (EMBC)*, 2021, pp. 1–4. Accessed: Jan. 25, 2022. [Online]. Available: <https://openaccess.city.ac.uk/id/eprint/27326/1/>
- [221] S. Chatterjee and P. A. Kyriacou, "Monte carlo analysis of optical interactions in reflectance and transmittance finger photoplethysmography," *Sensors (Switzerland)*, vol. 19, no. 4, Feb. 2019, doi: 10.3390/s19040789.
- [222] K. U. Maheswari and S. Sathiyamoorthy, "Soft tissue optical property extraction for carcinoma cell detection in diffuse optical tomography system under boundary element condition," *Optik (Stuttg.)*, vol. 127, no. 3, pp. 1281–1290, Feb. 2016, doi: 10.1016/j.ijleo.2015.10.100.
- [223] L. Ragan, I. Waczulikova, L. Guller, J. Bilicky, and J. Benuska, "Cella media distance in human brain in relation to age and gender," *Biomed. Pap.*, vol. 153, no. 4, pp. 307–313, 2009, doi: 10.5507/bp.2009.053.
- [224] F. B. Haeussinger, S. Heinzl, T. Hahn, M. Schecklmann, A. C. Ehlis, and A. J. Fallgatter, "Simulation of near-infrared light absorption considering individual head and prefrontal cortex anatomy: Implications for optical neuroimaging," *PLoS One*, vol. 6, no. 10, Oct. 2011, doi: 10.1371/journal.pone.0026377.

- [225] K. Budidha and P. A. Kyriacou, "Investigating the origin of photoplethysmography using a multiwavelength monte carlo model," *Physiol. Meas.*, vol. 41, no. 8, p. 084001, Sep. 2020, doi: 10.1088/1361-6579/aba008.
- [226] S. Chatterjee, J. P. Phillips, and P. A. Kyriacou, "Monte Carlo investigation of the effect of blood volume and oxygen saturation on optical path in reflectance pulse oximetry," *Biomed. Phys. Eng. Express*, vol. 2, no. 6, p. 065018, Dec. 2016, doi: 10.1088/2057-1976/2/6/065018.
- [227] C. D. Kurth, H. Liuf, W. S. Thayers, and B. Chance, "A dynamic phantom brain model for near-infrared spectroscopy," *Phys. Med. Biol.*, vol. 40, pp. 2079–2092, 1995.
- [228] Z. J. Chen *et al.*, "A realistic brain tissue phantom for intraparenchymal infusion studies," *J. Neurosurg.*, vol. 101, no. 2, pp. 314–322, 2004, doi: 10.3171/jns.2004.101.2.0314.
- [229] S. Pfaffenberger *et al.*, "Can a commercial diagnostic ultrasound device accelerate thrombolysis?: An in vitro skull model," *Stroke*, vol. 36, no. 1, pp. 124–128, Jan. 2005, doi: 10.1161/01.STR.0000150503.10480.a7.
- [230] H. Iida *et al.*, "Three-dimensional brain phantom containing bone and grey matter structures with a realistic head contour," *Ann. Nucl. Med.*, vol. 27, no. 1, pp. 25–36, Jan. 2013, doi: 10.1007/s12149-012-0655-7.
- [231] S. Bottan, "In-vitro model of intracranial pressure and cerebrospinal fluid dynamics," 2013. doi: 10.3929/ethz-a-009904657.
- [232] B. J. Mohammed and A. M. Abbosh, "Realistic head phantom to test microwave systems for brain imaging," *Microw. Opt. Technol. Lett.*, vol. 56, no. 4, pp. 979–982, Apr. 2014, doi: 10.1002/mop.28229.
- [233] G. Menikou, T. Dadakova, M. Pavlina, M. Bock, and C. Damianou, "MRI compatible head phantom for ultrasound surgery," *Ultrasonics*, vol. 57, no. C, pp. 144–152, Mar. 2015, doi: 10.1016/j.ultras.2014.11.004.
- [234] L. A. Dempsey, M. Persad, S. Powell, D. Chitnis, and J. C. Hebden, "Geometrically complex 3D-printed phantoms for diffuse optical imaging," *Biomed. Opt. Express*, vol. 8, no. 3, p. 1754, Mar. 2017, doi: 10.1364/BOE.8.001754.
- [235] A. Afshari *et al.*, "Cerebral oximetry performance testing with a 3D-printed vascular array phantom," *Biomed. Opt. Express*, vol. 10, no. 8, p. 3731, Aug. 2019, doi: 10.1364/boe.10.003731.
- [236] A. Afshari *et al.*, "Evaluation of the robustness of cerebral oximetry to variations in skin pigmentation using a tissue-simulating phantom," *Biomed. Opt. Express*, vol. 13, no. 5, p. 2909, 2022, doi: 10.1364/boe.454020.
- [237] A. Benninghaus, O. Balédent, A. Lokossou, C. Castelar, S. Leonhardt, and K. Radermacher, "Enhanced in vitro model of the CSF dynamics," *Fluids Barriers CNS*, vol. 16, no. 1, p. 11, Apr. 2019, doi: 10.1186/s12987-019-0131-z.
- [238] R. G. Nagassa, P. G. McMenamin, J. W. Adams, M. R. Quayle, and J. V. Rosenfeld, "Advanced 3D printed model of middle cerebral artery aneurysms for neurosurgery simulation," *3D Print. Med.*, vol. 5, no. 1, p. 11, Dec. 2019, doi: 10.1186/s41205-019-0048-9.
- [239] M. Roldan and P. A. Kyriacou, "Head Phantom for the Acquisition of Pulsatile Optical Signals for Traumatic Brain Injury Monitoring," *Photonics*, vol. 10, no. 5, 2023, doi: 10.3390/photonics10050504.
- [240] P. A. van Nijnatten, *Spectrophotometry - Accurate measurement of optical properties of*

- [255] K. L. Beals, C. L. Smith, and S. M. Dodd, "Brain Size, Cranial Morphology, Climate, and Time Machines¹," *Curr. Anthropol.* V01, vol. 25, 1984.
- [256] R. Grant *et al.*, "Human cranial csf volumes measured by mri: sex and age influences," *Magnetic Reson. Imagmg*, vol. 5, pp. 465–468, 1987.
- [257] R. Aghababian, *Essentials of emergency medicine*. Jones and Bartlett, 2006.
- [258] M. Matsumae *et al.*, "Age-related changes in intracranial compartment volumes in normal adults assessed by magnetic resonance imaging," *J. Neurosurg.*, vol. 84, no. 6, pp. 982–991, 1996, doi: 10.3171/jns.1996.84.6.0982.
- [259] K.-H. Chan, D. Miller, M. Dearden, and N. M. Dearden, "Intracranial blood flow velocity after head injury: relationship to severity of injury, time, neurological status and outcome," *Neurosurgery, and Psychiatry*, vol. 55, pp. 787–791, 1992, doi: 10.1136/jnnp.55.9.787.
- [260] A. T. Rai, J. P. Hogg, B. Cline, and G. Hobbs, "Cerebrovascular geometry in the anterior circulation: an analysis of diameter, length and the vessel taper," *J. Neurointerv. Surg.*, vol. 5, no. 4, pp. 371–375, Jul. 2013, doi: 10.1136/neurintsurg-2012-010314.
- [261] M. Nomoni, J. M. May, and P. A. Kyriacou, "Fabricating Novel PDMS Vessels for Phantoms in Photoplethysmography Investigations," in *Proceedings of the Annual International Conference of the IEEE Engineering in Medicine and Biology Society, EMBS*, Institute of Electrical and Electronics Engineers Inc., Jul. 2020, pp. 4458–4461. doi: 10.1109/EMBC44109.2020.9176476.
- [262] S. Mujagić, "The inner diameter of arteries of the circle of willis regarding gender and age on magnetic resonance angiography," *Acta Medica Salin.*, vol. 42, pp. 6–12, 2013, Accessed: Nov. 12, 2019. [Online]. Available: https://www.researchgate.net/publication/304081397_THE_INNER_DIAMETER_OF_ARTERIES_OF_THE_CIRCLE_OF_WILLIS_REGARDING_GENDER_AND_AGE_ON_MAGNETIC_RESONANCE_ANGIOGRAPHY/citation/download
- [263] C. E. Taylor, Z. W. Dzikowski, and G. E. Miller, "Automation of the Harvard Apparatus Pulsatile Blood Pump," *J. Med. Devices, Trans. ASME*, vol. 6, no. 4, Oct. 2012, doi: 10.1115/1.4007637.
- [264] R. Erbel and H. Eggebrecht, "Aortic dimensions and the risk of dissection," *Heart*, vol. 92, no. 1. BMJ Publishing Group, pp. 137–142, Jan. 2006. doi: 10.1136/hrt.2004.055111.
- [265] C. T. DOTTER, D. J. ROBERTS, and I. STEINBERG, "Aortic length: angiocardigraphic measurements," *Circulation*, vol. 2, no. 6, pp. 915–920, 1950, doi: 10.1161/01.CIR.2.6.915.
- [266] J. Krejza *et al.*, "Carotid artery diameter in men and women and the relation to body and neck size," *Stroke*, vol. 37, no. 4, pp. 1103–1105, Apr. 2006, doi: 10.1161/01.STR.0000206440.48756.f7.
- [267] F. A. Choudhry, J. T. Grantham, A. T. Rai, and J. P. Hogg, "Vascular geometry of the extracranial carotid arteries: An analysis of length, diameter, and tortuosity," *J. Neurointerv. Surg.*, vol. 8, no. 5, pp. 536–540, May 2016, doi: 10.1136/neurintsurg-2015-011671.
- [268] D. Tartière, P. Seguin, C. Juhel, B. Laviolle, and Y. Mallédant, "Estimation of the diameter and cross-sectional area of the internal jugular veins in adult patients," *Crit. Care*, vol. 13, no. 6, Dec. 2009, doi: 10.1186/cc8200.
- [269] Z. Feldman *et al.*, "Effect of head elevation on intracranial pressure, cerebral perfusion pressure, and cerebral blood flow in head-injured patients," *J. Neurosurg.*, vol. 76, no. 2, pp. 207–211, Feb. 1992, doi: 10.3171/jns.1992.76.2.0207.

- [270] J. D. Alarcon *et al.*, "Elevation of the head during intensive care management in people with severe traumatic brain injury," *Cochrane Database of Systematic Reviews*, vol. 2017, no. 12. John Wiley and Sons Ltd, Dec. 28, 2017. doi: 10.1002/14651858.CD009986.pub2.
- [271] T. J. Akl *et al.*, "In vitro performance of a perfusion and oxygenation optical sensor using a unique liver phantom," *Opt. Diagnostics Sens. XII Towar. Point-of-Care Diagnostics; Des. Perform. Valid. Phantoms Used Conjunction with Opt. Meas. Tissue IV*, vol. 8229, p. 822904, 2012, doi: 10.1117/12.908645.
- [272] I. Tachtsidis, "Biomedical Optics Research Laboratory (BORL)," *GitHub - multimodalspectroscopy/UCL-NIR-Spectra*, 2022. <https://github.com/multimodalspectroscopy/UCL-NIR-Spectra> (accessed Sep. 29, 2022).
- [273] J. M. May, E. Mejía-mejía, M. Nomoni, K. Budidha, C. Choi, and P. A. Kyriacou, "Effects of Contact Pressure in Reflectance Photoplethysmography in an In Vitro Tissue-Vessel Phantom," *Sensors 2021, Vol. 21, Page 8421*, vol. 21, no. 24, p. 8421, Dec. 2021, doi: 10.3390/S21248421.
- [274] F. Lange, L. Dunne, L. Hale, and I. Tachtsidis, "MAESTROS: A Multiwavelength Time-Domain NIRS System to Monitor Changes in Oxygenation and Oxidation State of Cytochrome-C-Oxidase," *IEEE J. Sel. Top. Quantum Electron.*, vol. 25, no. 1, 2019, doi: 10.1109/JSTQE.2018.2833205.
- [275] E. Kandel, J. H. Schwartz, and T. Jessell, *Principles of Neural Science*, 5th ed. New York: McGraw Hill, 2000.
- [276] T. Brinker, E. Stopa, J. Morrison, and P. Klinge, "A new look at cerebrospinal fluid circulation," *Fluids and Barriers of the CNS*, vol. 11, no. 1. BioMed Central Ltd., p. 10, May 01, 2014. doi: 10.1186/2045-8118-11-10.
- [277] F. Bevilacqua, D. Piguet, P. Marquet, J. D. Gross, B. J. Tromberg, and C. Depeursinge, "In vivo local determination of tissue optical properties: applications to human brain," *Appl. Opt.*, vol. 38, no. 22, p. 4939, 1999, doi: 10.1364/ao.38.004939.
- [278] T. Correia, A. Gibson, and J. Hebden, "Identification of the optimal wavelengths in optical topography using photon density measurement functions," *Biomed. Appl. Light Scatt. III*, vol. 7187, no. May 2014, p. 718718, 2009, doi: 10.1117/12.809295.
- [279] H. Magsood, F. Syeda, K. Holloway, I. C. Carmona, and R. L. Hadimani, "Safety Study of Combination Treatment: Deep Brain Stimulation and Transcranial Magnetic Stimulation," *Front. Hum. Neurosci.*, vol. 14, no. April, pp. 1–8, 2020, doi: 10.3389/fnhum.2020.00123.
- [280] M. Roldan and P. A. Kyriacou, "A non-Invasive Optical Multimodal Photoplethysmography-Near Infrared Spectroscopy Sensor for Measuring Intracranial Pressure and Cerebral Oxygenation in Traumatic Brain Injury," *Appl. Sci.*, 2023, doi: 10.3390/app13085211.
- [281] P. A. Kyriacou and J. Allen, *Photoplethysmography Technology, Signal Analysis and Applications*. London, United Kingdom: Elsevier, 2021. doi: 10.1016/C2020-0-00098-8.
- [282] M. Taylor-Williams, G. Spicer, G. Bale, and S. E. Bohndiek, "Noninvasive hemoglobin sensing and imaging: optical tools for disease diagnosis," *J. Biomed. Opt.*, vol. 27, no. 08, 2022, doi: 10.1117/1.jbo.27.8.080901.
- [283] K. Budidha and P. A. Kyriacou, "Photoplethysmography technology," in *Photoplethysmography Technology, Signal Analysis and Applications*, P. A. Kyriacou and J. Allen, Eds., ELSEVIER, 2021, pp. 43–67.
- [284] Y. Mendelson and B. D. Ochs, "Noninvasive Pulse Oximetry Utilizing Skin Reflectance

- Photoplethysmography," *IEEE Trans. Biomed. Eng.*, vol. 35, no. 10, pp. 798–805, 1988, doi: 10.1109/10.7286.
- [285] A. S. Tucker, R. M. Fox, and R. J. Sadle, "Biocompatible, High Precision, Wideband, Improved Howland Current Source With Lead-Lag Compensation," *IEEE Trans. Biomed. Circuits Syst.*, vol. 7, no. 1, Feb. 2013, Accessed: Feb. 24, 2022. [Online]. Available: <https://ieeexplore.ieee.org/stamp/stamp.jsp?tp=&arnumber=6221965>
- [286] K. Budidha, V. Rybynok, and P. A. Kyriacou, "Design and Development of a Modular, Multichannel Photoplethysmography System," *IEEE Trans. Instrum. Meas.*, vol. 67, no. 8, pp. 1954–1965, Aug. 2018, Accessed: Feb. 07, 2022. [Online]. Available: <https://ieeexplore.ieee.org/stamp/stamp.jsp?tp=&arnumber=8318902>
- [287] M. Elgendi, "Optimal signal quality index for photoplethysmogram signals," *Bioengineering*, vol. 3, no. 4, pp. 1–15, 2016, doi: 10.3390/bioengineering3040021.
- [288] C. Orphanidou, *Signal Quality Assessment in Physiological Monitoring*. in SpringerBriefs in Bioengineering. Cyprus: Springer International Publishing, 2018. doi: 10.1007/978-3-319-68415-4.
- [289] R. Krishnan, B. Natarajan, and S. Warren, "Two-stage approach for detection and reduction of motion artifacts in photoplethysmographic data," *IEEE Trans. Biomed. Eng.*, vol. 57, no. 8, pp. 1867–1876, 2010, doi: 10.1109/TBME.2009.2039568.
- [290] M. Elgendi, I. Norton, M. Brearley, D. Abbott, and D. Schuurmans, "Systolic Peak Detection in Acceleration Photoplethysmograms Measured from Emergency Responders in Tropical Conditions," *PLoS One*, vol. 8, no. 10, p. 76585, 2013, doi: 10.1371/journal.pone.0076585.
- [291] M. Roldan and P. A. Kyriacou, "Optical sensor for non-invasive intracranial pressure monitoring in traumatic brain injury," in *SPIE conference*, SPIE, Ed., San Francisco: SPIE West Photonics, 2023. doi: <https://doi.org/10.1117/12.2649746>.
- [292] C. El Hajj, "Machine learning techniques for the prediction of systolic and diastolic blood pressure utilising the photoplethysmogram," 2021.
- [293] J. Park, H. S. Seok, S.-S. Kim, and H. Shin, "Photoplethysmogram Analysis and Applications: An Integrative Review," *Front. Physiol.*, vol. 12, p. 2511, Mar. 2022, doi: 10.3389/FPHYS.2021.808451/BIBTEX.
- [294] S. Lipovetsky, "Pareto 80/20 law: derivation via random partitioning," *Int. J. Math. Educ. Sci. Technol.*, vol. 40, no. 2, pp. 271–277, 2009, doi: 10.1080/00207390802213609.
- [295] L. Zacchetti, S. Magnoni, F. Di Corte, E. R. Zanier, and N. Stocchetti, "Accuracy of intracranial pressure monitoring: systematic review and meta-analysis.," *Crit. Care*, vol. 19, p. 420, Dec. 2015, doi: 10.1186/s13054-015-1137-9.
- [296] S. Suzuki, S. Takasaki, T. Ozaki, and K. Yukio, "A tissue oxygenation monitor using NIR spatially resolved spectroscopy," in *SPIE conference on optical tomography and spectroscopy of tissue III*, California, 1999.
- [297] G. Themelis *et al.*, "Near-infrared spectroscopy measurement of the pulsatile component of cerebral blood flow and volume from arterial oscillations," *J. Biomed. Opt.*, vol. 12, no. 1, p. 014033, 2007, doi: 10.1117/1.2710250.
- [298] Z. Kováčsová, "A Novel Approach to Monitor Tissue Oxygen Saturation with Broadband Near-Infrared Spectroscopy," 2020.
- [299] A. A. Sanni and K. K. McCully, "Interpretation of near-infrared spectroscopy (NIRS) signals in

- skeletal muscle," *J. Funct. Morphol. Kinesiol.*, vol. 4, no. 2, 2019, doi: 10.3390/jfmk4020028.
- [300] H. L. Edmonds, "Detection and correction of brain oxygen: Surgical and Critical Care Applications of the INVOS Cerebral/Somatic Oximeter," 2018. [Online]. Available: [medtronic.com/covidien/en-gb/index.html](https://www.medtronic.com/covidien/en-gb/index.html)
- [301] R. N. Kreeger, C. Ramamoorthy, S. C. Nicolson, W. A. Ames, and et al., "Development and Evaluation of a Near Infrared Cerebral Oximeter for Congenital Heart Disease," in *Society of Thoracic Surgeons meeting*, Ft. Lauderdale, Florida, 2012.
- [302] P. B. Benni, D. MacLeod, K. Ikeda, and H. M. Lin, "A validation method for near-infrared spectroscopy based tissue oximeters for cerebral and somatic tissue oxygen saturation measurements," *J. Clin. Monit. Comput.*, vol. 32, no. 2, pp. 269–284, 2018, doi: 10.1007/s10877-017-0015-1.
- [303] S. N. Davie and H. P. Grocott, "Impact of Extracranial Contamination on Regional," no. 4, 2012.
- [304] A. V. Patil, J. Safaie, H. A. Moghaddam, F. Wallois, and R. Grebe, "Experimental investigation of NIRS spatial sensitivity," *Biomed. Opt. Express*, vol. 2, no. 6, p. 1478, 2011, doi: 10.1364/boe.2.001478.
- [305] G. Fischer, "EQUANOX Advance™ Sensor," 2011. www.noninequanox.com (accessed Jan. 06, 2023).
- [306] Hamamatsu Corporation, "Near infrared oxygenation monitor NIRO-200NX," 2019. www.hamamatsu.com (accessed Jan. 06, 2023).
- [307] D. Redford, S. Paidy, and F. Kashif, "Absolute and Trend Accuracy of a New Regional Oximeter in Healthy Volunteers During Controlled Hypoxia," vol. 119, no. 6, pp. 1315–1319, 2014, doi: 10.1213/ANE.0000000000000474.
- [308] J. Kim, J. Kim, and H. Ko, "Low-power photoplethysmogram acquisition integrated circuit with robust light interference compensation," *Sensors (Switzerland)*, vol. 16, no. 1, pp. 1–11, 2016, doi: 10.3390/s16010046.
- [309] J. B. Fischer *et al.*, "Non-Invasive Estimation of Intracranial Pressure by Diffuse Optics: A Proof-of-Concept Study," *J. Neurotrauma*, vol. 37, no. 23, pp. 2569–2579, 2020, doi: 10.1089/neu.2019.6965.
- [310] A. Ruesch, S. Schmitt, J. Yang, M. A. Smith, and J. M. Kainerstorfer, "Fluctuations in intracranial pressure can be estimated non-invasively using near-infrared spectroscopy in non-human primates," *J. Cereb. Blood Flow Metab.*, vol. 40, no. 11, pp. 2304–2314, 2020, doi: 10.1177/0271678X19891359.
- [311] A. Ruesch, D. Acharya, S. Schmitt, J. Yang, M. A. Smith, and J. M. Kainerstorfer, "Comparison of static and dynamic cerebral autoregulation under anesthesia influence in a controlled animal model," *PLoS One*, vol. 16, no. 1 January, pp. 1–16, 2021, doi: 10.1371/journal.pone.0245291.
- [312] F. A. J. Relander *et al.*, "Using near-infrared spectroscopy and a random forest regressor to estimate intracranial pressure," *Neurophotonics*, vol. 9, no. 04, pp. 1–16, 2022, doi: 10.1117/1.nph.9.4.045001.
- [313] A. Ruesch, J. Yang, S. Schmitt, D. Acharya, M. A. Smith, and J. M. Kainerstorfer, "Estimating intracranial pressure using pulsatile cerebral blood flow measured with diffuse correlation spectroscopy: erratum," *Biomed. Opt. Express*, vol. 13, no. 2, p. 710, 2022, doi: 10.1364/boe.452731.

- [314] A. Ruesch, J. Yang, S. Schmitt, D. Acharya, M. A. Smith, and J. M. Kainerstorfer, "Estimating intracranial pressure using pulsatile cerebral blood flow measured with diffuse correlation spectroscopy: erratum," *Biomed. Opt. Express*, vol. 13, no. 2, p. 710, 2020, doi: 10.1364/boe.452731.
- [315] W. B. Baker *et al.*, "Noninvasive optical monitoring of critical closing pressure and arteriole compliance in human subjects," *J. Cereb. Blood Flow Metab.*, vol. 37, no. 8, pp. 2691–2705, 2017, doi: 10.1177/0271678X17709166.
- [316] K.-C. Wu *et al.*, "Validation of diffuse correlation spectroscopy measures of critical closing pressure against transcranial Doppler ultrasound in stroke patients," *J. Biomed. Opt.*, vol. 26, no. 03, 2021, doi: 10.1117/1.jbo.26.3.036008.
- [317] R. Al-Halawani, S. Chatterjee, and P. A. Kyriacou, "Monte Carlo Simulation of the Effect of Human Skin Melanin in Light-Tissue Interactions.," *Annu. Int. Conf. IEEE Eng. Med. Biol. Soc. IEEE Eng. Med. Biol. Soc. Annu. Int. Conf.*, vol. 2022, pp. 1598–1601, Jul. 2022, doi: 10.1109/EMBC48229.2022.9871350.
- [318] M. Shimada, Y. Yamada, M. Itoh, and T. Yatagai, "Melanin and blood concentration in a human skin model studied by multiple regression analysis: assessment by Monte Carlo simulation.," *Phys. Med. Biol.*, vol. 46, no. 9, pp. 2397–2406, Sep. 2001, doi: 10.1088/0031-9155/46/9/309.
- [319] M. Mamouei, S. Chatterjee, M. Razban, M. Qassem, and P. A. Kyriacou, "Design and analysis of a continuous and non-invasive multi-wavelength optical sensor for measurement of dermal water content," *Sensors*, vol. 21, no. 6, pp. 1–12, Mar. 2021, doi: 10.3390/S21062162.